UNIVERSITÉ DE GRENOBLE

THÈSE

Pour obtenir le grade de

DOCTEUR DE L'UNIVERSITÉ DE GRENOBLE

Spécialité : **Physique Subatomique et Astroparticules**

Arrêté ministériel : 7 août 2006

Présentée par

Romain MAISONOBE

Thèse dirigée par **Oliver ZIMMER** et
codirigée par **Torsten SOLDNER**

préparée au sein du **Institut Laue-Langevin**
dans **l'École Doctorale de Physique**

Measurement of the angular correlation coefficient *a* between electron and antineutrino in neutron β-decay with the spectrometer *a*SPECT

Thèse soutenue publiquement le **25 Février 2014**,
devant le jury composé de :

M. Dominique REBREYEND
Directeur de Recherche CNRS, LPSC Grenoble, Président du jury

M. Nathal SEVERIJNS
Professeur, Katholieke Universiteit Leuven, Rapporteur

M. Etienne LIENARD
Maître de Conférence HDR, LPC Caen, Rapporteur

M. Oliver ZIMMER
Professeur, Institut Laue-Langevin de Grenoble, Directeur de thèse

Remerciements

Je tiens à remercier Oliver Zimmer et Torsten Soldner, respectivement directeur et encadrant de thèse, de m'avoir permis de participer à l'expérience aSPECT à l'ILL. Je les remercie pour leurs conseils et nos nombreuses discussions qui m'ont permis d'avancer dans mon travail. Je remercie également Martin Simson, post-doc à l'ILL, qui a pris le temps de me former sur le système de détection et de m'apprendre son fonctionnement et son assemblage sur le plan technique et électronique.

Mes remerciements vont également à Marcus Beck, Michael Borg, Werner Heil, Christian Schmidt et Alexander Wunderle de Institut für Physik, Universität Mainz (Allemagne) ; Michael Klopf et Gertrud Konrad de Institute of Atomic and Subatomic Physics, TU Wien (Autriche) ; Ferenc Glück de IEKP, Universität Karlsruhe (Allemagne) ; et Stefan Baeßler de Physics Department, University of Virginia, Charlottesville (USA). Merci à vous tous pour ces trois années.

Je tiens à remercier Etienne Liénard et Nathal Severijns d'avoir accepté de participer à mon jury de thèse en tant que rapporteurs. Mes remerciements vont également à Dominique Rebreyend d'avoir accepté de présider mon jury. Je les remercie pour leur jugement et leurs conseils dans l'écriture de la version finale de mon manuscrit.

Je remercie Christine Klauser, doctorante à l'ILL et au TU Wien, pour son aide et sa contribution dans la caractérisation du faisceau de neutrons à PF1b. Merci également pour nos passionnantes discussions. Dans un même cadre, je remercie Jacqueline Erhart , doctorante au TU Wien, avec qui j'ai travaillé à la mesure du champ magnétique en 2011.

J'envoie un grand merci aux quatre stagiaires ILL que j'ai eu la chance de co-encadrer durant ces trois années : Pierre Pauly, Daniel Payne, Pilar Guimera Milan et Romain Virot. Ce fut un réel plaisir de les rencontrer et de travailler avec eux (et de les faire travailler pour moi). Je leur souhaite également bon courage pour la suite, surtout à Romain qui a eu la chance (ou la malchance) de commencer sa thèse à l'ILL.

Je remercie la direction de l'Institut Laue-Langevin de Grenoble (qui a changé au cours de mes trois années de thèse) de m'avoir accueilli au sein de ce laboratoire international.

Plus particulièrement, mes remerciements vont aux membres du groupe NPP de l'ILL où j'ai travaillé. Un remerciement spécial pour Angelika Taffut, secrétaire du groupe, avec qui discuter était un réel plaisir. Je la remercie grandement pour son aide dans l'organisation de ma soutenance. Je remercie mes autres collègues : Felix, Florian, Peter, Camille (ESS), Aurélien, Michael, Ulli, Herbert, Fabien, ... Désolé si j'ai oublié des noms mais je n'oublie pas de les remercier.

Un grand merci à Didier Berruyer, notre technicien, qui a accepté un projet farfelu que j'ai testé en première année. Même si cela n'a pas fonctionné comme prévu, le projet restait très intéressant dans sa conception.

Je remercie Gaëlle et Isabelle, ingénieurs de sécurité à l'ILL. Et je m'excuse aussi auprès d'elles d'avoir été aussi maladroit et d'avoir eu des accidents. Pardon et merci aux techniciens, aux responsables et aux pontiers de l'ILL pour être intervenus à plusieurs reprises lors de la mise en place de la zone de test en 2012. Ces personnes sont si nombreuses que je ne peux toutes les citer mais je ne l'ai oublie pas.

Je remercie l'ensemble des enseignants et encadrants au cours de ma formation universitaire qui m'ont donné la possibilité de faire mes premiers pas dans la recherche en physique des particules (stages sur ATLAS) et d'intégrer le Master de physique subatomique. Merci à eux pour cela et pour leur soutient.

Mes derniers remerciements vont à mes parents et mon frère qui m'ont toujours soutenu dans ma passion pour les sciences et dans mon parcours. Ces remerciements vont également à l'ensemble de ma famille avec une pensée particulière pour mes grand-parents.

Merci à mes amis et plus particulièrement à Jonathan et Aurélie pour leur présence, leur soutient et leurs encouragements.

Contents

List of Figures

List of Tables

Introduction

Depuis les grecs de l'Antiquité, la vision d'un monde fait de briques insécables et immuables a grandement évolué au cours du XX$^{\text{ème}}$ siècle. De cette lointaine époque, les scientifiques ont conservé le nom d'atome pour décrire les composants de la matière. En revanche, ces briques ne sont ni insécables, ni immuables. De nombreuses expériences ont permis de montrer l'aspect composite de l'atome comprenant un noyau autour duquel gravitent des électrons. Mais on ne s'arrête pas là, le noyau atomique est lui aussi composite. Ernest Rutherford montra expérimentalement en 1919 que le noyau de l'atome d'hydrogène est présent dans chaque noyau atomique : en envoyant des atomes d'hélium, aussi appelés particules alpha, dans un gaz d'azote, il détecta la signature de noyaux d'hydrogène ($^4_2\mathrm{He} + {}^{14}_{7}\mathrm{N} \rightarrow {}^{17}_{8}\mathrm{O} + {}^1_1\mathrm{H}$). Il donna le nom de protons à ces noyaux d'hydrogène. Puis, en 1932, James Chadwick découvrit le neutron, le deuxième constituant du noyau atomique : cette fois, les particules alpha ont servi à bombarder du béryllium, ce qui a eu pour effet la production d'une particule non chargée : le neutron ($^4_2\mathrm{He} + {}^9_4\mathrm{Be} \rightarrow {}^{12}_{6}\mathrm{C} + n$).

Avec ces découvertes, les technologies ont évolué et les accélérateurs de particules sont montés en puissance pour aller plus loin au coeur de la matière. C'est en 1968 que l'hypothèse, émise par Gell-Mann et Zweig, sur l'existence de quarks composant les protons et les neutrons a été vérifiée expérimentalement. D'autres particules comme les quarks ont été mises en évidence : les leptons comprenant l'électron et ses compagnons plus massifs (le muon et le tau), ainsi que les neutrinos correspondants. Ces particules sont dites élémentaires et sont regroupées dans le Modèle Standard. Les expériences se multiplient, les détecteurs deviennent de plus en plus performants et les accélérateurs permettent d'atteindre des énergies de plus en plus élevées. Ces prouesses technologiques ont notamment permis en Juillet 2012 de détecter le boson de Higgs responsable de la masse des particules. Toutefois, le Modèle Standard est incomplet : la gravitation n'y est pas encore incluse, la matière noire contribuant à la masse manquante de l'Univers n'y est pas décrite...

Un autre point d'ombre au Modèle Standard concerne l'asymétrie baryonique dans l'Univers. Cela implique que ce modèle pourrait être une limite à basse énergie d'une description plus générale du monde physique. Le neutron se trouve être un candidat idéal pour tester le Modèle Standard à basse énergie. Cette particule, lorsqu'elle est libre hors d'un noyau, se désintègre suivant le processus bêta : un proton, un électron et un antineutrino sont émis. Un exemple d'étude consiste à mesurer le moment dipolaire du neutron : même si sa charge électrique est nulle, il est pourtant constitué de particules chargées (un quark *up* de charge +2/3 et deux quarks *down* de charge -1/3 chacun). L'association de ces charges pourrait conduire à un moment dipolaire électrique non nul. D'autres paramètres mesurables sont les coefficients angulaires qui sont définis entre les moments respectifs des produits de désintégration ainsi qu'avec le spin du neutron. Ces paramètres sont liés aux constantes de couplage de l'interaction faible qui décrit le processus de désintégration bêta. Une mesure de précision de ces coefficients de corrélation angulaire permet une détermination plus approfondie de certains paramètres du Modèle Standard. Les différents aspects théoriques sont abordés dans le premier chapitre.

L'expérience *a*SPECT sur laquelle j'ai travaillé au cours de ma thèse a pour objectif de mesurer, avec une précision inégalée, le coefficient de corrélation angulaire entre l'électron et l'antineutrino, noté a. L'antineutrino étant une particule interagissant peu avec la matière, aSPECT utilise une manière indirecte de mesurer a via la mesure du spectre d'énergie du proton. La forme de ce spectre d'énergie est corrélée à la valeur du coefficient. C'est dans cet objectif que le spectromètre a été conçu suivant des principes bien spécifiques présentés dans le chapitre deux. Les protons émis ont une énergie maximale de 751.4 eV. Il s'agit donc de particules à basse énergie qu'il faut distinguer des électrons de plus haute énergie et amener jusqu'au détecteur. Sur leur trajet, les protons sont sélectionnés en fonction de leur énergie grâce à une barrière de potentiel et ensuite comptés par le détecteur. La barrière de potentiel est ajustable et permet de balayer l'ensemble du spectre d'énergie des protons.

L'un des principaux challenges de cette expérience concerne la détection des protons. Le détecteur utilisé est un semi-conducteur dont le signal sortant est traité par une chaîne électronique : amplification du signal et traitement. Le troisième chapitre décrit l'ensemble de ce système de détection. Mes premiers travaux ont consisté à évaluer les performances et les limites du système tel qu'il était en 2011. Par la suite, des modifications ont été apportées afin d'améliorer la détection des protons.

L'expérience aSPECT se déroule à l'Institut Laue-Langevin de Grenoble où se trouve le réacteur nucléaire dédié à la recherche fournissant le plus haut flux de neutrons au monde. Le spectromètre est installé sur une ligne de faisceau de neutrons froids : PF1b. Le chapitre quatre regroupe la description de cette installation ainsi que la caractérisation du spectromètre (profils du faisceau, position du détecteur, ...).

En 2011, un temps de faisceau a été attribué à aSPECT permettant de tester les nouveaux composants et modifications apportés au spectromètre. En 2012, des tests hors faisceau ont été menés pour l'amélioration du système de détection. Cela a également été l'occasion de mener des investigations sur le vide et sa stabilité : le volume interne du spectromètre est d'approximativement 100 litres et la pression obtenue est de l'ordre de 10^{-9} mbar. Dans le chapitre cinq, je présente une analyse du vide à partir de mesures réalisée avec un spectromètre de masse.

J'ai effectué de nombreuses mesures de bruit de fond dans différentes configurations : hors faisceau de neutron en 2012 et dans les conditions d'un temps de faisceau en 2013. Ces mesures et analyses ont mis en évidence un bruit de fond complexe qui est composé d'une partie constante et d'une autre non-constante. Cette dernière est un problème dans la méthode de soustraction du bruit de fond. Une investigation détaillée a permis de trouver un modèle pour décrire ce bruit de fond non-constant et de calculer la correction résultante en fonction de la tension de la barrière de potentiel. Différents modèles ont été testés dont l'analyse et leur impact sur le coefficient a sont présentés dans les chapitre six et sept. De plus, plusieurs effets systématiques ont été testés durant ce temps de faisceau en 2013 et leur influence sur le coefficient a a été étudiée. Il s'agit d'une analyse et de résultats préliminaires qui sont présentés dans le chapitre sept : des analyses plus fines requièrent des simulations.

Introduction

Since the ancient Greeks, the vision of a world made of indivisible and immutable bricks has evolved greatly during the XX$^{\mathrm{th}}$ century. From those early days, scientists have kept the name "atom" to describe the components of matter. However, these bricks are not unbreakable or unchangeable. Many experiments have demonstrated the composite nature of the atom consisting of a nucleus and electrons orbiting around it. But it is not all, the atomic nucleus is also composite. Ernest Rutherford proved experimentally in 1919 that the nucleus of the hydrogen atom is present in each nucleus: by sending helium atoms, also called alpha particles, in nitrogen gas, he detected the signature of hydrogen nuclei (${}^{4}_{2}\mathrm{He} + {}^{14}_{7}\mathrm{N} \rightarrow {}^{17}_{8}\mathrm{O} + {}^{1}_{1}\mathrm{H}$). He gave the name of protons to these hydrogen nuclei. Then, in 1932, James Chadwick discovered the neutron, the second component of the atomic nucleus: this time, alpha particles were used to bombard beryllium, which has led to the production of an uncharged particle: the neutron (${}^{4}_{2}\mathrm{He} + {}^{9}_{4}\mathrm{Be} \rightarrow {}^{12}_{6}\mathrm{C} + n$).

With all of these discoveries, technologies have evolved and particle accelerators have become powerful to go further in the heart of the matter. It was in 1968 that the hypothesis proposed by Gell-Mann and Zweig about the existence of quarks has been verified experimentally. These particles are components of protons and neutrons. Other particles than quarks were discovered: leptons including electron and more massive companions (muon and tau), and the corresponding neutrinos. These are called elementary particles and are grouped in the Standard Model. Many experiments are proposed with detectors more sensitive and particles accelerators higher in energy. These technological improvements enabled, for example, to detect in July 2012 the Higgs boson which is responsible of the mass of particles. However, this Standard Model is incomplete: the gravitation has not yet been included into this model, the dark matter contribution to the missing mass of the Universe is not yet described.

Another unexplained point by the Standard Model concerns the baryon asymmetry in the Universe. These limitations imply that this model could be a low-energy limit of a more general description of the physical world. The neutron is an ideal candidate to test the Standard Model at low energy. This particle, when free out of a nucleus, decays following the beta process: a proton, an electron and an antineutrino are emitted. An example of study consists in measuring the electric dipole moment of the neutron: even if electric charge is zero, it is however made of charged particles (a *up* quark charge $+2/3\,e$ and two *down* quarks charge $-1/3\,e$ each). The combination of these charges could lead to a non-zero electric dipole moment. Other measurable parameters are the angular coefficients which are defined between the momenta of the decay products and with the neutron spin. These parameters are related to the coupling constants of the weak interaction which describes the beta-decay process. A precision measurement of the angular correlation coefficients allows a more detailed determination of some parameters of the Standard Model. These various theoretical aspects are presented and discussed in the first chapter.

The aSPECT experiment on which I worked during my PhD aims to measure with an improved accuracy the angular correlation coefficient between the electron and the antineutrino, called a. As the antineutrino has a weak interaction with matter, aSPECT used an indirect way to measure a by measuring the recoil proton energy spectrum. The shape of this spectrum is related to the value of the coefficient. It was in this objective that the spectrometer has been designed according to the principles presented in chapter two. The emitted protons have a maximum energy of 751.4 eV. So they are low energy particles which should be distinguished from electrons with higher energy, and then counted by the detector. On their path, protons are selected according to their energy by a potential barrier and then counted by the detector. The potential barrier is an adjustable electrostatic potential to scan the entire spectrum of proton energy.

A major challenge of this experiment concerns the detection of protons. The detector used is a semiconductor whose the output signal is treated by an electronic chain : amplification of the signal and processing. The third chapter presents this detection system. My first work consisted in evaluating the performances and limitations of the system in the configuration as it was in 2011. Thereafter, the system was modified to improve the detection of protons.

The aSPECT experiment takes place at the Institut Laue-Langevin in Grenoble where the nuclear reactor dedicated to the research delivers the world's higher neutron flux. The spectrometer is set up on a cold neutron beam line: PF1b. The chapter four presents the description of this installation and the characterization of the spectrometer (neutron beam profiles, position of the detector, ...).

In 2011, a beam time was attributed to aSPECT for testing new components and modifications of the spectrometer. In 2012 , tests without neutron beam were conducted for improvements of the detection. This was also used to conduct investigations about the vacuum and its stability: the main internal volume is approximately 100 liters and the pressure in the order of 10^{-9} mbar is obtained. In chapter five, I present an analysis of the vacuum from measurements made with a mass spectrometer.

I made several measurements of the background in different configurations: without neutron beam in 2012 and in the conditions of a beam time in 2013. These measurements and analysis highlighted that the background is complex and composed by a constant part and a non-constant one. This last part is a problem for the background subtraction. A detailed investigation allowed to find a model to describe this non-constant background and to calculate the resulting correction to apply in function of the voltage of the potential barrier. Different models were tested whose the analysis and the influence on the coefficient a are presented in chapters six and seven. Furthermore, several systematic effect were tested during the beam time of 2013 and their influence on the coefficient were investigated. This analysis gives preliminary results which are presented in the chapter seven: more investigations are required with simulations.

Chapter 1

Neutron particle physics

La physique des particules repose sur un cadre théorique développé dans les années 1960-1970 et appelé le *Modèle Standard*. Dans ce modèle sont recensées les *particules élémentaires* qui constituent la matière et décrivent trois des interactions fondamentales dans l'Univers. La base du Modèle Standard est une théorie quantique des champs compatible avec les principes de la mécanique quantique et de la relativité. Le neutron est une particule composite qui, lorsqu'elle est libre, se désintègre en un proton, un électron et un antineutrino. Des paramètres mesurables sont définis entre les moments de ces particules et le spin du neutron : les coefficients de corrélation angulaire. Ces coefficients sont liés dans la théorie *V-A* aux constantes de couplage de l'interaction faible. Ceci fait du neutron un laboratoire idéal pour tester le Modèle Standard à basse énergie en mesurant avec une grande précision de petites déviations par rapport aux prédictions du Modèle Standard. De plus, ces paramètres deviennent indépendants au-delà du Modèle Standard. En recoupant les différentes mesures de précision il est alors potentiellement possible de déboucher sur de la nouvelle physique.

1.1 The Standard Model

Elementary particles are listed in two groups in terms of their spin. A half-integer spin characterizes *fermions* which follow Fermi-Dirac statistics: two fermions with the same nature cannot be in the same quantum state. Particles with integer spin are *bosons* which follow Bose-Einstein statistics: the juxtaposition of identical quantum states for several bosons is allowed [1, 2].

These elementary particles are described by the theory of the Standard Model. The fundamentals for this theory were developed by Salam, Glashow and Weinberg in the 1960s.

1.1.1 Fermions

Fermions are the components of matter, they are "bricks" which are classified into two subgroups: the *quarks* and the *leptons*. In general, all fermions which are, for the moment, twelve, are classified in three families as it is represented in Tab 1.1.

Leptons can be free. In this group we can find the electron e and two massive versions of it: muon μ and tau τ. Each of these particles is associated to an almost massless neutrino ν that interacts only weakly with matter.

Quarks		Mass [MeV/c^2]	Electric charge [e]	**Leptons**	Mass [MeV/c^2]	Electric charge [e]
1st family	d	4.8	-1/3	e	$511\cdot10^{-3}$	-1
	u	2.3	2/3	ν_e	$< 10\cdot10^{-6}$	0
2nd family	s	95	-1/3	μ	106	-1
	c	$1.3\cdot10^3$	2/3	ν_μ	< 0.5	0
3rd family	b	$4.2\cdot10^3$	-1/3	τ	$1.8\cdot10^3$	-1
	t	$173\cdot10^3$	2/3	ν_τ	< 164	0

Table 1.1: Classification of the fundamental fermions.

Quarks, which are also six, cannot be observed in a free state. They are always bound to form composite particles called *mesons* where one quark is associated to one anti-quark[1], and *baryons* where three quarks are associated. The proton is composed of two *up* quarks (noted u) and one *down* quark (noted d). The neutron is composed of one *up* quark and two *down* quarks. The two pairs, *up* and *down*, and the electron compose the ordinary matter and they are stable because of their low mass.

Concerning the other families, particles are very massive and so they decay. The only possibility to observe them is to produce these particles with high energy collisions in accelerators such as the LHC.

1.1.2 Bosons

In addition to these twelve fermions, we have twelve **bosons** which carry fundamental interactions (see Tab 1.2). Actually, three of the four known fundamental interactions are described in the Standard Model:

- the electromagnetic interaction, which describes interactions between electrically charged particles, is carried by the *photon* (noted γ),
- the weak interaction, which manifests itself for example in β decays, is carried by the bosons W^+, W^- and Z^0,
- the strong interaction, which is responsible for the cohesion of the nucleons and the nucleus, is carried by eight *gluons* (noted g) between particles having a color charge[2] (these are quarks).

These three interactions have different characteristics due to the nature of their bosons. They are different in terms of range and of the kind of objects on which they act.

---

[1] Fermions each have one anti-fermion associated with the same physical characteristics but opposite additive quantum numbers, for example charges (electron's charge is *-1*, anti-electron, called positron, charge is *+1*).

[2] There are three color charges : red (R); blue (B), green (G). This quantum number was introduced to explain the fact that the proton can be composed of three quarks with the same spin which contradicts the Pauli exclusion principle. The gluon is composed of one color and one anti-color (noted $\bar{\cdot}$) : $R\overline{R}$, $B\overline{B}$, $G\overline{G}$, $R\overline{B}$, $R\overline{G}$, $B\overline{R}$, $B\overline{G}$, $G\overline{R}$, $G\overline{B}$. But the linear relation $R\overline{R} + B\overline{B} + G\overline{G} = 0$ reduces by 1 the number of degrees of freedom. This gives 8 gluons.

	Mass [GeV/c^2]	Electric charge [e]	Interactions	Range	Act on...
photon (γ)	0	0	electromagnetic	infinite	charged particles
W$^{\pm}$ Z^0	80.4 91.19	±1 0	weak	$< 10^{-18}$ m	leptons, quarks
gluons (g)	0	0	strong	$\approx 10^{-15}$ m	quarks

Table 1.2: Bosons and fundamental interactions.

1.1.3 The CKM matrix

All of these particles and their interactions are described precisely by the Standard Model which is based on quantum field theory. The quarks have a charge of +2/3 in the upper row and -1/3 in the lower row. Most transitions between the quarks happen within one family, but due to the weak interaction also decays between families are observed. In the Standard Model, the eigenstates of the quarks in weak interaction are not the same as their mass eigenstates. The weak eigenstates are linear combinations of the mass eigenstates from all three generations with the same charge. For the first two quark families, the linear combinations were formulated by Cabibbo in 1963 as a rotation matrix with a rotation angle θ_C (Cabibbo angle):

$$\begin{pmatrix} |d'\rangle \\ |s'\rangle \end{pmatrix} = \begin{pmatrix} \cos\theta_C & \sin\theta_C \\ -\sin\theta_C & \cos\theta_C \end{pmatrix} \cdot \begin{pmatrix} |d\rangle \\ |s\rangle \end{pmatrix} \tag{1.1}$$

Including the third quark generation, the previous is extended to 3×3 matrix: the Cabibbo-Kobayashi-Maskawa matrix. The CKM matrix is a unitary matrix about probability that quark changes flavor during weak interaction. It describes difference between free quarks eigenstates and quarks eigenstates in the weak interaction. We have the following relation where $|q\rangle$ are mass eigenstates, $|q'\rangle$ are flavor eigenstates and V_{ij} is the CKM matrix:

$$\begin{pmatrix} |d'\rangle \\ |s'\rangle \\ |b'\rangle \end{pmatrix} = \begin{pmatrix} V_{ud} & V_{us} & V_{ub} \\ V_{cd} & V_{cs} & V_{cb} \\ V_{td} & V_{ts} & V_{tb} \end{pmatrix} \cdot \begin{pmatrix} |d\rangle \\ |s\rangle \\ |b\rangle \end{pmatrix} \tag{1.2}$$

In the Standard Model theory, three quark generations are assumed. Due to this point, theory requires unitarity of the CKM matrix [3, 4]. One of the unitarity conditions for the first row is given by the following equation:

$$|V_{ud}|^2 + |V_{us}|^2 + |V_{ub}|^2 = 1 \tag{1.3}$$

However the Standard Model is not complete as if we see above for example it does not describe gravitation: the hypothesis of a boson called *graviton* was emitted. This boson has not been discovered yet but could give a quantum formalism for the gravitation in order to explain phenomena like black holes. Another point was not explained by field theory, the particles mass origin ; a mechanism was proposed in 1964 by Englert, Brout and Higgs [5, 6] which postulated the Higgs boson. This boson was discovered with the LHC at CERN in July 2012, and in 2013, François Englert and Peter Higgs received the Nobel Prize of Physics for their contributions. Furthermore, it cannot explain the number of quark generations, the baryon asymmetry in universe, the symmetry breaking, the existence of dark matter and dark energy. In this way, several experiments are proposed and take place at particles accelerators or in the field of astroparticles to investigate these different unknown points of the theory.

1.2 Neutron β-decay

The neutron decay is another way to investigate the Standard Model at the low-energy frontier. This process allows high precision measurements of small deviation from the Standard Model predictions [7]. So, the neutron is a powerful simple system which is used by several experiments as for example the investigation of a permanent electric dipole moment (EDM) [3], the neutron lifetime, the correlation coefficients... The experiment *a*SPECT aims to measure one of the correlation coefficients which are related to neutron decay. The following descriptions of the neutron decay and the correlation coefficients (next section) are based on the ones presented in the previous PhD theses done on the experiment *a*SPECT [8, 9, 10, 11].

1.2.1 The neutron

The neutron was discovered by James Chadwick in 1932 [12]. This discovery was done by bombarding beryllium with alpha particles: ${}_2^4\mathrm{He} +_4^9 \mathrm{Be} \rightarrow_6^{12} \mathrm{C} + n$. The neutron is a neutral particle with mass 0.1% higher than proton's mass, a spin of 1/2 and no electric charge. Free neutron decays due to its slightly higher mass compared to the sum of proton and electron mass. The lifetime of neutron is about 15 minutes, after which it decays emitting one proton p, one electron e^- and one anti-neutrino $\overline{\nu_e}$:

$$n \rightarrow p + e^- + \overline{\nu_e} + 782.3\,\mathrm{keV} \tag{1.4}$$

The energy released is given by the mass difference of the neutron compared to proton and electron [13]. The daughter nucleus is a single proton, so no nuclear structure corrections are necessary. The neutron decay is a weak interaction process which is described, in the Standard Model, by three parameters: the Fermi constant G_F[4], the first element of the CKM matrix $|V_{\mathrm{ud}}|$ (transition of a down quark to an up one), and the ratio of the weak coupling constants $\lambda = \left|\frac{g_{\mathrm{A}}}{g_{\mathrm{V}}}\right|$ (axial-vector and vector coupling constants). From neutron decay, several parameters can be measured experimentally: the neutron decay is a strongly over-determined process in the Standard Model description. In these parameters, angular correlation coefficients were defined between the participating particles and their spin. These coefficients are used to re-write the neutron decay rate as follow[14]:

$$\frac{\mathrm{d}W}{\mathrm{d}\Omega_e \mathrm{d}\Omega_{\overline{\nu}} \mathrm{d}E} \propto 1 + b\frac{m_e}{E_e} + a\frac{\overrightarrow{p_e} \cdot \overrightarrow{p_{\overline{\nu}}}}{E_e E_{\overline{\nu}}} + \overrightarrow{P_n} \cdot \left[A\frac{\overrightarrow{p_e}}{E_e} + B\frac{\overrightarrow{p_{\overline{\nu}}}}{E_{\overline{\nu}}} + D\frac{\overrightarrow{p_e} \times \overrightarrow{p_{\overline{\nu}}}}{E_e E_{\overline{\nu}}}\right] + \dots \tag{1.5}$$

where m_e is the mass of the electron, $\overrightarrow{p_{\overline{\nu}}}$, $\overrightarrow{p_e}$, $E_{\overline{\nu}}$ and E_e the momenta and energies of antineutrino and electron, respectively. $\overrightarrow{P_n}$ is the polarization of the neutron. The coefficients a, A, b, B, D are the angular correlation coefficients: the electron-antineutrino angular correlation coefficient a, the beta asymmetry A, the Fierz interference term b, the neutrino asymmetry B, the Triple correlation coefficient D. Some of these coefficients explicitly violate parity or time reversal invariance or both [7, 15, 16]. These coefficients can be measured experimentally.

1.2.2 The β-decay

In 1934, Enrico Fermi proposed the first theory for β-decay ([17]) based on the analogy with the theory of electromagnetic interaction (Fig. 1.1). Following this phenomenological description,

---

[3] The neutron has a global neutral electric charge but it is composed by quarks whose electric charges are not 0. An EDM should result from quarks distribution.

[4] The Fermi constant is known from μ-decay study.

(a) (b)

Figure 1.1: Neutron decay in term of Feynman graphs. a) An electron in an excited core emitting a photon. b) Neutron decay in Fermi's picture. The time arrow is pointing to the right.

the neutron decay is shown as a point-like interaction between the participating particles and the Hamiltonian can be written as:

$$\mathcal{H}_{\text{Fermi}}(x) = \frac{G_F}{\sqrt{2}} J^{\dagger}_{\mu}(x) \cdot J^{\mu}(x) + \text{h.c.} \tag{1.6}$$

with the Fermi coupling constant G_F, and the sum of the hadronic and leptonic currents $J_\mu = J^{\text{had}}_\mu + J^{\text{lep}}_\mu$. These currents are defined with the spinor field function Ψ_i of the particle i involved in the neutron β-decay, their adjoint function $\overline{\Psi_i}$, and the γ-matrices[5]:

$$\begin{aligned} J^{\text{had}}_\mu(x) &= \overline{\Psi_p}(x)\gamma_\mu\Psi_n(x) \\ J^{\text{lep}}_\mu(x) &= \overline{\Psi_e}(x)\gamma_\mu\Psi_\nu(x) \end{aligned} \tag{1.7}$$

In its original form, the theory of Fermi explicitly conserves parity. This theory was extended in 1936 by Gamow and Teller [19] requiring the introduction of other possible Lorentz invariants. One can create 16 linear independent 4×4 matrices from the γ-matrices as shown in Tab. 1.3.

Operator	Name	Number of matrices
$\overline{\Psi}\Psi$	Scalar (S)	1
$\overline{\Psi}\gamma_\mu\Psi$	Vector (V)	4
$\overline{\Psi}\gamma_\mu\gamma^\nu\Psi$	Tensor (T)	6
$\overline{\Psi}\gamma_5\Psi$	Pseudo-scalar (P)	1
$\overline{\Psi}\gamma_5\gamma_\mu\Psi$	Axial-vector (A)	4

Table 1.3: The five possible current-current interactions.

A general Hamiltonian for β-decay was proposed including all possible interaction terms which are invariant under Lorentz-, parity-, and time-reversal transformations. This Hamiltonian can be simplified [20] as:

$$\mathcal{H} = \frac{G_W}{\sqrt{2}} \sum_i \left[L_i \left(\overline{\Psi_p}\Gamma_i\Psi_n\right) \cdot \left(\overline{\Psi_e}\Gamma_i(1+\gamma_5)\Psi_\nu\right) + R_i \left(\overline{\Psi_p}\Gamma_i\Psi_n\right) \cdot \left(\overline{\Psi_e}\Gamma_i(1-\gamma_5)\Psi_\nu\right)\right] + \text{h.c.} \tag{1.8}$$

where G_W is the general weak coupling constant, $i \in [S, V, T, P, A]$, and the operators Γ_i correspond to the interactions given in Tab. 1.3:

---

[5] $\gamma^0 = \begin{pmatrix} \text{I} & 0 \\ 0 & \text{-I} \end{pmatrix}$, $\vec{\gamma} = \begin{pmatrix} 0 & \vec{\sigma} \\ -\vec{\sigma} & 0 \end{pmatrix}$, $\gamma^5 = i\gamma^0\gamma^1\gamma^2\gamma^3 = \begin{pmatrix} 0 & \text{I} \\ \text{I} & 0 \end{pmatrix}$, $\vec{\sigma}$ are the Pauli matrices.

$$\Gamma_S = 1\ ;\ \Gamma_V = \gamma_\mu\ ;\ \Gamma_T = -i\frac{[\gamma_\mu;\gamma_\nu]}{2\sqrt{2}}\ ;\ \Gamma_P = \gamma_5\ ;\ \Gamma_A = -i\gamma_\mu\gamma_5 \tag{1.9}$$

The eq. (1.8) is constructed in a way that the first part of the sum corresponds to left-handed currents and the second part to right-handed currents[6]: $(1+\gamma_5)\Psi_{\overline{\nu}}/2$ and $(1-\gamma_5)\Psi_{\overline{\nu}}/2$ are the left- and right-handed projections of the antineutrino wave functions, respectively. So, the parity is violated if $L_i \neq R_i$, and the time invariance is violated if the coupling constants have an imaginary part.

Selection rules for the β-transitions are defined and are divided into *allowed* and *forbidden* transitions. This classification depends on the transfer of orbital angular momentum to the leptons pair. If no angular momentum is transferred, this is an allowed transition. On the opposite side, if the outgoing lepton carries angular momentum, this is a forbidden transition. For allowed transitions, the selection rules are the following:

$$\begin{aligned} \Delta J = J_i - J_f &= 0,\ \pm 1, \\ \pi_i \pi_f &= +1, \end{aligned} \tag{1.10}$$

where J_i, J_f and π_i, π_f designate the spin and parity of the initial and final states [7].

The transfer of angular momentum can be regarded as a multipole expansion of the lepton wave function in terms of the product of momentum $|\overrightarrow{p}|$ and nuclear radius R. Due to the small size of the free neutron ($\approx$ 1 fm) and the rather low momentum transfer, its decay is considered as a pure allowed decay.

As the spin of electron and antineutrino are 1/2 each, they can couple to a total spin $\overrightarrow{S}$ of 0 or 1. If the spins couple to the singlet state $S = 0$, the transition is called Fermi decay. The transition to the triplet state $S = 1$ is called Gamow-Teller decay. Or, if we regard the spin $\overrightarrow{J}$ of the proton:

$$\begin{array}{ll} \Delta J = 0 & \text{Fermi decays} \\ \Delta J = 0,\ 1 \text{ (but not } 0 \rightarrow 0) & \text{Gamow-Teller decays} \end{array} \tag{1.11}$$

In Fermi decays the spin of the proton does not change ($\Delta J = 0$) and are mediated by scalar and vector couplings. In the case of Gamow-Teller decays[7], the spin can change if the spins of e^- and $\overline{\nu_e}$ couple to $S_z = \pm 1$ ($\Delta J = 1$). In these decays, axial-vector and tensor couplings are mediators. In the case of the free neutron both decay modes are realized.

1.2.3 The *V-A* theory

In 1957, the parity violation in β-decay was found experimentally by Wu *et al.* [18][8]. This means only left-handed components of vector and axial-vector couplings contribute to β-decay. So, only L_V and L_A remain in the eq. (1.8) which can be simplified to the Hamiltonian of the *V-A* theory:

$$\begin{aligned} \mathcal{H} &= \tfrac{G_W}{\sqrt{2}} \sum_{V,A} \left[L_i(\overline{\Psi_\text{p}}\Gamma_i\Psi_\text{n}) \cdot \left(\overline{\Psi_e}\Gamma_i\left[1+\gamma_5\right]\Psi_{\overline{\nu}}\right)\right] + \text{h.c.} \\ &= g_\text{V}(\overline{\Psi_\text{p}}\gamma_\mu(1-\lambda\gamma_5)\Psi_\text{n}) \cdot (\overline{\Psi_e}\gamma_\mu(1+\gamma_5)\Psi_{\overline{\nu}}) + \text{h.c.} \end{aligned} \tag{1.12}$$

---

[6] Left-handed particles are those with helicity $h = \frac{\overrightarrow{s}\cdot\overrightarrow{p}}{|\overrightarrow{s}||\overrightarrow{p}|} = 1$, particles with $h = -1$ are right-handed.

[7] Transitions between states of zero angular momentum ($0 \rightarrow 0$) are excluded: it is not possible to generate a triplet state for $J_i = J_f = 0$.

[8] In the decay of cobalt-60 atoms whose spins were aligned with a strong magnetic field, the electrons are preferentially emitted in a direction opposite to the direction of the nuclear spin

g_V and g_A are the vector and axial-vector coupling constants and λ is their ratio:

$$g_\mathrm{V} = G_W L_V \; ; \; g_\mathrm{A} = G_W L_A \; ; \; \lambda = \frac{g_\mathrm{V}}{g_\mathrm{A}} \tag{1.13}$$

However, this Hamiltonian still assumes a point-like interaction for the β-decay. As the neutron and the proton are not elementary particles, the Standard Model follows the V-A theory without the assumption of the point-like interaction. The β-decay is now described by the exchange of a $W^\pm$ boson between the leptonic and the hadronic current (see Fig. 1.2). The neutron decay is the transition of an up-quark into a down-quark by exchange of a W^- boson. Generally, the weak interaction is mediated by the exchange of 3 gauge bosons $W^\pm$ and Z^0, underlying the symmetries of the $SU_L(2) \times U(1)$ gauge group. These bosons are very massive and can exist only for very short times[9]. Thus, the exchange boson in the β-decay will couple to left-handed fermions and right-handed antifermions. This includes parity violation in the SM description of the weak interaction. The weak coupling constants get an additional factor $|V_\mathrm{ud}|$ to have a relation with the CKM matrix in eq. (1.2):

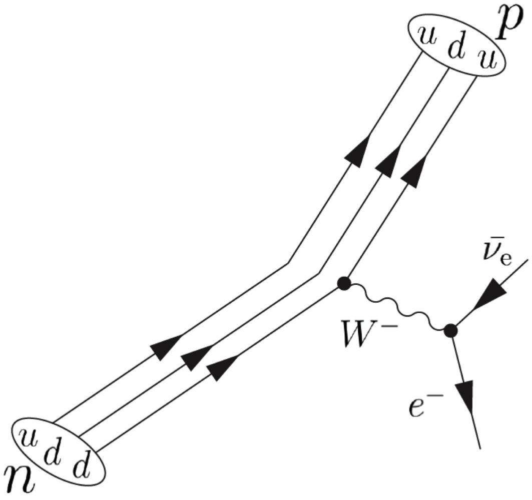

Figure 1.2: Feynman diagram of neutron β-decay.

$$G_\mathrm{V} = g_\mathrm{V} \cdot |V_\mathrm{ud}| \qquad G_\mathrm{A} = g_\mathrm{A} \cdot |V_\mathrm{ud}| \tag{1.14}$$

In the experiments, the measurable parameters can be related to the ratio of the weak coupling constants defined by $\lambda = \frac{g_\mathrm{A}}{g_\mathrm{V}}$.

1.3 The correlation coefficients

The correlation coefficients used to re-write the neutron decay rate in eq. (1.5), are measurable experimentally. They are angular correlation coefficients defined between the particles momenta and the neutron spin (Fig. 1.3). The electron-antineutrino angular correlation coefficient a is defined between the electron and antineutrino momenta, the beta asymmetry A is defined between the electron momentum and the neutron spin, and the antineutrino asymmetry B is defined between the antineutrino momentum and he neutron spin. There is another one defined between proton momentum and neutron spin: the proton asymmetry C.

---

[9] The lifetime of the W^- boson is determined by Heisenberg's uncertainty principle $\tau < \hbar/M_\mathrm{W,Z}$.

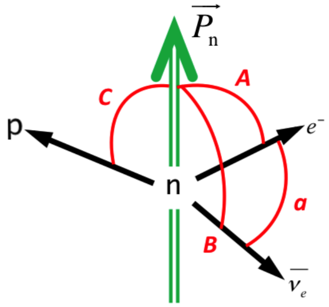

Figure 1.3: Correlation coefficients in neutron β-decay, with $\overrightarrow{P}_\mathrm{n}$ the neutron spin.

These coefficients are expressed in their general form in terms of the coupling constants L_i and R_i:

$$\begin{aligned}
&a = \tfrac{1}{\xi}\left(|L_V|^2 - |L_S|^2 + |L_T|^2 - |L_A|^2 + |R_V|^2 - |R_S|^2 + |R_T|^2 - |R_A|^2\right)\\
&A = \tfrac{1}{\xi}\mathrm{Re}\left(-|L_A|^2 - L_V L_A^* + |L_T|^2 + L_S L_T^* + |R_A|^2 + R_V R_A^* - |R_T|^2 - R_S R_T^*\right)\\
&B = B_0 + b_v \tfrac{m_e}{E_e}\\
&C = -x_C(A + B_0) - x_C b_v
\end{aligned} \tag{1.15}$$

with $B_0 = \frac{2}{\xi}\mathrm{Re}\left(|L_A|^2 - L_V L_A^* + |L_T|^2 - L_S L_T^* - |R_A|^2 - R_V R_A^* + |R_T|^2 - R_S R_T^*\right)$ and $b_v = \frac{2}{\xi}\mathrm{Re}\left(-L_S L_A^* - L_V L_T^* + 2L_A L_T^* + R_S R_A^* + R_V R_T^* - 2R_A R_T^*\right)$. The parameter ξ is the sum of the squares of the coupling constants. Its general form is presented in [20]:

$$\xi = \left(|L_S|^2 + |L_V|^2 + |R_S|^2 + |R_V|^2\right) + 3\left(|L_A|^2 + |L_T|^2 + |R_A|^2 + |R_T|^2\right) \tag{1.16}$$

The pre-factor 3 of the second part indicates the triplet state of the Gamow-Teller decay in contrast to the singlet state of the Fermi decay.

Within the Standard Model, this equation can be simplified to only the two coupling constants which are involved in the *V-A* theory, L_V and L_A:

$$\xi = |L_V|^2 + 3\,|L_A|^2 \iff \xi = \frac{|g_V|^2 + 3\,|g_A|^2}{{G_W}^2} \tag{1.17}$$

And so, the correlation coefficients can be expressed in terms of one parameter, the ratio of the weak coupling constants λ:

$$a = \frac{1 - |\lambda|^2}{1 + 3\,|\lambda|^2}, \quad A = -2\frac{|\lambda|^2 + \mathrm{Re}(\lambda)}{1 + 3\,|\lambda|^2}, \quad B = 2\frac{|\lambda|^2 - \mathrm{Re}(\lambda)}{1 + 3\,|\lambda|^2}, \quad C = x_C\frac{4\,|\lambda|^2}{1 + 3\,|\lambda|^2}. \tag{1.18}$$

with $x_C = 0.27484$. The parameter λ takes into account the renormalization of the axial vector current by the structure of the nucleon.

1.4 Beyond the β-decay

The neutron β-decay offers different ways to test the Standard Model at the low-energy frontier. The measurable parameters give information about the weak interaction process via the ratio λ. These studies allow to approach new physics beyond the Standard Model.

1.4.1 Tests of the Standard Model

The measurement of the correlation coefficients allows the determination of the ratio λ with different sensitivities (using the world average for $\lambda = -1.2701(25)$ [13]):

$$\frac{\mathrm{d}a}{\mathrm{d}\lambda} = 0.298, \quad \frac{\mathrm{d}A}{\mathrm{d}\lambda} = 0.374, \quad \frac{\mathrm{d}B}{\mathrm{d}\lambda} = 0.076, \quad \frac{\mathrm{d}C}{\mathrm{d}\lambda} = -0.124 \tag{1.19}$$

Thus, measurements of these coefficients provides different independent ways to access the parameter λ with different experimental systematics. The Fig. 1.4 shows the determination of the ratio λ in neutron decay experiments via the measurements of different correlation coefficients.

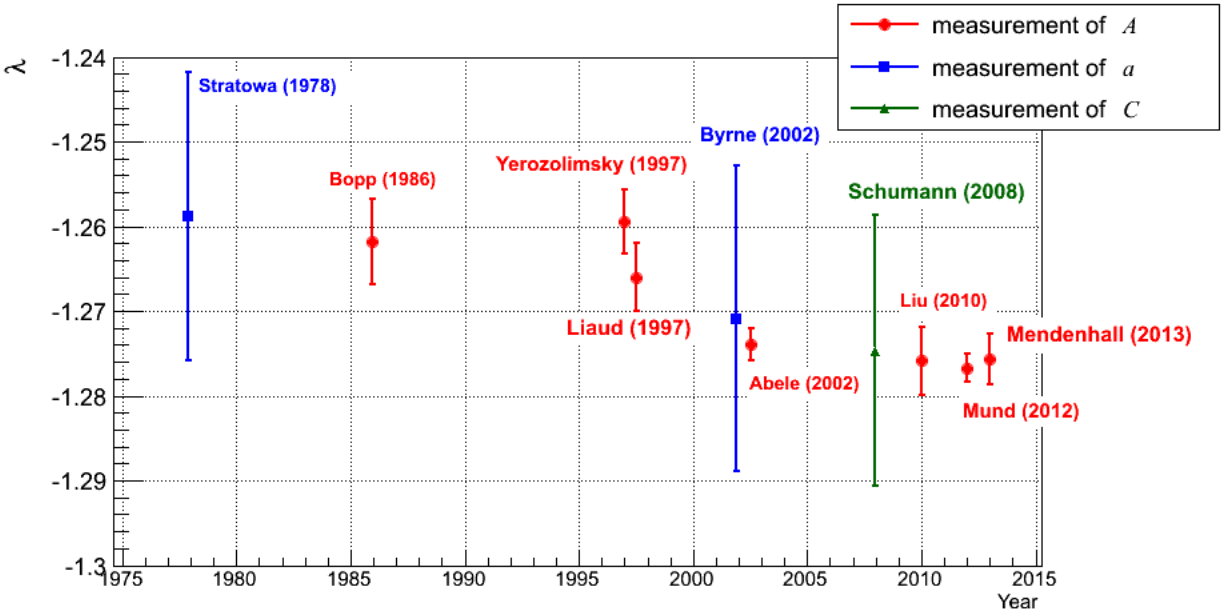

Figure 1.4: Determination of the ratio λ from measurement of the coefficient A, a and C. Values from [24, 26, 27, 28, 25, 29, 73, 30, 31, 32].

Then, λ in combination with the neutron lifetime τ_n, is used to calculate the first element of the CKM matrix[33, 34]:

$$|V_{\mathrm{ud}}|^2 = \frac{(4\,908.7 \pm 1.9)\mathrm{s}}{\tau_n(1+3\lambda^2)} \tag{1.20}$$

Considering the actual value of λ and τ_n, we can calculate $|V_{\mathrm{ud}}| = 0.97520(140)$ with a precision of 0.14% [35]. However, the most accurate determination of V_{ud} is done in super-allowed β-decay, $0^+ \to 0^+$. In this transition, we calculate $|V_{\mathrm{ud}}| = 0.97425(22)$ with a precision of 0.02% [35]. This is a pure Fermi transition characterized by the vector coupling $g_{\mathrm{V}} = G_{\mathrm{F}} \cdot V_{\mathrm{ud}}$ [36]. This precise value for V_{ud} is determined from the ft value (the strength of the transition) which relates, in this case, directly to the fundamental vector coupling constant.

Even if the accuracy is lower, the value of V_{ud} from neutron decay measurements is consistent with the super-allowed results. The advantage is that, in the case of the neutron, the corrections due to nuclear-structure interaction are negligible [40].

So, the correlation coefficients from neutron β-decay are part of testing the unitarity of the CKM matrix via the first condition in eq. (1.3). The unitarity, according the last value of the elements of the first line of the CKM matrix, is satisfied to a precision of 0.06%: $|V_{\mathrm{ud}}|^2 + |V_{\mathrm{us}}|^2 + |V_{\mathrm{ub}}|^2 = 1.00008(56)$[35].

1.4.2 Beyond the Standard Model

A non-unitarity CKM matrix could indicate, for example, the presence of a new generation of quarks. Additionally, this is also a way to measure potential small deviations from the Standard Model description: precise measurements of the correlation coefficients drive limits for physics beyond the Standard Model. Some example of new physics which can be approached here, is the search for contributions of scalar and tensor type interactions to the decay (i.e., scalar and tensor currents): this could be caused by the hypothetical existence of leptoquarks or charged Higgs bosons [7, 42]. Another example is the search for a right-handed contribution to the weak interaction via a new gauge boson: a right-handed W boson as shown in Fig. 1.5 [41]. The estimated improvements in the accuracy of the measurements would lead to a better restriction of the mass of the W_R boson ($m_2 > 574$ GeV).

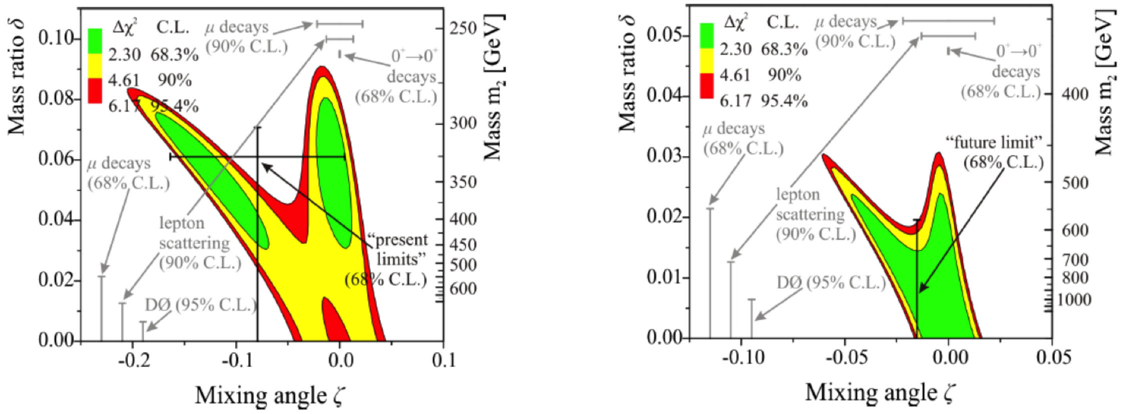

Figure 1.5: Allowed parameter regions for a right-handed W boson: left side, current limits from a, A, B, and τ_{n} in neutron decay ; left-side, projected future limits from neutron decay, assuming improved measurements of coefficients [41].

Angular correlations are also measured in nuclear beta decay. The experiments WITCH [37, 38] at ISOLDE and LPCTrap [39] at GANIL measure the nuclear recoil spectrum of trapped nuclei, in order to derive the $\beta - \nu$ correlation coefficient and to search for exotic interactions. More details about these experiments are presented in section 1.6.3.

1.4.3 Phenomenology: the Universe in a neutron[10]

Several phenomena share similitudes with the Feynman diagram of the β-decay (see Fig. 1.2). The following descriptions are from [16, 43]. This is the case for the nucleosynthesis processes where neutrons and protons are in a state of thermal equilibrium: $n + e^+ \rightleftharpoons p + \overline{\nu_e}$ and

---

[10] Original reference from Stephen Hawking: "the Universe in a nutshell".

$p + e^- \rightleftharpoons n + \nu_e$. In the first times after the Big Bang, the Universe became colder, and heavier element were formed with the breaking of the equilibrium. The neutron lifetime influences the relative abundance of primordial helium.

The β-decay gives also informations in proton-proton cycle of thermonuclear reactions inside stars: $p + p \to D + e^+ + \nu_e$. In this process, the capture of protons on protons is proportional to the axial-vector coupling constant $|g_\mathrm{A}|^2$.

An inverse neutron β-decay process occurs in the formation of neutron stars: $p + e^- \to n + \overline{\nu_e}$. This is also the case for the neutrino detection: the neutrino from a reactor interact with the proton of a target, then a neutron is emitted and detected, $\nu_e + p \to n + e^+$. Thus, the detection probability is related to the ratio λ.

1.5 Kinematics description

The free neutron β-decay is described by a three-body decay (Fig. 1.6) which is treated relativistically (using the four-momenta $p_i = (E_i, \overrightarrow{p_i})$). By using the masses of the particles, we can calculate the endpoint energy $E_{0,i}$ of the daughter particle i as follow:

$$E_{0,i} = \sqrt{m_{0,i}^2 + |\overrightarrow{p_i}|^2} \tag{1.21}$$

with $m_{0,i}$ is the rest mass of the respective particle ($i \in [p, e^-, \overline{\nu_e}]$). The resulting values for the different particles are shown in Tab. 1.4.

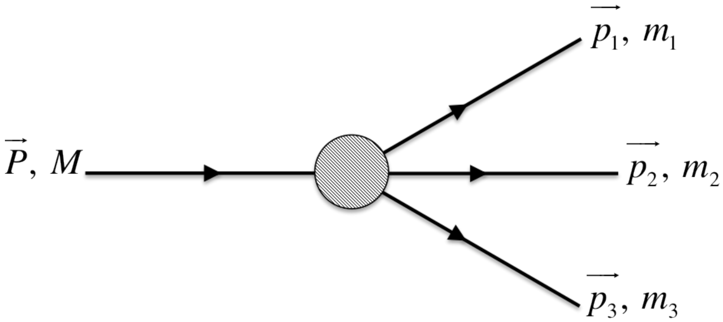

Figure 1.6: Three-body decay. An incoming particle with momentum $\overrightarrow{P}$ and mass M decays into three daughter particles with momenta $\overrightarrow{p_i}$ and mass m_i ($i = 1, 2, 3$).

Particle	Index i	$m_{0,i}$ (MeV)	$E_{0,i}$ (MeV)	$E_{0,i} - m_{0,i}$ (MeV)
Neutron	n	939.565346(23)		
Proton	p	938.272013(23)	938.272764(23)	0.000751(33)
Electron	e^-	0.510998910(13)	1.292581(53)	0.781582(53)
Antineutrino	$\overline{\nu_e}$	<0.000002	0.782008(54)	0.782008(54)

Table 1.4: Rest mass $m_{0,i}$, endpoint energies $E_{0,i}$ and maximal kinetic energies.

1.5.1 Lepton spectra

The calculation of the energy distribution can be done from the number of states in the available space phase. In the case of the electron, by neglecting the proton, this can be done in the phase space volume $d^3p_e d^3p_{\overline{\nu}}$. Thus, from the energy relation $E_0 = E_e + E_{\overline{\nu}} = m_\mathrm{n} - m_\mathrm{p}$ the electron spectrum is given by:

$$d\rho_e = \frac{(4\pi)^2}{(2\pi\hbar)^6} E_e \sqrt{E_e^2 - m_e^2} \cdot (E_0 - E_e)^2 dE_e \tag{1.22}$$

where E_0 is slightly larger than the value $E_{0,e}$. For the further calculations the more accurate value $E_{0,e}$ will be used.

However, the presence of the proton will shift the electron spectrum to slightly lower energies due to the Coulomb interaction between these two particles. Thus, the eq. (1.22) is modified including a correction by the Fermi function $F(E)$:

$$\rho^{'}(E_e) = \frac{(4\pi)^2}{(2\pi\hbar)^6} F(E) E_e \sqrt{E_e^2 - m_e^2} \cdot (E_{0,e} - E_e)^2 \tag{1.23}$$

The correction by the Fermi function affects mostly electrons at low energies and for the neutron decay conditions one can then set $F \approx 1$. And by analogy, the energy spectrum for the antineutrino is:

$$\rho^{'}(E_{\overline{\nu}}) = \frac{(4\pi)^2}{(2\pi\hbar)^6} \sqrt{(E_{0,\overline{\nu}} + m_e - E_{\overline{\nu}})^2 - m_e^2} \cdot (E_{0,\overline{\nu}} + m_e - E_{\overline{\nu}})^2 \tag{1.24}$$

Both electron and neutrino spectrum are plotted in Fig. 1.7.

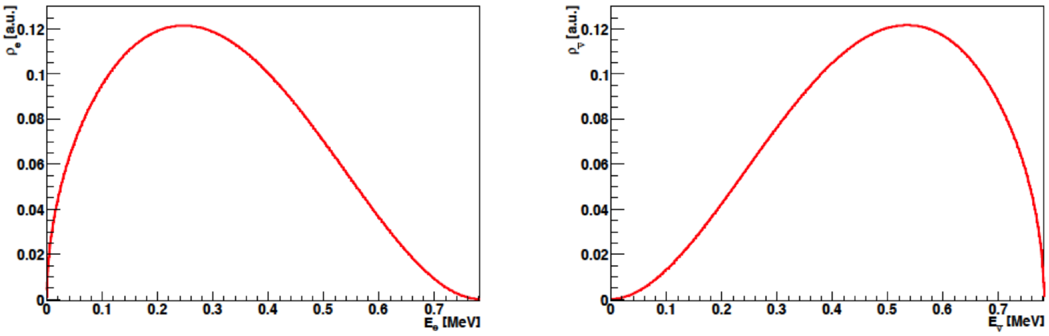

(a) (b)

Figure 1.7: Energy spectra of electrons (a) and neutrinos (b) from the decay of the free neutron.

1.5.2 Proton spectrum

The shape of the proton spectrum can be described theoretically as a function of the correlation coefficient a [21]:

$$\frac{dW(T)}{dT} \propto g_1(T) + a \cdot g_2(T) \tag{1.25}$$

with $g_1(T)$ and $g_2(T)$ being known functions of the kinetic energy T of the proton:

$$\begin{aligned} g_1(T) &= \left(\tfrac{\sigma - x^2}{\sigma}\right)^2 \sqrt{1-\sigma} \left[4\left(1 + \tfrac{x^2}{\sigma}\right) - \tfrac{4}{3}\tfrac{\sigma - x^2}{\sigma}(1-\sigma)\right] \\ g_2(T) &= \left(\tfrac{\sigma - x^2}{\sigma}\right)^2 \sqrt{1-\sigma} \left[4\left(1 + \tfrac{x^2}{\sigma} - 2\sigma\right) - \tfrac{4}{3}\tfrac{\sigma - x^2}{\sigma}(1-\sigma)\right] \end{aligned} \tag{1.26}$$

with the following parameters $\sigma = 1 - 2T\frac{m_n}{(m_n - m_p)^2}$ and $x = \frac{m_e}{(m_n - m_p)}$.

The shapes of g_1, g_2, and the linear combination of them for the present world average value for a (-0.103, in PDG) are shown in Fig. 1.8.

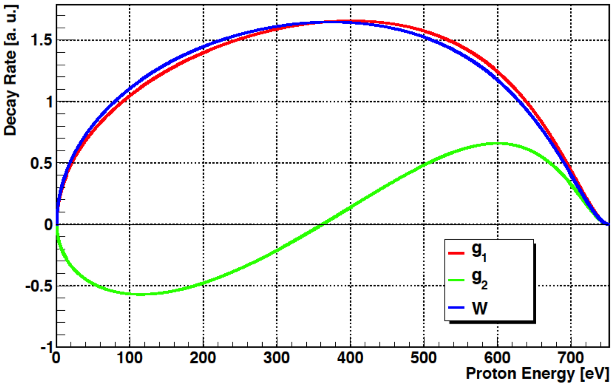

Figure 1.8: The theoretical functions g_1 and g_2 for the proton spectrum and the linear combination of them W for the present world average value of a

These kinematic characteristics are used to measure the coefficient a with indirect methods (see section 1.6) as the antineutrino has a very low interaction with matter. Due to the momentum conservation, the maximum kinetic energy for the proton is about 751.4 eV. The electron and the antineutrino carry the most of the released energy. In Fig. 1.9, we considered two extreme kinematic cases. The value $a = +1$ is related to the case where the electron and the the antineutrino are emitted with parallel momenta. In this configuration, the proton will carry a maximal recoil momentum and so the proton spectrum is shifted toward higher energies. In the

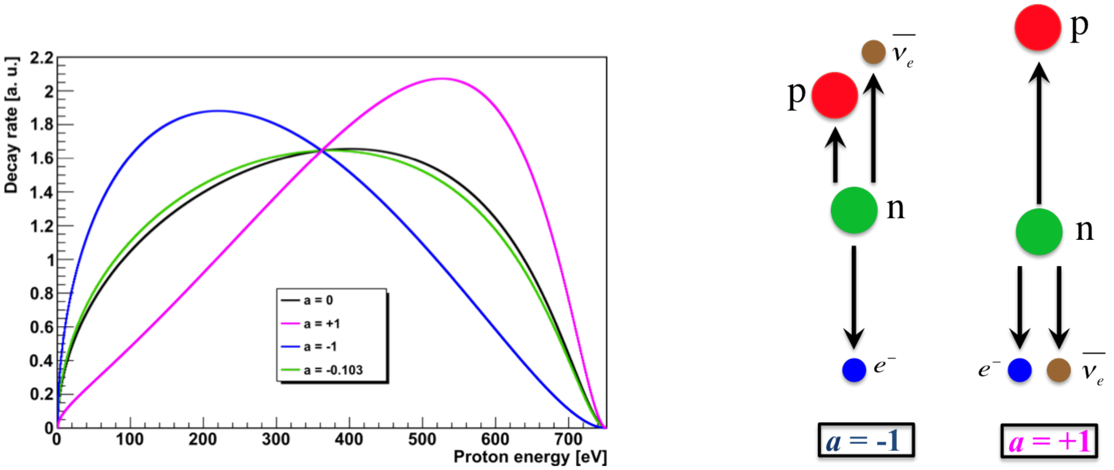

(a) Shape of the proton spectrum for hypothetical values of the coefficient a.

(b) Case $a = -1$, the proton is emitted is the same direction as antineutrino and its recoil energy is minimal and in the case $a = +1$, its energy is maximal.

Figure 1.9: Illustration of the impact of the kinematic of the neutron decay on the proton spectrum.

opposite configuration, $a = -1$, the antineutrino and the proton momenta are parallel and the proton energy will shift toward lower values.

1.6 Experimental measurement of the coefficient a

The aim of the experiment aSPECT is to measure the electron-antineutrino angular correlation coefficient a. Even if the electron asymmetry coefficient A has the better sensitivity towards λ, the coefficient a offers a good possibility for a measurement of λ with independent systematics. However, the experimental relative uncertainty of a is much bigger than for A. The present world average value is $a = -0.103(4)$ [13]. Actually, previous experiments gave a measurement of the coefficient a with an accuracy of 5% [24, 25].

1.6.1 Previous experiments

The first measurement of the coefficient a in neutron β-decay was realized by Grigorev *et al.* in 1968 [23] at the ITER research reactor in the Soviet Union: $a = -0.091(39)$. The method was to measure the proton spectrum in coincidence at a fixed electron energy, in order to reduce the background. The proton spectrum was measured by TOF through a focusing ellipsoidal electrostatic mirror. The signal of both electrons and protons were read with an oscilloscope, and the traces of events coincident (within a 5.5 μs time window) were photographed by a camera.

The first precision measurement of this coefficient was realized by Stratowa *et al.* [24] in 1978 at the ASTRA reactor of Seibersdorf (near Vienna): $a = -0.1017(51)$. The method used was to measure the proton spectrum. As shown in Fig. 1.10, the decay protons flew freely inside a through-going beam tube, with no direct view to the reactor core or onto the moderator (to reduce background). Only protons with a momentum almost parallel to the tube were analyzed in a spherical electrostatic spectrometer: the protons are selected for the energy of the spectrometer by the small solid angle defined by the apertures at z_1 and at z_2 (shown in the figure).

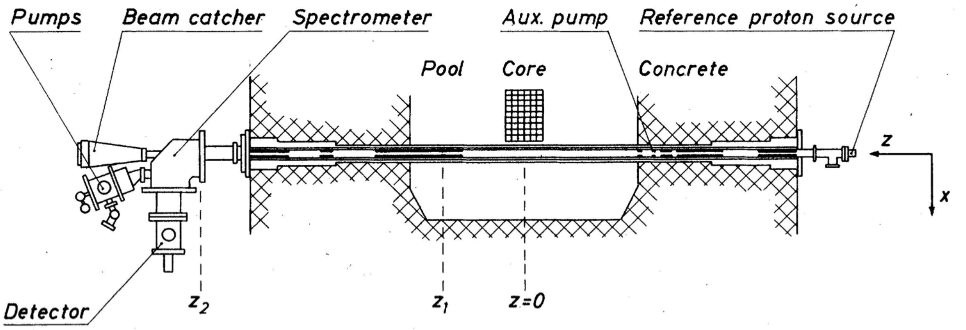

Figure 1.10: Experiment of Stratowa *et al.* [24]. The neutron decay volume was in-pile near the core of the reactor.

The proton spectroscopy method was also used by Byrne *et al.* [25] in 2002 at the ILL: $a = -0.1054(55)$. The decay protons were stored in a cryomagnetic ion trap with a variable mirror electrode (see Fig. 1.11). This adjustable potential allowed the energy-selection of the protons which were then accelerated onto a detector.

1.6.2 Ongoing and future experiments

The experiment aSPECT measures the proton energy spectrum to derive the coefficient a (see descriptions in Chapter 2). The method is similar to the one used by Byrne *et al.* in their

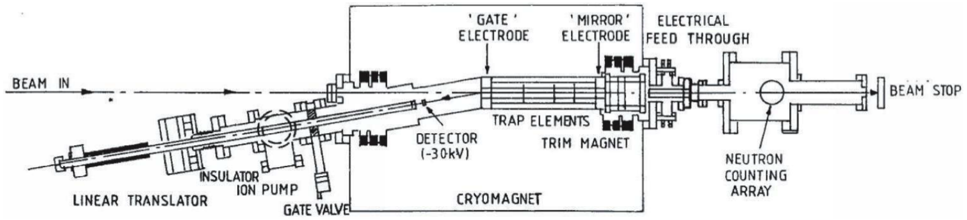

Figure 1.11: Experiment of Byrne *et al.* [25]. A cold neutron beam passed through the center of a quasi-Penning trap.

experiment, but we detect protons that pass the adjustable potential without storing them. The aim is to improve the accuracy of the coefficient a to 0.3% [48].

Another method to measure the coefficient a is based on the coincidence rates of electron and proton. This is the purpose of the experiment aCORN at the National Institute of Standards and Technology (NIST) whose objective is to obtain a value for the coefficient a with an accuracy of 0.5% [22]. The principle is to detect proton and electron from the same neutron. This was first described by Yerozolimsky and Mostovoy [44, 45]. The value of the coefficient a is related to an asymmetry in terms of the count rate in two kinematics regions corresponding to $\overrightarrow{p_\mathrm{p}} \uparrow\uparrow \overrightarrow{p_e}$ and $\overrightarrow{p_\mathrm{p}} \uparrow\downarrow \overrightarrow{p_e}$ (projection of the momenta on the spectrometer axis): in the first case protons and electrons are emitted in the same direction, and in the second case these particles are emitted in opposite direction. There is no energy-selection of the particles, they are collimated regarding their momentum along the vertical axis of the spectrometer (see Fig. 1.12).

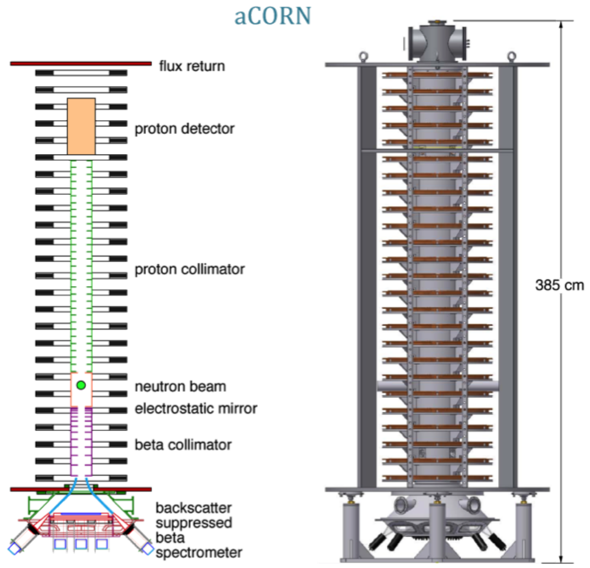

Figure 1.12: Experiment aCORN [22]. Protons and electrons are detected in coincidence.

This second method is also used in the experiment Nab [46] at the Spallation Neutron Source (SNS) in Oak Ridge, Tennessee. As for aCORN, the electron energy and the time between electron and proton detection will be measured. This experiment aims to measure the coefficient a at the 10^{-3} accuracy level [46].

A future experiment, PERC [47], is in preparation and will be a clean, bright, and versatile source of neutron decay products. The emitted protons and electrons are collected by a strong longitudinal magnetic field (see Fig. 1.13). This is designed to improve the sensitivity of neutron decay studies by one order of magnitude. This facility can be used with different secondary spectrometers. The coefficient a could be measured via the proton spectrum from an unpolarized neutron beam, by connecting a retardation spectrometer as aSPECT or a magnetic spectrometer.

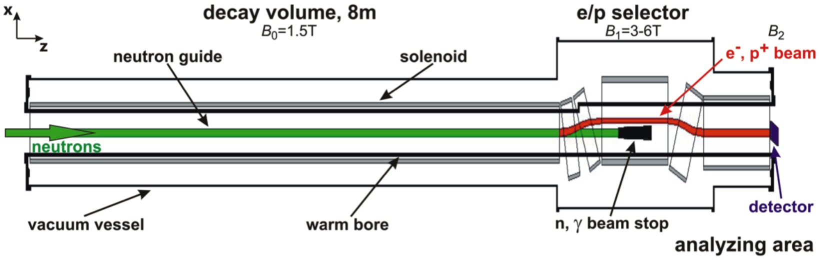

Figure 1.13: Principle of PERC [47]. Measurement of several coefficient using (un)polarized, pulsed/continuous neutron beam.

1.6.3 Nuclear β-decay experiments

As mentioned in section 1.4.1, correlation coefficients can be measured in the decay of nuclei with different systematics than in neutron decay. The experiment WITCH [37, 38]akes place at ISOLDE (CERN). In this experiment, different nuclei are investigated, for example ^{35}Ar. The nuclei are decelerated and trapped in a Penning trap called “cooler trap” (see Fig. 1.14). The ion cloud is then transferred toward a second Penning trap called “decay trap”. The ions from beta decay are energy-selected by a potential barrier in the same way as in the spectrometer aSPECT. Those with sufficient energy overcome the barrier and are accelerated toward a micro-channel plate detector. The coefficient a can be inferred from the ion recoil energy spectrum. This experiment aims to measure the angular correlation coefficient a with an accuracy of 0.5%.

Another example is the experiment LPCTrap [39] at GANIL (France). The aim is to measure the decay of ^{6}He and then heavier nuclei (e.g., ^{19}Ne) stored in a Paul trap. In a first time, the beam is decelerated using a Radio Frequency cooler-buncher (RFQCB) as shown in Fig. 1.15. The bunches are then transported by a first pulsed cavity to a second one which reduces the kinetic energy of the ions. Then, the ions are transferred into the Paul trap. Two set-ups are used at the trap to detect both electrons and recoil ions from the decay. A spectrometer is used to separate the charge states of the recoil ions. Actually, the correlation coefficient a was measured in the decay of of ^{6}He nuclei: $a = -0.3335(73)_{\text{stat.}}(75)_{\text{syst.}}$ [39]. Measurements were recently performed with ^{35}Ar nuclei and the analysis is in progress.

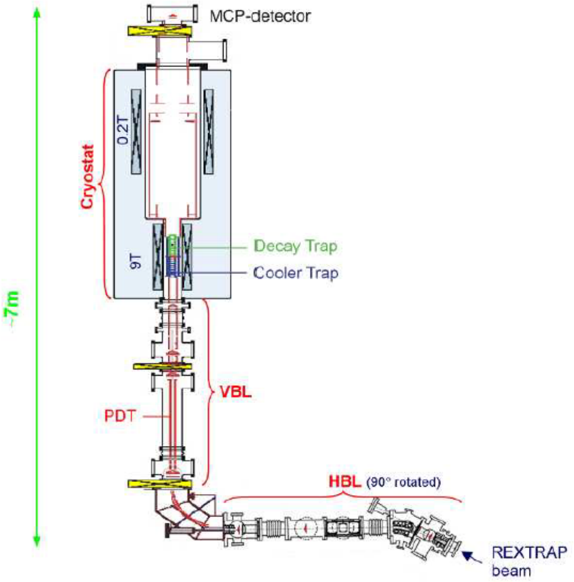

Figure 1.14: Schematic overview of the experiment WITCH installed at ISOLDE [38]. Radioactive ions are cooled and bunch in the Horizontal Beam Line (HBL), then decelerated in the Vertical Beam Line (VBL) before to be injected in the Cooler Trap. After cooling, the ions are transferred into the Decay Trap.

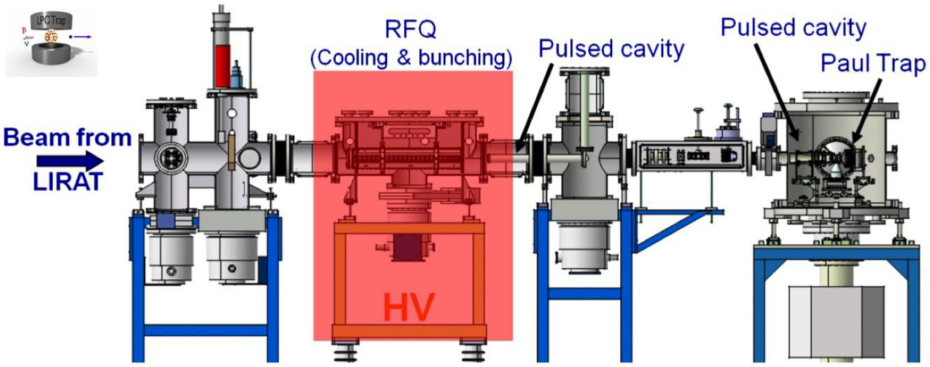

Figure 1.15: Schematic overview of the LPCTap set-up installed at the beam line SPIRAL at GANIL [39].

Chapter 2

The *a*SPECT experiment

---

*a*SPECT est une expérience dont l'objectif est de mesurer le coefficient de corrélation angulaire *a* entre l'électron et l'antineutrino avec une précision sans précédent : $\Delta a/a \approx 1\%$ contre les 5% de précision pour les précédentes mesures. Etant donné que l'antineutrino interagit peu avec la matière sa détection est difficile. Le spectromètre *a*SPECT mesure donc le coefficient *a* via une méthode indirecte : sa valeur est extraite du spectre d'énergie des protons. Ces particules sont émises avec une énergie inférieure au keV et sont guidées vers le détecteur par un champ magnétique et électrique complexe. Avant d'être détectés, les protons sont sélectionnés en fonction de leur énergie grâce à une barrière de potentiel. Ceux qui franchissent cette barrière sont ensuite accélérés par un potentiel de -15 kV avant d'être comptés par le détecteur. En ajustant le potentiel de sélection, on reconstruit le spectre des protons. L'efficacité de la sélection en énergie des protons est exprimée par la fonction de transmission du spectromètre. Pour cela, l'ensemble des électrodes et des bobines ont été pensées dans l'objectif d'optimiser le transport et la détection des protons (ceci est présenté dans les thèses précédentes dont les descriptions servent de base à ce chapitre).

2.1 The retardation spectrometer

The principle of *a*SPECT is to measure protons from neutron decay which are guided toward the detector by a strong magnetic field. As these particles have low energies ($E_{p,\,\mathrm{max}} = 751.4$ eV), they have to be accelerated. However, this means that the energy measured will not help to obtain the proton spectrum. The other possibility is to select protons by their energy before to be accelerated and to count those who reach the detector. The proton selection is done by an electrostatic retardation potential which is variable allowing to cover all the proton's energy range.

The schematic view in Fig. 2.1 shows that the spectrometer *a*SPECT has a cylindrical shape. It is installed at a beam line of unpolarized cold neutrons[1] which pass through the spectrometer. A fraction of about 10^{-8} of the neutrons decays in the region inside the spectrometer called the **Decay Volume** (DV), which is grounded. The protons emitted from this region are guided toward the detector on the top of the spectrometer. Protons emitted toward the bottom (lower hemisphere) are reflected adiabatically by an electrostatic **Mirror Electrode** (ME). Therefore the spectrometer achieves 4π acceptance for protons created in the DV. Then, protons

---

[1] Neutrons coming from the cold source of the ILL reactor have energies of about 0.05 to 25 meV.

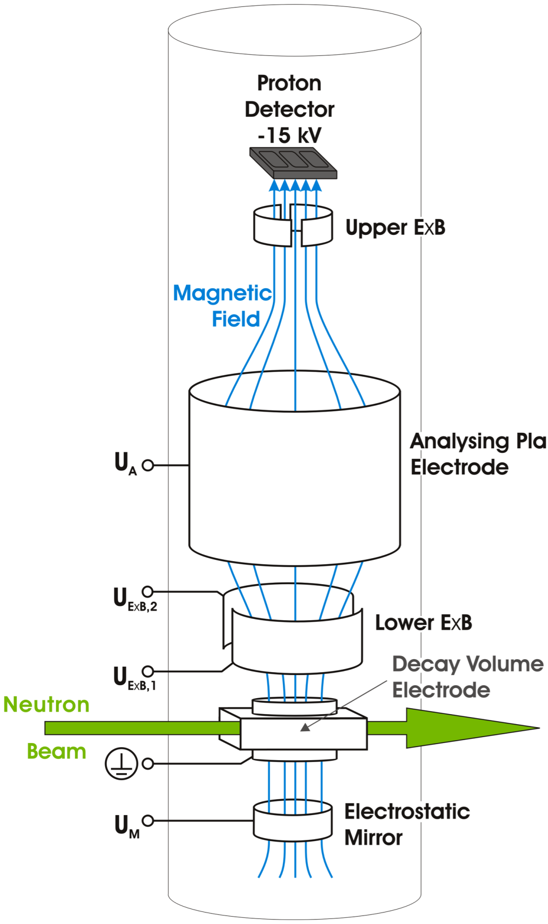

Figure 2.1: Scheme of the spectrometer *a*SPECT. The green line is the neutron beam and the blue ones are the magnetic field lines.

are energy-selected by the potential barrier, U_A, created by the **Analyzing Plane** electrode (AP). Considering the endpoint energy for protons, the voltage for the AP will be set to values between 0 and 780 V. Protons with enough kinetic energy will pass the AP and will be focused onto the detector by the strong magnetic field. To be detected, these low-energetic particles are post-accelerated by a high voltage (typically -15 kV) applied at the detector electrode.

The other protons which cannot overcome the AP potential are reflected and thus trapped between the Mirror and the AP. They are then removed by a $\overrightarrow{E} \times \overrightarrow{B}$ drift created at the electrodes **Lower** $E \times B$ (lExB). These electrodes are placed between the DV and the AP. Other electrodes, **Upper** $E \times B$ (uExB), placed before the detector are used to help for the post-acceleration of protons against the strong magnetic mirror effect. These electrodes are also used to shift the protons with respect to the detector.

2.2 Concepts of the spectrometer

The descriptions of the principles which involve in the spectrometer *a*SPECT are presented in the previous PhD theses [8, 9, 10, 11], and the following presentations are based on them and the publication of Ferenc Glück [48]. The spectrometer is composed by a set of electrodes and superconducting coils which produce strong magnetic and electric fields. These are made in a configuration to optimize the proton motion inside the spectrometer.

2.2.1 Adiabatic invariance

The potential barrier created at the AP electrode is only sensitive to the longitudinal energy component of the proton. So, the momentum of the proton has to be transferred to the parallel component without changing the kinetic energy. This is the principle of the “adiabaticity”. In order to obtain this, the magnetic field was designed to be lower in the AP than in the DV (i.e., $B_\mathrm{A} < B_0$), and it decreases adiabatically between these two regions. As shown in Fig. 2.2, from their emission in the DV, protons are guided by the strong magnetic field and gyrate around the field lines. Due to the magnetic field gradient between the DV and the AP, the transverse energy component is transferred to the longitudinal component.

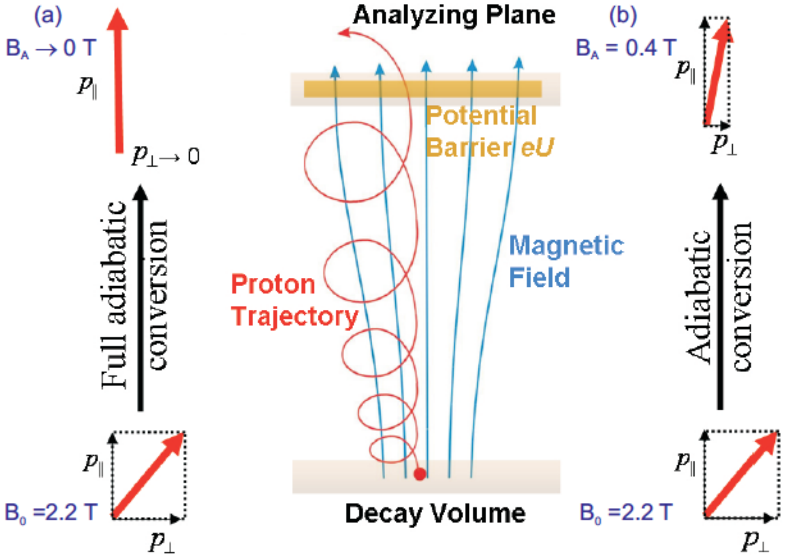

Figure 2.2: Principle of the adiabatic conversion of the proton motion between the Decay Volume and the Analyzing Plane. The protons emitted from the DV gyrate around the magnetic field lines (blue lines). (a) Case of full transfer of the transverse to the longitudinal momentum, $p_\shortparallel = p$ and $p_\perp = 0$. (b) Case of the adiabatic conversion for the given magnetic field strengths of aSPECT. Picture from [9].

In the magnetic field $\overrightarrow{B}$, protons have a helical motion (red line in Fig. 2.2) induced by the Lorentz force:

$$\overrightarrow{F_\mathrm{L}} = q \cdot (\overrightarrow{v} \times \overrightarrow{B}) \tag{2.1}$$

with q is the charge of the particle and $\overrightarrow{v}$ its velocity which can be expressed in terms of a longitudinal and a transversal components. As the kinetic energy does not change during the proton motion, we can express the initial velocity of the proton as:

$$v_0^2 = v_\parallel^2 + v_\perp^2 \tag{2.2}$$

The circular component of the velocity form a periodic motion. This induces some adiabatic invariants as the magnetic moment[2] $\mu = \frac{p_\perp^2}{2mB}$. This invariance allows to write the following

---

[2] The adiabatic invariant parameter is $\gamma\mu$ where $\gamma = \frac{1}{\sqrt{1-v^2/c^2}}$ is the relativistic factor which can be set to 1 as the protons are at low energy in neutron decay.

equation between the initial transverse velocity $v_{\perp 0}$ and the one at any point along the z-axis $v_\perp$:

$$\frac{v_\perp^2}{B} = \frac{v_{\perp 0}^2}{B_0} \tag{2.3}$$

with B_0, the magnetic field in the DV ($z = 0$), B, the one along the z-axis. And so, using the eq. (2.2), the parallel velocity of the proton at any position along the z-axis is given by:

$$v_\parallel^2 = v_0^2 - v_{\perp 0}^2 \cdot \frac{B(z)}{B_0} \tag{2.4}$$

Following this equation, we define the ratio between the magnetic field B_A in the AP and the one B_0 in the DV as $r_\mathrm{B} = \frac{B_A}{B_0}$. A full adiabatic conversion can be reached when the velocity is fully transferred to its parallel component: this means for $r_\mathrm{B} = 0$. This ideal case requires a long distance between the DV and the AP and so a huge spectrometer size. The compromise chosen for *a*SPECT was to set $r_\mathrm{B} \approx 0.2$ (this configuration is shown in the case (b) in Fig. 2.2). It was calculated that the energy resolution by this ratio is sufficient for our aimed accuracy in the coefficient a [48]. So when a particle is moving from a strong to a weak magnetic field, the parallel velocity component is enlarged. This effect is called *inverse magnetic mirror effect* (see Fig. 2.3).

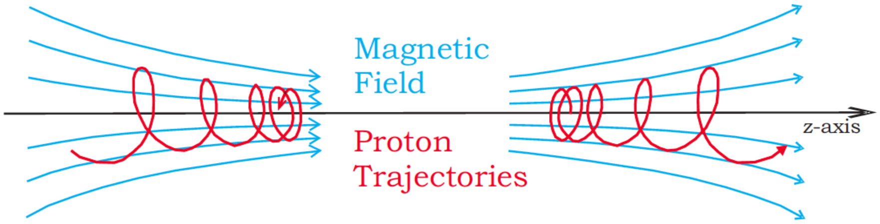

Figure 2.3: Sketch of the normal and the inverse magnetic mirror. Field lines and proton trajectories in the normal (left) and the inverse (right) magnetic mirror effect. Picture from [8].

2.2.2 Transmission function

The transmission function $F_\mathrm{tr}(T_0)$ represents the probability of a proton with a given initial kinetic energy T_0 and emission angle θ (with respect to magnetic field lines in the DV) to overcome the potential barrier U_A applied in the AP. As for the velocity, the kinetic energy of the proton can be decomposed into a longitudinal and a transversal component with respect to the z-axis:

$$T_\parallel = T \cos^2\theta \quad \text{and} \quad T_\perp = T \sin^2\theta \tag{2.5}$$

The magnetic moment $\mu = \frac{p_\perp^2}{2mB}$ is invariant in the adiabatic approximation. This is valid at any position between the DV and the AP along the protons trajectories, and this allows to establish a relation for the angle θ:

$$\frac{T_0 \sin^2\theta_0}{B_0} = \frac{T \sin^2\theta}{B} \quad \Longrightarrow \quad \sin^2\theta = \frac{B}{B_0}\frac{T_0}{T}\sin^2\theta_0 \tag{2.6}$$

where T_0 and θ_0 are the initial kinetic energy and the initial angle of the protons (in the DV). We know that most of the kinetic energy is transferred to the longitudinal component during the path from the DV to the AP. Due to the adiabatic approximation, the total kinetic energy stays constant. So, the longitudinal component of the kinetic energy can be calculated as follow:

$$T_{\parallel} = T(1 - \sin^2\theta) = T - \frac{B}{B_0} T_0 \sin^2\theta_0 \tag{2.7}$$

The total energy of the proton is defined as $E = T + V$ (with V as the potential energy). The electrodes of the DV are grounded which implies that the protons are emitted in potential $V_0 = 0\,\text{V}$. So, for $z = 0$, in the DV, the total energy is $E_0 = T_0$. For any other position along the z-axis with an electric potential U applied, the potential energy is $V = e(U - U_0)$, and so the kinetic energy is $T = E - e(U - U_0) = T_0 - e(U - U_0)$ due to the total energy conservation.

Along their trajectories, protons need to have $T_{\parallel} > 0$ in order to not be reflected. Then, they will reach their minimum of longitudinal kinetic energy in the AP: $T_{\parallel}$ will be equal to the potential energy of the AP. So, the proton can overcome the potential barrier U_{A} at the AP if it has the minimal initial kinetic energy given by:

$$T_{\text{tr}} = \frac{e(U_{\text{A}} - U_0)}{1 - \frac{B_{\text{A}}}{B_0}\sin^2\theta_0} \tag{2.8}$$

This transmission condition is a function of the initial angle θ_0 between the proton momentum and the magnetic field lines (along the z-axis). As shown in Fig. 2.4, the transmission function can be divided in three parts. The function has two minima $T_{\text{tr}}^{\text{min}}$ reached for $\theta_0 = 0°$ and for $\theta_0 = 180°$. Then, it is maximal, $T_{\text{tr}}^{\text{max}}$, for $\theta_0 = 90°$:

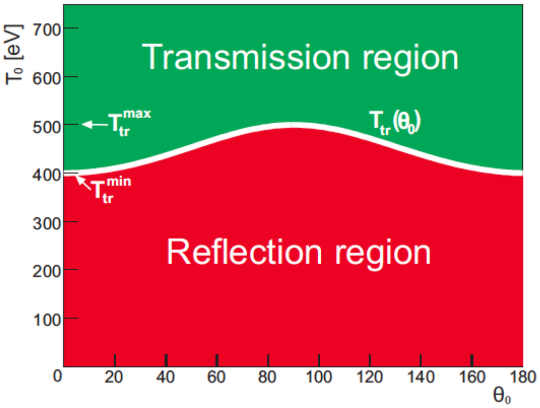

Figure 2.4: Angular dependence of $T_{\text{tr}}(\theta_0)$ for $e(U_{\text{A}} - U_0) = 400\,\text{eV}$. Only protons with initial kinetic energy $T_0 > T_{\text{tr}}(\theta_0)$ will be transmitted. Picture from [9].

$$T_{\text{tr}}^{\text{min}} = e(U_{\text{A}} - U_0) \quad \text{and} \quad T_{\text{tr}}^{\text{max}} = \frac{T_{\text{tr}}^{\text{min}}}{1 - \frac{B_{\text{A}}}{B_0}} \tag{2.9}$$

So, if a proton has an initial kinetic energy $T_0 \leq T_{\text{tr}}^{\text{min}}$, it will be reflected. On the opposite case, if $T_0 \geq T_{\text{tr}}^{\text{max}}$, the proton will overcome the potential barrier at the AP. The last case concerns the intermediate kinetic energies, $T_{\text{tr}}^{\text{min}} < T_0 < T_{\text{tr}}^{\text{max}}$. In this, the transmission is obtained by dividing the number of transmitted protons by the total one emitted in the same hemisphere towards the detector. This gives the following equation:

$$F_{\text{tr}}(T_0)|_{T_{\text{tr}}^{\text{min}} < T_0 < T_{\text{tr}}^{\text{max}}} = 1 - \cos\theta_0^{\text{max}} \tag{2.10}$$

where $\theta_0^{\max}$ is the maximal angle at which protons are still transmitted through the AP. From the eq. (2.8), we obtain the kinetic energy for this angle and it is possible to formulate the adiabatic transmission function $F_{\mathrm{tr}}(T_0)$ shown in Fig. 2.5:

$$F_{\mathrm{tr}}(T_0) = \begin{cases} 0 & \text{if } T_0 \le T_{\mathrm{tr}}^{\min} \\ 1 - \sqrt{1 - \frac{B_0}{B_{\mathrm{A}}}\left(1 - \frac{T_{\mathrm{tr}}^{\min}}{T_0}\right)} & \text{if } T_{\mathrm{tr}}^{\min} < T_0 < T_{\mathrm{tr}}^{\max} \\ 1 & \text{if } T_0 \ge T_{\mathrm{tr}}^{\max} \end{cases} \tag{2.11}$$

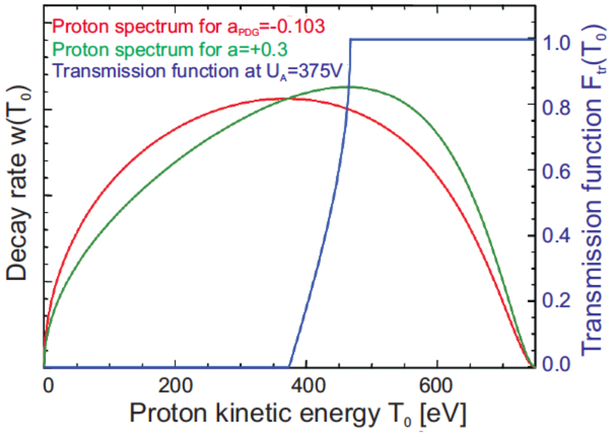

Figure 2.5: Adiabatic transmission function (blue curve) for a potential barrier voltage of 375 V. Picture from [9].

The transmission function depends only on the electrostatic potential difference $e(U_{\mathrm{A}} - U_0)$, and the ratio of the magnetic field strengths in the DV and in the AP, $r_{\mathrm{B}} = \frac{B_{\mathrm{A}}}{B_0}$. As long as the adiabatic conditions are fulfilled, the transmission function is independent of the explicit electromagnetic field.

2.3 Technical description

The experiment *a*SPECT was proposed in 2000 [49] and was used first at the FRM II at Munich. The technical descriptions of the spectrometer are already presented in the previous PhD theses [8, 9, 10, 11]. Since 2011, improvements were made on the spectrometer and some of them are presented here. Those concerning the electrode system will be presented in detail in the PhD thesis of Alexander Wunderle [50].

2.3.1 Vacuum and cryogenic setup

The main component of the spectrometer is a cryostat[3] with cylindrical shape: Ø=0.76 m and a total outer length of ≈3.30 m. As shown in Fig. 2.6, there are two separated vacuum sections. The first one surrounds the superconducting coils and insulates them from external heat: this is the "isolating vacuum" which can reach a pressure of about 10^{-5} mbar. The second section is the "bore tube" in which neutrons decay and protons move. The bore tube is also

---

[3] The cryostat was manufactured by Cryogenics Ltd.

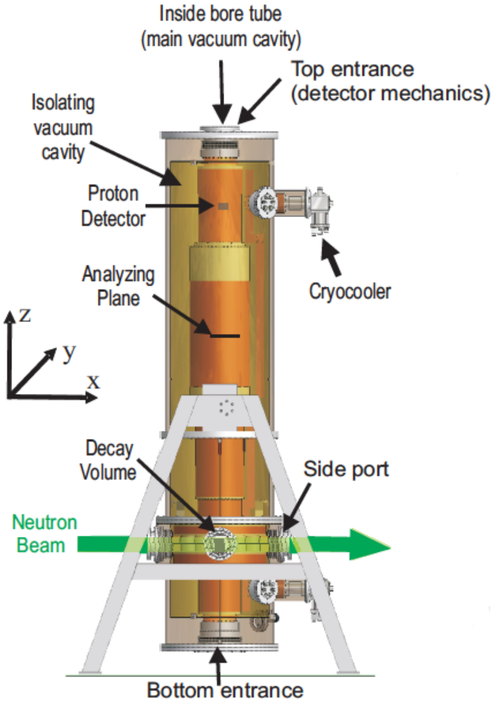

Figure 2.6: Technical view of the spectrometer *a*SPECT. Picture from [9].

cylindrical with Ø=200 mm, and the vacuum (called "main vacuum") can reach a pressure down to about 10^{-9} mbar. In this section ultra high vacuum (UHV) conditions are needed to suppress scattering processes with residual gas molecules inside the spectrometer. The main volume has one aperture at the top and one at the bottom, and four side ports (Ø=150 mm) at the level of the neutron beam ($z = 0$) .

The vacuum inside the bore tube is ensured by turbo pumps and getter pumps. Typically, one turbo pump is connected to one side port of the spectrometer. This turbo is connected to a second turbo pump and backed by a primary pump: this forms a "cascading" system. The second turbo, also called "cascading" pump will ensure the compressing ratio of the pumping. The same system is also used for the insertion mechanics of the detector which is placed on the top of the spectrometer (see Chapter 3). On a second side port, an external getter pump is connected (see Fig. 2.7). Additionally, internal getter pumps (SAES) are mounted at the electrode system (for more details, see Appendix A). Each port can be closed by gate valves.

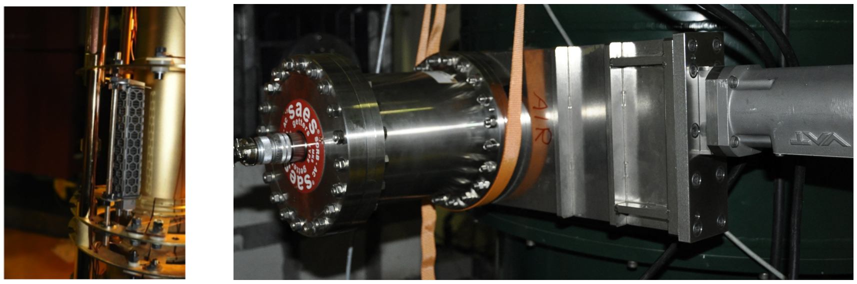

Figure 2.7: Internal getter pump mounted at the electrode system (left). External getter pump connected to the cryostat perpendicularly to the neutron beam line (right).

Cryogenic conditions are required as the magnet operates at high current in superconducting coils (in "persistent mode"). To obtain these conditions, two cold heads are mounted to the cryostat. They consist in "cold fingers" which thermally couple the helium lines to the spectrometer. The helium is provided by two compressors and is pumped by two cryocoolers[4] to the spectrometer. The cryocooler at the first stage has a cooling power of 35 W (about 70 K) and is coupled to the inner bore tube. At the second stage, the cooling power is 1 W (about 4.2 K) and it is coupled to the superconducting coils. The low temperature in the bore tube forces the residual gas ions to freeze out on the surface. This increased the UHV in the main vacuum section.

The vacuum was investigated and improved after the beam time of 2011 and studies with a mass spectrometer were performed in 2012 (see Chapter 5).

2.3.2 Magnetic and electric fields

The spectrometer *a*SPECT is composed of a set of coils and a set of electrodes. These create magnetic and electric fields which allow the application of the principles for the proton's motion (see 2.2). The sets are presented in the Fig. 2.8 along the z-axis of the spectrometer.

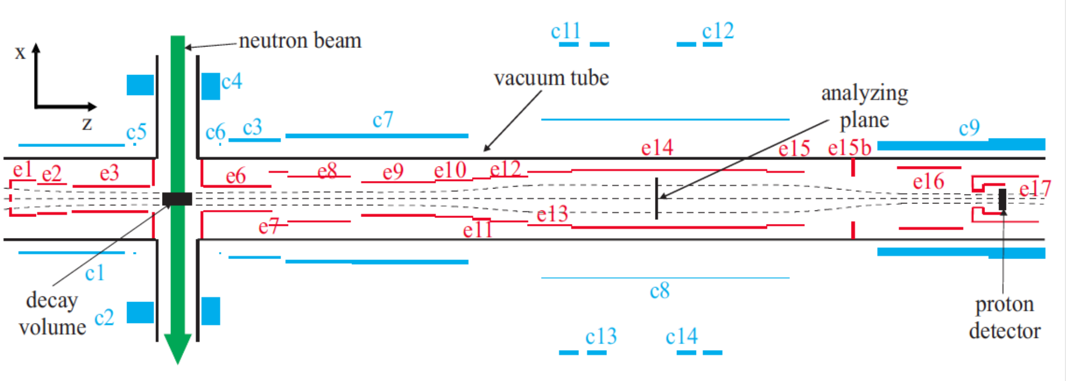

Figure 2.8: Scheme of the coils (blue) and the electrodes (red) inside *a*SPECT. Picture from [9].

The magnetic field is provided by nine superconducting coils (c1 to c9) made of NbTi (with a transition temperature $T_C \approx 9$ K). These coils operate in a serial configuration except for the coils c5 and c6. These two coils are correction coils used to adjust the shape of the magnetic field in the DV: they generate a small field gradient below the lower end of the DV in order to avoid potential traps[5]. The two pairs c11/c12 and c13/c14 are external coils used to adjust the local maximum of the field in the AP. One pair is operated in Helmholtz configuration to alter the magnetic fields in the AP and so the ratio r_{B}. The other pair is operated in anti-Helmholtz configuration[6]. This system creates a field gradient in the z-direction in order to adjust the local maximum of the $\overrightarrow{B}$ field at the same height as the maximum of the electric potential in the AP electrode. That is why, the magnetic field has to be very well known and so several measurements were performed (see Appendix B).

At the detector, the magnetic field is 2 times higher than in the DV. This allows to focus the protons towards the detector which can be a small detector (see Chapter 3). The magnetic mirror effect induced is strong enough to stop electrons and to reduce significantly the background related to these electrons.

---

[4] Cryocoolers Sumitomo RDK408D.

[5] A maximum of the $\overrightarrow{B}$ field in the middle of the DV would generate a trap for particles with very low longitudinal momentum due to the magnetic mirror effect.

[6] Anti-Helmholtz configuration: the current in one coil is going in the opposite direction than in the other one.

A set of electrodes generates a complex electric field. The electrodes e1 to e15 form the “electrode system” (described in the next section) which includes the ME, the DV, the lExB and the AP electrodes. The electrodes uExB are represented by e16 in Fig. 2.8. The electrode e17 is called “detector electrode” (or “detector cup”) and generates the high acceleration potential for the protons before their detection. The electrodes were designed to provide a homogeneous electric potential in the DV and in the AP: $e(U_\mathrm{A} - U_0) < 10\,\mathrm{meV}$.

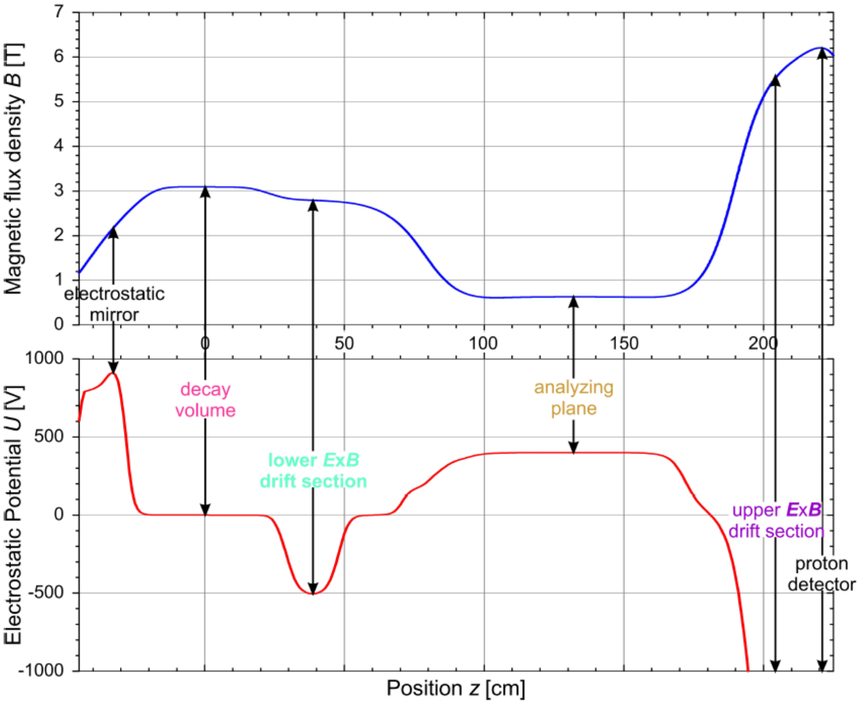

Figure 2.9: Magnetic and electric fields along the z-axis of the spectrometer. Picture from [10].

Shapes of the magnetic and electric fields are shown in Fig. 2.9. These fields could also provide traps for charged particles. The first example is the potential barrier at the AP which blocks particles with not enough energy. These particles will oscillate between the AP and the ME, and will be finally removed by the lExB electrodes. But a part of them could interact with other particles. Furthermore, the potential barrier U_A is positive and the AP electrode is relatively long (see section 2.3.3), this region could become a trap for negatively charged particles like electrons. This could be also the case at the ME electrodes with a positive voltage. These conditions can generate a background in the signal measured during a beam time. This was investigated in detail with and without the neutron beam, and the results are presented in Chapter 6.

2.3.3 Presentation of electrodes

Most of the electrodes are part of a global system called the “electrode system”. It consists of four long rods (2.4 m length) where the electrodes e1 to e15 are fixed as shown in Fig. 2.10. In contrast to the coils, the electrode system is independent of the cryostat: it can be moved out of the spectrometer via the bottom flange of the bore tube. All the system is made of OHFC[7] copper because of the required UHV conditions in the main volume. As the homogeneity of an

---

[7] OHFC: Oxygen Hydrogen Free Copper.

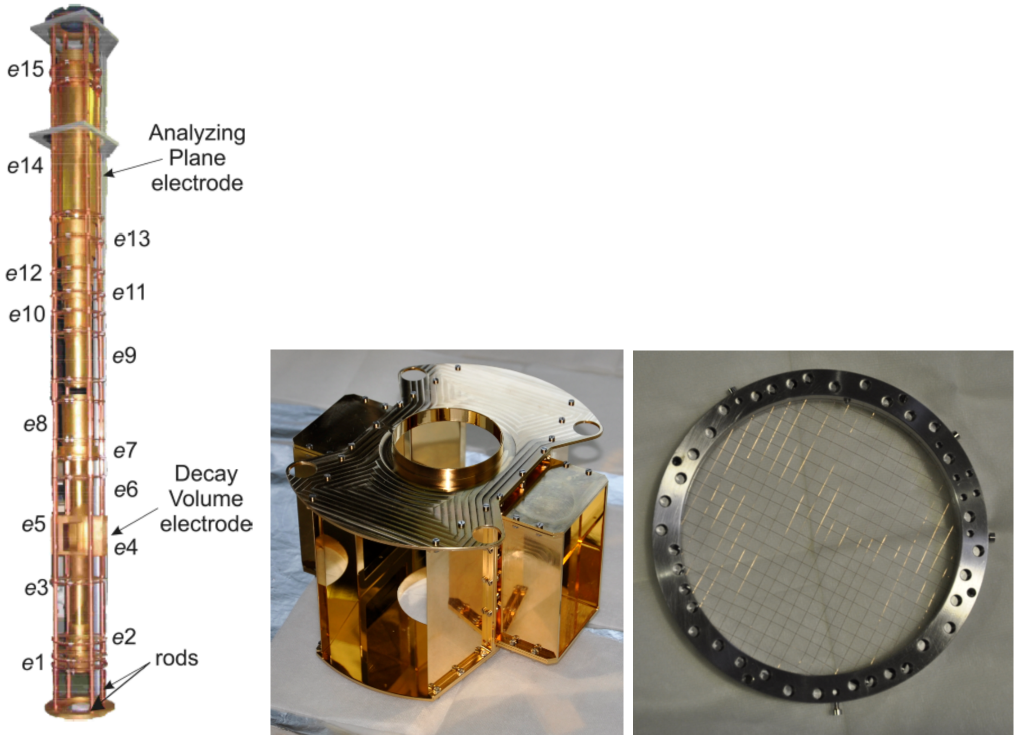

Figure 2.10: The Electrode System (left), the Decay Volume (center), and the Electrostatic Mirror (right).

electrical potential depends on the *work function*[8] of the electrode surface, the electrodes are gold coated. This compensates the mechanical stress induced by the manufacturing which degrades the surface conditions. For reason of adhesion, a thin layer of silver (1 μm) was coated between the copper substrate and the gold layer (2 μm). The diameter of the electrodes is large enough that all protons emitted in the DV will be imaged onto the detector. The powering is ensured by Kapton-insulated wires. The other electrodes, uExB and the detector electrode, are independent of the electrode system.

The *electrostatic Mirror Electrode* (e1, e2) is used to reflect protons emitted from the DV into the lower hemisphere. It consists of a grid of copper wires (this avoids a too low potential in the center) placed at the electrode e1, and a quadrupole electrode e2. These electrodes are set to a global positive voltage able to reflect all protons. The reflection is adiabatic as it does not change the total energy of the proton.

The *Decay Volume* (e3-e6) is held at 0 V and is divided in three parts. The neutron beam (x-axis) passes through a central part which has a rectangular shape (110 × 70 mm). The cylindrical electrodes e3 and e6 are adjacent to the central part which is also cylindrical (220 mm length and a 64 mm inner diameter) .

The *Analyzing Plane* electrode (e14) has a length of 620 mm and a diameter of 140 mm. In Fig. 2.11(a), we present the original AP electrode with a cylindrical shape. It was replaced in 2013 by an octagonal geometry in order to improve the surface conditions: with the cylindrical one,

---

[8] The work function is related to the material and the crystal structure of the surface. If the electrodes are made from single crystals with a defined, uniform orientation, they would provide the best potential homogeneity.

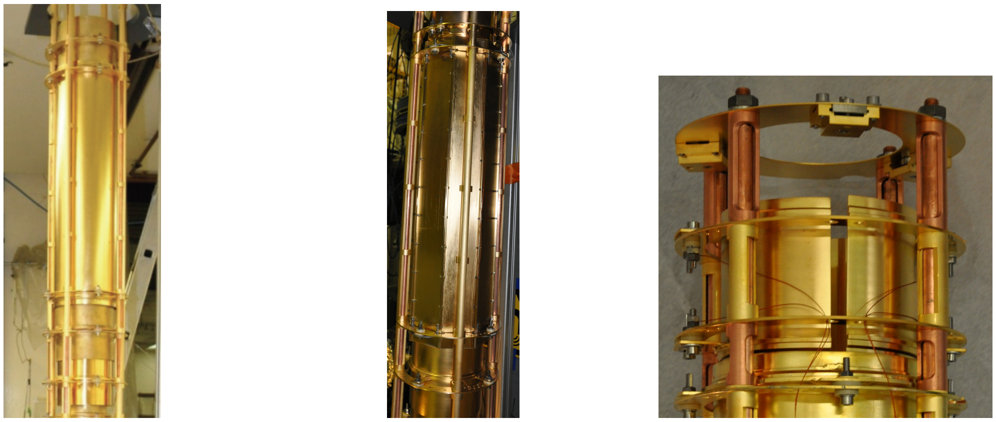

(a) AP with cylindrical shape used in 2011 and 2012.

(b) AP with octagonal shape used in 2013.

(c) Electrode e15 as a dipole in 2013

Figure 2.11: The AP electrode e14 and the electrode e15 above the AP.

the fixations to the rods induced small torsions locally on the surface and caused inhomogeneous local electric field. The octagonal one presents flat surfaces which are more homogeneous in the coating. In addition, their work function can be measured precisely with the Kelvin probe. This electrode provides the retardation potential U_{A} which is set to values in the range from 0 to +780 V. To ensure the adiabatic movement of the protons in this region, additional electrodes e10 to e13 and e15 are electrically coupled with e14 (see voltages in Tab. 2.1). They are cylindrical but e15 was changed in 2013 to become a dipole electrode composed of two half cylinders (see Fig. 2.11(c)).

Two pairs of $\overrightarrow{E} \times \overrightarrow{B}$ electrodes (see Fig. 2.12) provide an electric field perpendicular to the magnetic field. They induce a drift velocity $\overrightarrow{u}$ on charged particles in addition to their gyration:

$$\overrightarrow{u} \propto \frac{\overrightarrow{E} \times \overrightarrow{B}}{B^2} \tag{2.12}$$

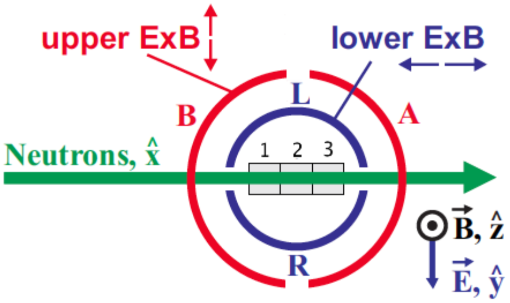

Figure 2.12: Scheme of the $\overrightarrow{E} \times \overrightarrow{B}$ electrodes and their orientation with respect to the neutron beam and the detector pads.

Therefore the charged particles will drift perpendicularly to both magnetic and electric fields and the displacement will be proportional to the time spent in the fields.

The *lower ExB* electrode (e8) is placed between the DV and the AP. It is composed of two half cylinders which are typically set to different negative potentials to produce an electric dipole field perpendicular to the neutron beam axis. This electrode is used to remove trapped protons which cannot overcome the potential barrier U_{A}. At each oscillation, they will be displaced by a few millimeters and finally drift towards the bore tube where they are absorbed.

The *upper ExB* electrode (e16) is installed in front of the detector. As for the lExB, this electrode is composed of two half cylinders made of stainless steel with a diameter of 130 mm and a length of 160 mm. The main purpose of uExB is to ensure the post-acceleration of the protons against the magnetic mirror created by the increasing magnetic field at the detector region. Its dipole configuration is also used to shift the protons distribution with respect to the detector. This drift can separate spatially electron and proton from the same neutron decay (called "coincidence event"). The voltages for the uExB are chosen to minimize the edge effect (see section 2.4). The lExB and uExB electrodes are shown in Fig. 2.13.

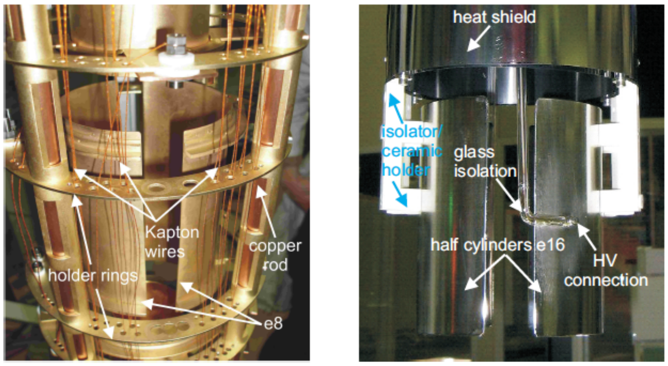

(a) Lower ExB electrode.

(b) Upper ExB electrode made of stainless steel with heat shields for detector.

Figure 2.13: The $\vec{E} \times \vec{B}$ drift electrodes: the lExB (left) made of OFHC copper and integrated in the electrode system, and the uExB (right) made of stainless steel (picture from [9]).

The *Detector Electrode* (e17), also called *Detector Cup*, is made of stainless steel with an inner diameter of 45 mm and an outer one of 109.4 mm. This electrode contains a UHV-feed-through where the detector is mounted (see Chapter 3). It is held on the acceleration voltage of -15 kV (standard configuration). The surface is electropolished and a long cylindrical tube covers all possible edges (screws, ...) as shown in Fig. 2.14.

Typical voltages applied to each electrode during a beam time are presented in Tab. 2.1.

2.3.4 Mechanical set-up

The support structure of the spectrometer is made of Armco iron and consists of a square base of about 2 m sides with pillars (20×20 cm^2) on each corner, and a platform on the top of pillars. The global height is about 5 m (see Fig. 2.15). The spectrometer is hold above its center of gravity by two massive shafts to transversal bars. These fixations allow to rotate the spectrometer by 90° and put it in the horizontal configuration for the insertion of the electrode system through the bottom aperture of the bore tube. The top platform has a hole for the installation of the insertion mechanics of the detector (see Chapter 3). The holding fixations of

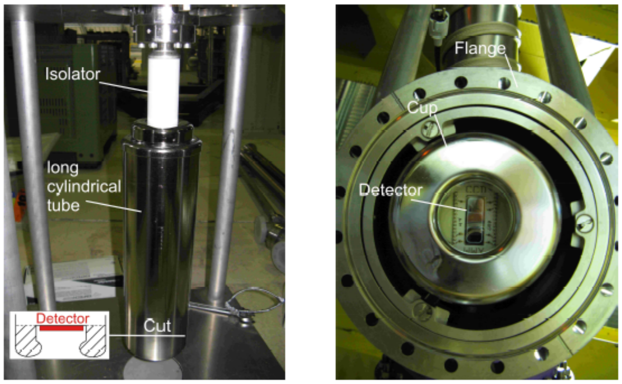

(a) Electrode e17 and mechanics (side view).

(b) View from below onto cup and detector.

Figure 2.14: The Detector Electrode e17 (picture from [9]).

Electrode	Voltage	Comments
e1	800 V	Electrostatic mirror (grid on bottom side)
e2	1000 / 820 V	Electrostatic mirror (quadrupole electrode)
e3 to e6	grounded	Decay volume electrodes
e7	grounded	Usable for systematic checks
e8	-1000 | -50 or -200 | 0 V	Lower ExB drift electrodes
e10	$0.435331 \times U_{\mathrm{A}}$	Variable
e11	$0.683960 \times U_{\mathrm{A}}$	Variable
e12	$0.892352 \times U_{\mathrm{A}}$	Variable
e13	$0.991040 \times U_{\mathrm{A}}$	Variable
e14	U_{A}	Analyzing plane electrode
e15	$0.985094 \times U_{\mathrm{A}}$	Variable
e16	-2 | -2 or -3.7 | -4.7 kV	Upper ExB drift electrodes
e17	-15 kV (typically)	Detector cup electrode

Table 2.1: Typical settings of the electrodes.

the spectrometer offer also the possibility to adjust the orientation of the DV with the neutron beam line.

The material of the structure makes that it acts as an antimagnetic screen reducing stray fields. However it has a minor influence on the magnetic field inside the bore tube.

2.4 Systematic effects

A good knowledge of the systematic effects related to the experimental apparatus is essential for high precision measurements. Several systematics were discussed and described in publications for the proposal of *a*SPECT [48, 49].

2.4.1 The proton transmission

The transmission function in eq. (2.11) describes the protons motion in *a*SPECT. So, a very good knowledge of this function is required via the ratio r_{B} between the magnetic field in the AP and the one in the DV, and via the electric field difference $e(U_{\mathrm{A}} - U_0)$.

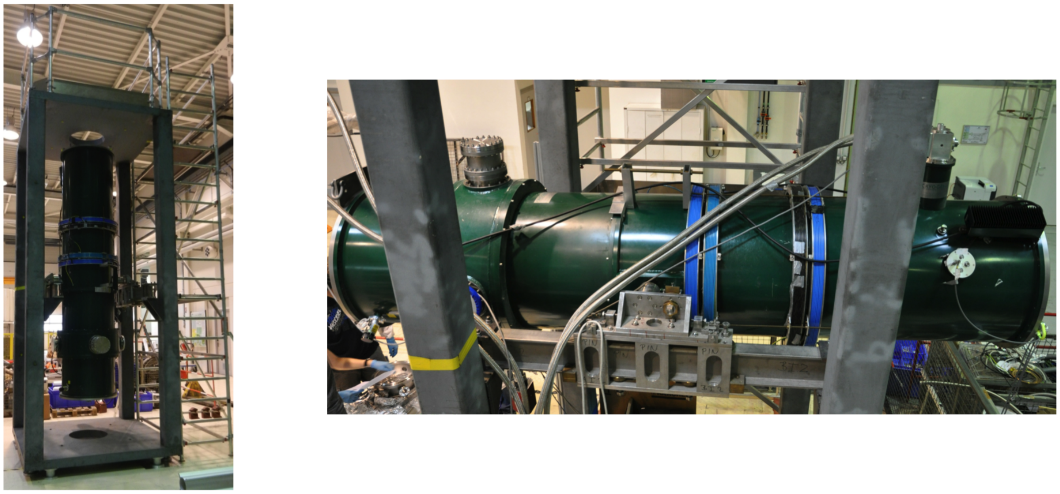

Figure 2.15: The spectrometer *a*SPECT installed in the preparation zone of ILL. This photo shows how the spectrometer is held by the support structure and in its horizontal configuration (right).

For the expected accuracy on a, it was calculated that the ratio r_{B} should have a relative uncertainty of 10^{-4}. This implies a very good stability of the magnetic field which is measured in the AP and in the DV by NMR electrodes (Fig. 2.16). These electrodes are placed inside the bore tube, on the electrodes system and are based on nuclear magnetic resonance of either polarized ^{3}He or Hydrogen (more details in [11]).

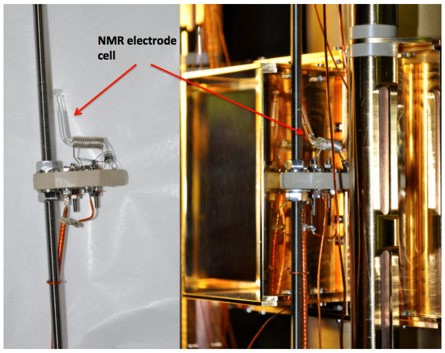

Figure 2.16: NMR electrode composed by a cell containing polarized ^{3}He or Hydrogen, placed next to the Decay Volume (right) in the Electrode System.

Concerning the electric potential, it has to be less than 1 mV in the DV, and its variations in the AP have to be less than 2 mV. For this, the electrodes have to provide an uniform electric potential without being perturbed by the neighboring ones (the field penetration is the main source of deviations): the length of the AP electrode minimizes this effect as does the setting of the electrodes e10 to e13 and e15 to a similar potential. Another source of perturbation can be the accumulation of charged particles around the AP (this region can be a trap for negative charged particles). These charged particles can also be absorbed by the electrodes surface and induce a change in the potential. This effect can be controlled by investigations of the work function of the electrodes surface with a Kelvin probe (more details in [10]). The gold coating reduces this effect.

Another effect is the **non-adiabatic proton motion**. This occurs if the magnetic moment μ, which is considered to be constant in the adiabatic approximation, deviates from its initial value: the adiabaticity is destroyed and the transmission function changes. This can happen between the AP and the DV where the protons move through different regions with high electric and magnetic fields gradients. The amplitude of the oscillations of μ increases with the fields gradient. However, it was calculated that, in the AP, μ is close to its initial value: the charged particles seem to have some kind of "memory" [48] of their initial orbital momentum. The trapped protons between the AP and the DV perform several oscillations and so, have a higher probability to change their trajectories non-adiabatically and to pass the AP. This induces an uncertainty in the transmission function and the measured spectra. This effect can be compensated by the drift field of the lExB. Configurations have to be tested in the limit that the negative potential will not affect the protons and their gyration length. A break of the adiabaticity condition was already observed for $|U_8| > 3\,\mathrm{kV}$.

2.4.2 The interactions with residual gas

On their way to the detector, protons may interact with molecules from residual gas in the main volume. Due to these interactions, the kinetic energy of the proton or the angle θ between the proton momentum and the magnetic field line can change. And so, the transmission function will vary. These interactions with residual gas can occur in different processes: elastic scattering, inelastic energy loss, charge exchange. The collision probability is proportional to the residual gas density and to the pressure (since the temperature inside the main bore tube is constant, $\approx 70\,\mathrm{K}$). A critical pressure p_{cr} is defined at which a considered type of collisions introduces a systematic effect on the coefficient a at a level of $\frac{\Delta a}{a} = 10^{-3}$.

The **elastic scattering** processes affects the energy and the pitch angle θ. The scattering probability is proportional to the path length and therefore to the time a proton spends within the flux tube. This effect is more important for trapped protons since they perform several oscillations before they are removed by the lExB-drift electrode. The critical pressure for different settings of the lExB electrode has been calculated [48] for different values of U_8 (see Tab. 2.2).

U_8 [kV]	-3	-0.3	-0.03
p_{cr} [mbar]	$5 \cdot 10^{-8}$	10^{-8}	$1.4 \cdot 10^{-9}$

Table 2.2: Critical pressure values of elastic p-H_2 scattering for different settings of lExB electrode.

In **inelastic scattering** processes (for example, inelastic p-H_2 collisions), protons can loose energy due to the large cross-section for rotational and vibrational excitations. Electronic excitation and ionization are negligible for protons below 1 keV. The energy losses are in the range of 50 to 1000 meV.

In **charge exchange** processes, a proton could capture an electron from the rest gas molecules. This results in a hydrogen atom and a positive molecular ion with low energy: $\mathrm{p} + \mathrm{M} \rightarrow \mathrm{H} + \mathrm{M}^+$. If this process happens below the AP, the ions would not be detected (blocked by the potential barrier). The critical pressures for different gases have been calculated using published cross-sections (see Tab. 2.3). According to these considerations, the vacuum inside *a*SPECT should be better than 10^{-8} mbar.

This residual gas was investigated during offline tests of *a*SPECT (see Chapter 5). The vacuum was studied with several mass spectrometer measurements at the different steps of the vacuum procedure.

Gas	H_2	Ar	N_2	O_2	He
p_{cr} [mbar]	$2 \cdot 10^{-8}$	10^{-8}	$2 \cdot 10^{-8}$	$4 \cdot 10^{-8}$	10^{-6}

Table 2.3: Critical pressure p_{cr} values of the charge exchange process for different residual gases.

2.4.3 The background

In high precision measurements, the background is a systematic effect which has to be known precisely. In the *a*SPECT experiment, the aim is to obtain a background as low as possible, stable in time and independent of the AP voltage. It can be distinguished into two kinds of background: correlated and uncorrelated.

The correlated background can be induced if electrons emitted simultaneously with protons can reach the detector. In this case, electron and proton are detected in near coincidence. When they are emitted directly towards the detector, the electrons have flight times of about 10 ns[9], and for protons it is about 6 μs. If the dead time is too long, the proton event will not be detected. For high AP voltages, protons spend more time to pass this electrode and their time of flight is longer. As the dead time of the electrons is 4.2 μs, no correlated protons should be lost.

The uncorrelated background can be induced by γ-radiation and cosmic rays, positive ions coming from residual gas or the electrodes, and high energy electrons created by neutron capture. Again, this can be divided in two groups: beam-related and environmental background. During a beam time, it is possible to measure the background with the neutron beam by applying a retardation potential of $U_{\mathrm{A}} \sim 800\,\mathrm{V}$ (higher than the endpoint energy of protons, so they will be all blocked). Due to the small opening angle of the detector, the γ-radiations are suppressed, and external charged particles are “shielded” by the strong magnetic field. The cosmic rays represent a small contribution to the spectra. The ions from the ionization of rest gas molecules are low energetic charged particles of several eV. They can be blocked by the potential barrier at the AP but a part can also be detected and participate to the measured spectra. This last point represents an AP-dependent background.

During my PhD, I performed a detailed analysis of the background and its different components. The spectrometer *a*SPECT can be adjusted by using different settings for the electrodes which can have an influence on the background. The different measurements and results are presented in the Chapter 6.

2.4.4 Doppler effect due to the neutron motion

In acoustics and optics the Doppler effect describes the frequency's shift of a source moving with respect of a recipient (the shift depends on the direction of the movement). In *a*SPECT, the decaying neutron is moving. This may change the observed energy of the outgoing proton in the laboratory system with respect to the energy in the center-of-mass system (CMS) of the decaying neutron. At the ILL, the cold neutron beam used for *a*SPECT has an average kinetic energy of $\langle T_{\mathrm{n}} \rangle = 5\,\mathrm{meV}$. A proton with a kinetic energy T_{CMS} in the CMS has an energy in the laboratory system of $T_{\mathrm{LAB}} = T_{\mathrm{CMS}} + \delta T$ with $\delta T = \sqrt{\langle T_{\mathrm{n}} \rangle \cdot T_{\mathrm{CMS}}}$. This would have an impact with respect to the aimed 10 meV accuracy of the proton energy in the CMS.

Furthermore, the magnetic field in *a*SPECT is transverse to the neutron beam line (x-axis) and the protons are emitted equally in the full solid angle. Some of them are emitted in the opposite direction of the neutrons motion. Due to the Doppler effect, these protons will have a

---

[9] The electrons move with velocities close to the light speed due to their high energy.

lower energy in the laboratory system than in the CMS and so, a part of them will not be able to overcome the potential barrier at the AP.

In the case of aSPECT, the effects on a were calculated for a typical neutron velocity distribution and different voltages at the AP. Considering $U_{\mathrm{A}} < 500\,\mathrm{V}$, this systematic effect has a impact lower than 10^{-4}.

2.4.5 Edge effects

The neutron beam which passes through the spectrometer is larger than the detector area. As seen in the electrodes description, the DV is 70 mm larger with a 64 mm diameter top aperture for the outgoing protons. The detector is composed by three pads aligned with the neutron beam axis, and with an active area of 100 mm^2 each. In aSPECT, the magnetic field projects the shape of the neutron beam onto the detector. This means that the edge effect describes the systematic impact of an inhomogeneous neutron beam profile on the coefficient a.

As the proton gyration radius is $r_{\mathrm{g}} \propto \sqrt{T_{\perp}}$, the beam width onto the detector depends on the kinetic energy of the protons. Fig. 2.17 illustrates the edge effect related to the beam profile. So, due to their gyration motion, some protons from the projection area of the detector can miss the detector. And in the same way, protons from the outside of the projection area can be detected.

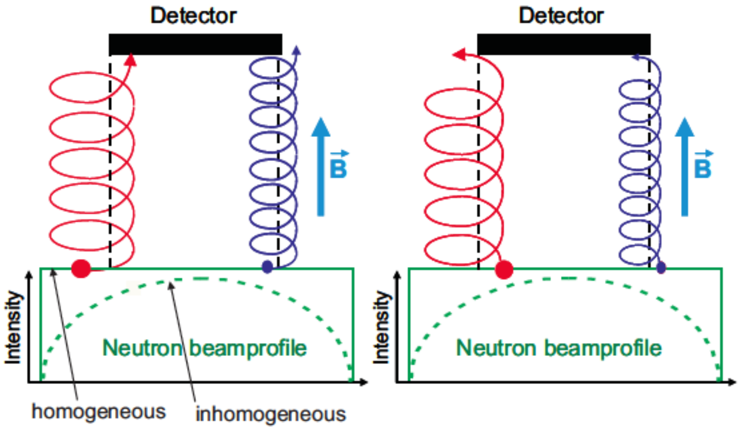

Figure 2.17: Illustration of the edge effect due to the gyration motion of the protons. In the case of a homogeneous neutron beam profile (full green line), the effects is canceled. But in the case of an inhomogeneous beam profile (dashed green line), this effect depends on the kinetic energy of protons: it is caused by an AP voltage dependent distribution of gyration radii for protons at the detector. Picture from [9].

In an ideal case, the neutron beam profile is homogeneous and the edge effect is canceled. Here, the probability for a proton from outside of the projection area to hit the detector is the same as the probability for a proton from inside the projection area to miss the detector.

In the case of an inhomogeneous beam profile, the probabilities are not the same and depend on the kinetic energy. The edge effect concerns especially the direction transversal to the neutron beam as the profile can be considered flat along the beam axis.

In order to minimize the edge effect, the neutron beam is collimated before its arrival in the DV: a collimation system is placed in the beam line before the DV (see details in [9]).

2.4.6 The detection efficiency

Due to the dead layer and the response function of the detector, not all protons hitting the detector will be detected. The fraction of detected protons is characterized by the detection efficiency (i.e., probability for a proton to be detected). This depends on the energy and the impact angle of protons. The impact energy of protons is between the acceleration voltage of the detector and the acceleration plus the endpoint energy of the proton spectrum: $T_{\mathrm{Det}} \approx 15^{+0.75}_{-0}\,\mathrm{keV}$.

Some protons which hit the detector can be back-scattered: a proton is scattered several times inside the detector and finally leaves without having fully deposited its energy. However, the negative high acceleration potential traps this proton which can hit the detector a second time with a similar energy. The two hurts are separated by a very short time of about $0.5\,\mu$s. So, it is not possible that one back-scattered proton is counted as two events. The probability of Rutherford backscattering of protons in the entrance window ($\approx 30\,$nm thick aluminum layer) of the detector depends on the impact energy T_{Det}:

$$P_{\mathrm{Rutherford}} \propto \frac{1}{(T_{\mathrm{Det}})^2} \tag{2.13}$$

Therefore, this leads to a slight distortion of the measured spectra to lower pulse-heights (see details in [8]).

Chapter 3

The detection system

Le détecteur utilisé dans aSPECT est un semi-conducteur (*Silicon Drift Detector*, SDD). Il mesure l'énergie déposée par une particule chargée. Le signal émis étant de faible amplitude, il est pré-amplifié et traité par diverses cartes électroniques. Le détecteur est placé à l'intérieur du cryostat via un système d'insertion permettant d'intervenir sur le SDD sans perturber les conditions dans le volume principal sous ultra-vide. Le signal pré-amplifié est transmis vers une boîte électronique placée hors du champ magnétique, au-dessus du spectromètre. Cette boîte contient la première partie du système d'acquisition qui traite le signal avant d'en transmettre les données à l'ordinateur. L'analyse s'effectue ensuite via des programmes développés en C++/ROOT. Ce système de détection permet une bonne séparation des évènements protons du bruit électronique. Sa description est basée sur celle présentée dans la thèse de Martin Simson [8]. De nombreux tests ont été menés afin d'en améliorer les performances et de le calibrer. De plus, dans le but de supprimer les problèmes liés à la saturation dans les signaux, de nouvelles cartes électroniques ont été implémentées pour le temps de faisceau en 2011.

3.1 General presentation

The detection system used in aSPECT is composed of a detector (a Silicon Drift Detector presented in section 3.2) and electronic boards (preamplifier, shaper and ADC presented in section 3.3). This system is installed in a set up called "detector mechanics" which is fixed on the top aperture of the main bore tube of the cryostat.

3.1.1 The detection chain

The Fig. 3.1 shows how the different parts of the detection chain are connected to each other. The detector, placed inside the main bore tube, sends a quite small signal. As the main electronic processing is placed outside of aSPECT (above the antimagnetic screen), the output signal has to be amplified: this is the purpose of the preamplifier board connected just after the detector. The detector is divided in three pads which each send a signal. Thus, after the preamplifier, three signals are sent by coaxial cables to the next step of the electronics: the shaper. This board is placed inside an electronics box with the ADC board and the voltage divider board. This box is installed on the top of the detector mechanics (see section 3.1.2). After being treated by the shaper and the ADC boards, signals are sent to the DAQ computer via an optical fiber.

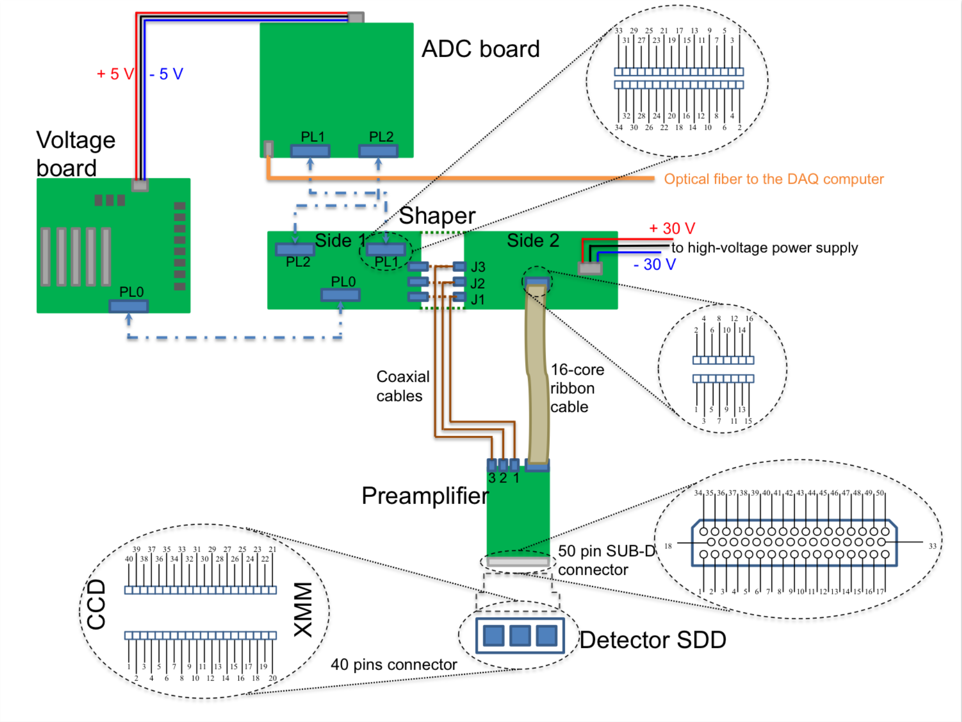

Figure 3.1: Connections of the different components of the detection system: detector, preamplifier, shaper, voltage board, ADC board.

All of the electronics is powered by three input voltages ±30 V and 0 Vwith the help of several DC-DC voltage converters. The input voltages are created by a laboratory power supply also on the high potential of the acceleration voltage. The power supply is connected to the standard 230 V AC power via an insulating transformer (see Fig. 3.2). In this transformer the primary

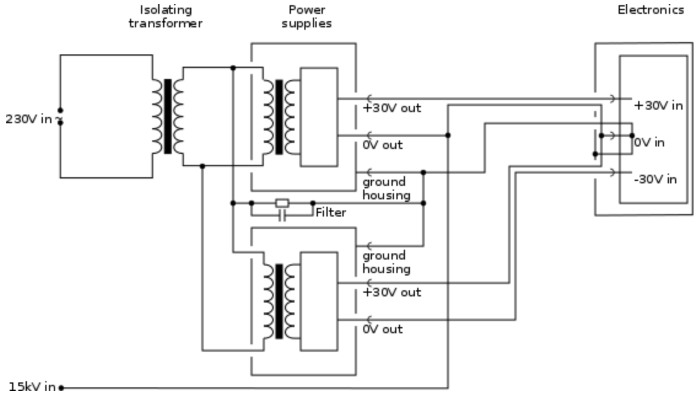

Figure 3.2: Connection scheme between power supplies and electronics. The power supplies are connected to a transformer and provide +30 V and −30 V for the electronics. This connection scheme was optimized to avoid high voltage current flow problem and to protect power supplies.

and secondary windings are electrically separated, so that the power can be fed to the primary side of the transformer on earth potential and taken out on the secondary side on high voltage. To protect against the high voltage, both the power supply and the insulating transformer are inside a perspex box.

The SDD and the electronics need several different supply voltages from 5 to 200V to be operated. All these voltages have to be provided on the high potential of the acceleration voltage, and are created by the voltage divider board (see Fig. 3.3). The use of this additional board allows to reduce the amount of power supplies needed.

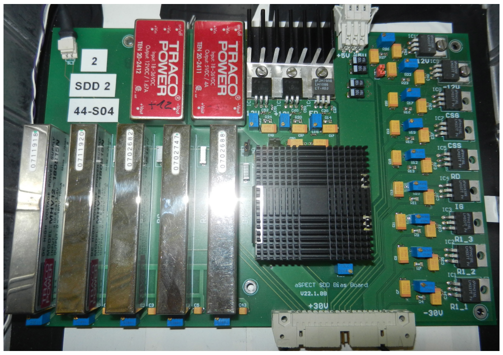

Figure 3.3: Voltage divider board.

3.1.2 The detector mechanics

The detector mechanics is used for the insertion of the detector inside the main bore tube (see Fig. 3.4(a)). The lower part of the mechanics is on high voltage and is separated from the

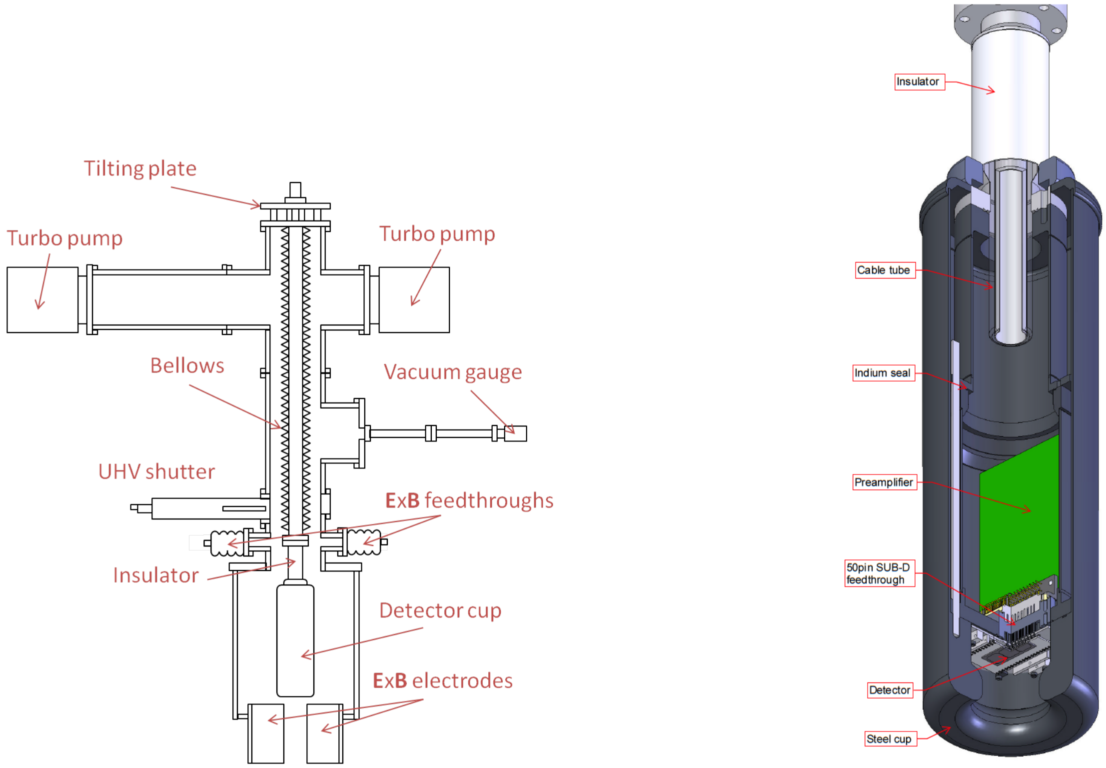

(a) Insertion mechanics of the detector in its version for 2012 and 2013.

(b) High voltage part of the detector mechanics.

Figure 3.4: Movable detector mechanics above the uExB electrodes (scheme based on [8]).

upper part on ground potential by a ceramics tube (insulator). The lower part is composed by two nested tubes. The inner one has an indium sealed flange (this allows a larger diameter in the lower part where the preamplifier is placed, see Fig. 3.4(b)) and is closed on one side by the holder of the detector. The outer tube (with outer diameter of about 110 mm) has a massive stainless steel cup on the bottom to shield the detector from radioactive background (mostly γ from the neutron apertures and from neighboring instruments). To avoid electrical breakdowns, all edges are carefully rounded and electro-polished. In a same way, the screws to connect the lower part to the insulator are covered with two semicircular, rounded, and electropolished pieces.

This set up is independent from the general structure. This allows to perform maintenance works on the detector without warming up the cryostat and without venting the main vacuum. The top aperture of the main bore tube can be closed by a UHV vacuum shutter. Thus, the detector is retractable via the use of a membrane bellows which separates the inner steel tube at atmospheric pressure from the UHV inside the spectrometer. At the cross-piece of the mechanics, two turbo pumps are connected in order to reach a stabilized low pressure before opening the gate valve and inserting the detector in the spectrometer[1]. The membrane bellows allows for a total movement distance of about 70 cm, which is enough to extract the detector from its measurement position. The central tube can be separated in two parts: in the retracted configuration, the height of system is higher than the height of the crane in the guide hall of the ILL.

In the measurement configuration, the electronics box is placed on top of the mechanics (see Fig. 3.5). It is installed in a plexiglas box to protect persons against the high voltage. The cables between the preamplifier (in the lower part) and the shaper (in the electronics box) are contained in an acrylic glass tube inside the central stainless steel tube. A thin walled steel tube that just fits inside the acrylic tube is connected to the high voltage and thus ensures that the cables are inside a homogeneous potential (this also helps to shield against electrostatic noise).

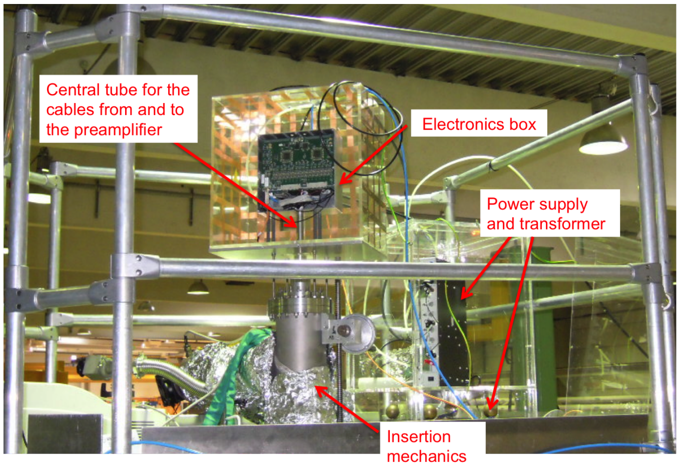

Figure 3.5: Insertion mechanics installed on the top of the spectrometer with the electronics box inside a plexiglas box placed on top of the mechanics. On the right, the power supply for the electronics and the transformer are also placed inside a second plexiglas box.

In order to avoid potential water condensation on the inside of the ceramics tube (this can cause electrical breakdowns), a tube is inserted to blow pressurized air for cooling onto the preamplifier board. Inside the spectrometer, the ceramics tube is cooled passively by the cold bore tube around. A second pressurized air tube is used to cool the digital electronics inside the aluminum box.

---

[1] In 2011, only one turbo pump was connected to the detector mechanics, a second turbo was installed in 2012 to improve the vacuum in the system and avoid spike in pressure while opening the gate valve.

3.2 The Silicon Drift Detector

The detector used in the experiment aSPECT is a Silicon Drift Detector (SDD). This kind of detector is efficient for low-energy proton detection. The implementation of this new detector in the experiment aSPECT was performed by Martin Simson [51, 52].

3.2.1 The principle of the Silicon Drift Detector

The principle of a silicon drift detector (SDD) was first described by E. Gatti and P. Rehak in 1984 [53]. This kind of semi-conductor detector is based on the principle of the sidewards depletion. Semi-conductor detector are interesting as they can produce more charged particles in comparison with a gas detector: in the case of semi-conductors the minimum energy to create one electron-hole pair is about 3 eV (to create one electron-ion pair in a gas detector, the minimum energy is about 30 eV)[2].

The SDD consists of a thin silicon wafer with a continuous n-doped layer on one side and p-doped strips on the other side. Then an electrical field in reverse bias mode is used both for depleting the detector and creating the field gradient to collect charges created by particles impact [54, 55]. To obtain the sidewards depletion, two separate fields are applied. The bulk material of the detector (see Fig. 3.6) is n$^-$ doped silicon, and on one side a smooth p$^+$ layer is implemented, whereas the other side has a structure of concentric p$^+$ rings[3]. The back contact is put to a positive voltage of about 150 V, the rings on the front side have different potentials, starting with about -15V on the innermost ring and rising to about -230 V on the outermost ring. The n$^-$ doped regions between the rings have a rather high resistivity and thus act as voltage divider. In these conditions, a potential valley (see Fig. 3.7) is created inside the detector. Free electrons created inside the valley will drift towards the center of the front side of the detector, where they are collected by a small n$^+$ doped anode.

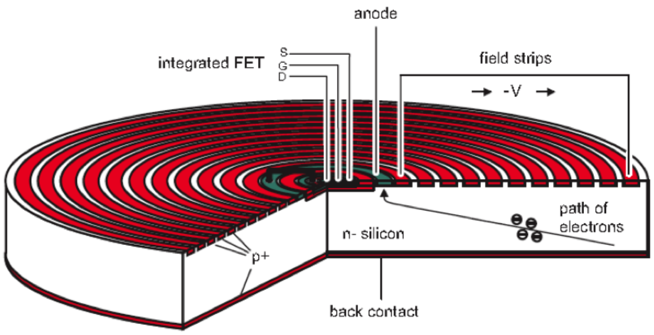

Figure 3.6: The principle of a silicon drift detector [51]. The gate (G) of the integrated FET is connected to the anode and represents the first amplification stage which reduces the pick-up of noise by wires.

3.2.2 The detector in the spectrometer aSPECT

The detector used in aSPECT consists of a set of three SDD implemented in a row of one silicon chip (see Fig. 3.8). Each of those detector pads has an active area of 100 mm^2 in the form of a square with a side length of 10.3 mm and rounded edges with 2 mm radius. The charge

---

[2] In a silicon semi-conductor, the gap is 1.12 eV and to create one electron-hole-pair an average of 3.6 eV is needed.

[3] The superscript "-" refers to a minor degree of doping, a "+" indicates a strong doping.

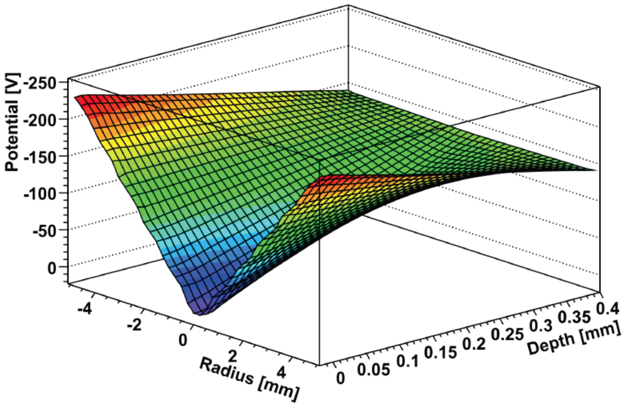

Figure 3.7: A simulation of the potential inside a SDD detector with typical values. Free electrons created within the potential valley drift towards the center on the front side, where they are collected by the anode. For better visibility of the potential valley, the axis of the potential is plotted inverted (picture from [8]).

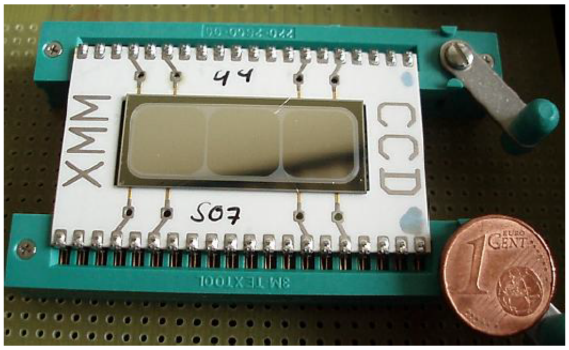

Figure 3.8: The detector chip used in aSPECT. Each pad will be enumerated by the corresponding channel of the ADC (ch 5, ch 6, ch7 with the old shaper ; ch 19, ch 20, ch 21 with the new shaper). On this photo, the detector is inserted in two 20 pins socket zero-insertion-force connectors.

carriers have a maximum drift length of 6.4 mm. The chip has a total size of $34 \times 14 \times 0.45$ mm^3. The potential valley is created by 73 rings implemented on the backside of the detector. The entrance side of the detector is covered with a protective layer of 30 nm of aluminum. Each single pad is surrounded by a separation mesh. A common multi guard ring structure surrounds all three pads to reduce the leakage current on both entrance and ring structure side. This detector was manufactured by PNSensor [56]: the chip is mounted on a special UHV-suitable ceramics board.

An interesting specification of this detector is the FET[4] on the detector chip itself. This allows to minimize the cable length from the detector to the first amplification stage to essentially zero and so to decrease the capacitive noise and the pick-up of external noise[5]. The length of the cable from the detector to the first amplifying device is crucial, as the non-amplified signals are very small. Furthermore, a temperature diode is implemented on the detector chip which changes its output voltage depending on the temperature. Wires are bonded between the chip

---

[4] Field-effect transistor.

[5] Every cable acts as an antenna and picks up electromagnetic noise.

and the board to provide electrical connection. Seven bond pads with a size of $150 \times 150\,\mu\text{m}^2$ are arranged in the center of each pad on the ring structure side. As shown in Fig. 3.8, the ceramics board has 40 pins with a pitch of 0.1 inch. This is a standard distance as the chip is meant to be inserted in two 20 pins socket zero-insertion-force connectors. A special holder for the use inside the spectrometer in UHV conditions was designed by Martin Simson (see Fig. 3.9). This holder is made of only ceramics, stainless steel, and gold coated springs. On one side the detector is introduced and clamped, on the other side the holder offers a 50 pin SUB-D connector to connect the first part of the electronics (i.e., the preamplifier, see section 3.3.1). This holder is then fixed to the insertion mechanics (see section 3.1.2).

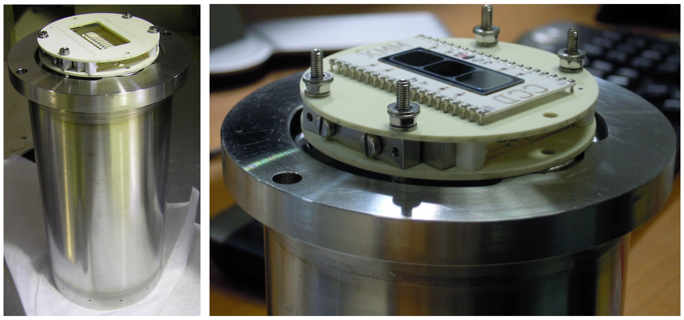

Figure 3.9: Special holder to use the detector in UHV conditions inside the spectrometer *a*SPECT.

3.3 The electronic processing

As mentioned above, the output signal from the detector is quite low. This implies a pre-treatement of the signal which is done by two electronics boards before the acquisition. The electronics for the detection system was mainly developed by Martin Simson and by M. Lenk at the University of Mainz (especially for the shaper board).

3.3.1 The preamplifier

The first stage of the signal amplification is operated by an electronic board called "preamplifier". This board is connected directly after the detector, via a 50 pin SUB-D connector (see Fig. 3.10) to be placed on the detector holder. This configuration allows to reduce the noise which could otherwise be induced by a long cable between the detector and the electronics board.

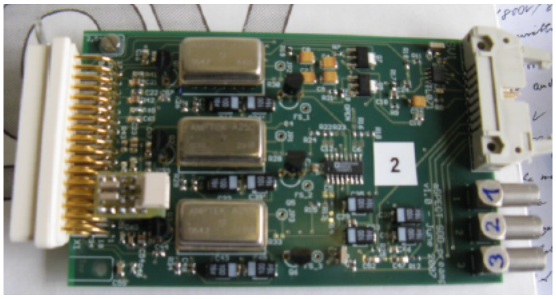

Figure 3.10: The preamplifier board.

The amplification of the signal from each detector pad is performed in two stages. First amplification stage is made by three Amptek A250 chips (one per detector channel), and the second amplification stage is ensured by one Analog Devices AD 8024 chip. Then, the signals from the three pads are transferred to the next step of the electronics: the shaper. The preamplifier is also used to distribute the various voltages needed to operate the detector.

3.3.2 The shaper

The shaper is an adapter board placed inside the electronics box (see Fig. 3.11). The purpose of this electronics board is to shape the signals and to distribute them to the ADC.

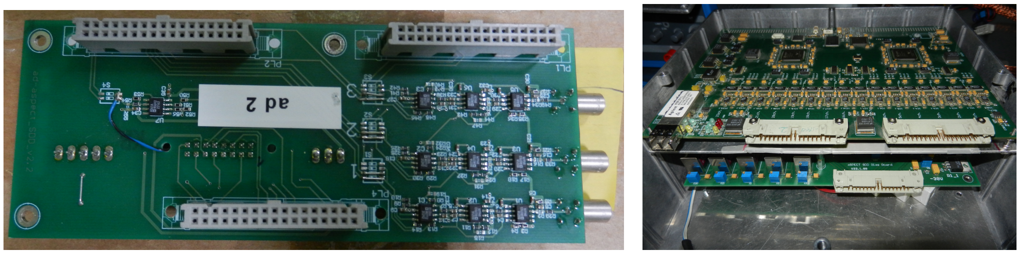

Figure 3.11: The shaper board (left) is connected to the voltage divider board (right, bottom board) and the ADC board (right, top board) inside the aluminum box. The three coaxial cables from the preamplifier are connected to the shaper (3 channels). This shaper is the old one used for the previous beam-time in 2008 and at the beginning of the beam-time of 2011. It was replaced by the new shaper during this last beam-time.

The incoming signal from the preamplifier consists in a steep rising part and a long exponentially falling part. The shaper is sensitive to the rising part and it reduces the pulse. In this way, the signal can be treated by the digital electronics. For the old shaper (used at the beginning of 2011), the shaping is done by a chain of two Analog Devices AD 847N and one AD 8138 chip for each channel. A new shaper was designed for the beam time in 2011 with a more complex shaping chain as it is divided in more channels than the old shaper (see section 3.6.2).

3.3.3 Data acquisition system

The output signals from the shaper are sent to the sADC[6] board which is installed inside the electronics box (see Fig. 3.11). The ADC allows to analyze signals from up to 32 channels in parallel. The old shaper gives three signals in three channels, and the new shaper uses six channels (see Tab. 3.3).

For each channel, the signal is continuously digitized by a 12 bit ADC. The sampling frequency is 20 MHz, resulting in time bins with a width of 50 ns. The events typically have a length of about 4 μs, so this frequency offers a good compromise of a good time resolution and keeping the data volume at a reasonable level. After digitizing the signals are treated by two Xilinx Virtex-II 1000 field programmable gate arrays (FPGA). Each FPGA provides data buffering and processing for 16 channels. As the raw rate of data is too large (about 28.6 MB/s per channel), the two FPGAs analyze the data with a trigger algorithm. This trigger algorithm continuously compares two windows (w1 and w2) of the signal as shown in Fig. 3.12. The window w1 is used to determine the baseline, whereas w2 is separated from w1 by the window distance. An event is registered by the electronics if the mean value of w2 will be higher than the one of w1 and the threshold condition is fulfilled[7]. An additional parameter in the algorithm, called delay, can

---

[6] Sampling Analogue to Digital Converter.

[7] If the mean values of windows 1 and w2 differ by more than an externally set threshold, the trigger condition is fulfilled.

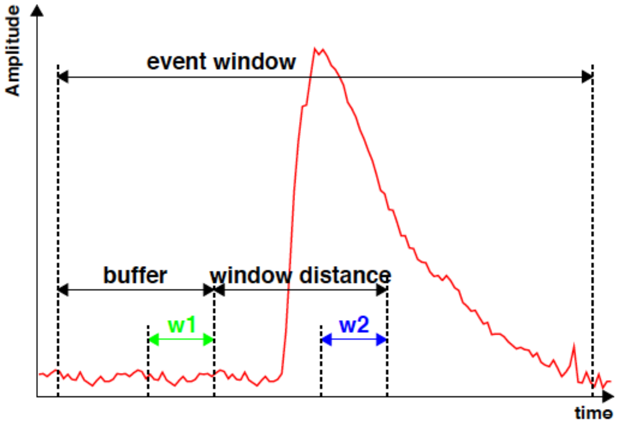

Figure 3.12: Overview of the average windows and buffer used by the trigger algorithm.

be set, so that this threshold condition has to be fulfilled several times in a row before a trigger decision is made. This helps to suppress triggers on noise. The exact stored region around the event is determined by the length of the event window and the trigger buffer. This buffer ensures that a sufficient amount of data before the event is stored.

The lengths of the two windows w1 and w2, the trigger buffer, and the event window as well as the delay can be set from the control program. The window distance is fixed to 16 time bins. Usually for the measurements during the beam-time, both w1 and w2 were set to a length of 16 time bins (set to "4" in the control panel as the length is calculated as 2^4 time bins), the delay was 3 time bins, the trigger buffer had a length of 15 time bins, and the event window was set to 80 time bins.

For each channel, the data accepted by the trigger is stored in a buffer on the ADC board. This can store up to 1024 ADC values. Then, the data is sent via a HOTLINK interface (i.e., an optical data transfer standard using fiber optics) from the FPGAs to the DAQ computer. This optical connection allows to operate the digital electronics at the high-voltage of the detector whereas the DAQ computer stays at ground potential. All the unused channels of the ADC are set to very high thresholds to be sure that no trigger can occur in those channels. The data from the sADC board is received by a card mounted in one of the Peripheral Component Interconnect (PCI) buses in the DAQ PC[8].

The raw data is stored in ".dat" files and then decoded by C++ software into a ROOT-tree [57]. These parameters contain information about the pulse height, timing and the classification of events (see Appendix C).

3.4 Status of the detection chain

After beam time in 2008 [8], a saturation problem of the electronics was found (see Fig. 3.13). For high energy events, the shaper (the one used in 2008, called "old" in this document) had a saturation which could induce a cut-off in the pulse shape. But, for very high energetic events, the preamplifier also may saturate. The detector gives a pulse which consists of a steep rising part with a rise time of typically 25 ns and a long decay with a decay time of about 150 μs. If an event occurred shortly after, it will sit on the shoulder of the previous pulse (top right side of the

---

[8] This PCI card consists of a mother card which is actually plugged into the PCI bus and a mezzanine card plugged into a socket on the mother card. The mezzanine card is needed, as *a*SPECT uses the HOTLINK standard for data transfer. [8]

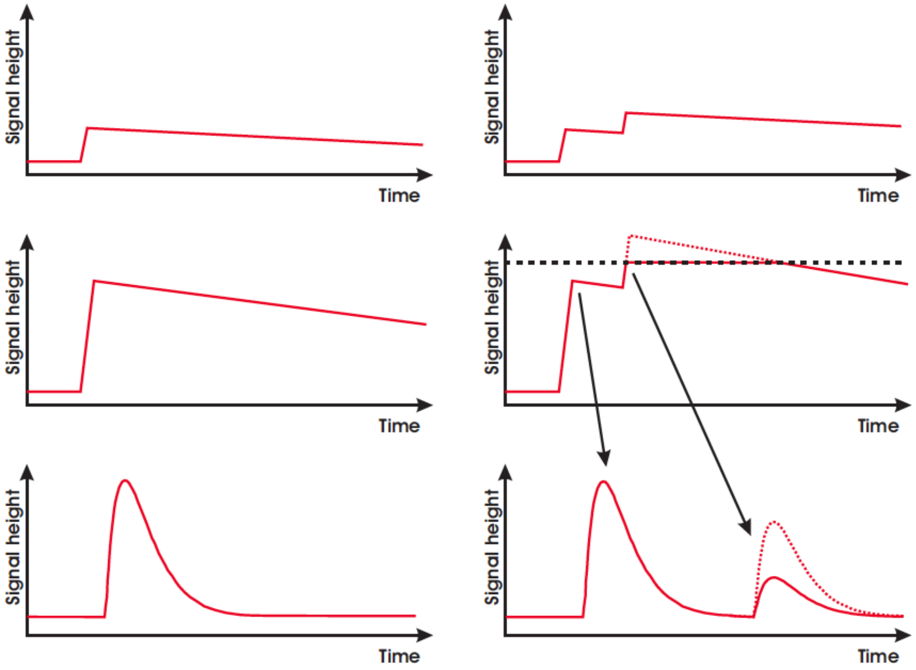

Figure 3.13: Schematic of the preamplifier saturation: signal from the detector, top ; signal after the preamplifier, middle ; signal after the shaper, bottom. Left: Single event. Right: Saturation for subsequent events (picture from [8]).

figure). Then, the shaper differentiates and integrates the signal and is mostly sensitive to the rising edge of the signal. The height of the pulse after the shaper is proportional to the change in pulse-height before the shaper. But if an electron deposits so much energy in the detector bringing the preamplifier close to saturation, the following event, shortly after, will drive the electronics board into saturation. In this condition, a cut-off on the second peak will occur, and after the shaper, the peak will have a lower pulse-height as well.

Investigations were performed by Martin Simson during his PhD and then by me during the first year of my PhD. We made different tests to identify the problems and the limits of the actual electronics dedicated to the detection in *a*SPECT. These tests are presented in the following section 3.5 and those concerning the new electronics are shown in the section 3.6. The identification of the different electronics components follows the one presented in Tab. 3.1. In the following sections, the reference is indicated.

3.5 Tests of the detection system

In 2011, several tests were performed on the detection system in order to improve the signal detection and to characterize the saturation problems found before. A set-up was built allowing to make measurements with the detector without installing the complete mechanics.

3.5.1 Test set-up

The detector is installed on a copper holder with the 40 pins connector. This holder is placed inside a small vacuum chamber (cylinder) closed by two main flanges (see Fig. 3.14). Outside of the chamber, on the flange holding the detector, there is a 50 pin SUB-D connector to connect

Reference	Component	Description
p1_1	Preamplifier	Designed by Martin Simson [8], this board was used in 2008 and had an amplification leading to saturation for high-energy electrons and subsequent protons.
p1_1a	Preamplifier	Designed by Martin Simson, this board has an amplification lower than the one of p1_1. It was used from 2011 to 2013 (for this last year, the amplification was reduced by 23%).
p1_m	Preamplifier	Designed by M. Lenk to replace the p1_1 trying to avoid the saturation problem.
sha_1	Shaper	Designed by Martin Simson [8], this board has a linear amplification with saturation for high-energy electrons. It was used at the beginning of 2011.
sha_p	Shaper	Designed by M. Lenk, this was the prototype with adjustable components in order to design the new shaper sha_2. It was used during the tests.
sha_2	Shaper	Designed by M. Lenk, this board has channels with a non-linear amplification for high-energy events and channels with a linear amplification. It was used from 2011 to 2013.

Table 3.1: Identification of the different electronic boards tested.

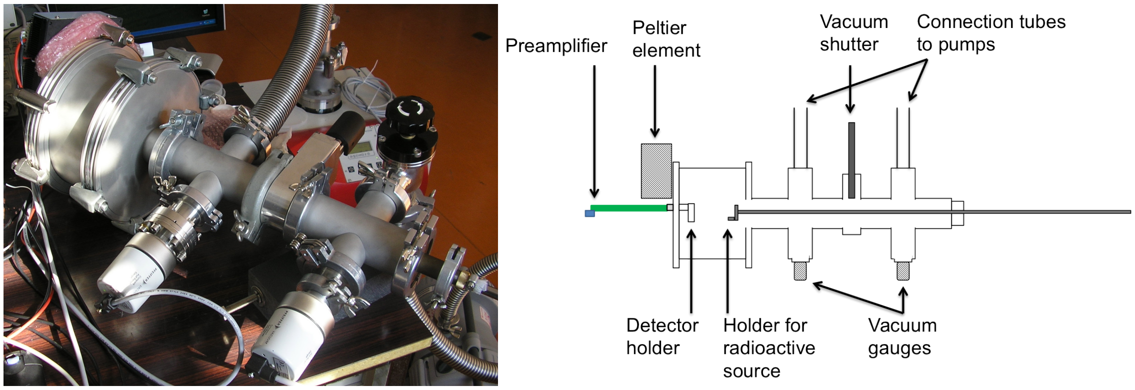

Figure 3.14: The test set-up pumped by two pumping stations (left). Detailed sketch of the test set-up (right). The shutter allows moving out the source without breaking the vacuum in the main chamber where the detector is installed.

the preamplifier board directly after the detector. Then the preamplifier is connected to the shaper inside the electronics box for the signal treatment and the voltage powering.

The system is pumped by a pumping station. A small volume can be separated by a vacuum shutter. This volume is used for the insertion of a radioactive source (for example, Barium source ^{133}Ba). A vacuum of about 10^{-5} mbar can be reached inside this system.

A Peltier element is used to cool down the copper holder of the detector and thus the detector. In *a*SPECT, the detector is inserted in the bore tube whose temperature is around 70 K in operating mode. The test set-up can produce conditions comparable to those inside *a*SPECT.

3.5.2 Temperature effects

To test the detection chain a radioactive source was used inside the vacuum chamber: a Barium source ^{133}Ba[9]. By electron capture, the Barium will convert into Cesium with emission of gamma and conversion electrons.

Using the SDD, preamplifier p1_1 and shaper sha_1, the measured spectrum can provide useful information for the improvements (see Fig. 3.15). A shown on this figure, the electronic noise was very present in the spectrum. The first step to reduce the noise was to improve the isolation of the HV cable between the electronics box and the preamplifier. But the main influence comes from the temperature at the detector (see Fig. 3.16(a)). The count rate around the electronic noise decreased from 916.3(1.5) Hz at 0 °C to 18.9(2) Hz at -9 °C. This represents a decrease to 2% of the electronic noise count rate.

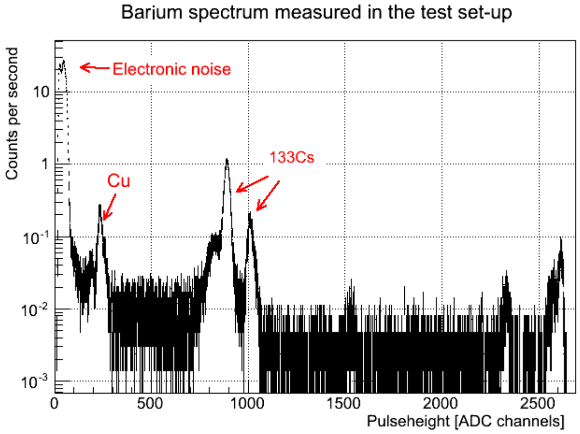

Figure 3.15: Barium spectrum using the detector Dummy (used only for tests), the preamplifier p1_1 and shaper sha_1. By electron capture, the following reaction occurs $^{133}\mathrm{Ba} + e^- \rightarrow ^{133}\mathrm{Cs}$. So the K$\alpha$ and Kβ rays of the Cesium are detected. The peak just above the electronic noise is due to X-rays from the Copper holder.

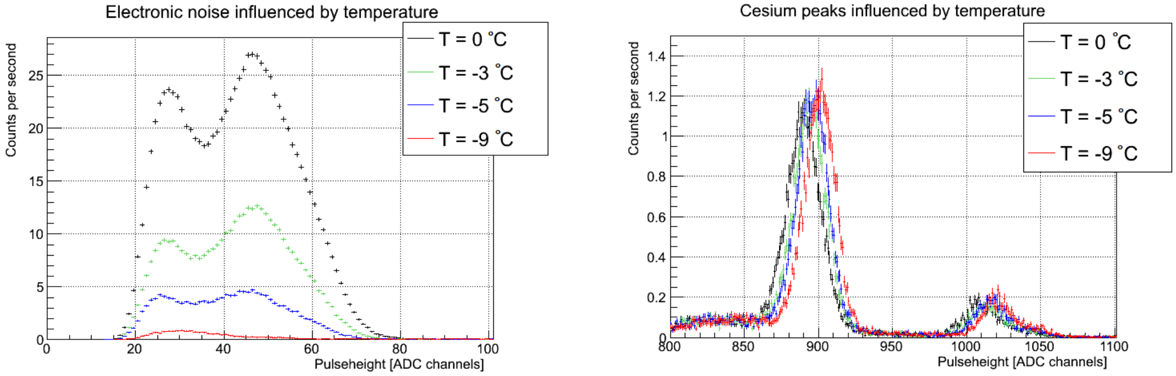

(a) Electronic noise.

(b) Cesium peaks (Kα and Kβ) positions (energy)

Figure 3.16: Influence of the temperature. These spectra were measured with the detector Dummy, the preamplifier p1_1 and the shaper sha_1.

---

[9] The Barium source was provided by the ILL radio-protection service and has the following characteristics: $2.4 \cdot 10^5$ Bq, DDγ at 5 cm: $10\,\mu$Gy/h

Furthermore, the temperature has an effect on the signal amplification (see Fig. 3.16(b)). The mean position of the Cesium K-peaks changes with temperature. From 0 °C to -9 °C, the signal position was shifted by about 1.3% (Tab. 3.2). This effect can be also part of a temperature influence on the preamplifier as this board was connected to the test set-up and below the Peltier element: a change in temperature can affect the electronic process and so the amplification of the signal.

Peaks	T = 0 °C	T = -3 °C	T = -5 °C	T = -9 °C
Kα (30.85 keV)	889.8(1)	893.6(1)	895.6(1)	900.5(1)
Kβ (34.90 keV)	1008.9(4)	1013.8(5)	1018.0(3)	1023.1(3)

Table 3.2: Dependence of the position of the Cs peaks in [ADC channels] on the detector temperature.

A temperature-related effect occurred during measurements. During the beam-time, continuous measurements were run during days and nights. The proton peak position oscillated following a day/night cycle (see Fig. 3.17). This is related to a temperature effect on the electronics. In order to minimize this effect, a compressed air tube is placed inside the electronics box. Further, a method was developed to minimize the influence of this drift on the extracted count rate (see section 3.7).

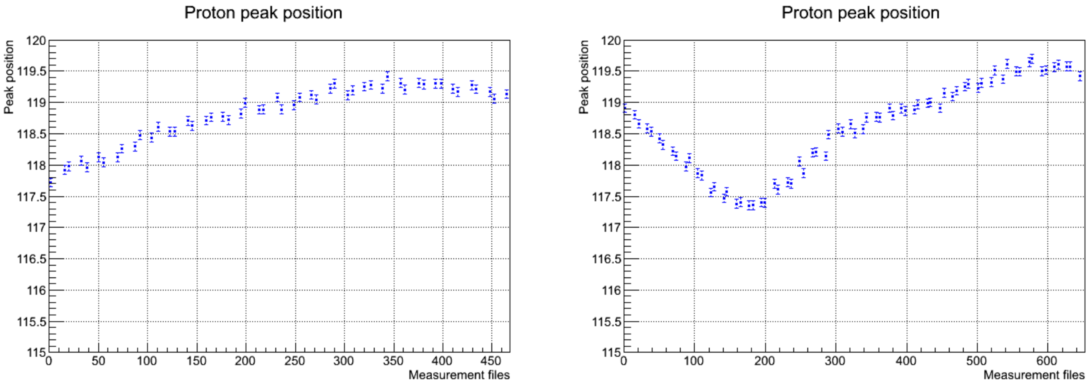

Figure 3.17: Proton peak evolution during two consecutive continuous measurements during the beam-time in 2011 with preamplifier p1_1a and shaper sha_2. The first one (left) was started at 20:00 and stopped at 11:30 after which the second one (right) was started, which stopped at 9:30 in the next morning.

3.5.3 Simulation of the electronics chain

In order to characterize the limits of the detection chain, we simulated it using the software LTspice IV[10]. This software allows to simulate the electronic process for an incoming signal from the detector within the preamplifier p1_1 and the shaper sha_1. The incoming signal was calculated analytically with a C++ program[11]: electron and proton events are calculated for

---

[10] The simulation file of the electronics chain was made by M. Heinz Lenk, electronician at the Institut für Physik, Universität Mainz , Germany. LTspice is a software for the simulation of electronics developed by Linear Technology [58].

[11] Martin Simson developed a C++ program to calculate the output voltage of the detector for a given energy of incoming particles.

different energies detected (for electrons [0 - 1] MeV, for protons [0 - 12] keV, with the acceleration potential) and different time delay between the electron's detection and the proton's one (from 2 to 20 μs). The resulting data file was used as input signal for the simulation of the electronics (see Fig. 3.18). This software allowed to check the signal after the shaper for different input parameters: electron and proton energies, and time delay.

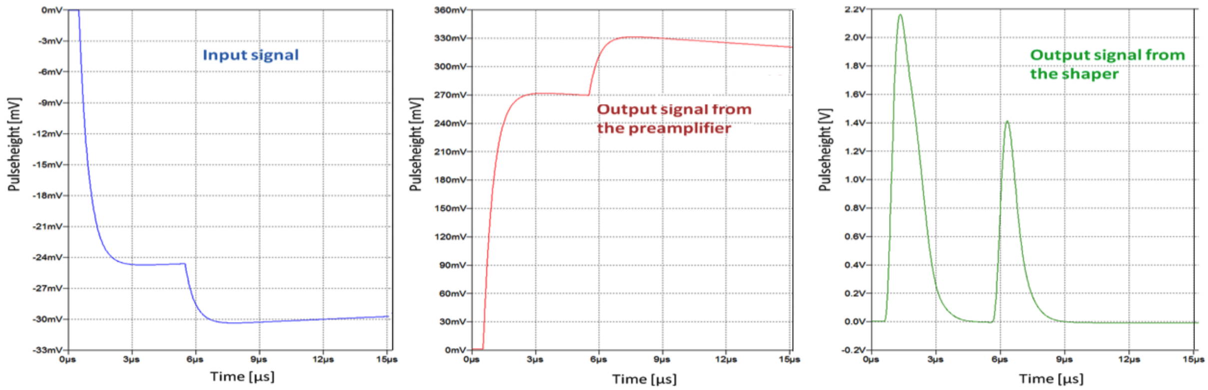

Figure 3.18: Example of signal after the shaper from an electron of 50 keV followed after 5 μs by a proton of 12 keV.

The first observation was that the electronics did not have a linear amplification for proton energies above 7 keV (see Fig. 3.19(a)). The simulations with an electron event before the proton showed that the proton signal was too close to the electron signal saturation. The saturation due the electron appears slightly below 2.7 V, corresponding to an electron energy of 200 keV (see Fig. 3.19(b)).

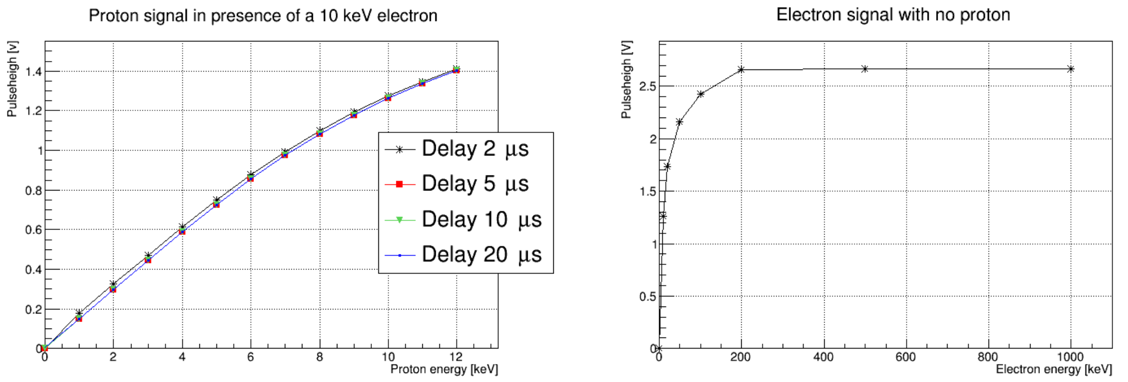

(a) Output signal of the shaper sha_1 for protons with different energies and detected after an electron of 10 keV for different time delay. The electron induces a signal of 1.3 V.

(b) Output signal of the shaper sha_1 for different electrons energies and without proton.

Figure 3.19: Main results from the simulation of the detection chain.

Similar results were obtained by testing the detection chain with a pulse generator connected to the preamplifier p1_1. The output signal from this board was sent to the shaper sha_1. A readout software allows to check the signal from the pulse generator, the one from the preamplifier and the one from the shaper (see Fig. 3.20). The saturation of the preamplifier (red line) was observed for an input signal of 480 mV from the pulse generator: the signal from the preamplifier

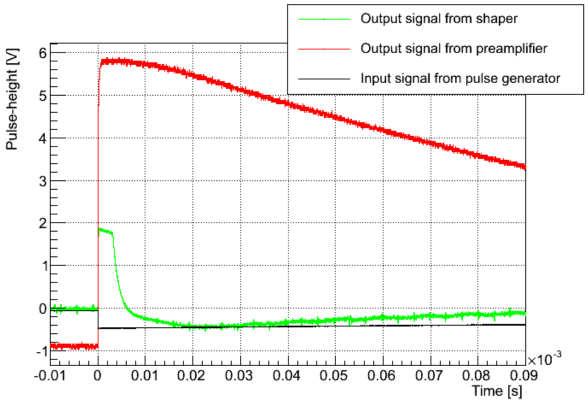

Figure 3.20: Saturation of the output signal from the preamplifier p1_1 obtained with an input signal of 480 mV. This saturation was also visible in the output signal from the shaper sha_1. The input signal is negative and the preamplifier inverts and amplifies the pulse.

has a plateau of about 8 μs before starting to decay. The saturation was also visible after the shaper (green line). This input signal of 480 mV could correspond to events with an energy around 960 keV (as for example high-energy electrons).

3.6 Improvements of the electronics

Before the start of the beam-time of 2011, solutions were proposed to avoid the saturation problems of the electronics for the detection system. For this, the preamplifier board was improved and a new shaper board (sha_p and then sha_2) was developed at the Institut für Physik of Universität Mainz, Germany. Several tests were performed in order to adjust this new electronics for the detection in aSPECT.

3.6.1 The new preamplifier

The saturation observed previously would cause a loss in proton detection and so a shift on the coefficient a because of the correlation (see details in [8]). In parallel to the tests of the “old” electronics, a new preamplifier was designed at Mainz (called “p1_m” or “Mainz preamplifier”). This device has a linear amplification and a larger output signal than possible with the shaper sha_1. As it was done previously, we used the pulse generator connected to the preamplifier p1_m to test the output signal (see Fig. 3.21(a)). The output signal is linear for input signals below 200 mV, then there is a saturation around 8 V. The comparison was completed with a measurement in presence of the Barium source (see Fig. 3.21(b)): the preamplifiers were connected to the detector in the test set-up and the ^{133}Ba source was used. The output signal from the preamplifier was read with an oscilloscope: this is the signal induced by the Kα-line of the Cesium (30.85 keV). We detected an output signal of about 190 mV with the preamplifier p1_1, and about 450 mV with the preamplifier p1_m. In this configuration, if an electron hits the detector with an energy of 750 keV (the endpoint for the electron energy spectrum is 782 keV), this would induce an output signal from the preamplifier p1_m of about 10 V: this is above the saturation limit. Furthermore, this kind of high signal would induce a saturation in the shaper sha_1 and would result in a loss of count rate (see section 3.6.2).

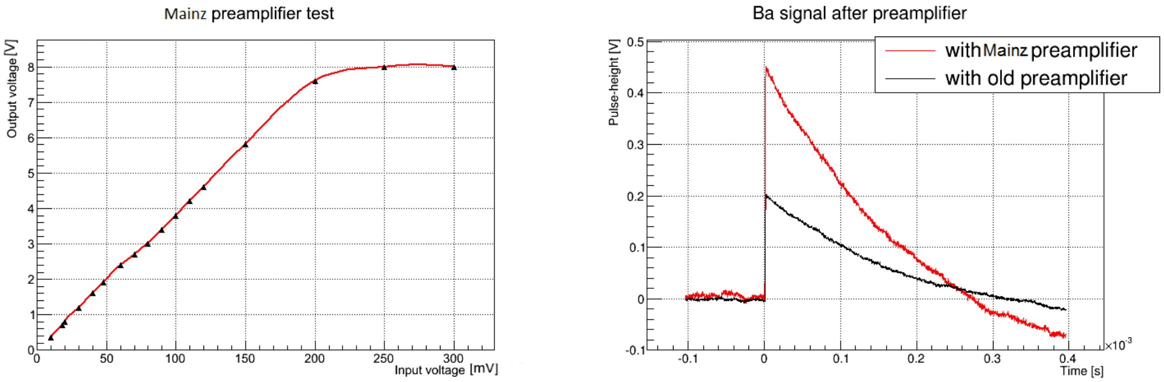

(a) Output signal with an input signal from a pulse generator.

(b) Barium signal after the preamplifier p1_1 and p1_m.

Figure 3.21: Test of the preamplifier p1_m (Mainz preamplifier).

After these tests and results, the preamplifier p1_1 was adapted[12] in order to obtain the preamplifier p1_1a: the amplification of the first stage was reduced (the Amptek A250 module). This assured a linear amplification in the range up to 1 MeV (i.e., an input voltage of 500 mV). So, in comparison with the old version p1_1 of the preamplifier, for the same input voltage as in Fig. 3.20, of 480 mV, the saturation was not reached by the new version p1_1a as shown in Fig.3.22 .

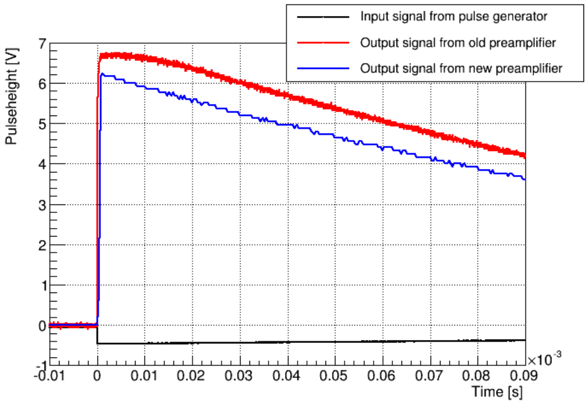

Figure 3.22: Comparison between the preamplifier p1_1 and the p1_1a one (called “new” in the plot) using the same input signal from a pulse generator (480 mV as for the Fig. 3.20).

The final test was a Barium spectrum measurement inside the test set-up (see Fig. 3.23). The copper lines are due to radiation from the holder of the detector inside the test set-up. The main K-lines detected are from the ^{133}Cs. There is also a small peak close to the Kα-line of ^{133}Cs, we called it “escape” and it is due to the difference between the ^{133}Cs radiation and the X-rays from the Silicon of the detector itself. Its energy is given by:

$$E_{\text{escape}} = E_{\text{Cs, K}\alpha} - E_{\text{Si, K}\alpha} = 29.11(10)\,\text{keV}. \tag{3.1}$$

---

[12] The preamplifier board p1_m from Mainz was perturbed by the magnetic field in *a*SPECT and the signals were not stable.

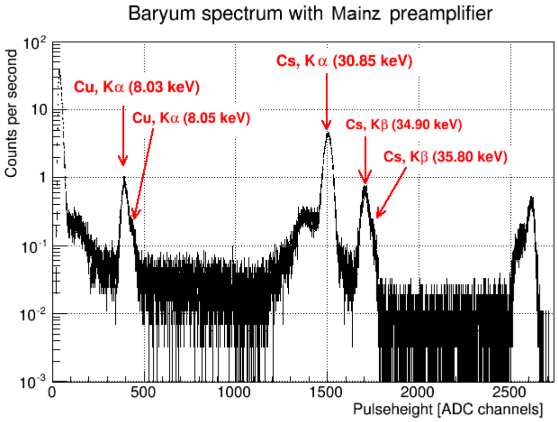

Figure 3.23: Barium spectrum measured in the test set-up with the preamplifier p1_1a and the shaper sha_1. Identification of the Copper lines (Cu, Kα) and the Cesium 133 lines (Cs, Kα and Kβ) with [59, 60]. The right peak results from the saturation of the old shaper.

This identification gave the energy corresponding to the ADC channels. This was also useful for some energy calibration during several tests for the new shaper (see section 3.6.2).

During the beam-time in 2013, the preamplifier p1_1a was again modified. We reduced its amplification by 23% in order to keep the proton peak, in the measured spectrum with neutron beam, in the linear amplification region of the new shaper.

3.6.2 The new shaper

The shaper was also part of the saturation problem. The shaper sha_1 had a linear amplification and this resulted in a saturation of the signal for the electrons with high energy. This was observed during the beam time of 2011 via a spectrum measured in presence of the neutron beam (see Fig. 3.24). The left side of the spectrum is dominated by the electronic noise which is then followed by the protons peak: this two parts are well separated with this system and so the proton count rate can be extracted easily. The other region, on the right-side of the protons peak, is dominated by the electrons and is ended by a straight peak resulting from the saturation

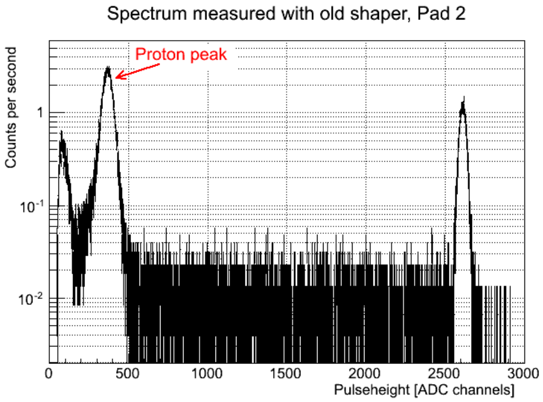

Figure 3.24: Example of spectrum measured during the beam-time of 2011 with the shaper sha_1 and the preamplifier p1_1a: electronic noise on the left, then the proton peak, and on the right the peak due to the electrons saturation.

of the old shaper in the high-energy range. From the point of view of the signal from the shaper (see green line Fig. 3.20), there was a plateau after the rising part. In the decreasing part, there was an undershoot which changed the trigger condition: the baseline of the signal was modified and so a coincidence proton would not be detected.

So, in order to avoid this problem, a new shaper board sha_2 was designed by M. Lenk at the Institut für Physik, Universität Mainz. This new electronics board includes a compensation circuit that reduces the signal amplitude for high incoming signal. The aim was to obtain a non-linear amplification above a certain value. In addition, for each input channel, a second output was added to provide the signal with a linear amplification (and low to avoid saturation): this would give information on electrons. As there are three input channels from the three pads of the detector, the new shaper gives six output channels. The channels with a non-linear amplification are optimized for the signals in the protons region, we call them "p-channels", and the other with a linear and low amplification over the full region are called "β-channels".

This new shaper board was built following several investigations performed on a prototype sha_p with just one input channel. The shaper sha_p board offered possibilities to check the evolution of the signal inside the electronic circuit and to modify different components on the board. In this way, we tested the acquisition of the Barium spectrum via the prototype connected to the preamplifier p1_m (see Fig. 3.25). The β-channel with a very low, linear amplification presented a peak potentially induced by a high-energy gamma or an electron conversion from the Barium decay process. The amplification in the p-channel was different than with the shaper sha_1 in Fig. 3.23. We also noted that the right peak of saturation is not present with the prototype. The same test was done using another radioactive source: Bismuth ^{207}Bi[13]. As shown in Fig. 3.26, the K-lines peaks position of the Cu, the Cs and the Pb (from Bi decay) were used to check the amplification of the shaper sha_p. We observed a non-linear correlation between the detected energy and the peak position on the spectrum: the non-linear amplification was obtained, in order to avoid the saturation risk. The energy calibration can be approximated using an exponential function (red line on the figure), $f = p_0 \cdot (1 - \exp(^{-E}/_{p_1}))$, where f gives the peak position in ADC channels and E is the energy detected in keV. The parameter p_1 can be interpreted as the upper limit for linear amplification in the energy calibration (here, $p_1 \sim$ 20 keV). We confirmed this effect by using the pulse generator directly connected to the input

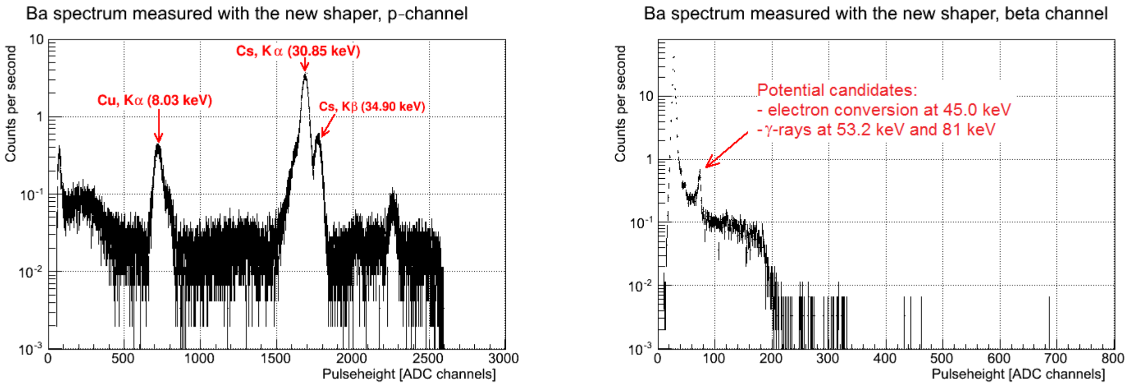

(a) p-channel. The peak on the right is induced by overflow.

(b) β-channel.

Figure 3.25: Barium spectrum measured in the test set-up with the shaper sha_p.

---

[13] ^{207}Bi, provided by the ILL radio-protection service, is a beta and gamma source of $3.1 \cdot 10^4$ Bq, DDγ at 5 cm of 30 μGy/h, and DdD$\beta\gamma$ contact of 250 μSv/h.

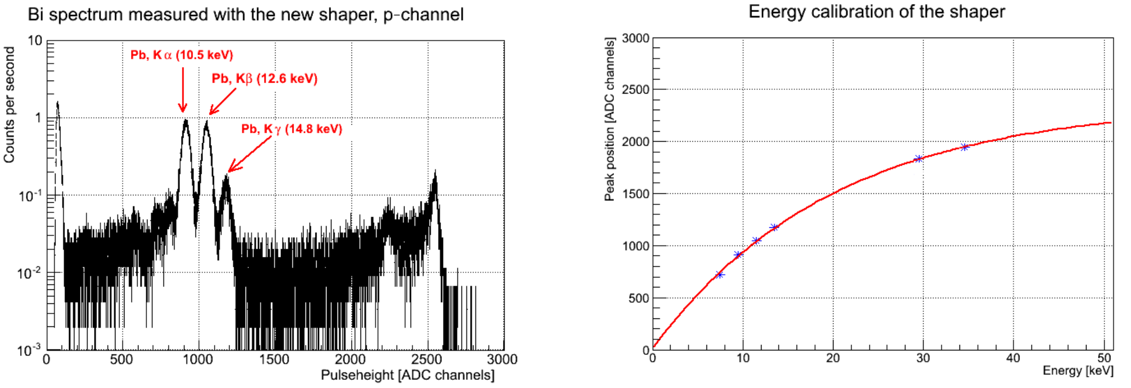

(a) Bi spectrum.

(b) Energy calibration sha_p using the Ba and Bi peaks

Figure 3.26: Measurements with the sha_p and identification of peaks from the K-lines of Pb.

channel of the prototype sha_p. The output signal was then recorded by the readout software (see Fig. 3.27). The amplification is non-linear above 100 mV input signal: this corresponds to a detected energy of about 20 keV.

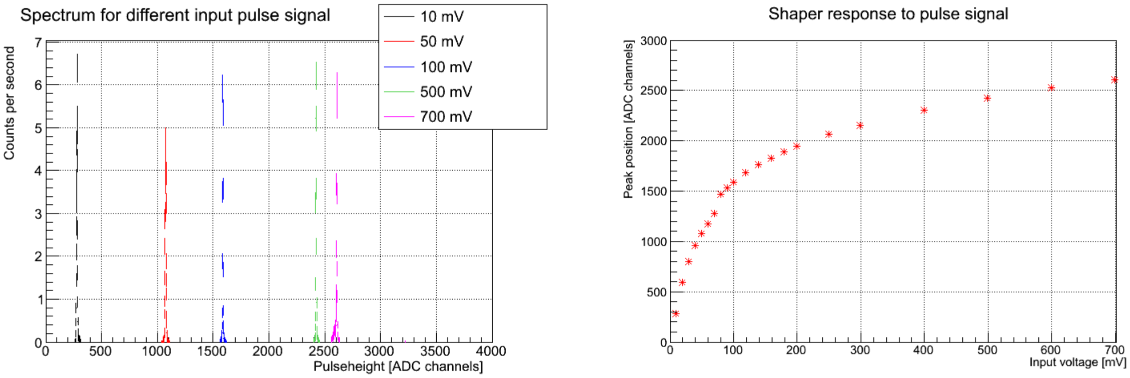

(a) Example of measured spectrum.

(b) Response range of the shaper sha_p.

Figure 3.27: Test of the sha_p response to different input signals from a pulse generator. The peak positions were extracted to obtain the complete response curve of the prototype shaper.

From this work, the shaper sha_2 was built at Mainz (see Fig. 3.28). For this new electronics

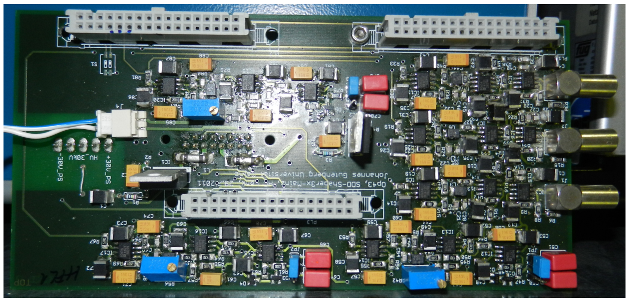

Figure 3.28: The new shaper sha_2 also called “Mainz shaper”.

board, the signal amplification was adapted. Another change was done on the control panel for the DAQ acquisition: with the shaper sha_1, the event window was set to 100 time bins, with the shaper sha_2, the event window is now set to 80 time bins. With the final version of the shaper sha_2 and the new adaptations, we performed a measurement with the Barium source, shown in Fig. 3.29. In the p-channel of the Barium spectrum, the previous peak (Kα-line at 30.85 keV) is in the non-linear amplification region. The main peak observed now at ADC channel 198.4, corresponds to electrons emission from ^{133}Ba with an energy at 25.11 keV[14]. The K-lines from the Cu in previous spectra are not present as the detector was mounted on the insertion mechanics. We considered the peak at ADC channel 135.7 which is also induced by electron emission with an energy of about 17.2 keV [59, 60].

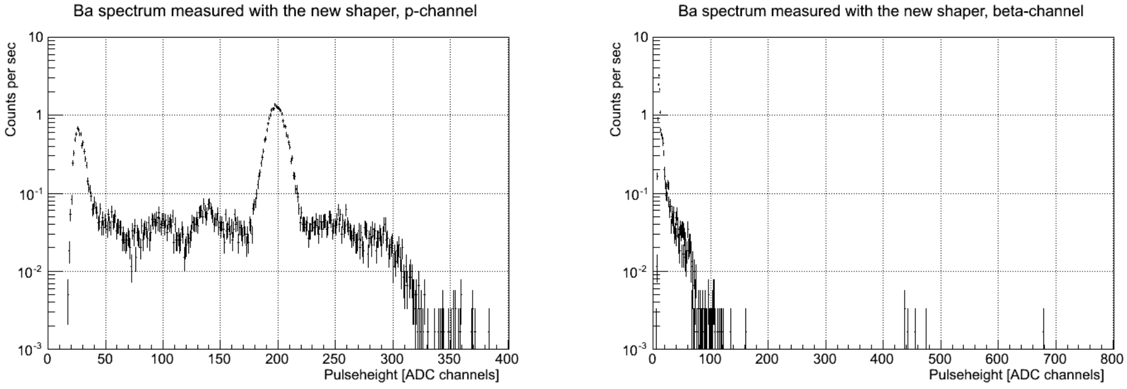

(a) p-channel. (b) β-channel.

Figure 3.29: Barium spectrum measured in the insertion mechanics with the shaper sha_2 and the preamplifier p1_1a.

According to simulations performed by Martin Simson [8], a proton with a kinetic energy of 15 keV will lose 6.3 keV in the dead layer of the SDD (30 nm of aluminum), and a proton of 10 keV will lose 4.8 keV. We note E_{det}, the energy detected (i.e., the kinetic energy minus the lost energy in the dead layer of the detector). Combing with the peaks positions from the Barium spectrum, we can propose a calibration curve between the peak position Pos (in ADC channels) and the energy detected E_{det} (in keV):

$$Pos = 13.62(28) \cdot E_{\text{det}} + 0.18(88) \tag{3.2}$$

This equation is available for the "p-channels" and below the upper limit of the linear amplification. This calibration is used for data from the beam time of 2011 and the offline tests in 2012 (the amplification of p1_1a is reduced by 23% for the data taken in 2013).

The shaper sha_2 was used during the main part of the beam-time of 2011, the one of 2013 and during the test measurements in 2012. In presence of the neutron beam, we measured a spectrum which can be divided in three parts as shown in Fig. 3.30. The first region can be defined from ADC channel 0 to $\sim$30 and is dominated by **electronic noise**. The upper limit of this region is subject to adjustment as it defines also the lower limit of the next region dominated by the **protons**. This region is defined around the proton peak in order to keep the upper limit still in the linear amplification energy region (in general $\lesssim$ 150 ADC channels). Above, the **electrons** dominate and undergo the non-linear effect resulting in a "compressed" part. The

---

[14] From bibliography [60], the energy for Auger electron is between 24.41 and 25.80 keV, as we see one peak, we considered the mean value.

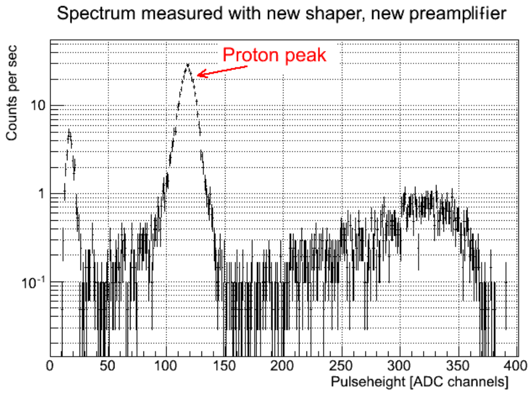

Figure 3.30: Spectrum measured during the beam-time 2011 using the preamplifier p1_1a and the shaper sha_2. The first peak is due to electronic noise, the main one are the protons, and the electrons signal is non-linear amplified. This results in a "compressed" electron part of the spectrum.

high energy electrons are also visible in the linear channel (β-channel) of the shaper, and in the p-channel, the saturation induced by these particles is avoided. The channel identification changed in comparison to the shaper sha_1 as now we have two channels per detector pad after the shaper sha_2 (see Tab. 3.3).

	Shaper sha_1	Shaper sha_2	
		Proton channels	Beta channels
Pad 1	ch 5	ch 19	ch 22
Pad 2	ch 6	ch 20	ch 23
Pad 3	ch 7	ch 21	ch 24

Table 3.3: Output channels identification to detector pad for the old and the new shaper.

3.7 Status of the new detection chain during the beam time

During the beam time of 2011, we tested both old and new electronics for the detection. The detector was inserted inside *a*SPECT and the magnet was switched on. All the electrodes voltages were set to 0 V for the first test with the acceleration voltage called "Det-HV" (except the electrodes uExB which were set to -1|-1 kV). We ramped the acceleration potential to different voltage in order to test the linearity of the amplification for the detected protons. The Fig. 3.31 shows this test with the preamplifier p1_1a and the shaper sha_1. The main effect of the detection system is a good separation between the protons peak and the electronic noise: this allows a reliable determination of the count rate in the proton region. The variation of the proton energies detected with the acceleration potential can be fit by a linear function. The same measurements were made after the installation of the shaper sha_2 and still with the preamplifier p1_1a (see Fig. 3.32). The separation of the proton peak from the electronic noise is still good and the proton energies detected are in the linear amplification region of the shaper sha_2 (see section 3.6.2). Typically, the continuous measurements made during the beam time were run with an acceleration potential at -15 kV which offers a good compromise of separation from electronic noise without being in the non-linear amplification region of the shaper.

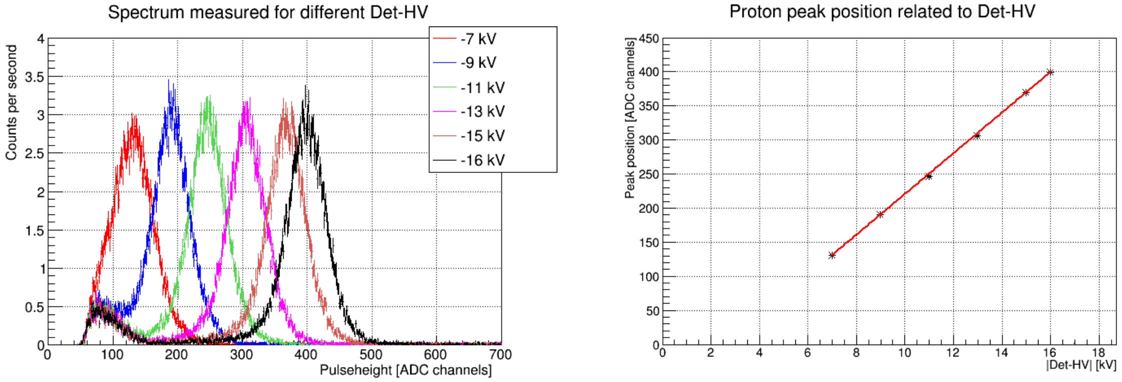

(a) Zoom on the proton peaks. Measurement time for each spectrum was 150 s.

(b) Linear variation of the proton peak position with the Det-HV.

Figure 3.31: Measurements for different acceleration voltages Det-HV with the neutron beam. We observed a good separation of the proton peak from the electronic noise. These measurements were done with the preamplifier p1_1a and the shaper sha_1.

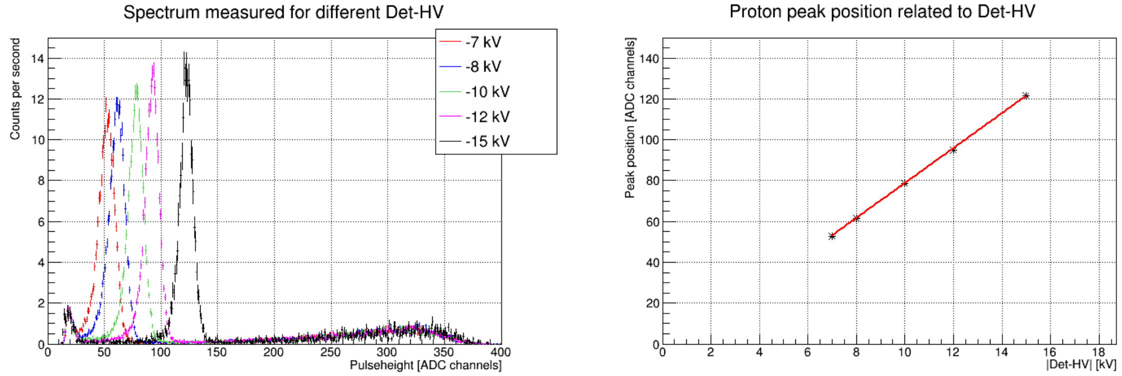

(a) "Proton" channel. Measurement time for each spectrum is 120 s.

(b) Linear variation of the proton peak position with the Det-HV.

Figure 3.32: Measurements for different acceleration voltages Det-HV with the neutron beam. These measurements were done with the preamplifier p1_1a and the shaper sha_2.

During the beam time of 2013, we tested a new data acquisition system provided by the Instrument Control Service of the ILL (see the description in Appendix D). This system can replace the current DAQ system and also the shaper: the output signals from the preamplifier p1_1a are directly sent to the new data acquisition system. In this configuration, the full dynamic range of the preamplifier can be covered with a sufficient resolution for the proton signal, as shown in Fig. 3.33. This system was mainly investigated by Romain Virot during his internship [64]. As it covers the full dynamic range, no saturation due to high-energy electrons was observed, it offers a great reproducibility and a stable acquisition. However, the lack of time did not allow us to take measurement more than a few days. More investigations are required to fully understand the new DAQ with aSPECT.

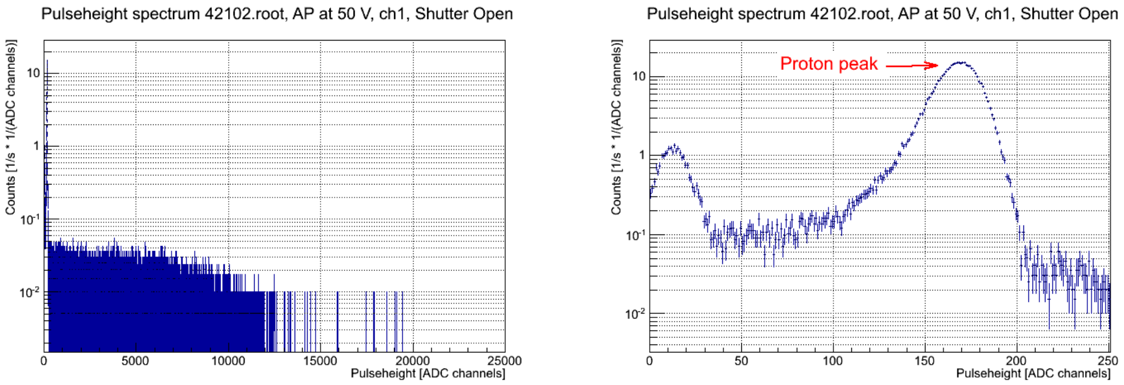

(a) Full range.

(b) Zoom on the proton region.

Figure 3.33: Measurement with the new DAQ connected after the preamplifier p1_1a in 2013. One file measured with the AP at 50 V, Det-HV at -15 kV and with the neutron shutter opened during 200 s.

3.8 Corrections for the count rate

In our analysis, we calculated the proton count rate integrated in the corresponding region in the measured spectra. The resulting values have to be corrected to compensate some effect from the electronics.

3.8.1 Correction of the proton peak position

As mentioned in section 3.5.2, the proton peak position changed in time due to the temperature effect of the day/night cycle. As shown in Fig. 3.34, during one continuous measurement (see description in Chapter 4), we observed a drift of the proton peak position for the same electrodes setting. Between these two measurements, the temperature increased in the guide hall at the ILL, and this had an impact on the electronics and so on the integration limits to extract the count rate in the proton region. During all the complete measurement, we observed an effect of the temperature on the proton peak position of the order of about 2.5%. To correct for this

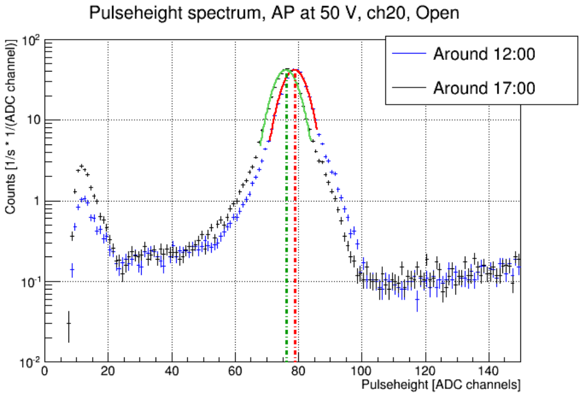

Figure 3.34: Comparison of two spectra with AP at 50 V from the same continuous measurement in 2013. These spectra were measured for 200 s each and at a different time during the same day in June.

effect, a method was tested to adapt the integration limits in function of the displacement of the proton peak. The idea is to find the position of the proton peak and to use it as reference for the integration limits. The upper limit is found to be at the separation between the ending part of the proton peak and the beginning of the electron region (see Fig. 3.30). However, we have to be careful that the upper limit is not set in the non-linear amplification part. For the lower limit, the aim is to find the limit with the electronic noise which is influenced by the temperature: its amplitude increased with the temperature of the electronics. The tested method is to apply a constant fit in a small range below the center of the region between the proton peak and the electronic noise. The obtained parameter is used as reference for the comparison with the value of each point of the spectrum in the low region. This is a downward comparison which gives the last bin containing a value above the fit parameter and so, related to the end of the electronic noise region. The lower integration limit is taken as this bin plus one.

This method is sensitive to the statistical fluctuations observed in spectra. We organized continuous measurement with a cycling structure for the AP voltages: we defined blocks with these voltages in a given order, and they are repeated several times. Each block contains typically six files measured with AP at 50 V. The displacement of the proton peak was observed to be very low in one block. Thus, the method is applied to the sum of the spectra with AP at 50 V in one block. This summed spectrum offers a better identification of the integration limits for one block as the statistical fluctuations are reduced. This method gives an automatic procedure to adapt the count rate integration limits to the changing amplification due to the temperature. Some relations with the coefficient a and the integration limits are discussed in Chapter 7.

3.8.2 Dead time correction

The dead time of the DAQ is defined as the duration of the event window plus the electronics latency. This time is the minimal delay between two consecutive events on the same channel. It results in a “non-extendable” [54] dead time and so in a reduction of the count rate depending on the absolute count rate. To correct this loss of events we need to apply a dead time correction expressed as:

$$C_{\text{corr}} = \frac{C_{\text{meas}}}{1 - C_{\text{total}} \cdot T_{\text{dead}}} \tag{3.3}$$

where C_{total} and C_{meas} are, respectively, the total trigger rate in one pad channel and the count rate in the region of interest, C_{corr} is the corrected count rate in the region interest, and T_{dead} is the dead time per event.

In the case of aSPECT, an event has a length of $4\,\mu$s. The electronics of the DAQ system processes an event in $0.2\,\mu$s. Thus, the next event has a minimum time difference of $T_{\text{dead}} = 4.2\,\mu$s.

It is important to know the dead time value precisely in order to apply a good correction. An uncertainty on this parameter results in a systematic error on the a value in two different ways: the total trigger rate and thus the (uncorrelated) dead time correction depends on the analyzing plane voltage U_{A}, and protons can be detected correlated to electrons if the dead time is larger than the minimum delay for a proton. In our case, the event length is short enough to avoid that protons after correlated electrons are lost. So, we only need to correct for the uncorrelated dead time.

Chapter 4

The installation at the neutron beam line

L'expérience aSPECT se déroule à l'Institut Laue-Langevin (ILL) de Grenoble. L'ILL est doté d'un réacteur nucléaire de recherche offrant le flux de neutrons le plus élevé au monde. Le spectromètre est installé dans une zone expérimentale, PF1b, desservie par un guide de neutrons froids. Cette zone est partagée par différentes expériences de physique des particules et nucléaire. Cela implique que le spectromètre doit être démonté puis remonté dans cette zone. Cette opération demande une certaine préparation quant à l'orientation et le positionnement du spectromètre par rapport à la ligne de faisceau. Les différents instruments utilisés sont contrôlés via des programmes LabVIEW : cela permet d'effectuer des acquisitions de données suivant un schéma (ouverture/fermeture du faisceau, ajustement des tensions...). Une fois le spectre de proton reconstruit, il est approximé à l'aide d'une fonction dont l'un des paramètres libres est le coefficient a. Avant ces acquisitions, de nombreuses mesures sont effectuées pour caractériser le spectromètre : profils du faisceau de neutron, position et orientation du détecteur, configuration des électrodes...

4.1 The Institut Max von Laue - Paul Langevin

The Institut Laue-Langevin, founded in 1967 by the French Republic and the Federal Republic of Germany, is an international research center for neutron science and technology. ILL is the world's leader in neutron research providing the most powerful neutron source. Every year, the ILL welcomes approximately 1500 researchers and more than 800 experiments. The nuclear reactor provides very high flux of neutrons to about 40 instruments that can be used for many different fields of research, from biology to particle physics [61].

4.1.1 Presentation of the High-Flux Reactor

The nuclear reactor used at the ILL is a high-flux reactor (see Fig. 4.1). It delivers the highest thermal neutrons flux in the world with $1.5 \cdot 10^{15}$ neutrons per cm^2 and per second. The nominal power of the reactor is 58.3 MW and it emits neutrons from the fission process of ^{235}U. The neutrons have an energy of several MeV (fast neutrons). They are moderated to thermal energies of about 25 meV by a heavy water (D_2O) tank surrounding the fuel element. The mean

Figure 4.1: Top of the ILL nuclear reactor. The blue light emanating from it is caused by the Cherenkov effect (picture from [61]).

neutron velocity is 2200 m·s^{-1}. The reactor operates for several cycles of 50 days with continuous operation each year. Between the cycles, the fuel element is changed.

For the experiment *a*SPECT, placed in the PF1b zone (see section 4.1.2), the neutrons are moderated to even lower velocities (to mainly improve the neutron transport in neutron guides and the fraction of the decaying neutrons) in a "vertical cold source" placed in the heavy water tank closed to the reactor core. This is a spherical vessel filled with liquid deuterium at 25 K. The "cold" neutrons which are extracted have an average velocity of 800 m·s^{-1}. Then, these particles are guided to the PF1b zone via the neutron guide called "H113".

4.1.2 The experimental zone: PF1b

The PF1b (Polarized cold neutron beam facility) zone is dedicated to particle and nuclear physics experiments. The neutron beam provided at this place is the strongest unpolarised one in the world currently available for this kind of experiments. PF1b is an instrument which is shared between different experiments as *a*SPECT, PERKEO, ... This is why, before each beam-time allocated to *a*SPECT, the spectrometer has to be first mounted in the experimental zone (see section 4.2). The neutron guide H113 provides a neutron flux of $2 \cdot 10^{10}$ neutrons per cm^2 and per second. This beam has an average wavelength between 4.0 and 4.5 Å. According to the de Broglie hypothesis, $\lambda = \frac{h}{p}$, where λ is the wavelength, p is the momentum of neutron and h is the Planck constant, this neutron beam has an average energy of 5 meV. This beam facility was well described in [62].

The zone is an area of about $10 \times 3\,\mathrm{m}^2$ (see Fig. 4.2). The neutron guide H113 ends inside the casemate. In addition to the main shutter of the guide (not shown in figure), there is a second shutter made of B$_4$C installed for *a*SPECT. This fast neutron shutter can be operated by users and be coupled to some measurement structure for example. An additional guide has to be installed to provide neutrons inside the experimental area. The zone ends with a beam stop. Parts of the installation, including power supplies, electronics, computers... are installed upstairs out of the experimental zone.

4.2 Installation of *a*SPECT

As it was mentioned, the PF1b zone is shared between different particle and nuclear physics experiments. Before the beam-time, the spectrometer *a*SPECT has to be installed: the holding structure (anti-magnetic screen), the electrode system, the connections to the neutron guide, ... This is also an important step for the experiment as some technical aspects influence systematic effects.

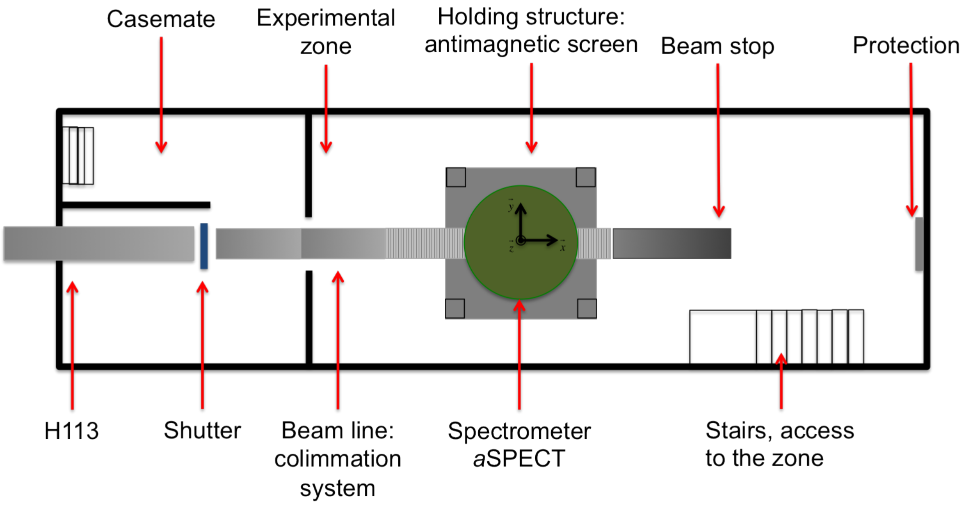

Figure 4.2: General view of the PF1b zone with the example of the *a*SPECT installation. The experiment is installed down-stairs, in the experimental zone. The connection with the neutron beam is done via an extension installed inside the casemate where the guide H113 ends. The second shutter (on this picture) is installed after H113 and can be monitored during measurement.

4.2.1 Assembly of the spectrometer

The aperture of the neutron guide H113 is 60 × 200 mm^2. After the neutron shutter, an additional 2 m guide, with a size of 50 × 116 mm^2(called "n-guide" in Fig. 4.3), is placed to guide the neutron beam out of the casemate. The first part of the installation is the alignment with the neutron beam line in order to optimize the number of neutrons arriving in the Decay Volume. This is also to minimize the edge effect and to avoid that neutrons hit the spectrometer walls. The distance between the end of the H133 guide and the center of the Decay Volume is about 5.5 m.

The anti-magnetic screen structure (Fig. 2.15) is mounted step by step: the basis, the columns, the transversal bars and the platform on the top (this piece, after fixing the spectrometer on the structure). As the global installation is heavy, the base platform is aligned to the beam line using a theodolite. This reduces mainly the risk of too high misalignment. After the installation of the spectrometer, we still have the possibility to move the complete structure using four air cushions[1]. Then, fine adjustments can be made by moving the cryostat inside the magnetic screen. For this we act on the fixations on the transversal bars which allow a displacement within a certain range in the xy-plane.

The connection between the neutron beam at the exit of the casemate and the entrance of the Decay Volume is made by additional tubes containing apertures with different size to collimate the neutron beam. This is another contribution to minimize the edge effect: the beam should have a homogeneous spatial distribution over the width of the DV which is smaller than the size of the neutron guide. For this, a **collimation system** was built (presented in section 4.2.2). On the other side of the spectrometer, neutrons which did not decay inside the DV, are collected inside the beam-stop. This piece is a sintered boron carbide plate at the end of a big vacuum vessel made from aluminum ($150 \times 50 \times 50\,\mathrm{cm}^3$). The side walls of this aluminum box are covered from the inside with boron loaded aluminum to absorb scattered neutrons.

When the alignment and the connections are all right, the vacuum is achieved inside the main volume. In parallel the detector and the preamplifier are installed in the detector mechanics

---

[1] The overall weight of the system is higher than the maximum load of the crane in the neutron guide hall.

before being placed on the top flange of the spectrometer closed by the shutter. The vacuum is then achieved inside the mechanics before opening the shutter and moving the detector down inside the cryostat (more information about the vacuum procedure inside *a*SPECT is available in Appendix A). The other parts of the detection system (electronics box, plexiglas boxes, power supplies...) are then installed.

4.2.2 The collimation system

The collimation system was built with different apertures, the positions and size of which where optimized with Monte Carlo simulation [9]. This was studied in order to obtain a broad flat beam profile causing a small edge effect. In order to avoid background radiation which cannot be shielded, there should be only minimal collimation inside the spectrometer. For the same reason, no primary neutrons should hit the inner walls, and no scattered neutrons have to be avoided as well.

This system is composed of two parts: the *external collimation system* connected after the exit of the casemate, and the *internal collimation system* installed inside the main volume of the spectrometer. The internal one consists of two parts along the neutron beam axis: one before the entrance of the Decay Volume and the second one after the exit. The main vacuum of *a*SPECT is separated from the vacuum inside the guiding tube (at the order of 10^{-2}mbar at the entrance side) by windows at the entrance and the exit sides of the spectrometer. These windows are MgAl3Zn1 foils with a thickness of 250 μm.

The external collimation begins with a 2 m long aluminum tube containing boron apertures, P_0 and P_1, to collimate the beam. This tube is connected directly after the n-guide at the exit of the casemate. P_1 is placed at the end of the tube to block the halo of the neutron beam (see Fig. 4.3). The external collimation system includes a third aperture P_2 placed in front of the entrance window with a size of $45 \times 70\,\mathrm{mm}^2$, adapted to the dimensions of the Decay Volume electrode and comprising a certain tolerance. P_0 and P_2 are made of 5 mm thick boron carbide (BC_4). The boron isotope ^{10}B has a high absorption cross-section: $\sigma_{n,\alpha} = 2840\,\mathrm{b}$ for neutrons at thermal velocities of $v_0 = 2200\,\mathrm{m/c}^2$. ^{10}B emits one photon per neutron absorption (in 75% of cases):

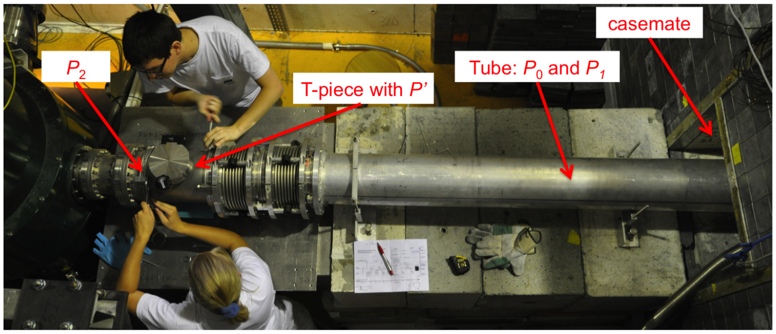

Figure 4.3: Installation of the external collimation system connected to the n-guide inside the casemate.

$$^{10}\mathrm{B} + n \rightarrow {}^{4}\mathrm{He} + {}^{7}\mathrm{Li} + \gamma. \tag{4.1}$$

The BC_4 is glued on 50 mm thick lead plates used for radiation shielding in the neutron beam direction. P_1 is made of several layers of boron loaded rubber glued on an aluminum holder. And the backside of this holder is covered by boron rubber (see Fig. 4.4). The outer shape of

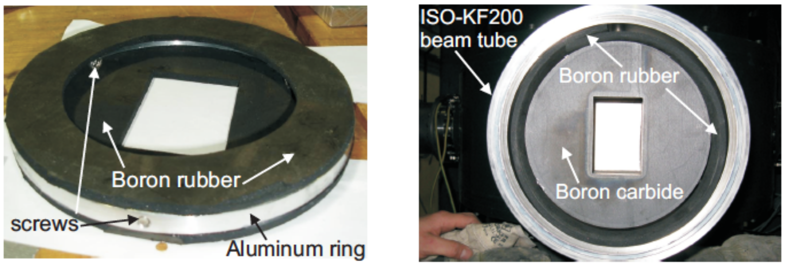

(a) Halo-diaphragm P1, backside (b) Diaphragm P2, front

Figure 4.4: Apertures P_1 and P_2 of the external collimation system. Picture from [9].

diaphragms is cylindrical and is adapted to the tube.

The collimation induces also γ-radiation. In order to suppress radiation by neutrons (e.g., scattered neutrons), the inner surfaces of all beam tubes are covered with boron loaded rubber (Fig. 4.4(b)). An additional layer of 5 mm boron loaded rubber was bent around the tubes from outside. Several layers of lead bricks and plates (total thickness of 10-15 cm) are stacked all around the beam-line to shield gamma rays from neutron capture. To complete the external collimation system, the diaphragm P_0 is placed inside the casemate after the end of the n-guide. This aperture blocks about 50% of the incoming neutrons. It is surrounded by 1m thick concrete walls and a 10 cm thick wall of lead bricks in the beam direction.

The radiation produced at the entrance side of the beam-line should not disturb the measurement of a as the proton detector is about three meters away from P_2 and sees only a very small solid angle. Charged particles (emitted outside the flux-tube) are shielded by the strong magnetic field of *a*SPECT and thus cannot reach the detector.

The internal collimation system is placed inside the main volume of the spectrometer and is divided in two parts along the x axis: between the windows and the DV, at the entrance and the exit side. The internal beam line has a total length of 125 cm. On the entrance side of the DV, three diaphragms (E_1, E_2 and E_3) are placed, with only the aperture E_2 designed to re-shape the beam to a size of $45 \times 70\,\mathrm{mm}^2$. Two diaphragms ($A_1$ and A_2) are at the exit side of the DV. The internal collimation mainly prevents primary neutrons from hitting the inner spectrometer walls. It is made of isotopically enriched ^{6}LiF for reasons of UHV requirements and radiation shielding. In comparison with ^{10}B, neutrons are absorbed in the following process:

$$^6\mathrm{Li} + n \to {}^4\mathrm{He} + {}^3\mathrm{H} \tag{4.2}$$

The absorption cross-section for neutrons of ^{6}Li is about four times lower than the one of ^{10}B. It is high enough that a 5 mm thick plate of ^{6}LiF absorbs practically all neutrons. The internal diaphragms are made of ^{6}LiF-stripes which were glued onto rectangular holders of boron glass plates for the version in 2011 (thickness of 8 mm, see Fig. 4.5). The boron glass helps to absorb scattered neutrons. After the beam time of 2011, we changed the internal collimation as the previous one was non conductive and fragile. For the new internal collimation system (used for the beam time in 2013), the boron glass was replaced by boron-nitride (in order to have a conductive version). The new LiF pieces have been coated with Titanium in the MultilayerLab of the ILL. Then these pieces were glued (Epo-Tek H27D) onto the DiMet plates. This new system (Fig. 4.6) presents a better mechanical stability.

The position, size and relative absorption of each aperture (informations from [9]) are presented in Tab. 4.1 and Fig. 4.7.

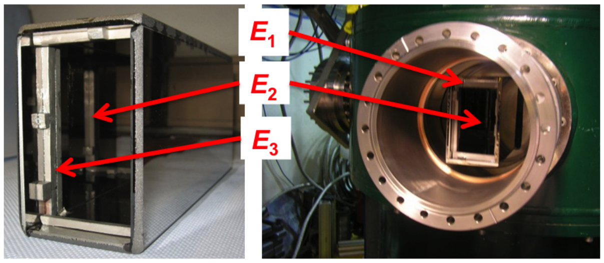

Figure 4.5: First part of the internal collimation system in 2011 (diaphragms E_1, E_2 and E_3) placed at the entrance side of the DV (right). The flange is then closed by the Al window.

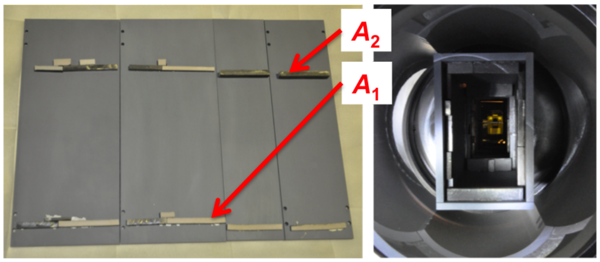

Figure 4.6: The new internal collimation system used during the beam-time of 2013. Left: before mounting the second part placed after the DV (diaphragms A_1 and A_2). Right: the first part at the entrance side of the DV.

Apertures	Width [mm]	Height [mm]	Distance to DV [mm]	Rel. absorption [%]
n-guide	50	116	End at -3175	-
P0	45	70	-3174	45.7
P1	50	75	-1600	20.8
P'	50 or 15	75 or 75	-824	
P2	45	70	-690	13.3
Entrance window	Ø = 110		-625	
E1	48	80	-480	0.3
E2	45	70	-280	2.9
E3	48	80	-120	0.1
DV			0	
A1	48	90	120	0.8
A2	47	80	280	1.1
Exit window	Ø = 140		625	
Beam-stop			2270	15.0

Table 4.1: The collimation system at ILL: positions, sizes and relative absorption of the diaphragms. 100% corresponds to the intensity at the end of the neutron guide (these values were calculated without the additional aperture P'). Information from [9]. Distance along the x-axis.

In 2011, a T-piece was added on the beam-line between P_1 and P_2 (see Fig. 4.3). This piece is used to insert an additional diaphragm *P'* with two possible configurations. The first configuration consists in an aperture *P'* with the same size as P_1, $50 \times 75\,\mathrm{mm}^2$: this corresponds to so-called standard neutron beam. In the second configuration, this aperture has a size to redesign the beam profile, $15 \times 75\,\mathrm{mm}^2$: this corresponds to a reduced neutron beam. This

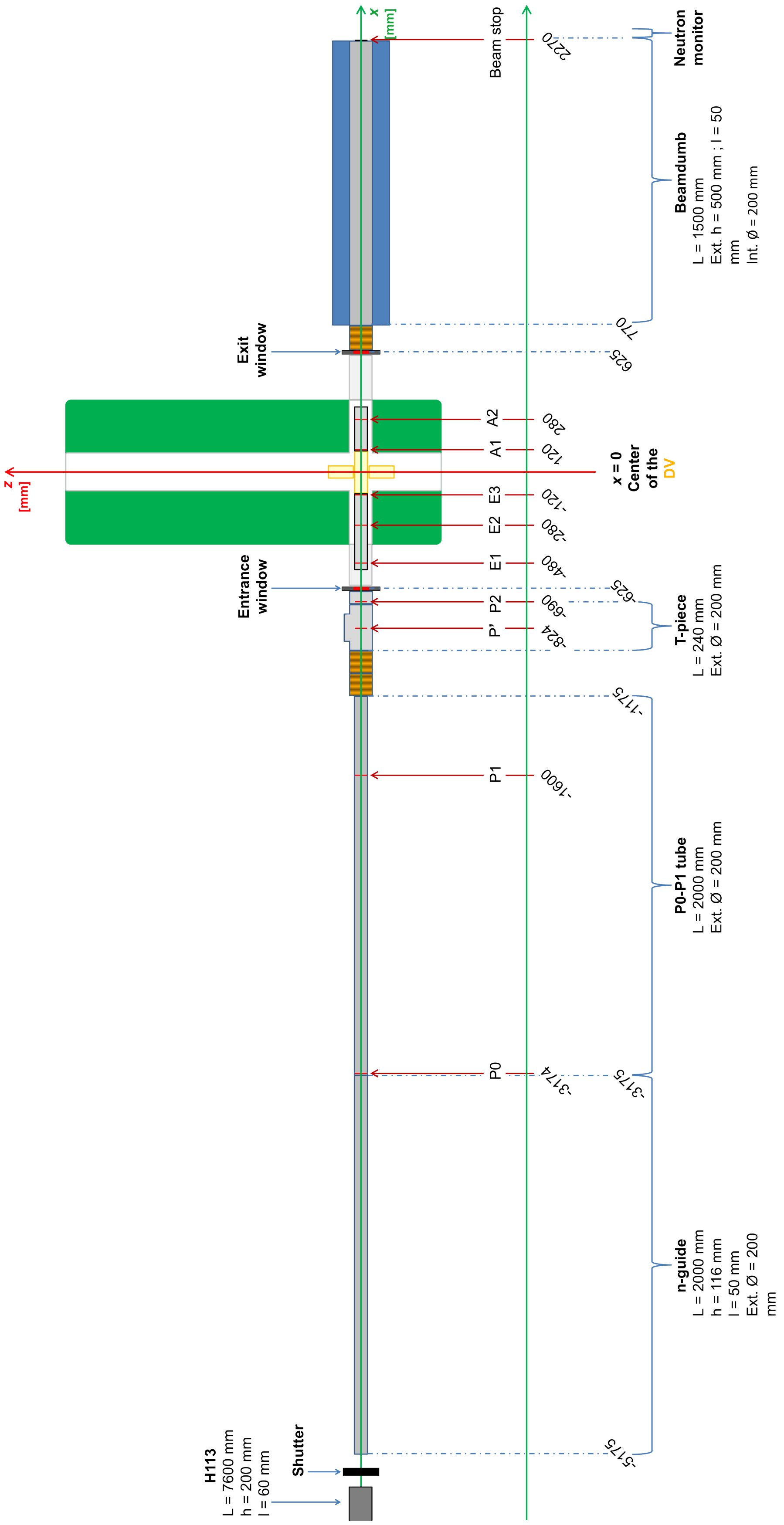

Figure 4.7: Installation of the collimation system at PF1b to bring the neutron beam with an appropriate profile to the DV inside *a*SPECT, and the beam stop for the non-decaying neutrons.

facility is used to investigate the edge effect.

4.3 Procedure for measurements with *a*SPECT

The power supplies for the different electrodes are monitored by several PCs. The control and the readout of several devices are made via LabVIEW software. The communication between the different PCs is done via DataSocket, a standard developed by National Instruments which allows to transfer data values via the network. Different experimental parameters (pressure, temperature, voltage, current) are registered in log files to keep track of the "history" of the experiment.

4.3.1 Measurements structure

The control system allows to perform measurements with different settings for the electrodes and with/without neutron beam (via the additional neutron shutter). It is also possible to implement an automatic system to run continuous measurements. A basic measurement cycle, as shown in Fig. 4.8(a), is structured as follows:

- start of the acquisition with the neutron shutter closed,
- after 10 s, the AP voltage is ramped from 0 V to U_{A},
- 20 s after U_{A} was stabilized, the neutron shutter is opened for t_{op},
- 20 s or 50 s after the neutron shutter was closed, the AP voltage is ramped to 0 V,
- the acquisition stops 10 s after U_{A} was stabilized to 0 V.

This procedure is optimized for the investigation of stability and trap filling. The voltages for AP are $U_{\mathrm{A}} = 0$, 50, 100, 250, 350, 400, 450, 500, 550, 600, 780 V (see Fig. 4.8(b) for example). For continuous measurements, we defined blocks composed of measurements with the different AP voltages in a mixed order to get rid of drifts and to check for longer time constants: if a deep trap was not fully discharged, there may be a difference if the subsequent trap is deep as well or shallow.

From this structure, different parts of one measurement were defined to extract spectra and count rates. The main part is when the neutron shutter is open (called "Open" in histograms). Spectra from this Open part are extracted considering the first event after the action "open shutter" is finished, and the last event before the action "close shutter" starts. The explanation is similar for the two time intervals with the neutron shutter closed. The "Close1" part is from the first event after the AP is ramped to U_{A} to the event before the action "open shutter" starts. For the "Close2" part, the events considered are between the first one after the action "close shutter" is finished and the one before starting to ramp down the AP to 0 V. Thus, both parts Close1 and Close2 are measured with the AP set to U_{A} and the neutron shutter closed. The length of the intervals is given by statistics and may result in under/over determination of rate in case of low rate compared to high rate.

The structure of each file in a continuous measurement is written in a log file ("action.log") indicating the time and the event number corresponding to the beginning and the end of each action (ramp U_{A}: start/end ; shutter: open/close).

I wrote a C++ software to extract data from the ROOT-Tree of each measurement and read the corresponding "action.log" file. This software extracts the spectra measured for each time interval: the beginning ("1" in Fig. 4.8), Close1, Open, Close2, and the ending part ("2" in

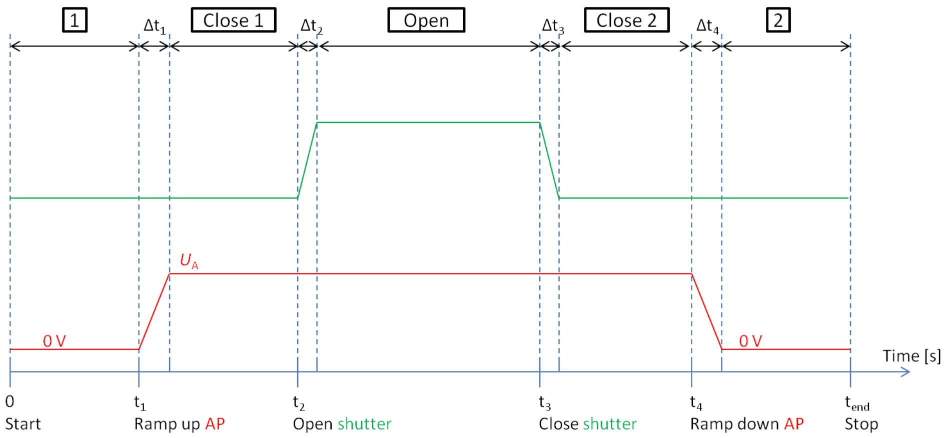

(a) Time structure.

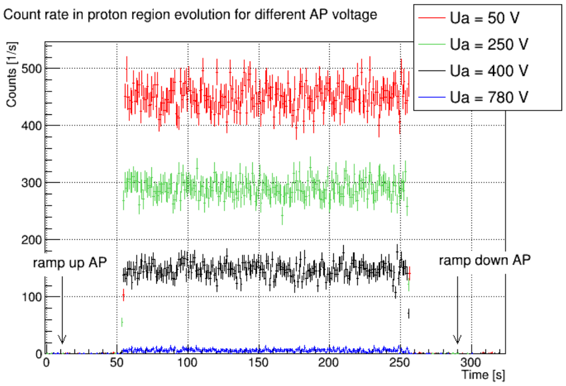

(b) Example of the evolution of the count rate in the proton region for different AP voltages.

Figure 4.8: Structure of measurement.

Fig. 4.8). Each spectrum is attributed to the corresponding AP voltage in order to check the stability and then to obtain the mean spectrum for the different voltages over the continuous measurement.

4.3.2 Extraction of the coefficient *a*

The measurement of the electron-antineutrino angular correlation coefficient a with the spectrometer aSPECT is indirect. From the measurements with the different AP voltages U_A, we build the integrated proton spectrum as shown in Fig. 4.9. The extraction of the coefficient a is done by fitting the experimental data points of the integrated proton spectrum. The fit function is described by:

$$\rho_\mathrm{tr}(U_\mathrm{A}) = N_0 \int_0^{T_\mathrm{max}} F_\mathrm{tr}(T)W(T)\mathrm{d}T \tag{4.3}$$

where $F_\mathrm{tr}(T)$ is the transmission function described by (2.11) and $W(T)$ is defined by (1.25). The free fit parameters are the proton rate at $U_\mathrm{A} = 0\,\mathrm{V}$, noted N_0, and the correlation coefficient a included in the function $W(T)$.

We performed a blind analysis of the coefficient a (see Chapter 7). We used fit function slightly different considering more fit parameters as for example the ratio r_B included in the

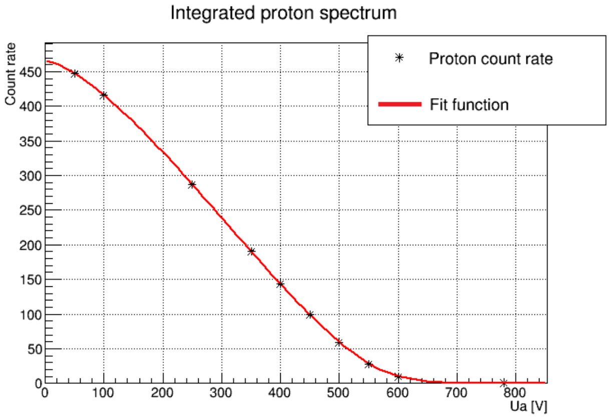

Figure 4.9: Example of integrated proton spectrum measured during the beam time of 2013. The proton count rate is integrated for the different AP voltages. The points are fitted by a function whose free parameters are the coefficient a and the count rate for AP at 0 V.

transmission function (this parameter is also measured experimentally and can be fixed in the function). Another free parameter in the fit was an offset due to a constant background. For the usual fit function above, the count rate measurement with AP at 780 V has to be subtracted. However, as described in Chapter 6, the background measurement with AP at 780 V is more complex than a stable count rate.

As the spectrometer aSPECT measures with high precision the proton spectrum, we can consider the measurement of another correlation coefficient: the proton asymmetry. Some estimations and perspectives are presented in Appendix E.

4.4 Characterization of the experiment

The measurements performed to extract the coefficient a are completed by additional measurements and tests. These are necessary to investigate the systematic effects and their influence on the uncertainty of the coefficient a.

4.4.1 The neutron beam profile

The neutron beam profile is measured using copper foils installed at different places along the neutron beam line. Those foils are made of natural copper which is composed of roughly 2/3 of ^{63}Cu and 1/3 of ^{65}Cu. Under a neutron beam, those two isotopes will capture neutrons to form respectively ^{64}Cu and ^{66}Cu which are both beta emitters with a respective half-life of $\tau = 12.700(2)\,\mathrm{h}$ and $\tau = 5.12(14)\,\mathrm{min}$ [69, 70]. About one hour after the activation, only the ^{64}Cu is still really active. By using an X-ray image plate and scanner, the copper foils can then be read out with a size of $200\,\mu\mathrm{m}$/pixel.

At the beginning of the beam time in 2013, we made this measurement with two coppers foils placed respectively in front of the entrance window and behind the exit window of aSPECT (see Fig. 4.10).

This analysis was mainly conducted by Romain Virot [64]. This first acquisition allowed to check the neutron beam profile without any impact on the spectrometer vacuum quality: to measure the beam profile inside the DV, the vacuum would be severely deteriorated by installing

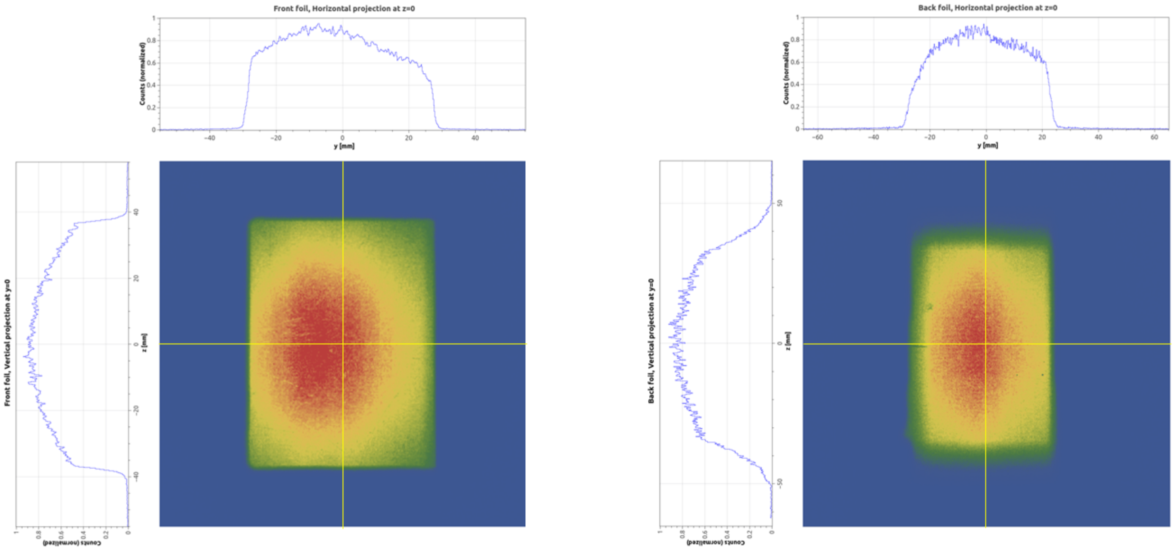
Front foil, Horizontal projection at z=0

Back foil, Horizontal projection at z=0

(a) Entrance window.

(b) Exit window.

Figure 4.10: Neutron beam profile with the standard collimation system. Picture from [64].

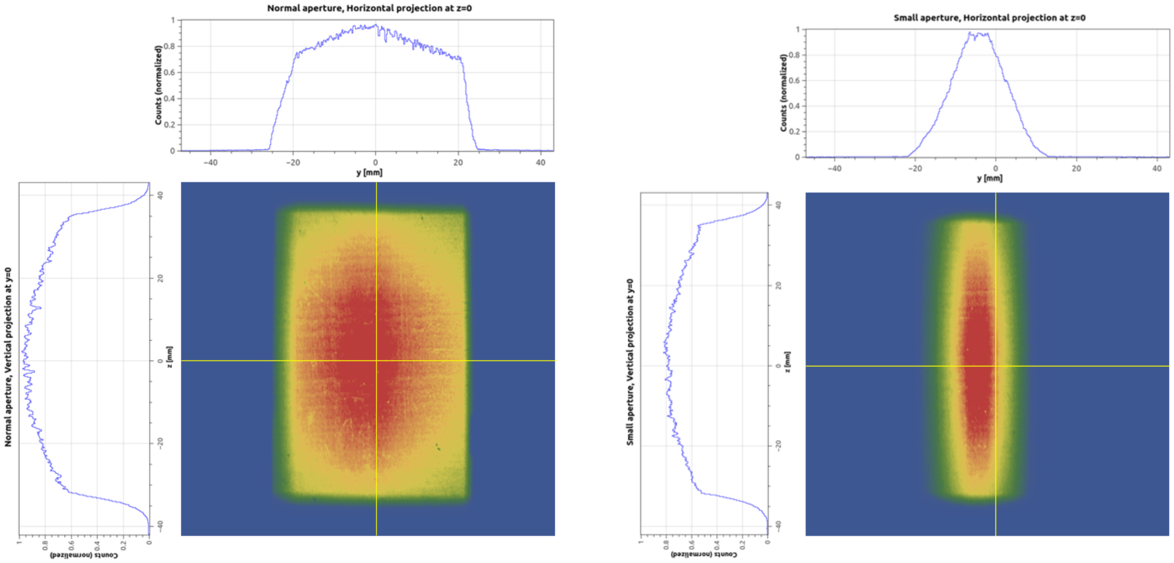
Normal aperture, Horizontal projection at z=0

Small aperture, Horizontal projection at z=0

(a) Normal aperture.

(b) With narrow aperture.

Figure 4.11: Neutron beam profile inside the DV with different aperture P'. Picture from [64].

the copper foil on the manipulator[2]. Thus, those measurements were done at the very end of the beam time and with two different apertures placed in front of the entrance window (aperture P' in Fig. 4.7): the first one is 50×75 mm (this the standard one used for the main measurement during the beam time), and the second is 15×75 mm (this aperture is called the "narrow" one). The beam profiles at the entrance and exit of *a*SPECT indicate that the neutron beam is

---

[2] The manipulator is installed at the cross-piece on a side port of the spectrometer (see example on Fig. 6.19). It allows to move copper foil or gold foil (see Chapter 6) inside the DV. However, the installation of the foil requires to vent the cross-piece.

symmetric along the z-axis but is shifted by several millimeters toward y<0 (see the orientation in Fig. 4.2). From the profile inside the DV, with the normal aperture, we denote the same shift.

Concerning the narrow beam profile (see Fig. 4.11), it is symmetric in both directions but not centered along the x-axis. The narrow aperture was intentionally shifted towards the y<0 in order to obtain the maximum beam intensity at about the same position as with the full beam. This profile and the *a* measurement realized with this aperture will be used to determine the edge systematic effect.

4.4.2 Position and orientation of the detector

As the insertion mechanics is independent from the spectrometer, the detector, when inserted inside the bore tube, may be shifted from the center position along the z-axis. And, the orientation of the three pads may be also shifted from the ideal configuration, i.e. aligned along the neutron beam direction (the x-axis). In 2013, the mechanics for the insertion of the detector was modified to include a positioning system in the horizontal plane (x,y): the tilting plate shown in Fig. 4.12. However, since this tube is quite long (approximately 130 cm) and the detector cup quite heavy the reproducibility of the position is low. Several scans and tests have been realized with the detector mechanics outside and inside aSPECT. The result is that the reproducibility of the detector position when moving the detector up and down is not perfect and is only reproducible within approximately 2.5 mm. In order to get the most precise detector position, the position of the moved down detector cup has been measured with the detector mechanics outside *a*SPECT (see Fig. 4.13). The measured positions were the following:

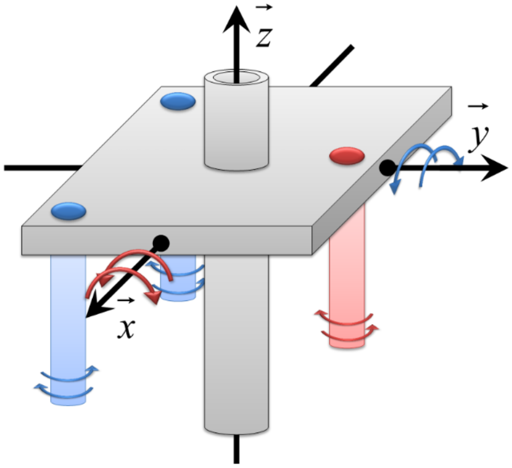

Figure 4.12: Tilting plate placed on the top of the insertion mechanics. By turning the red screw, the plate is titled around the x-axis allowing to scan the y-direction. By turning the blue screws, the plate is titled around the y-axis allowing to scan the x-direction.

- −0.68(18) cm shift in the x-direction: the detector cup is shifted toward the reactor (x<0).
- +0.18(18) cm shift in the y-direction: the detector cup is slightly shifted toward y>0.

Therefore this position is the one, within the reproducibility uncertainty, indicating the center of the detector inside *a*SPECT. It is however not known or really predictable: the detector cup is quite heavy, and moving the detector inside the cryostat can induce a deviation of the initial position in the xy-plane.

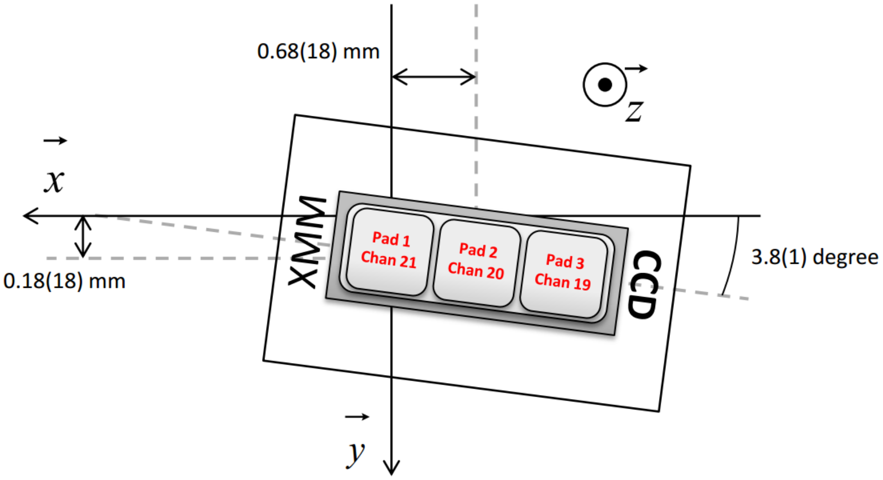

Figure 4.13: Position and orientation of the detector during the beam time of 2013 from mechanical scan.

The other part of this investigation is to know the position of the detector, when inserted inside the bore tube, projected to the DV. For this, we used copper wires mounted on the manipulator (see Fig. 4.14) which were activated by neutron capture. By translating the manipulator, the y-axis can thus be scanned and related to the detector position from the resulting count rates. Furthermore, by placing a copper wire on the side of the holder parallel to the y-axis, one can scan the x-axis by turning the manipulator. This is the projection for electrons (with negligible influence of the electrodes system which was off). The protons are drifted by the electrostatic potentials which has to be taken into account by simulations.

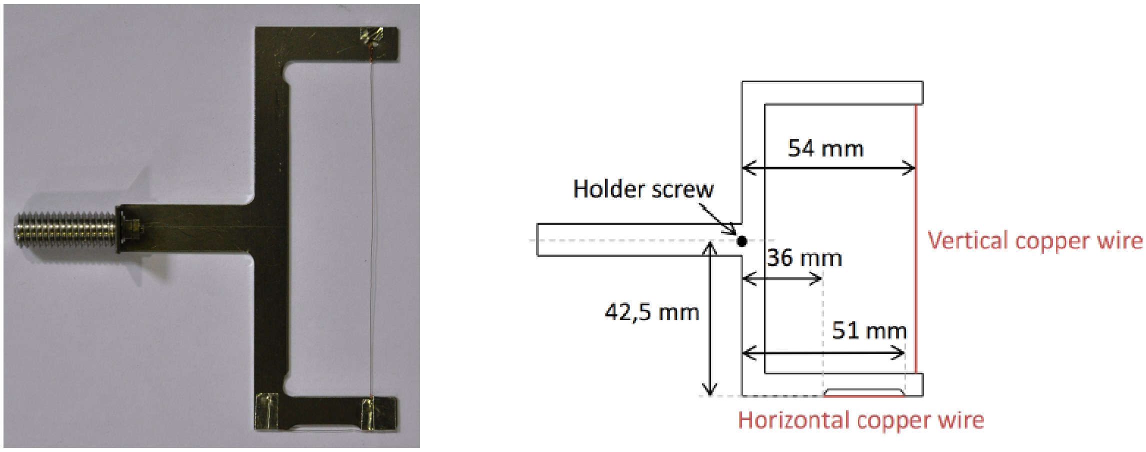

(a) Copper wires on the special holder.

(b) Sketch and dimensions.

Figure 4.14: Copper wires installed on a holder fixed to the manipulator. The vertical one was used to scan the projected area along the y-axis. The horizontal one was used to scan along the x-axis at a fixed y position.

For the x-scan, the manipulator was positioned inside the DV. The angle read on the manipulator -25 deg corresponds to the position $x = 0$ for the horizontal copper wire. To convert the manipulator angle into the x-position: $x = -\sin(\text{angle} + 25\,\text{deg}) \times 4.2\,\text{mm}$. The results for

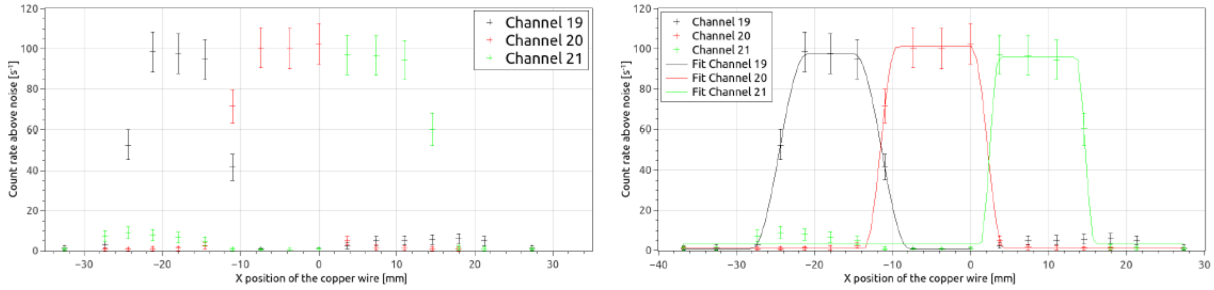

(a) (b)

Figure 4.15: (a): Count rate for each channel depending on the x-position of the activated copper wire. (b): Fit of the data using a phenomenological function. Figures from [64].

the x-scan are presented in Fig. 4.15. To fit the data, a phenomenological function has been developed by Romain Virot [64]:

$$f(x) = \begin{cases} a_0 & \text{if } x < x_0 \\ \frac{a_0+a_1}{2} + \frac{(a_1-a_0)\times\sin(\frac{\pi}{2}\times\frac{x-\text{LowerEdge}}{\text{EdgeWidth}})}{2} & \text{if } x_0 < x < x_1 \\ a_1 & \text{otherwise} \\ \frac{a_0+a_1}{2} - \frac{(a_1-a_0)\times\sin(\frac{\pi}{2}\times\frac{x-\text{HigherEdge}}{\text{EdgeWidth}})}{2} & \text{if } x_2 < x < x_3 \\ a_0 & \text{if } x > x_3 \end{cases} \tag{4.4}$$

$$\text{with} \quad \begin{array}{ll} x_0 = \text{LowerEdge} - \text{EdgeWidth} & x_2 = \text{HigherEdge} - \text{EdgeWidth} \\ x_1 = \text{LowerEdge} + \text{EdgeWidth} & x_3 = \text{HigherEdge} + \text{EdgeWidth} \end{array} .$$

The EdgeWidth is defined as the half-width of the increasing part before the plateau in the graph (this parameter is the same for the decreasing part) which can be described by a sinusoidal function. The x-value corresponding to $f(x) = \frac{a_0+a_1}{2}$ in the increasing part of the graph is attributed to the LowerEdge parameter, and the one corresponding in the decreasing part of the graph is attributed to the parameter HigherEdge.

The poor angular resolution of this data set limits the precision of the analysis, therefore rough fit parameters had to be indicated for the fitting algorithm to converge. As this fit function is truncated into several parts and the data points are not numerous, uncertainties given for the fit parameters are huge and not realistic. Therefore the position uncertainty is defined as 1.8 mm which is approximately half of the distance between each acquired point, as there is often a direct transition from 0 counts to the full count rate between two points.

Pad (channel)	Center of detector projection in x [mm]	Width of the detector projection in x [mm]
1 (ch21)	+8.6 ± 1.3	12.3 ± 2.5
2 (ch20)	−4.7 ± 1.3	13.7 ± 2.5
3 (ch19)	−18.0 ± 1.3	13.2 ± 2.5

Table 4.2: X-coordinates of the detector projection.

For the y-scan, the wire is aligned with the reference axis for a read value of +33.5 mm, meaning that the $y = 0$ position for the copper wire corresponds to a read value of 34.0 mm. In

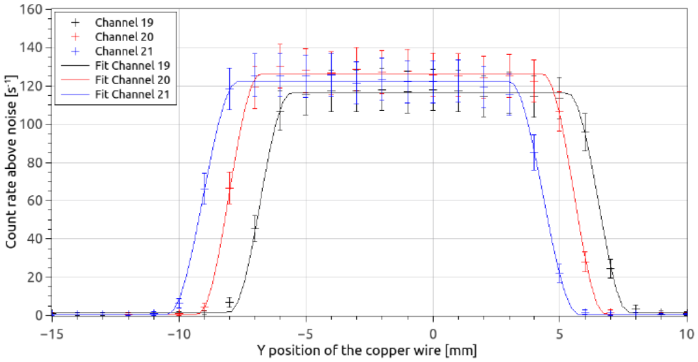

Figure 4.16: Count rate for each channel depending of the y-position of the activated copper wire. Figure from from [64].

Fig. 4.16, a better spatial resolution compared to the x-scan is observed, with the uncertainties of the fitting parameters being relevant. The distance on the manipulator was measured with a caliper rule with a 0.1 mm uncertainty. The edges positions given by the fit are known with a 0.02 mm uncertainty. The measured projection widths are larger than the dimension of one pad, $10 \times 10\,\mathrm{mm}^2$. This is explained by the gyration motion of the particles as shown in Fig. 2.17 (in section 2.4.5): particles emitted outside of the direct projection of the detector in the DV can reach the detector due to their gyration radii.

Pad (channel)	Center of detector projection in y [mm]	Width of the detector projection in y [mm]
1 (ch21)	-2.35 ± 0.07	13.4 ± 2.5
2 (ch20)	-1.23 ± 0.07	13.6 ± 2.5
3 (ch19)	-0.14 ± 0.07	13.3 ± 2.5

Table 4.3: Y-coordinates of detector projection.

4.4.3 The uExB scan

The electrodes uExB generate an electric field allowing to align the protons onto the detector. During the beam time, we performed several scans to find the best alignment of detector and beam at the lowest background. The scans were done with a fixed offset (2 kV, 3 kV, 4 kV) defined as $\frac{\text{uExB\_A} + \text{uExB\_B}}{2}$, and by varying the difference uExB_A - uExB_B. A larger offset increases the scanning range, but it also increases the acceleration and so the speed of protons in uExB electrodes: this would reduce the drift distance for the same difference uExB_A - uExB_B. This offset also influences the background.

In the conditions of the beam time of 2013, the offset of -2 kV was found to be good candidate for the measurements. We performed a scan by varying the electrodes uExB in accordance with the chosen offset (see Fig. 4.17), and observed that the background, measured with AP at 780 V, is quite stable between the configurations. The measurements with AP at 50 V are consistent with the one at 780 V. The application of a fit on these experimental points gives different maxima for uExB_A voltage: -1.46 kV for channel 19, -1.34 kV for channel 20, and -2.11 kV for channel 21. Therefore, we used, during the beam time of 2013, the settings uExB = -1.75|-2.25 kV, for the measurements dedicated to the extraction of a: this configuration is a adjusted average of the previous values obtained for each channel.

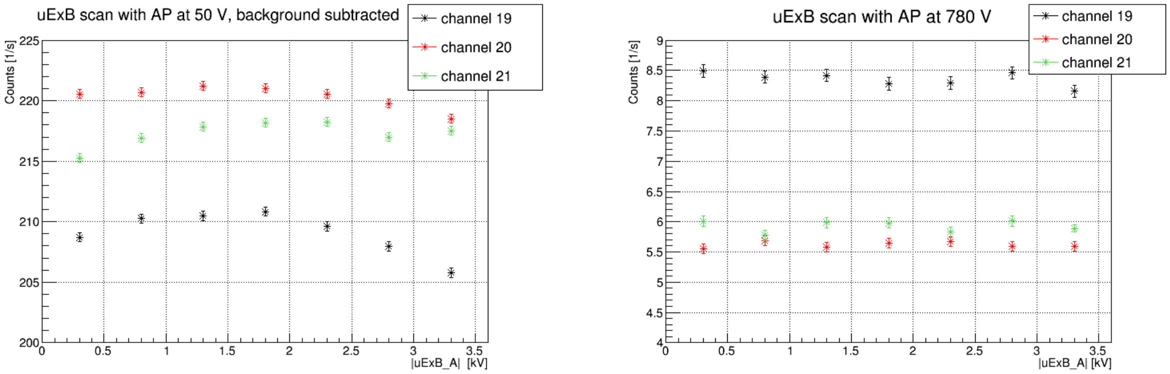

(a) With AP at 50 V. Measurement time for each point is about 20 min.

(b) With AP at 780 V. Measurement time for each point is about 10 min.

Figure 4.17: Scan uExB with an offset fixed at -2 kV. These measurements were done with Det-HV at -15 kV and the other electrodes at 0 V. The count rate were extracted from the proton region.

The same measurements were performed for a uExB scan in the case of a reduced neutron beam profile, by changing the size of the aperture $P^{'}$ (see Fig. 4.18). This scan was done in the same configuration as the previous one. After fitting, we obtained new maxima for the uExB_A voltage: -0.92 kV for channel 19, -1.15 kV for channel 20, and -1.85 kV for channel 21. As the detector was not centered on the x-axis (see section 4.4.2), and the spectrometer had a misalignment of 0.23° with the reference axis at PF1b (measured with a theodolite during the installation of the spectrometer, see section 4.2), we tried to compensate this by placing the reduced size aperture $P^{'}$ in order to center the beam axis with the detector position. This resulted in an modification of the edge effect and so of the uExB voltages.

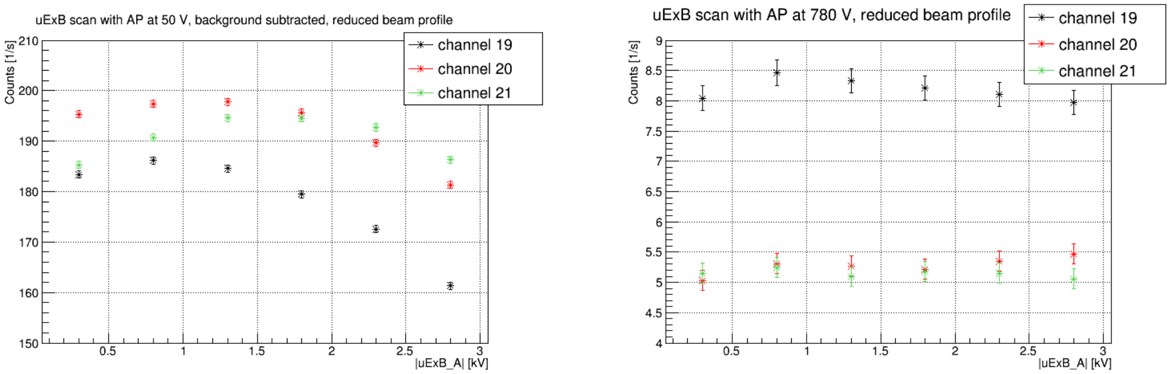

(a) With AP at 50 V. Measurement time for each point is 400 s.

(b) With AP at 780 V. Measurement time for each point is 200 s.

Figure 4.18: Scan uExB with an offset fixed at -2 kV and with a reduced neutron beam profile. These measurements were done with Det-HV at -15 kV and the other electrodes at 0 V. The count rate were extracted from the proton region.

During the beam time of 2013, we took some data with the electrode e15 in asymmetric settings. This allows to reduce a part of the background described in Chapter 6. However, this may change the edge effect and so the results about the scan with uExB. From Fig. 4.19, we

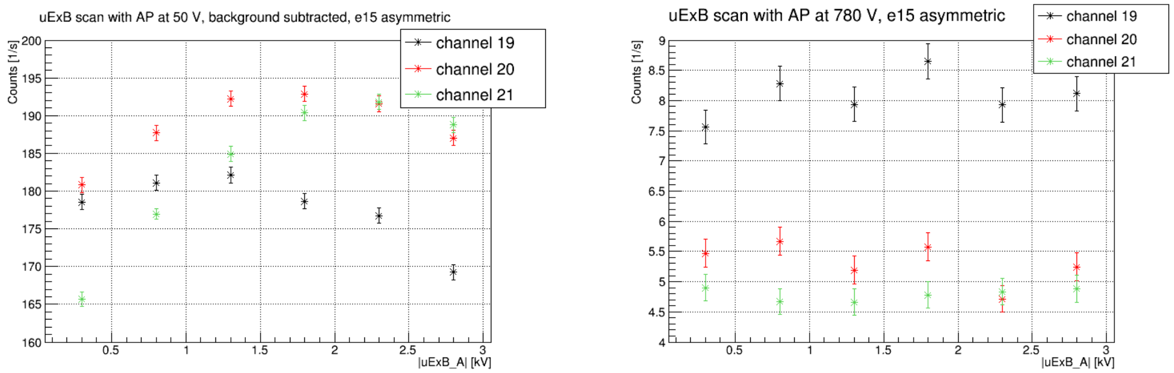

(a) With AP at 50 V.

(b) With AP at 780 V.

Figure 4.19: Scan uExB with offset fixed at -2 kV and the electrode e15 in asymmetric settings. Measurements were made with Det-HV at -15 kV and other electrodes at 0 V, and with 100 s shutter opened.

calculated the maximum for the uExB_A voltage for the different channels of the detector (fit of the experimental points): for channel 19, the maximum count rate could be reached for uExB_A at -1.15 kV, for the channel 20, this should be -1.77 kV, and -2.23 kV for the channel 21.

4.4.4 Investigation of discharges

During the beam time of 2011, we found some instabilities in the applied electrodes voltages. The settings used in the previous beam time for the electrodes were found to be unstable in 2011: so we investigated for stable settings These instabilities are characterized by leakage currents in the electrodes system. Due to electric noise and the finite resistance of power supplies, the current measured is never 0: this is a constant current “background”. However, discharges between electrodes caused an increase in the current. Different reasons can explain these instabilities.

Problem with connections. The configuration of the PF1b zone implies some difficulties for positioning and connecting cables: the power supplies are upstairs and we need regularly to act on the beam-line. During the installation, it is possible that some connection broke or was damaged. We observed an influence due to isolation problems between cables, as for example shown in Fig. 4.20: when we changed the voltage of the lExB right electrode, the current of one electrode of the Mirror was influenced. The behavior of the current was related to the configuration of the lExB electrodes. This effect could change the real voltage of the electrode because of the finite resistance of the cables. However, the small drift induced by this effect is not dangerous for the electrode and can be fixed by improving the isolation of cables.

“Bad” vacuum. In the case of insufficient vacuum, the rest gas molecules inside the main volume of the spectrometer could be ionized by electrons emitted due to the strong electric field (field emission). These particles can hurt the electrodes surfaces and generate leakage current. To suppress this, we checked the vacuum in detail by searching any leaks and fixing them. As shown in Fig. 4.21(a), the pressure[3] was not stable, during these tests, and some spikes occurred at the same time with the instabilities of the current at the detector electrode (Fig. 4.21(b)).

Surfaces properties of electrodes. If the surfaces of the electrodes are not well uniform due to some spikes, this can increase field emission or ionization close to the surface. And again,

---

[3] The pressure mentioned was measured at a long tube fixed to the bottom chamber installed at the bottom flange of the spectrometer. This allows to have the vacuum sensor out of the magnetic screen.

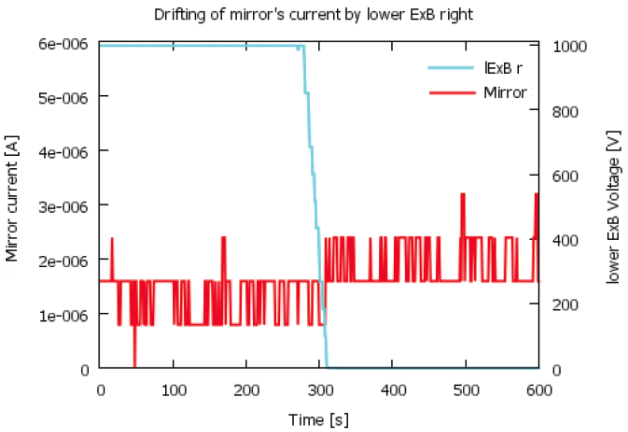

Figure 4.20: Influence of the change of the electrode lExB right (lExBr) on the current of one electrode of the Electrostatic Mirror. Note: the voltage for lExB is in reality **negative**.

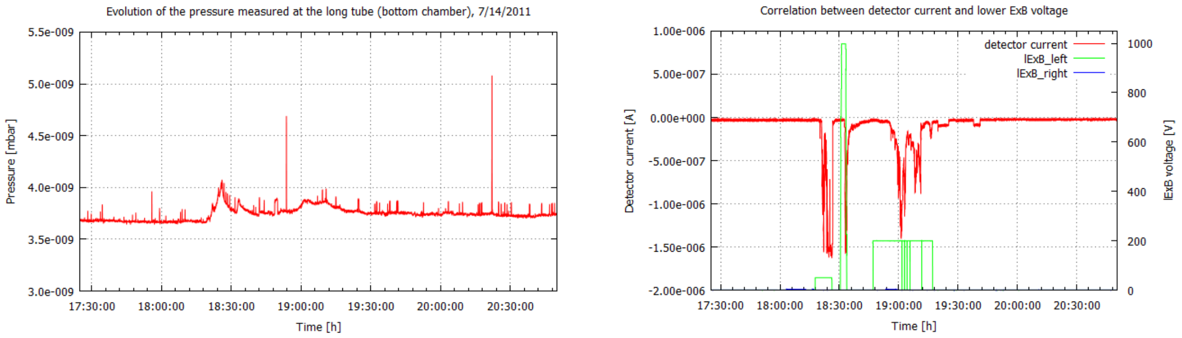

(a) Pressure measured at the long tube at the bottom chamber, during the HV tests.

(b) Evolution of the current at the detector electrode e17 when adjusting the lExB voltages.

Figure 4.21: Instability of the pressure and of the electrodes settings.

this can induce leakage current. This effect can be combined with the previous one about the vacuum status.

Penning traps. In *a*SPECT, the electric and magnetic fields are complex (see Chapter 2) and form traps for charged particles. Due to the accumulation of these particles, the saturation of the trap could be reached leading to discharges [63].

During the beam time of 2011, we tried to minimize these effects by using electrodes settings as stable as possible. The cables were checked and replaced if necessary. For the vacuum status, several leak tests were done. The surface of the detector cup was also improved by polishing. After this beam time, more improvements were proposed and achieved: the electrodes system was rebuilt and re-coated (to improve the surface properties), an additional turbo pump was installed at the detector mechanics... All of this led to a better stability of the electrodes setting and of the vacuum during the offline tests in 2012 and the beam time of 2013.

4.4.5 Tests of the magnetic mirror effect

As described in Chapter 2, the magnetic field is corrected inside the DV in order to avoid possible trapping of protons inside this region. The correction coils induce a slope of the magnetic field lines with a maximum below the DV. Thus, a magnetic mirror is created which ensured that particles leave the DV quickly. This shape can be experimentally checked by measuring the count rate with and without the Electrostatic Mirror (see Fig. 4.22). Using the same setting for the other electrodes, the count rate integrated on the proton peak was 218.7(1.5) s^{-1} without Mirror, and 421.5(2.1) s^{-1} with Mirror. The count rate increased by a factor 1.93(2) due to the presence of the Mirror. Thus, without Mirror, the count rate is higher than half of the one measured with Mirror: this is due to the magnetic mirror inside the DV which makes that about 51% of the protons are directly oriented towards the detector (from the experimental values we obtained 51.9(4)%).

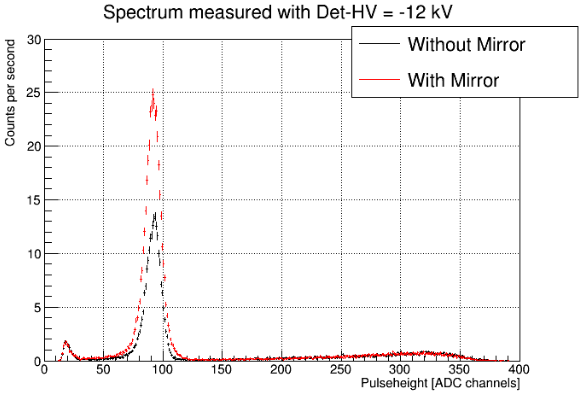

Figure 4.22: Measurement with the neutron beam, the new preamplifier and the new shaper. Comparison with and without the Electrostatic Mirror and with AP at 50 V. Measurement time was 100 s for each spectrum.

Chapter 5

The vacuum investigations

La qualité du vide dans aSPECT a un impact important sur de nombreux effets systématiques. Il est donc essentiel d'avoir un vide stable dans le temps et qui soit de l'ordre de 10^{-9} mbar. En 2012, le spectromètre était installé dans une zone hors-faisceau afin de tester ses composants. Cela a été également l'occasion de tester le vide et de l'étudier à l'aide d'un spectromètre de masse. Des acquisitions ont été réalisées à différentes étapes de la procédure suivie pour atteindre le vide dans aSPECT : activation des pompes (primaires et turbo), dégazage des parois internes des brides et des tubes... Ceci a permis de suivre l'évolution des principaux composés gazeux tels que l'hydrogène, l'azote, l'eau, l'oxygène... Des mesures ont également été faites pendant la phase de refroidissement du cryostat. En fin de procédure, les résultats montrent la présence d'un gaz résiduel constitué d'hydrogène, d'eau et d'azote. Le même protocole a été réalisé en 2013 en présence de nouveaux composants du spectromètre installé sur la ligne de faisceau à PF1b. Les résultats de l'analyse des spectres de masse montrent que la pression partielle des molécules gazeuses restantes induirait sur le coefficient a un effet systématique $\delta a < 10^{-4}$.

5.1 Procedures for the vacuum in aSPECT

In the beam time a vacuum of about 10^{-9} mbar was measured on a 2 m long, warm CF40 vacuum tube attached to the bottom flange of the spectrometer. This long tube is needed, as the vacuum is measured by a cold cathode gauge which uses a strong permanent magnet. This permanent magnet has to be sufficiently far away from the main magnet as the magnetic field of aSPECT would perturb the measurement with a cold cathode. Inside the main bore tube the vacuum should be a lot better. This gauge is taken as reference for the vacuum evolution and especially for the mass spectra analysis.

The vacuum inside the main volume of the spectrometer aSPECT is made by turbo pumps and getter pumps (see section 2.3.1). One turbo pump is connected to the cross-piece on a side port of the spectrometer. In order to improve the pumping efficiency, a second turbo is connected in cascade, i.e. between the first turbo and the primary pump. This method is useful to improve the compression ratio for light gases (as H_2 for example). The second step to improve the vacuum is to make outgasing of the inner surfaces of tubes (cross-piece, bottom chamber, detector mechanics...). For this, heating bands are placed around the different connection tubes. The effect of the outgasing is clearly visible in the pressure evolution: the pressure increased in the first phase indicating that molecules are removed from the surfaces, and then it decreased when the molecules were evacuated by pumping. The last step for vacuum is the activation of the getter pumps. These pumps complete and maintain the vacuum by removing small amounts of gas. They consist in a deposit of reactive material and when molecules strike it, they are removed by chemical combination or adsorption. When the pressure is stabilized, the cryocoolers are switched on. More details about the procedures for the vacuum inside *a*SPECT are presented in Appendix A.

5.2 Mass spectrum measurements

Following the observations during the beam-time of 2011 concerning the discharges (see section 4.4.4), the spectrometer was installed in a preparation zone without beam in 2012. Different modifications and improvements were carried out on it (mentioned in Chapter 2). This situation was also an opportunity to investigate the vacuum as it was a possible cause for the observed discharges. For this, we connected a mass spectrometer to the main volume and took mass spectra at the different steps of the vacuum and cooling procedure.

5.2.1 The mass spectrometer

The mass spectrometer used for *a*SPECT is "PrismaPlus$^{\text{TM}}$Compact Mass Spectrometer System QMG 220" (PTM 28602-44510) from Pfeiffer Vacuum [66]. In 2012, we connected it at the entrance side port of the spectrometer where the neutron beam line is supposed to be connected (see Fig 5.1). This device is a quadrupole mass spectrometer based on the principle

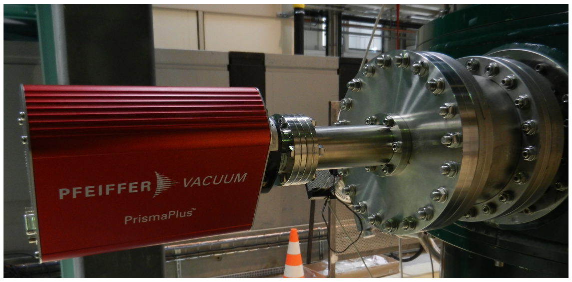

Figure 5.1: Mass spectrometer connected at the entrance side of the spectrometer (in 2012).

of the separation of charged molecules in a gas related to their mass-charge ratio, $^m/_q$. To be detected the molecules first have to be ionized. With our mass spectrometer, the ionization is done by electrons emitted from a tungsten filament. If the electron energy is sufficient, when colliding with one molecule, an electron can be expelled leading to the formation of a radical ion: $M + e^- \rightarrow M^+ + 2e^-$. Depending on its internal energy, the radical ion can then become fragmented. This is usually the case for complex molecules: several ion fragments are produced and detected. The different kinds of ions are then separated according to their mass-charge ratio using magnetic and/or electric fields. In the case of a quadrupole mass spectrometer (see Fig. 5.2), the separation is ensured by a high-frequency quadrupole electric field generated by four hyperbolic rods[1]. When ions are injected inside this system (called analyzer) in the direction of the field, the high-frequency of the electric field causes them to oscillate at right-angles to the axis of the field[2]. Thus, some ions pass through the analyzer while others strike the rods, being neutralized an pumped away as gas. After the analyzer, ions hurt the collector and give up their

---

[1] The voltage between these electrodes is composed of a high-frequency alternating component V $\cos\omega t$ and a superposed constant voltage U.

[2] The ions motion in such a system is describes my the Mathieu differential equations.

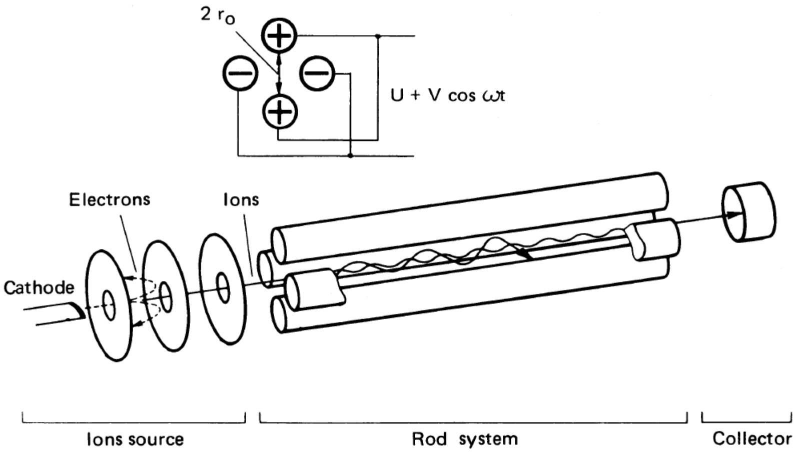

Figure 5.2: Principle of a quadrupole mass spectrometer. Electrons are emitted at the cathode and ionize gas molecules. Ions are separated in the rod system by an electric field (picture from Pfeiffer document).

charge. This produces a current which is converted in an output signal proportional to the ion current.

5.2.2 Mass spectrum analysis

The data acquisition and control of the mass spectrometer are made by computer with the software “Quadera®”. The acquisition is made in a mass range and at a speed defined by the user: typically we made two measurements for each point, one between 0 and 200 amu, and the second between 0 and 50 amu (to focus on the main components, see section 5.3). The acquisition speed was 500 ms/amu. Example spectra obtained are shown in Fig. 5.3.

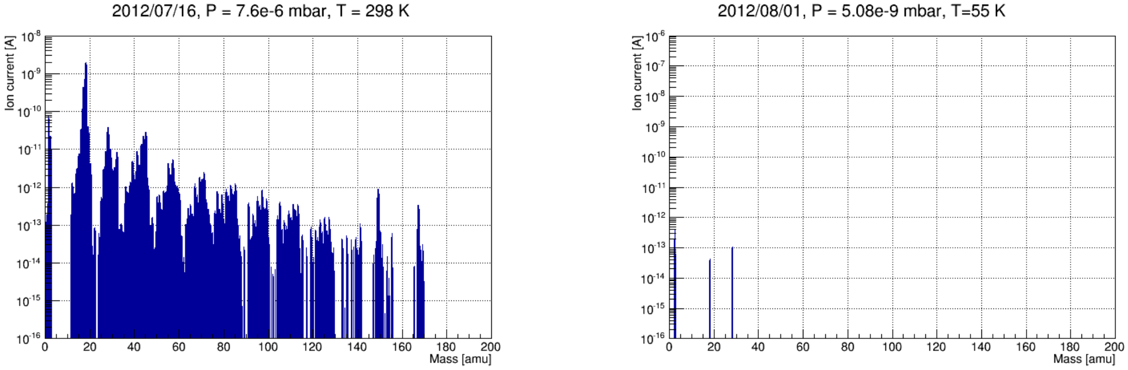

(a) Two days after starting the pumps. (b) After reaching stable low pressure and temperature.

Figure 5.3: Example of mass spectra measured inside *a*SPECT in 2012. The spectrometer was complete: electrodes system, uExB, cross-piece, bottom chamber.

Different mass spectra were measured at several pressures and then temperatures (while cooling down the cryostat). From the measured mass spectra, we observed the evolution of the rest gas composition: we focused on the main components as shown in Tab. 5.1.

Components	Detected ions	Corresponding mass [amu]
Hydrogen	H^+ ; $H_2{}^+$	1 ; 2
Nitrogen	N^+ ; $N_2{}^+$	14 ; 28
Oxygen	O^+ ; $O_2{}^+$	16 : 32
Water	OH^+, H_2O^+, H_3O^+	17, 18, 19
Carbon dioxide	$CO_2{}^+$	44

Table 5.1: Main components of the rest gas measured in the main volume of *a*SPECT.

5.3 Rest gas evolution in the main volume

In 2012, the first mass spectra measurements were coupled with the pressure measured by a sensor connected directly at the bottom flange. This was before the complete installation of *a*SPECT. Then for the comparison between the tests in 2012 and in 2013, the reference pressure is the one measured at the long tube mentioned in section 5.1. The temperature indicated on the graphs in the next paragraph was measured at the bottom of the bore tube. Some spikes appear in the pressure curves. They are related to the activation of the filament (tungsten) of the mass spectrometer.

5.3.1 Offline preparation zone

In order to have a reference, the first mass spectra were measured with an "empty" *a*SPECT, i.e. without electrodes system, detector mechanics, cross-piece, bottom chamber... We just tested the vacuum inside the cryostat alone and pumped by one turbo pump connected to a cascading one and the primary one. All the other flanges were closed (just one vacuum sensor connected to the bottom flange).

The pumps were started on 05/05/2012 in Fig. 5.4 (the evolution is divided in two graphs as there was a general power cut in the zone), and we note that the main gas components decreased as fast as the pressure. The cascading pump was activated on 05/30 (and after the general power cut, cascading was restarted on 06/04) improving the pumping efficiency and the evacuation of gas molecules as shown in Fig. 5.5(a). After 06/11, the pressure increased as we performed bake out of the flanges (using heating bands, see Appendix A). The quantity of gas molecules increased also, except for the oxygen which disappeared quickly after the activation of the cascading pump.

After reaching a quiet stabilized pressure, the cryocoolers were switched on. In Fig. 5.6, the pressure decreased with the temperature of the bore tube and also the main gas components. At the end, with a temperature of 55 K, the mass spectrometer only measured some hydrogen inside the main volume of *a*SPECT. But, in Fig. 5.7, when we stopped the cryocoolers and the temperature started to ramp up, water and nitrogen re-appeared but no oxygen or carbon dioxide. These two last mentioned molecules were mainly removed by the pumping efficiency. However for water and nitrogen, the interpretation was that they were frozen on the main bore tube surface (the melting temperature for water is 273.15 K, and for nitrogen, 63.15 K (be careful, the temperature on the graph is just related to the one inside the bore tube). The pressure was still low, about $3.3 \cdot 10^{-9}$ mbar and the influence on the vacuum composition was not so high (see Fig. 5.5(b)).

The same procedure was repeated after the installation of the electrodes system, uExB electrodes, bottom chamber, cross-piece... The spectrometer was complete but without the internal collimation system and the NMR electrodes. The pressure indicated is the one measured manually as there was a problem with computers: this explains the shape of the pressure curve on the following graphs. We started to pump on 07/23 with the turbo pump at the cross-piece and

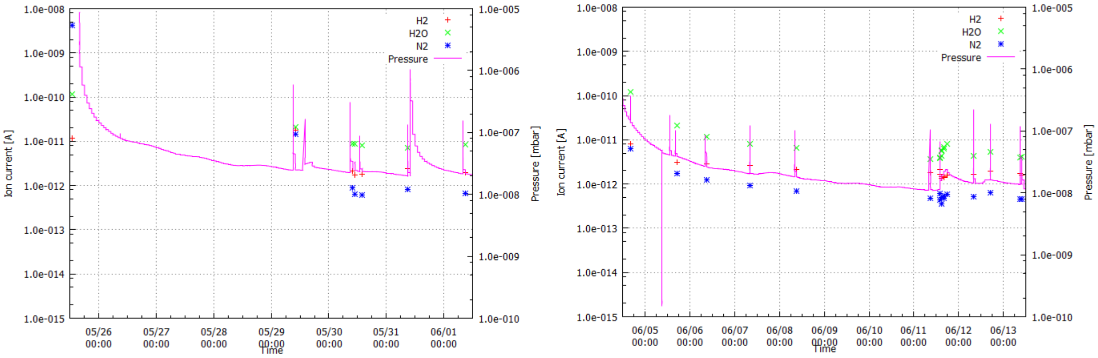

(a) H_2, H_2O, N_2

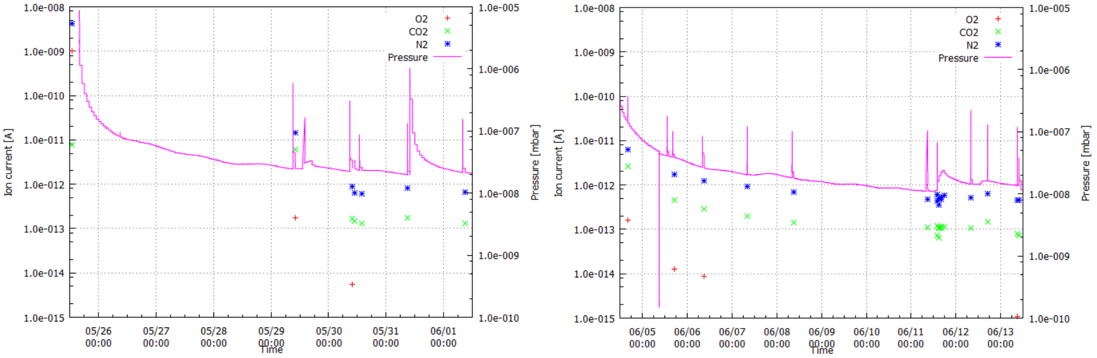

(b) O_2, CO_2

Figure 5.4: Evolution of vacuum and main components of the rest gas in "empty" *a*SPECT.

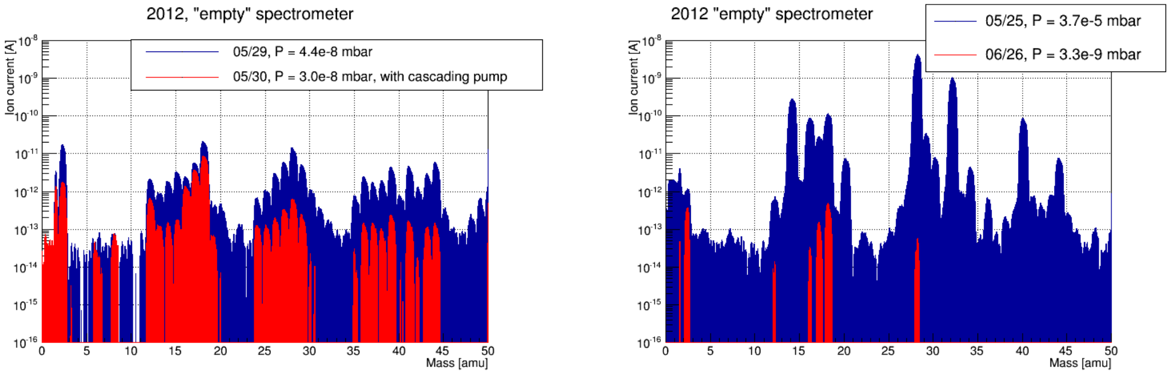

(a) Before and after the activation of the cascading pump.

(b) Beginning of the test and at the end for the same temperature

Figure 5.5: Mass spectra comparison.

with one turbo pump connected on the top aperture (at the detector mechanics place). In Fig. 5.8, we noted an increase of the pressure and the gas molecules presence on 07/24 afternoon when starting the outgasing of different parts (bottom chamber, cross-piece, side tubes). At the end of the bake-out process, the cryocoolers were switched on and the quantity of gas molecules decreased with the temperature (Fig. 5.9). After reaching the low temperature, only hydrogen, water and nitrogen are visible in the rest gas (Fig. 5.10).

According to the documentation of the mass spectrometer [67], we can calculate the partial

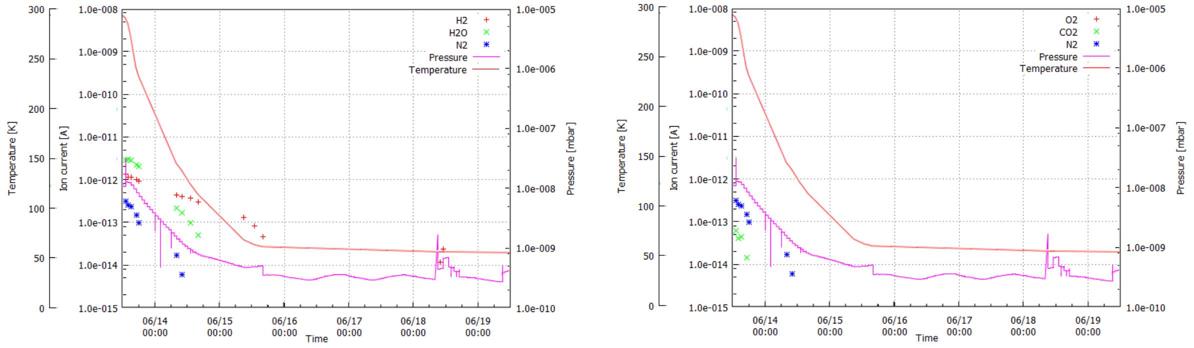

(a) H_2, H_2O, N_2 (b) O_2, CO_2

Figure 5.6: Evolution inside "empty" *a*SPECT while cooling down the cryostat.

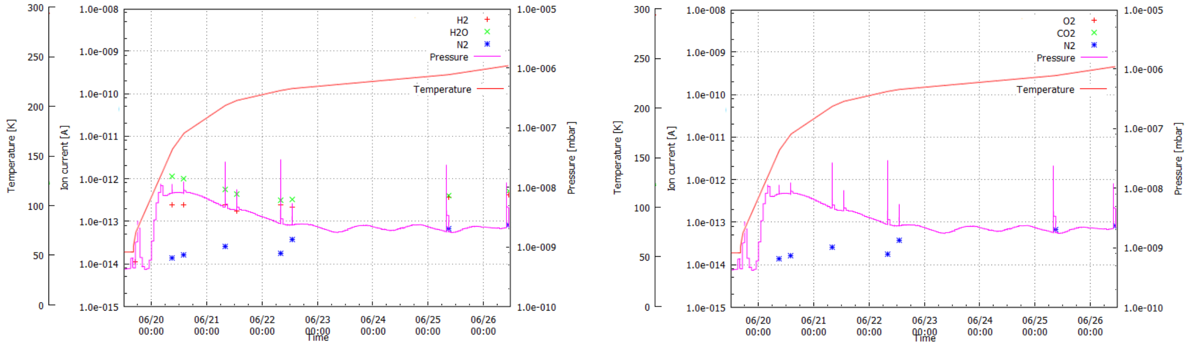

(a) H_2, H_2O, N_2 (b) O_2, CO_2

Figure 5.7: Evolution inside "empty" *a*SPECT while ramping up the temperature.

pressure of each component of the rest gas. The partial pressure of one component of a gas is the pressure that this component should have if it was the only one in the volume. So, the partial pressure p_i is calculated in mbar as follow:

$$p_i = \frac{I_i}{S_i} \tag{5.1}$$

where I_i is the ionic current measured in Ampere (A) for the component i, and S_i is the sensitivity for the corresponding gas (in A/mbar). The sensitivity is given in the documentation of the mass spectrometer and the ionic currents are measured from Fig. 5.10. The values and the calculated partial pressure for the main gas components are given in Tab. 5.2. Using the Dalton law about

Components	Sensitivity [A/mbar]	Ionic current [A]	Partial pressure [mbar]
H_2	$13 \cdot 10^{-5}$	$3.64 \cdot 10^{-13}$	$2.8 \cdot 10^{-9}$
H_2O	$20 \cdot 10^{-5}$	$8.84 \cdot 10^{-14}$	$4.42 \cdot 10^{-10}$
N_2	$20 \cdot 10^{-5}$	$1.02 \cdot 10^{-13}$	$5.1 \cdot 10^{-10}$

Table 5.2: Partial pressure of the main rest gas molecules still present in the volume of *a*SPECT after reaching $5.08 \cdot 10^{-9}$ mbar (at the referenced sensor) and low temperature. The sensitivities are given by the mass spectrometer documentation [67]. The ionic current are measured from Fig. 5.10.

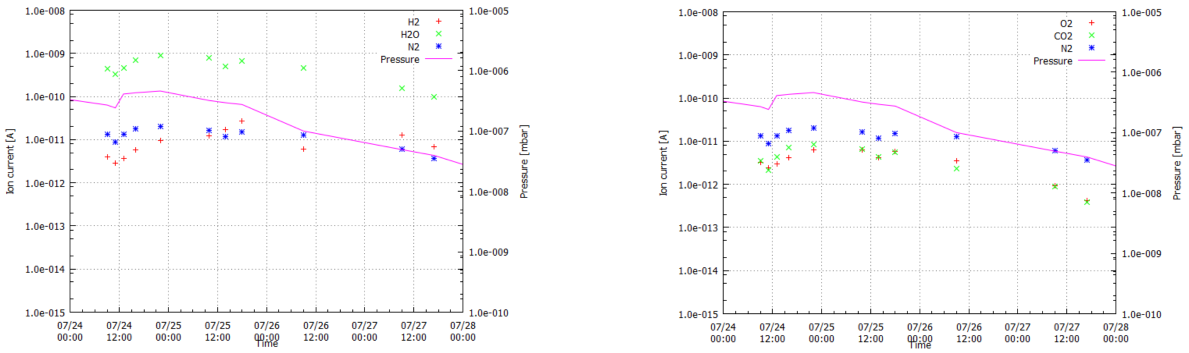

(a) H_2, H_2O, N_2 (b) O_2, CO_2

Figure 5.8: Evolution of vacuum and rest gas composition inside *a*SPECT with the electrodes system.

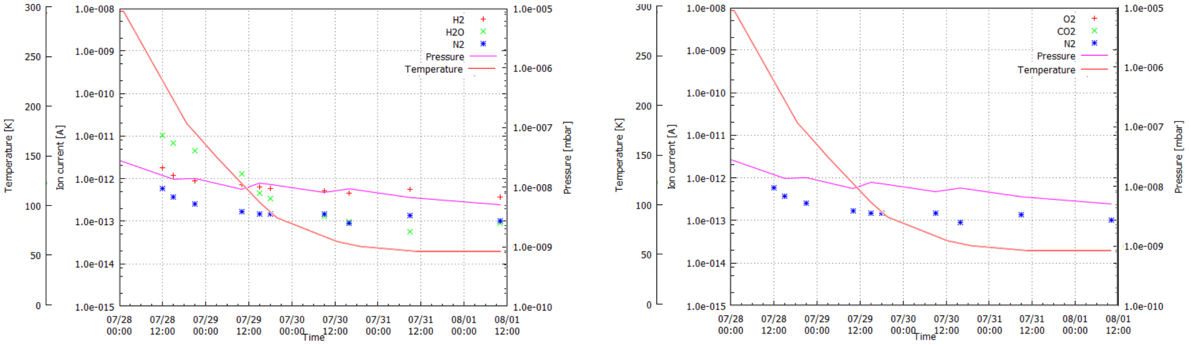

(a) H_2, H_2O, N_2 (b) O_2, CO_2

Figure 5.9: Evolution of vacuum and rest gas composition inside *a*SPECT with the electrodes system while cooling down the cryostat.

the fact that the total pressure of a gas is the sum of the partial pressures of each component of this gas, we can estimate the composition of the rest gas inside *a*SPECT (see Fig. 5.11). We continue with the ideal gas law and the temperature inside the bore tube $T = 60\,\mathrm{K}$ (value from the PhD thesis of Michaël Börg [9]). It is possible to estimate the volumetric concentration of each gas component i:

$$P \cdot V = n \cdot R \cdot T \quad \Rightarrow \quad C = \frac{n}{V} = \frac{P}{R \cdot T} \tag{5.2}$$

where P is the pressure in Pa ($1\,\mathrm{bar} = 10^5\,\mathrm{Pa}$), V is the volume containing the gas (in m^3), T is the temperature of the gas (in K), and $R = 8.31\,\mathrm{J/mol/K}$ is the constant of ideal gas. We obtained the following concentration for the main components at low pressure and low temperature:

- $C_{\mathrm{H_2}} = 5.61 \cdot 10^{-10}\,\mathrm{mol/m^3}$,
- $C_{\mathrm{H_2O}} = 8.86 \cdot 10^{-11}\,\mathrm{mol/m^3}$,
- $C_{\mathrm{N_2}} = 1.02 \cdot 10^{-10}\,\mathrm{mol/m^3}$.

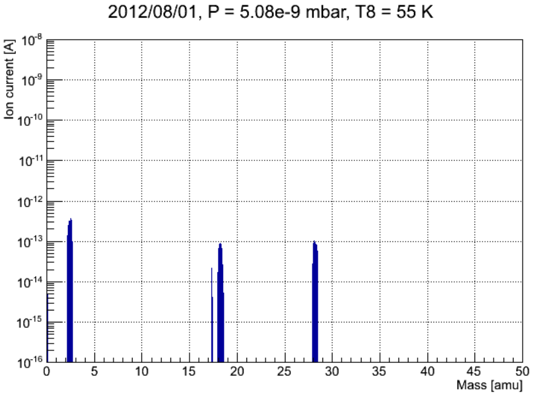

Figure 5.10: Mass spectrum measured at low pressure and low temperature in *a*SPECT (2012). We identified hydrogen (2 amu), water (17, 18 and 19 amu) and nitrogen (28 amu).

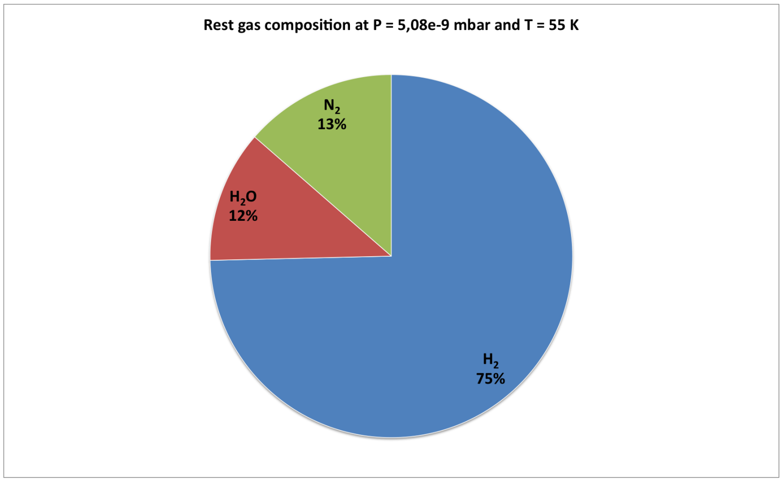

Figure 5.11: Composition of the rest gas inside *a*SPECT at low pressure and low temperature.

5.3.2 Before the beam-time at PF1b

A new beam time was dedicated to *a*SPECT in 2013 and the spectrometer was back to PF1b. After the installation, the mass spectrometer was again connected, but this time to the cross-piece (on a side port of the main volume) as shown in Fig. 5.12. In 2013, the spectrometer was in its complete configuration: entrance and exit windows, the new internal collimation system, the electrodes system with new components, new connectors for the uExB electrodes. We started to pump on 04/25 with the turbo pump at the cross-piece and the one on the top of the spectrometer. The cascading pump was activated on 05/02 and the shutter on the top aperture was closed on 05/03 and opened after: the pumping efficiency was ensured by one turbo pump (see Fig. 5.13). The spikes in pressure observed after the 05/03 were due to the activations of the internal getter pumps. On 04/30, we observed an influence on the gas molecules quantities due to the closure of the shutter at the cross-piece (only the turbo on the top was connected).

After the activation of the cryocoolers, the temperature decreased and also the gas molecules quantity (Fig. 5.14). However, this time more molecules stayed present in the rest gas at low pressure and low temperature. This could be explained by the technical differences of the spectrometer between 2012 and 2013 configuration. One of them was the installation of the new internal collimation system: the porosity of the material of this system could cause the

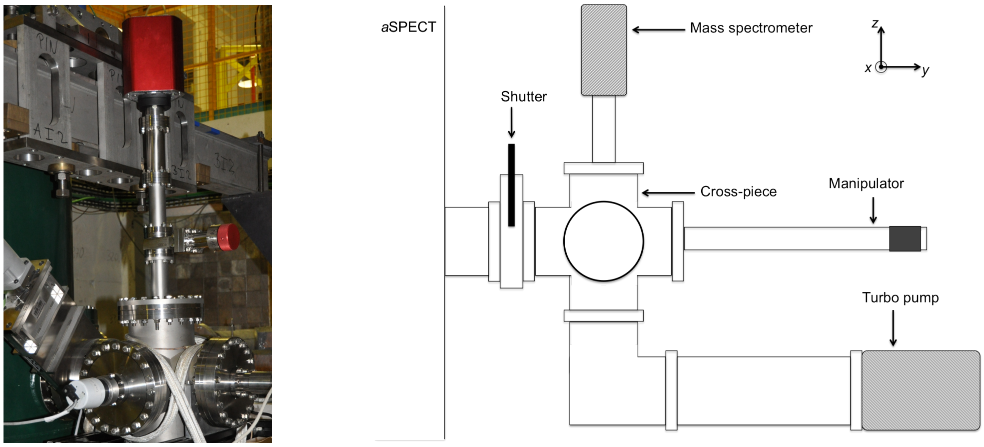

(a) Mass spectrometer in 2013.

(b) Sketch of the cross-piece on a side port of the spectrometer.

Figure 5.12: Mass spectrometer installed on the cross-piece in 2013. The cross-piece is separated from the main volume by a vacuum shutter.

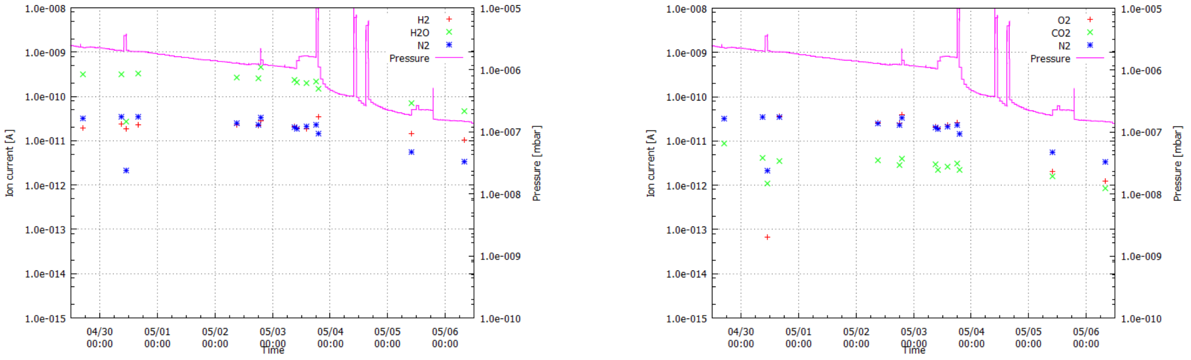

(a) H_2, H_2O, N_2

(b) O_2, CO_2

Figure 5.13: Evolution of main components of the rest gas inside "full" *a*SPECT systems installed at PF1b.

presence of gas molecules for a longer time in the main volume. With time, they were removed by pumping. From the last measurement with the mass spectrometer, we can deduce the partial pressure for the three main components considered in the analysis of 2012 (see Tab. 5.3).

Components	Sensitivity [A/mbar]	Ionic current [A]	Partial pressure [mbar]
H_2	$13 \cdot 10^{-5}$	$1.39 \cdot 10^{-12}$	$1.07 \cdot 10^{-8}$
H_2O	$20 \cdot 10^{-5}$	$6.19 \cdot 10^{-13}$	$3.10 \cdot 10^{-9}$
N_2	$20 \cdot 10^{-5}$	$3.39 \cdot 10^{-13}$	$1.70 \cdot 10^{-9}$

Table 5.3: Partial pressure of the main rest gas molecules still present in the volume of *a*SPECT after reaching $2.6 \cdot 10^{-8}$ mbar measured at the cross-piece ($4.0 \cdot 10^{-9}$ mbar at the referenced sensor) and low temperature. The sensitivities are given by the mass spectrometer documentation [67].

It is also important to note some differences between the measurements in 2012 and in 2013

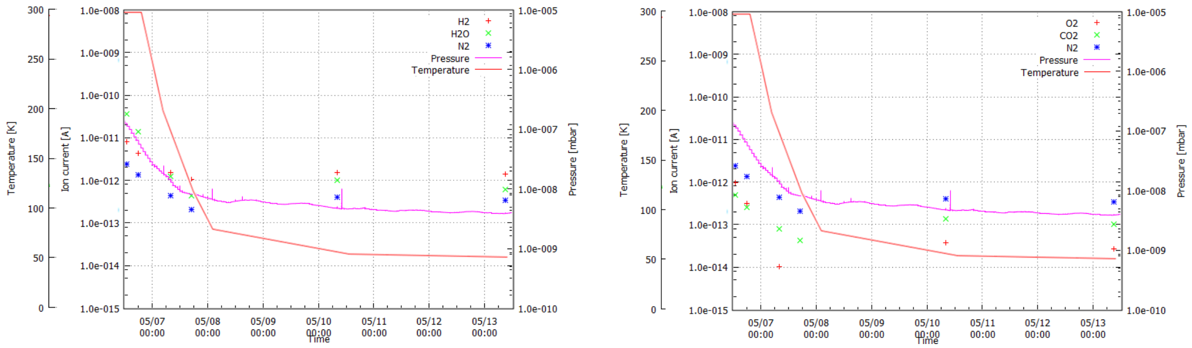

(a) H_2, H_2O, N_2 (b) O_2, CO_2

Figure 5.14: Evolution inside "full" *a*SPECT systems at PF1B while cooling down the cryostat.

for the mass spectra. This is probably related to the technical differences between those two measurements which are resumed in the following Tab. 5.4:

	2012	2013
Internal collimation system	without	new one
Electrodes system	re-coated	re-coated, new AP geometry, new Mirror electrode, e15 as a dipole
uExB electrodes	with	new connections with kapton cables
MaAlZn windows	without	with
NMR electrodes	without	with

Table 5.4: Technical differences between 2012 and 2013 for the spectrometer *a*SPECT.

5.4 Summary

The rest gas in operating conditions mainly consists of hydrogen, water and nitrogen. These molecules can be ionized (as there are detected by the mass spectrometer) and induce discharges by hurting electrodes surfaces or the detector. This last point is part of the background analysis detailed in Chapter 6.

In section 2.4.2, different kind of interactions with the rest gas molecules were presented. According to simulations from [48], a critical pressure was defined as the limit above which, the considered interaction process will induce a systematic effect on the coefficient a of $\delta a = 10^{-4}$ (see Tab. 2.2 and 2.3). The partial pressures for the main components of the rest gas were calculated from the mass spectra analysis and were found to be below the estimated critical pressures. Thus, the systematic effect induced on a should be $\delta a < 10^{-4}$.

When we made vacuum inside *a*SPECT, several leak tests were performed (as described in Appendix A). After connecting the leak tester to the main volume, some Helium was sprayed around the different flanges (connections between pieces). When all flanges are correctly fixed, the baseline read by the leak tester is at the order of $10^{-9}\,\text{mbar}\cdot\text{l/s}$ (connected to the main volume of the spectrometer).

Chapter 6

Background studies

Le bruit de fond est un effet systématique important qui doit être connu avec précision afin d'être soustrait aux données mesurées. Lors des tests hors faisceau en 2012, des mesures ont été réalisées avec différentes configurations et en absence de source ionisante interne (absence de neutron). Un bruit de fond "interne" lié au spectromètre a été mis en évidence : ions et rayons-X. Dans la configuration standard des électrodes et en présence d'un vide de l'ordre de 10^{-10} mbar, les simulations montrent que ce bruit de fond "interne" induit une dérive de l'ordre de 10^{-5} sur $\frac{\Delta a}{a}$. L'influence des électrons sur le bruit de fond a été testée en utilisant une source β (pastille d'or activée). En plus d'être détectés, les électrons ionisent le gaz résiduel engendrant une nouvelle composante du bruit de fond dont l'effet sur $\frac{\Delta a}{a}$ est de l'ordre de 10^{-4} . Les investigations se sont poursuivies dans les conditions du temps de faisceau en 2013. En présence du faisceau de neutron et en bloquant tous les protons, on mesure un taux de comptage avec une dépendance temporelle. L'analyse montre une décomposition de ce bruit de fond en une partie constante et une autre non-constante. Cette dernière composante présente aussi une dépendance sur la tension de la barrière de potentiel : après fermeture du faisceau, un taux de comptage "résiduel" est mesuré plus important pour les tensions élevées. Une analyse approfondie permet de modéliser le bruit de fond non-constant et d'appliquer une correction sur les données du spectre des protons. Une solution technique a été testée afin de réduire ce bruit de fond lors des mesures : la mise en place d'un champ électrique de dérive au-dessus de la barrière de potentiel.

6.1 Trap conditions in *a*SPECT

For a high precision measurement, the background has to be as low as possible and stable in time. Typically, the background count rate in the proton region was measured at the order around 5 Hz (dominated by the electrons from the decay), and it has to be known with an accuracy of 10 mHz in order to keep the systematic uncertainties of the coefficient a below $\frac{\Delta a}{a} = 0.1\%$ [9, 10]. Another condition for the background has to be known: its relation with the AP voltage U_{A}.

6.1.1 Electric and magnetic trapping

The magnetic and electric fields are complex and can form traps for the charged particles. These potential traps are shown in Fig. 6.1. Due to the retardation principle, protons with insufficient kinetic energy are trapped between the AP and the Mirror before their removal by the lExB. The depth of this trap depends on the voltage of the potential barrier. The traps at

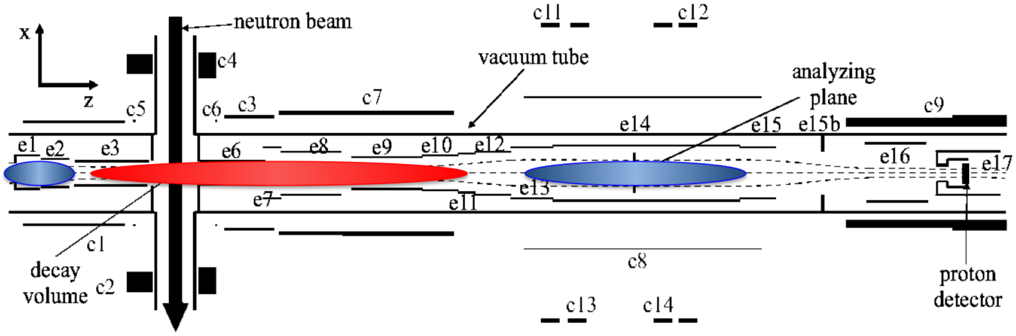

(a) Electric trapping. Traps for positively charged particles are indicated in red, and for negatively charged particles are indicated in blue.

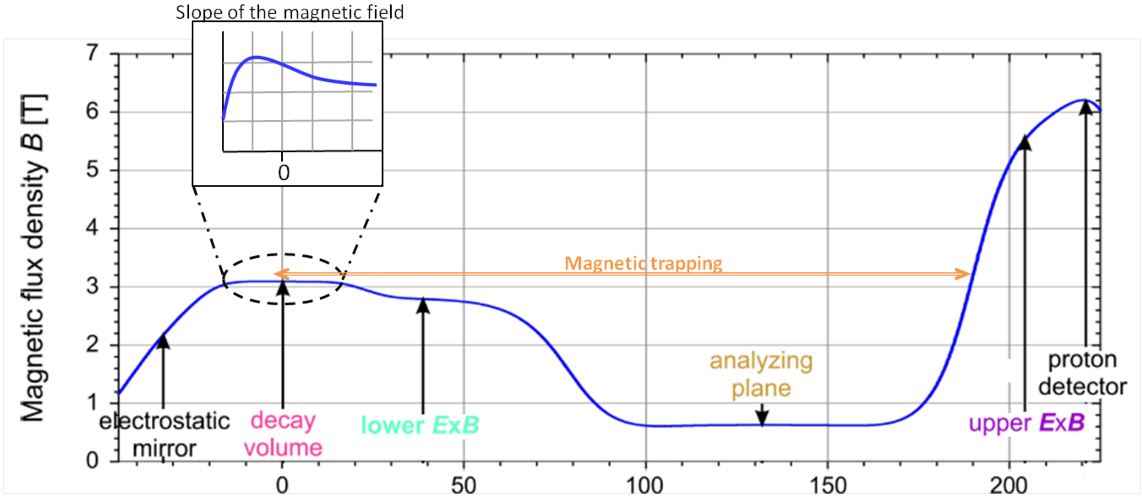

(b) Magnetic trapping. A slope of the magnetic field is created in the DV with a maximum below this region. This ensures that protons leave the DV quickly and avoids traps due to local minima in a constant field. However, a magnetic trap between the field maximum below the DV and the corresponding field close to the detector is found.

Figure 6.1: Potential traps in the spectrometer *a*SPECT.

the AP are only a few hundred volts deep. At the mirror electrode, a wire system was installed to prevent electron trapping. The decay electrons are not trapped electrically, but they can ionize the rest gas molecules (see Chapter 5): creation of ions and secondary electrons. However, they can be trapped by the magnetic mirror effect (for electrons with large emission angles, see Chapter 2) as shown in Fig. 6.1(b).

6.1.2 Count rate instabilities

In 2011, independently of the electrode configuration, a discharge effect visible in the count rate was observed by playing with the AP voltage (see Fig. 6.2). Without the neutron beam (Fig. 6.2(a)), we started a measurement with $U_{\mathrm{A}} = 0\,\mathrm{V}$. The potential barrier was then ramped up to 780 V. About 100 second later, the count rate started to increase slightly. The AP was ramped down to 0 V (at second 140). This resulted in a huge increase in count rate followed by a quick decrease after reaching the 0 V. The same phenomenon was observed with the neutron beam (Fig. 6.2(b)). As before, the count rate started to increase about 60 seconds after setting the AP at 780 V. And, a big increase was measured when ramping the AP to 0 V. The main

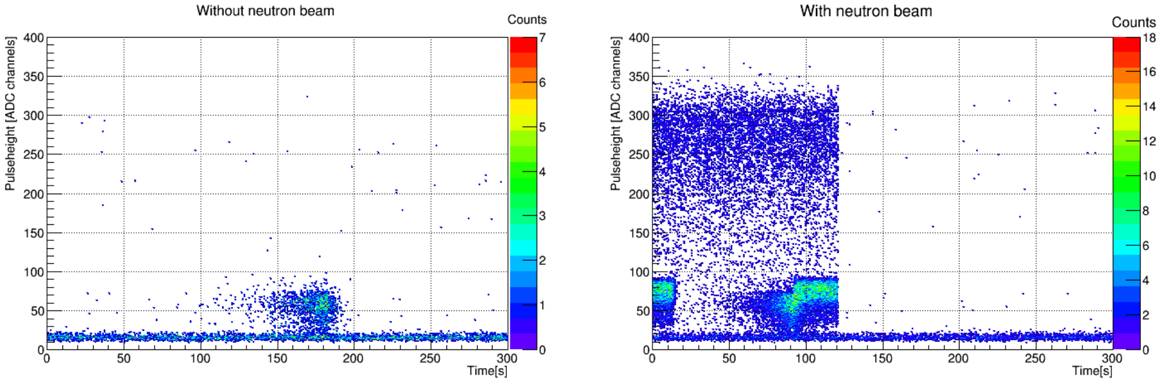

(a) The AP is at 0 V at second 175.

(b) The AP is ramped to 780 V at second 10, and to 0 V at second 90. The shutter is closed at second 120.

Figure 6.2: Instabilities measured in 2011. Pulseheight versus time, for AP set at 780 V.

influence of this effect was observed in the proton region, defined in the range ADC channels [30-150], as shown in Fig. 6.3. These tests show that particles can be trapped in the AP and

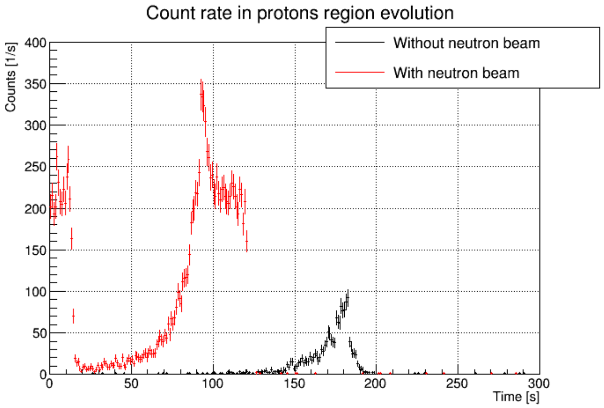

Figure 6.3: Instabilities in 2011. Time evolution of the count rate in the proton region for the measurement with and without neutron beam, and the AP at 780 V. Projection from Fig. 6.2.

these traps can empty inducing a discharge, even without neutron decay products. Hence there was another source of the particles inside the spectrometer, which might be related to the quality of the vacuum and surface properties of the electrodes. To investigate this effect, several test measurements were performed in 2012 without neutron beam, and the results are presented in section 6.2.

6.1.3 Tests of stability

The measurement structure described in section 4.3.1 is made to reduce the risk of discharge described above. In 2011, the cycle was done with the neutron shutter opened for 20 s (see Fig. 6.4). The first aim of the parameters optimization is to obtain a count rate stable in time for each AP voltage when the neutron shutter is open. This stability test can be done using the χ^2 test. The χ^2 test is very useful as it indicates the deviation of the observed data from an expected distribution [54, 65]. The mathematical formula to calculate the χ^2 value for a data

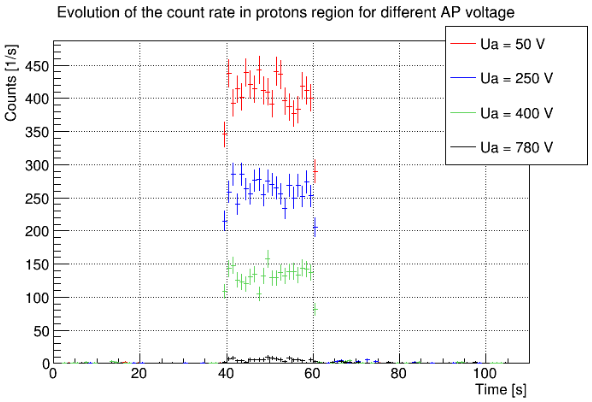

Figure 6.4: Example of measurement with different AP voltages during the beam time of 2011. Evolution of the count rate measured in the proton region: ramp up AP to U_A at second 10, open neutron shutter 5 s after stabilization of AP for 20 seconds, ramp down AP to 0 V at second 70. Measurement with Det-HV at -15 kV, uExB at -3|-3 kV, lExB at -100|0 V, and the Mirror on.

set $x_i = \{x_1, x_2, ..., x_k\}$ is expressed as following:

$$\chi^2 = \sum_{i=1}^{k} \frac{(x_i - \mu_i)^2}{\sigma_i^2}, \tag{6.1}$$

where μ_i are the expected values from the initial hypothesis and σ_i are the standard deviations. In the ideal case of only statistical fluctuations and in the limit of infinite measurements, the χ^2 are distributed with:

$$f(x,\nu) = \frac{(\frac{x}{2})^{(\nu/2)} \exp(-\nu/2)}{\Gamma(\nu/2)}, \tag{6.2}$$

with $\Gamma(\nu/2)$, the gamma function, x the value of χ^2 and ν the number of degrees of freedom.

The data analysis is mainly done using C++ programs with ROOT tools. We fit the count rate in the proton region with neutron shutter open. As the count rate is expected to be stable in time, the fit was done with a constant function for each measurement file. The constant parameter and the χ^2 of the fit result were extracted to plot the distributions for each AP voltage (see Fig. 6.5). The distributions of the constant fit parameter should be Gaussian: the count rate was stable from one file to the other for a given AP voltage. The χ^2 distributions for each AP voltage are compatible to the theoretical one obtained for the same degree of freedom in the case of lower AP voltages: for higher voltages, as for example 780 V shown in Fig. 6.5(c), the count rate evolution during shutter opened can not be approximated by a constant fit. This implies that for higher AP voltages, another process should get involved during measurement with the neutron shutter opened (see details in section 6.5).

Instability was also observed for the count rate evolution after closing the neutron shutter. This instability was found to be related to the AP voltage. We observed the evolution of the count rate at the beginning of the measurement (i.e., before opening the neutron shutter) and the one at the end of the measurement (i.e., after the interval with the neutron shutter opened). The evolutions shown in Fig. 6.6, were both measured in the proton region and without neutron beam. In the first part of the measurement (Fig. 6.6(a)), when the AP was ramped from 0 V to U_A, we observed no effect on the count rate which stayed stable (see section 6.2 for this component of the background). However, in the last part of the measurement (Fig. 6.6(b)), we noted differences in the count rate for the different AP voltages. When the AP was ramped from

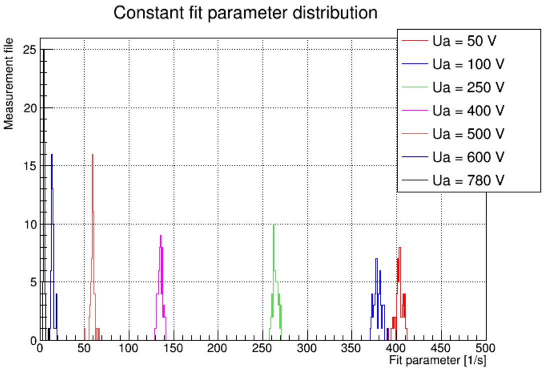

(a) Distribution of the constant parameter for the different AP voltages.

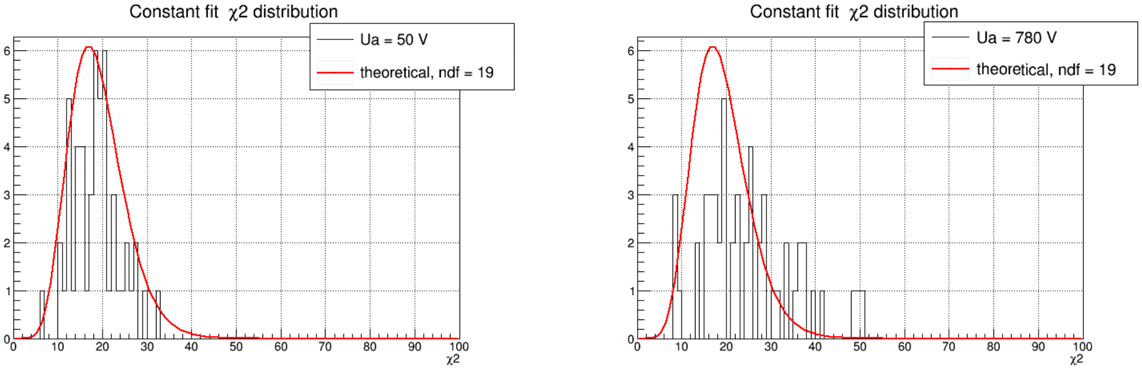

(b) χ^2 distribution for $U_\mathrm{A} = 50\,\mathrm{V}$ (number of degrees of freedom, ndf, is 19).

(c) χ^2 distribution for $U_\mathrm{A} = 780\,\mathrm{V}$ (number of degrees of freedom, ndf, is 19).

Figure 6.5: Stability test of the count rate in the proton region using a constant fit when neutron shutter is open. Continuous measurement made in 2011 during 2.6 hours.

U_A to 0 V, the count rate decreased and went back to the level measured in the beginning of the measurement. This effect is more visible for higher AP voltages and indicates the existence of an AP dependent background during the measurements (see results in section 6.5).

6.1.4 The lExB scan

The electrodes lExB are used to remove particles trapped between the AP and the DV. The following results correspond to the measurements in 2013. This trapping effect is investigated by testing several configurations for the dipole as shown in Fig. 6.7. The impact of the created electric field was investigated by setting the AP at 780 V in order to find the configuration which reduced the background best. The count rate was found to be lower for about 200 V potential difference between the electrodes, for the lExB configurations $-1| - 200\,\mathrm{V}$ and $-200| - 1\,\mathrm{V}$ by regarding the two pads. This difference between the two pads can be understood with the misalignment of the detector shown in section 4.4.2. The pad related to the channel 19 (not shown in figure) was placed intentionally in the projection of an electrode (see section 6.2.2): the count rate was measured between 7.3-7.5 s^{-1} for the configurations from $-50| - 100\,\mathrm{V}$ to $-200| - 1\,\mathrm{V}$. The count rate increased to 9.2 s^{-1} for lExB $= -500| - 1\,\mathrm{V}$, and to 15.2 s^{-1} for lExB $= -1000| - 50\,\mathrm{V}$. So, the orientation and strength of the electric field in the lExB electrodes are important as the effects induced also depend on the position of the detector.

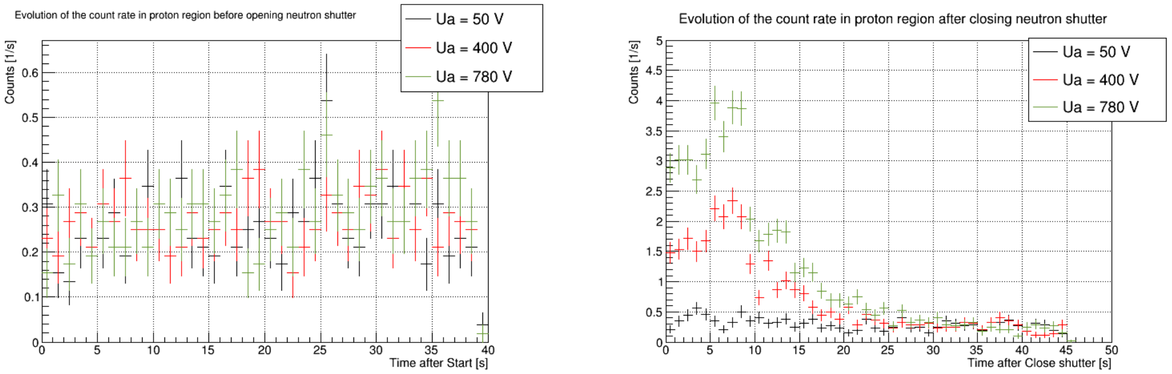

(a) Before opening the neutron shutter. The AP was ramped up to U_A after second 10.

(b) After closing the neutron shutter. The AP started to ramp from U_A to 0 V after second 5.

Figure 6.6: Evolution of the count rate in the proton region with neutron shutter closed. These graphs are mean values over one continuous measurement (about 35 min per AP voltage in the considered periods).

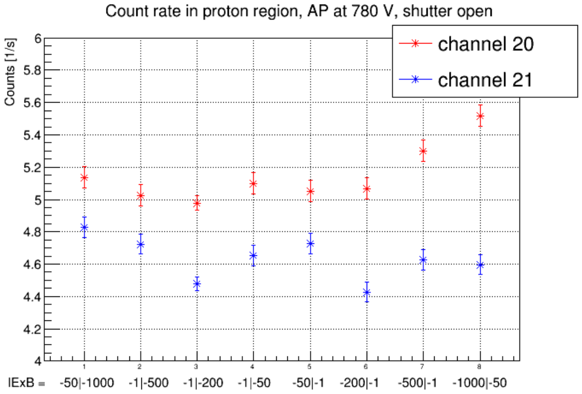

Figure 6.7: Influence of the lExB configuration on the count rate measured in the proton region with AP at 780 V and shutter open, in 2013. Measurement time per point was 800 s.

6.2 The spectrometer-related background

In 2012, we performed test measurements with the spectrometer installed out of the neutron beam line. This highlighted details about the background: even without ionizing particles from neutron decay inside the main volume, we detected count rate in the proton region. This represents an "internal" background which is related to the technical aspects of the spectrometer as described in the following sub-sections. The same measurements were conducted with the final setup of the beam time of 2013 before the reactor starts.

6.2.1 The offline measurements

The measurements without the neutron beam highlighted details in the measured spectra. Two peaks appeared in the proton region (see Fig. 6.8). Their position (found with a gaussian fit: ADC channel 77.3 for the 1^{st} and ADC channel 101.9 for the 2^{nd}) is slightly below the one of the proton peak observed in 2011 (at ADC channel 119.3 for the mean position measured with the same settings). In order to identify the source of these peaks, we measured with different

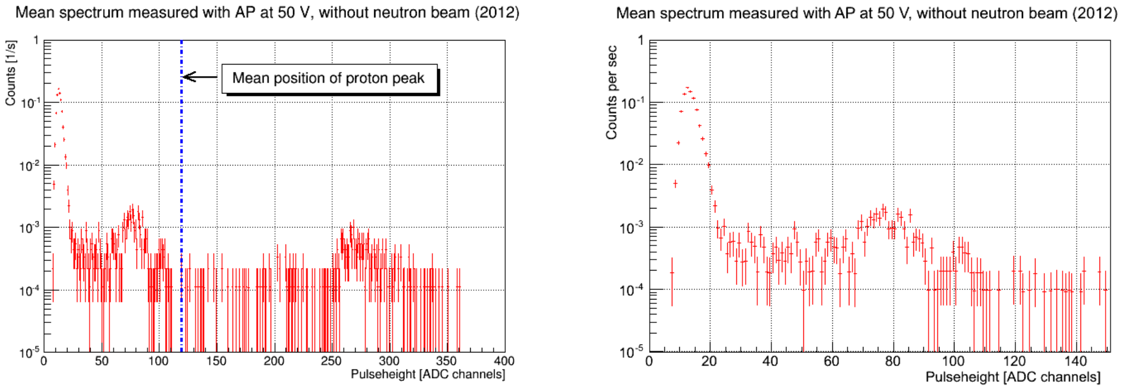

(a) Full range spectrum measured with the AP at 50 V. The mean position of the proton peak is indicated for reference. The "peak" in the electron region is induced by cosmic events.

(b) Zoom on the proton region.

Figure 6.8: Spectrum measured without neutron beam in 2012 with Det-HV at -15 kV, uExB $= -3| - 3\,\mathrm{kV}$, lExB $= 0| - 200\,\mathrm{V}$ and with Mirror. The measurement time was 2 hours and 30 minutes

acceleration voltages (Det-HV) at the detector electrode. In Fig. 6.9, the position of the first

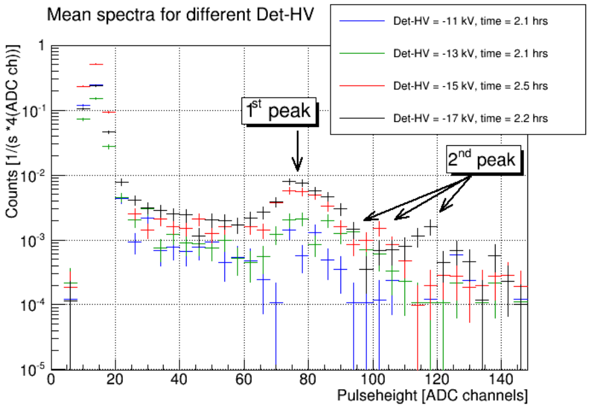

Figure 6.9: Spectra measured with different acceleration voltages Det-HV (zoom on the proton region). Rebinning with a factor 4.

peak did not change with the acceleration potential but it was influenced in terms of count rate (it decreased for low voltage). The second peak was mostly influenced in terms of energy: the position of this peak moved to low energy with decreasing acceleration potential (all is resumed in Fig. 6.10). The hypothesis for the first peak is related to the original function of the detector: the **X-ray** detection. By electron impact, X-rays can be generated via Bremsstrahlung (as in a standard X-ray tube) or via removal of electrons from shell of material atoms. In the case of Bremsstrahlung, the energy of X-rays changes with the energy of electrons: this is not what is observed during tests (for both two peaks). So, in our case, the X-rays are emitted via the second process: characteristic energy of X-rays for de-excitation of atoms. The impact electrons can be emitted by field emission: induced by the electrostatic field present in *a*SPECT. In this process, the number of generated electrons is proportional to the electric field value squared

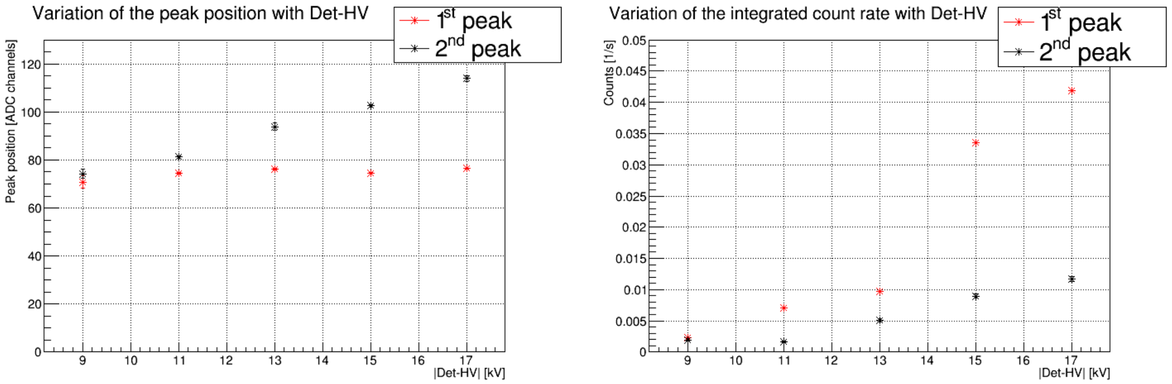

(a) Peak position (i.e. detected energy) variation.

(b) Count rate variation.

Figure 6.10: Behavior of the two peaks in the proton region for different acceleration voltages Det-HV.

(the electronic emission current is $j(E) \propto |E|^2$ according the Fowler-Nordheim equation[1] [68]). The X-ray energies are related to the nature of the material of the electrodes. The electrode system is made of copper and gold coated. The uExB electrodes and the one for the acceleration potential are made of stainless steel (alloy of iron and carbon with a small amount of chromium to give the stainless property). These materials can emit X-rays by electron impact (see Tab. 6.1). The position of the peak is extracted using a Gaussian fit with ROOT. By regarding a measurement with higher statistics, we found that the peak of X-rays is in fact a double peak (see Fig. 6.11). Using the equation of calibration eq. (3.2) for the detection chain, we calculated the corresponding detected energy for X-rays double peak: 5.52(13) keV and 6.09(14) keV (statistical error only). Thus, according to the Tab. 6.1, the detected X-rays are emitted from the stainless steel of the electrodes (these peaks correspond to the one from Cr and Fe respectively). The difference between the experimental values and the one in the table is due to the temperature effect on the electronics (see section 3.5.2). In the following analysis, we consider the region of the X-rays as the one including the double peak.

Material	X-ray energies [keV]							
	$K_{\alpha,1}$	$K_{\alpha,2}$	$K_{\beta,1}$	$L_{\alpha,1}$	$L_{\alpha,2}$	$L_{\beta,1}$	$L_{\beta,2}$	$L_{\gamma,1}$
Iron, Fe	6.40384	6.39084	7.05798	0.705	0.705	0.7185	-	-
Carbon, C	0.277	-	-	-	-	-	-	-
Chromium, Cr	5.41472	5.405509	5.94671	0.5728	0.5728	0.5828	-	-
Copper, Cu	8.04778	8.02783	8.90529	0.9297	0.9297	0.9498	-	-
Gold, Au	68.8037	66.9895	77.984	9.7133	9.6280	11.4423	11.5847	13.3817

Table 6.1: Energies of principal K- and L-lines X-ray emission for the material of the electrodes inside *a*SPECT [59].

As the second peak was mainly influenced in terms of energy, the hypothesis is that it is induced by **ions**. According to mass spectrometer measurements (see Chapter 5), we know that the rest gas inside *a*SPECT mainly consists of hydrogen, water and nitrogen. These particles, if ionized, are accelerated by the potential and then detected. From the measurement with

---

[1] Fowler-Nordheim equation: $j(E) = K_1 \frac{|E|^2}{\Phi} \exp(-K_2 \frac{\Phi^{3/2}}{|E|})$ where E is the electric field, K_1, K_2 are parameters related to the material and the field geometry and Φ is the work function.

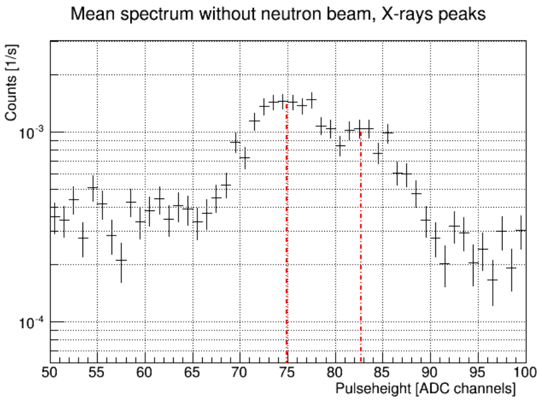

Figure 6.11: Zoom on the peak of X-rays from a measurement with Det-HV =-15 kV, uExB = $-3|-3\,\mathrm{kV}$, lExB = $0|-200\,\mathrm{V}$ and with Mirror. Measurement time was 21 hours. This is a double peak for the X-rays: positioned at ADC channel 74.95(37) and at ADC channel 82.70(45).

Det-HV at -15 kV, we calculate that ions have an energy of about 12 keV which is below the one of protons in the same settings. One possible explanation for this lower energy in the case of hydrogen would be that the ions are created at a lower potential difference to the detector than the DV. However, the corresponding volume is rather small compared to the spectrometer. A trap would be needed in this region to explain the observations. Therefore in the case of heavier ions (nitrogen, water), they will loose more energy in the dead layer of the detector than protons (according to previous simulations in [8], nitrogen ions with a kinetic energy of 15 keV would loose about 11 keV). One possible source for ionization, without the neutron beam, was mentioned above: electrons from field emission. Other processes can occur to ionize the rest gas molecules, such as thermal ionization (or surface ionization). In this case, a neutral molecule can lose its peripheral electron by hurting the material of the surface with a work function higher than the ionization energy of the molecule: for hydrogen this energy is 15.4 eV, for water it is 12.6 eV and for nitrogen it is 15.5 eV. The work function of the gold of the electrode system is at the order of 5 eV (value from discussion with the group). So this process cannot occur in *a*SPECT. This ion part of the background is related to the vacuum condition (see section 6.2.3).

Within the same electrodes configuration (with Det-HV at -15 kV), the proton count rate during the beam time of 2011 and the one of 2013 was measured at about 440 s^{-1}. In 2012, after reaching stabilization (see section 6.2.3), the X-ray count rate was about $3 \cdot 10^{-2}\,\mathrm{s}^{-1}$, and the ion count rate was about $3 \cdot 10^{-3}\,\mathrm{s}^{-1}$. These values give the orders of magnitude of these peaks for the "internal" background measured in 2012. They were also measured in 2013 before the reactor started. In 2013, we noted that the count rate in the proton region was higher than in 2012: the ion count rate was about $5 \cdot 10^{-3}\,\mathrm{s}^{-1}$ in 2013. This difference could be explained in the same way as for the difference of the mass spectra in Chapter 5: the technical differences between 2012 and 2013, in Tab. 5.4, due to the improvements described previously. However, the following conclusions are effective for both measurements in 2012 and in 2013 concerning the "internal" background.

6.2.2 The dependence on the configuration of the electrodes

The "internal" background was identified and it was found stable in time ten days after the insertion of the detector in the main volume (see Fig. 6.17 in section 6.2.3). The second step now is to find any dependence on the electrodes settings. We performed several measurements with a similar structure as during the beam time: continuous measurement containing measurement files taken at different AP voltages. First of all, as shown in Fig. 6.12, the discharges observed

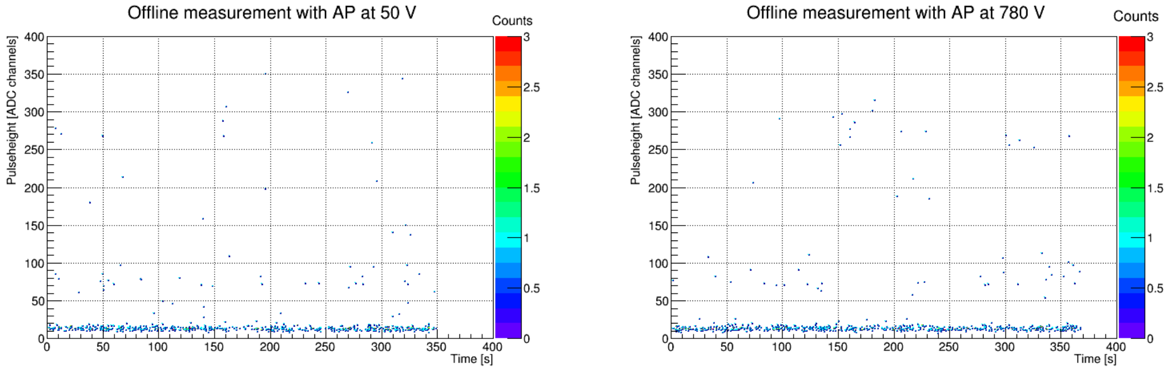

(a) Ramp AP to 50 V at second 10, and to 0 V at second 320.

(b) Ramp AP to 780 V at second 10, and to 0 V at second 320.

Figure 6.12: Offline measurements, eight days after insertion of the detector in 2012. Example of one file measurement for the two AP voltages, with Det-HV = -15 kV, uExB = $-3| - 3\,\mathrm{kV}$, lExB = $-50| - 1000\,\mathrm{V}$ and with Mirror

during the beam time of 2011 with the neutron shutter closed (see Fig. 6.2), were not observed anymore during the offline tests.

The measurement structure, without the neutron beam, was decided as follows: the AP is ramped from 0 to U_A 10 seconds after the acquisition started, when the AP voltage is stabilized the acquisition is continued for 300 seconds before starting to ramp down the AP to 0 V, and the measurement stopped 10 seconds after reaching the 0 V. I focused the analysis on the count rate acquired during the period with the AP stabilized at U_A (300 s as measurement time for this part).

The electric field generated by the lExB electrodes is one of the adjustable parameters (see section 6.1.4). It is important to know if the configuration of these electrodes has an influence on the “internal” background. In 2012, we tested three settings for the lExB: 0|-200 V, -50|-1000 V, and -425|-625 V. In Fig. 6.13, the count rate integrated on the X-ray peak and the one integrated

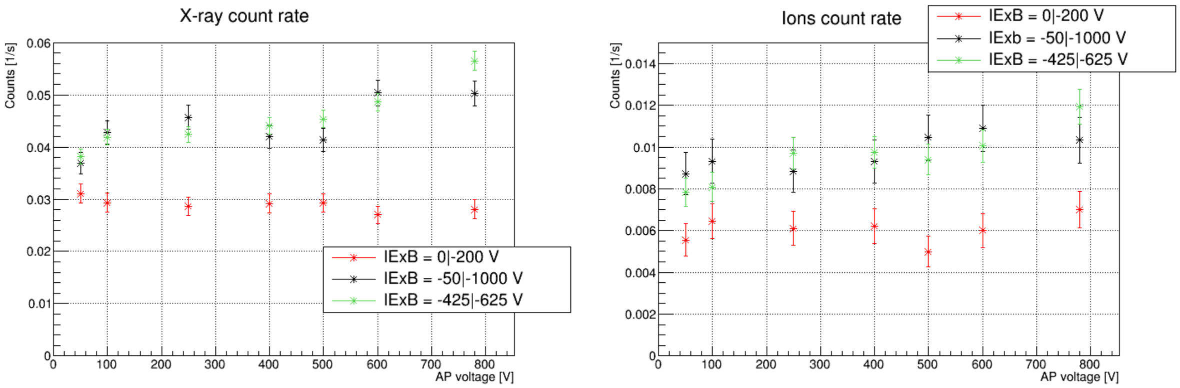

(a) X-ray count rate.

(b) Ions count rate.

Figure 6.13: Count rate dependence on the AP voltage for different lExB configurations in 2012. Continuous measurement during 21.2 hours for 0|-200 V, during 20.5 hours for -50|-100 V, and during 40.3 hours for -425|-625 V.

on the ion peak have a negligible AP dependence for lExB in the standard configuration defined by 0|-200 V. The configuration -425|-625 V was chosen as it has the same potential difference as with 0|-200 V and the same mean potential as with -50|-1000 V. The influence of this configuration is close to the one of the -50 |-1000 V configuration. So, the “internal” background is more influenced by the mean potential generated at the lExB electrodes than by the potential difference: the mean potential corresponds to a trap depth (see section 6.1.1). These electrodes must not be positive compared to the DV to avoid a mirror for protons. Therefore, lExB with 0 V trap depth (e.g. -100|+100 V) is not possible. We also performed measurements with lower field (as shown in section 6.1.4). The best results were obtained for lExB = 0|-200 V or -200|0 V.

The electrodes uExB are also adjustable as they create an electric field to align the proton beam onto the detector during the beam time. So we tested two configurations for the uExB staying in the standard one for the lExB (i.e., 0|-200 V). From Fig. 6.14, we observe that the configuration of the uExB electrodes has a negligible influence on the “internal” background. The electric field at these electrodes seems to not participate highly in the X-ray emission (see section 6.2.1). The main influence on the X-ray production thus comes from the acceleration potential at the detector. The observation is similar concerning the ion part which was not highly influenced by the potential at the uExB.

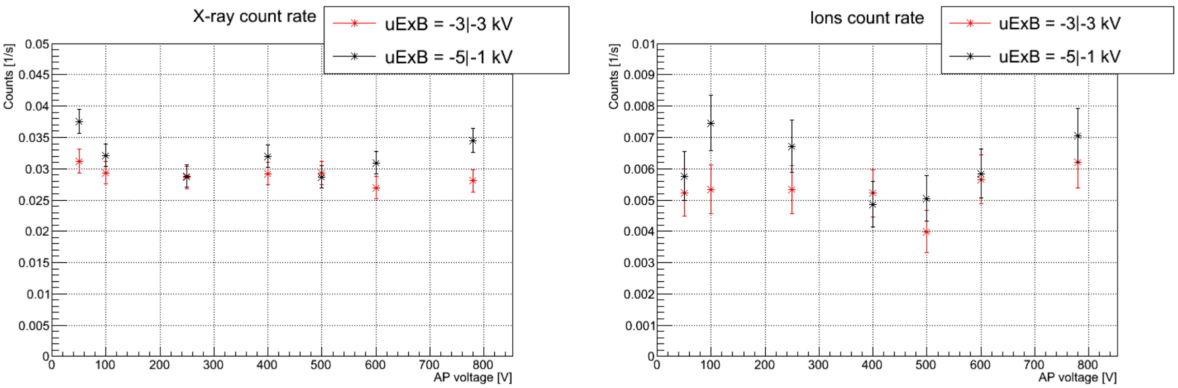

(a) X-ray count rate.

(b) Ions count rate.

Figure 6.14: Count rate dependence on the AP voltage for different uExB configurations in 2012. These measurements were made with the standard lExB = 0|-200 V. Measurement time of 21.2 hours with uExB at -3|-3 kV, and of 19.3 hours with uExB at -5|-1 kV.

For the beam time of 2013, the detector was aligned intentionally such that pad of channel 19 sees the electrode system, in order to be sure that the others do not (see Fig. 6.15(a)). As shown in Fig. 6.15(b), the ”internal” background count rate was higher than for the two other pads. We observed also during the beam time a slightly lower decay product rate on channel 19 and substantially higher proton background which is an indication that the protons could be liberated from H_2O sitting on the surfaces of the electrodes projected onto this detector pad.

6.2.3 The dependence on the vacuum conditions

The rest gas molecules are responsible for one component of the “internal” background: the ions. Thus, the quality of the vacuum should influence the ion count rate. We deteriorated the vacuum inside the main volume, increasing the pressure by a factor 2 (see Fig. 6.16). For this, we reduced the speed of one turbo pump(“stand by” mode) and heated the cross-piece. The

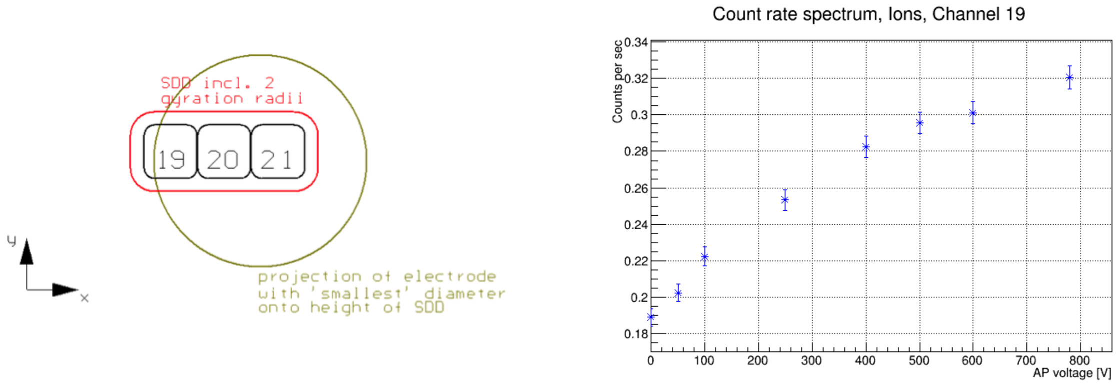

(a) Projection of the detector position. The pad related to channel 19 "sees" one electrode. This picture is from a discussion with the colleagues of the *a*SPECT group.

(b) Ion count rate measured on channel 19 in 2013. Continuous measurement with the reactor off during 14 hours.

Figure 6.15: Detector position for the beam time in 2013.

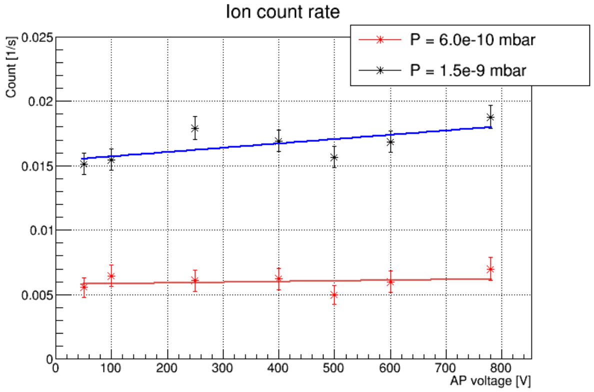

Figure 6.16: Ion count rate dependence on the AP voltage for the same lExB configuration but at two different pressures. Measurement time of 21.2 hours at $6.0 \cdot 10^{-10}$ mbar, and of 55 hours at $1.5 \cdot 10^{-9}$ mbar. A linear fit is applied for both configurations. At $6.0 \cdot 10^{-10}$ mbar, the slope is $5.3(10.3) \cdot 10^{-7}\,\mathrm{s}^{-1}\mathrm{V}^{-1}$, and at $1.5 \cdot 10^{-9}$ mbar, it is $3.4(1.3) \cdot 10^{-6}\,\mathrm{s}^{-1}\mathrm{V}^{-1}$.

count rate of ions was influenced by this effect: it increased by a factor two. And we noted that the AP dependence increased significantly.

Due to this vacuum dependence, the count rate of the "internal" background has a partial time dependence. In Fig. 6.17, we see that the count rate in the proton region has a time dependence since the insertion of the detector inside the main volume of *a*SPECT. Just to remind this part of the procedure: the vacuum is first made in the main volume and in the detector mechanics but independently as these two volumes are separated by a shutter. When the two vacua are at a stable low pressure, the shutter is opened and the detector is moved down to its position in the main volume. Some more rest gas molecules are added to the main volume (see the pressure evolution in Appendix A) at this moment and with the first high voltage tests, frozen molecules can be removed from the surfaces. This is an explanation for the decreasing count rate in time. Then, it was quite stabilized about ten days after the insertion of the detector.

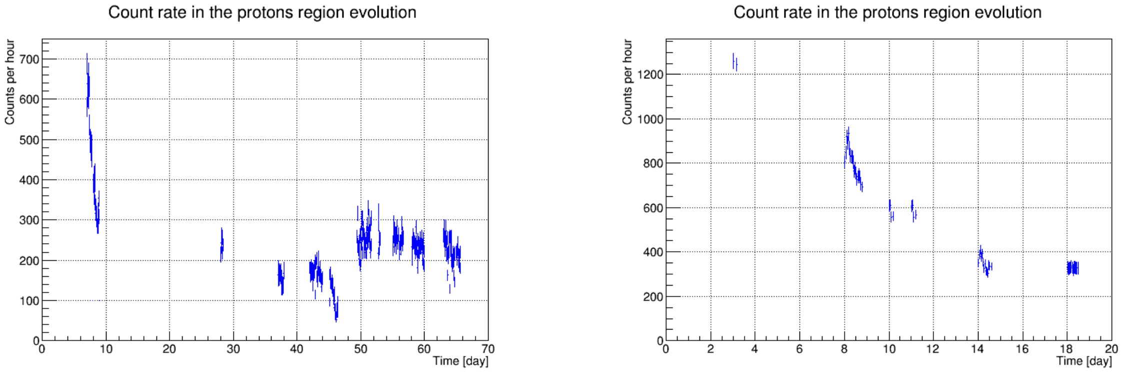

(a) Offline measurements in 2012. (b) Measurement before the reactor restarted in 2013.

Figure 6.17: Time evolution of the count rate in the proton region since the insertion of the detector inside the main volume (i.e., day 0).

6.2.4 The impact on the coefficient a

In the standard configuration for the electrodes and in stable good vacuum condition, the “internal” background in the proton region is stable with a negligible AP dependence. In order to quantify the influence of this background on the coefficient a, we used a proton spectrum simulated using the eq. (1.25) with the actual world average value $a = -0.103$ (see Fig. 6.18). Then, we used the fit function (4.3), plus an offset to assume a constant background at 780 V, to extract the coefficient a and its accuracy. The same procedure is applied on the simulated proton spectrum plus the contribution of the “internal” background integrated on the proton region. To obtain this contribution, the AP dependence is modeled via a linear fit function and the obtained count rates are normalized to be added to the simulated spectrum: the resulting parameters from the fit define the function to calculate the “internal” background for each AP voltage considered in the simulation. Using the fit parameters errors, we can define a higher and lower limits for the background correction (for a linear fit, we used the error on the slope to obtain the highest and the lowest slopes compatible with the error bars).

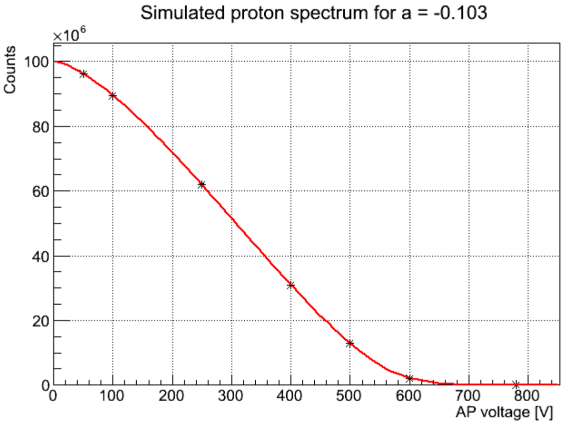

Figure 6.18: Simulation of the proton spectrum with $a = -0.103$. Fit (red) for the extraction of the coefficient a.

Thus, the "internal" background induces a drift $\left(\frac{\Delta a}{a}\right)_{\text{Simul+BG}} - \left(\frac{\Delta a}{a}\right)_{\text{Simul}}$ on the correlation coefficient a of:

- $+4.32^{+0.21}_{-0.20} \cdot 10^{-5}$, with lExB = 0|-200 V and at the pressure of $6.0 \cdot 10^{-10}$ mbar,
- $+7.19^{+0.26}_{-0.25} \cdot 10^{-5}$, with lExB = -50|-1000 V and at the pressure of $6.0 \cdot 10^{-10}$ mbar,
- $+1.17^{+0.02}_{-0.02} \cdot 10^{-4}$, with lExB = 0|-200 V and at the pressure of $1.5 \cdot 10^{-9}$ mbar.

The influence of the "internal" background on the coefficient a is at a low order: its impact on the correlation coefficient is negligible. And, as already observed, the lowest influence is found with the standard configuration lExB $= -0| - 200\,\text{V}$ and with a good vacuum below 10^{-9} mbar.

6.3 The electron-related background

From neutron decay, electrons are emitted with an endpoint energy of 781.6 keV. These electrons act in two ways for the background. On a first hand, these particles dominate the background in measured spectra. And on the other hand, they can ionize the rest gas molecules (see section 6.2).

6.3.1 The offline measurements with a beta source

In the case of the ionization of rest gas molecules, the out-coming ions can be trapped in the AP, accelerated and detected. In 2012, the influence of the electrons was imitated by placing a beta source inside the DV: we used an activated gold foil. The isotope ^{198}Au is a pure β-emitter with the endpoint energy 960.5 keV for the main branch (98.99%). The gold foil was activated at the neutron beam line of PF1b. Then the foil was installed on the manipulator mounted at the cross-piece (see Fig. 6.19). With this system, we inserted step by step the gold foil and we chose different positions to make measurements. Thus, we obtained the position of the gold foil relative to the detector pads (see Fig. 6.20). The detector used during the offline tests in 2012

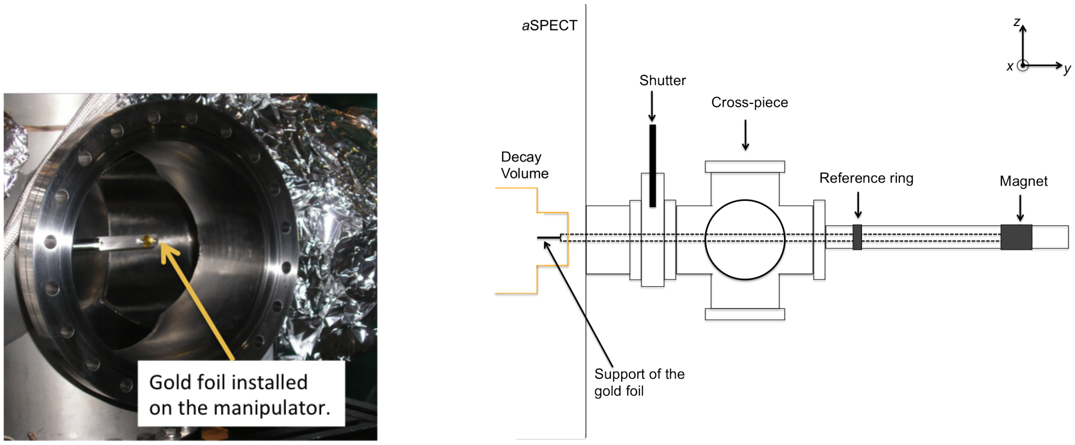

(a) Gold foil. (b) Sketch of the manipulator at the cross-piece.

Figure 6.19: Installation of the gold foil on the manipulator. A rod inside the tube is moved via a magnet. The gold foil is placed at the extremity of this rod and can be inserted inside the DV. The distance is measured between the reference ring and the movable magnet. This indicates the position of the gold foil in the DV and relative to the detector pads.

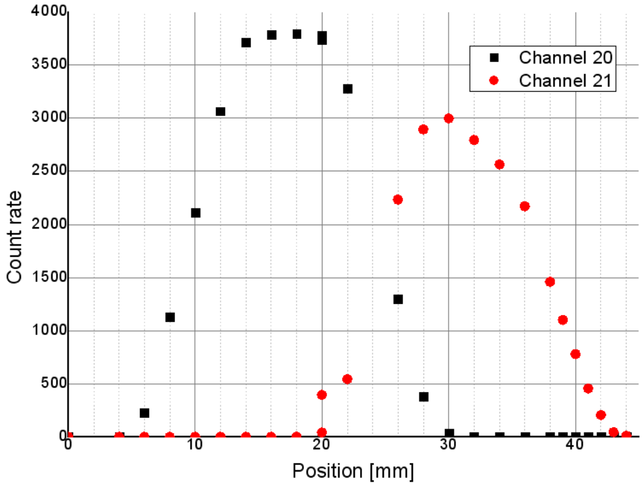

Figure 6.20: Coordinates of the gold foil position inside the DV, relative to the two pads of the detector in 2012: Channel 20 for the central pad, and Channel 21 for the external pad. The count rates were integrated on all spectrum range. The magnet was in its nominal configuration (70 A).

had only two working pads: the central pad (channel 20 of the shaper) and one of the external pads (channel 21 of the shaper). It is important to note that the detector was not aligned along the x-axis: the external pad "channel 21" was oriented towards positive values along the y-axis (towards the cross-piece).

In the presence of the gold foil in the DV, the electrons dominated all the pulse-height range with a maximum in the electron region (i.e., the non-linear amplification part of the new shaper), as shown in Fig. 6.21.

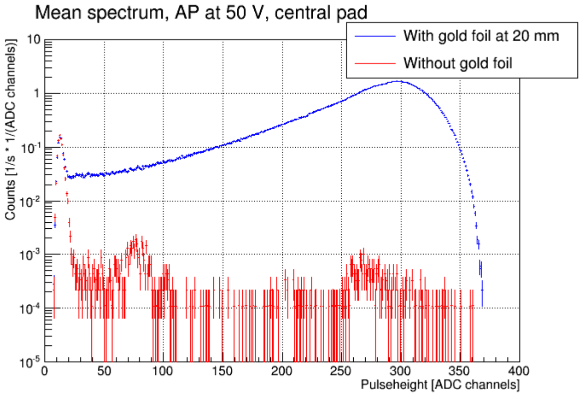

Figure 6.21: Background and gold foil spectrum with Det-HV at -15 kV and AP at 50 V on the central pad. Measurement time is 2.5 hours without the gold foil and 5 hours with the gold foil.

6.3.2 The influence of the electrodes settings

In the same way as with the "internal", background, we tested the possible influence of the electrodes configurations on the count rate measured with the source. But, this time, the identification of the ion and X-ray peaks is not possible as the rate from the electrons was much higher than the background and therefore the statistics to identify the background peaks could not be reached (see Fig. 6.21). However, we are interested on the background in the proton region. So, for the following analysis, the count rates have been integrated in the proton region which includes the X-ray and ion peaks. The AP dependence of the background has been analyzed by calculating the count rate relative to the one measured with AP at 50 V. This value was taken as reference due to the stability of the count rate during continuous measurements for this voltage. As shown in Fig. 6.22, the distribution of the number of counts in the proton region with AP at 50 V is consistent with the Poisson distribution expected from statistics. For higher AP voltage, the distribution deviates from the Poisson distribution: as shown for AP at 780 V in Fig. 6.22(b). The Poisson law is a probability law which describes the behavior of events occurring in a given length of time, if they occur independently, at a constant rate [65]. If the mean number of events is μ for a given length of time, the probability to obtain x events is given by:

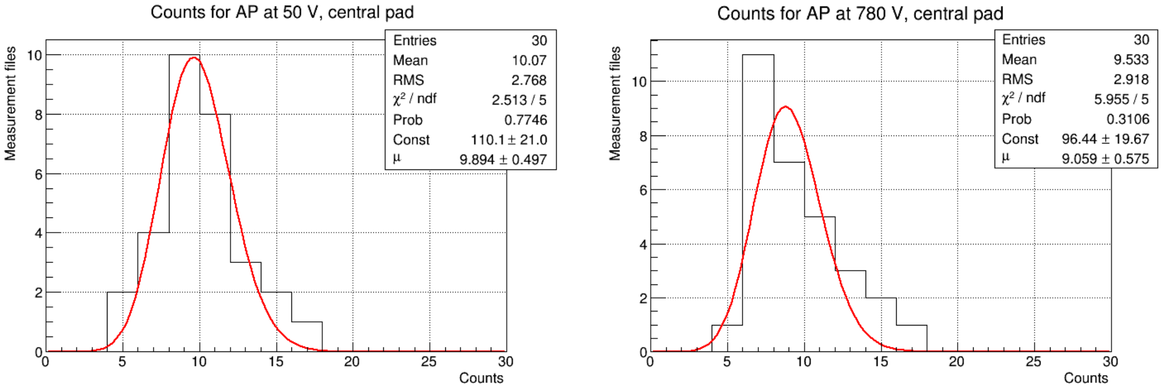

(a) For AP at 50 V.

(b) For AP at 780 V.

Figure 6.22: Distribution of the number of counts, in one file, in the proton region for the central pad during one continuous measurement without gold foil and with Det-HV at -15 kV. A fit using the Poisson distribution is applied in red.

$$P(x) = \mu^x \frac{e^{-\mu}}{x!} \tag{6.3}$$

The fit parameters used in Fig. 6.22 correspond to μ, called the Poisson parameter, and a normalization constant. For AP at 50 V, the Poisson parameter μ resulting from the fit is more compatible with the mean of the distribution than the one obtained in the case of AP at 780 V. This was also observed in other continuous measurements made with the same electrodes settings. This motivated the choice of the count rate at 50 V as reference and the fact that this method allowed to remove the electrons and to see only the influence of the AP. The electron rate is decaying with time and therefore it is different between continuous measurements. The decay law followed by the radioactive gold foil is given by:

$$N(t) = N_0 \cdot e^{-t/\tau} \tag{6.4}$$

with N_0 as the initial number of radioactive gold atoms (^{198}Au), τ is the half-life equal to 2.9647 days in the case of gold.

The most probable origin of non-statistical fluctuation is a trap. Depending on the location of the trap, it may be influenced by the lExB electrodes. We made measurements with two configurations already tested without gold foil: 0|-200 V (which is the standard configuration) and -50 |-1000 V. As shown in Fig. 6.23, even if the proton region of the spectra is dominated by

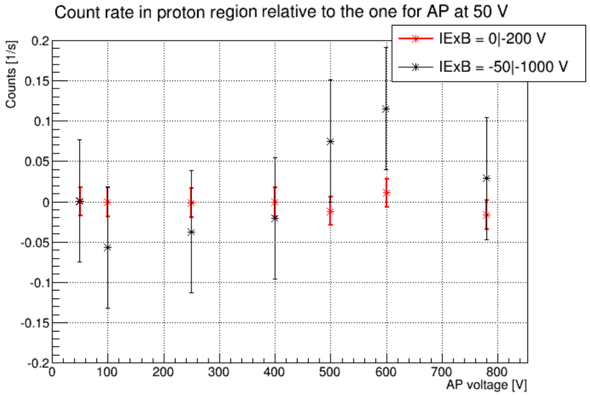

Figure 6.23: AP dependence of the count rate in the proton region for two configurations of the lExB electrodes, central pad. The gold foil was placed at 20 mm (center of the central pad). The count rates for AP at 50 V have been subtracted. The measurement at 0|-200 V was done during about 24 hours (17 days after the activation of the gold foil), and the one at -50|-100 V during about 10 hours (22 days after the activation of the gold foil). The delay between these two measurements is 5 days inducing a reduction of the gold foil activity by about 81%.

electrons, we observe some indication for an influence of the electrode settings on the background (the statistics for lExB at -50 |-1000 V is insufficient for a final conclusion).

6.3.3 The "side-effect" of the electrons

The gold foil was then placed at 40 mm, i.e. centered on the external pad (entrance of the DV). And in the same way as with the "internal" background, we measured spectra with a deteriorated vacuum (see Fig. 6.24). The two measurements used as reference for the comparison were done

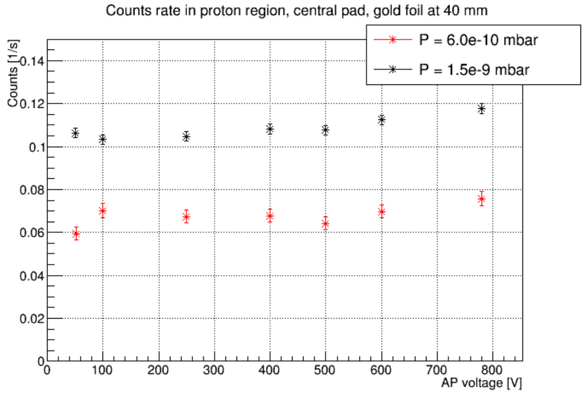

Figure 6.24: Measurement on the central pad with the gold foil at 40 mm (centered on the external pad). AP dependence of the count rate in proton region of the central pad for two vacuum conditions. Measurement time is about 15.6 hours at $6.0 \cdot 10^{-10}$ mbar and about 40 hours at $1.5 \cdot 10^{-9}$ mbar.

11 days after the activation of their respective gold foil[2], with the same settings and with the source at the same place. The observations are that the count rate is still influenced by the

---

[2] A second gold foil was used for the measurements with deteriorated vacuum: the second gold foil was similar to the first one and activated in the same conditions.

vacuum quality: increase by a factor 2. In comparison for the same region of integration, we noted differences without the gold foil and with the gold foil at 40 mm for the central pad (see Tab. 6.2). With the electron source not directly centered on one pad, we observed a "side-effect" on the pad right next. The higher count rate in the protons region is induced by the presence of the electrons and it is related to the vacuum.

	Good vacuum ($6 \cdot 10^{-10}$ mbar)	Bad vacuum ($1.5 \cdot 10^{-9}$ mbar)
Without gold foil	$(3.24 \pm 0.19) \cdot 10^{-2}\,\mathrm{s}^{-1}$	$(6.92 \pm 0.17) \cdot 10^{-2}\,\mathrm{s}^{-1}$
Gold foil at 40 mm	$(5.93 \pm 0.29) \cdot 10^{-2}\,\mathrm{s}^{-1}$	$(10.63 \pm 0.22) \cdot 10^{-2}\,\mathrm{s}^{-1}$

Table 6.2: Count rate in the protons region for the central pad (mean values for AP at 50 V).

This difference in count rate is in a large fraction due to new peaks in the proton region shown in Fig. 6.25(a). The ion peak measured without gold foil (in red) above the ADC channel 100 is "adsorbed" by a higher peak, due to the presence of the gold foil, with a mean energy closer to the one of the proton peak. Concerning the AP dependence of the count rate in the proton region (Fig. 6.25(b)), it slightly increased in presence of the beta source. The emitted electrons gyrate around the magnetic field lines from the DV to the detector. Even if they do not reach the central pad, they can ionize the rest gas molecules (see Chapter 5 and Fig. 6.26). These ions can also ionize other molecules filling a trap. They can be accelerated by the high potential and be detected on the central pad of the detector.

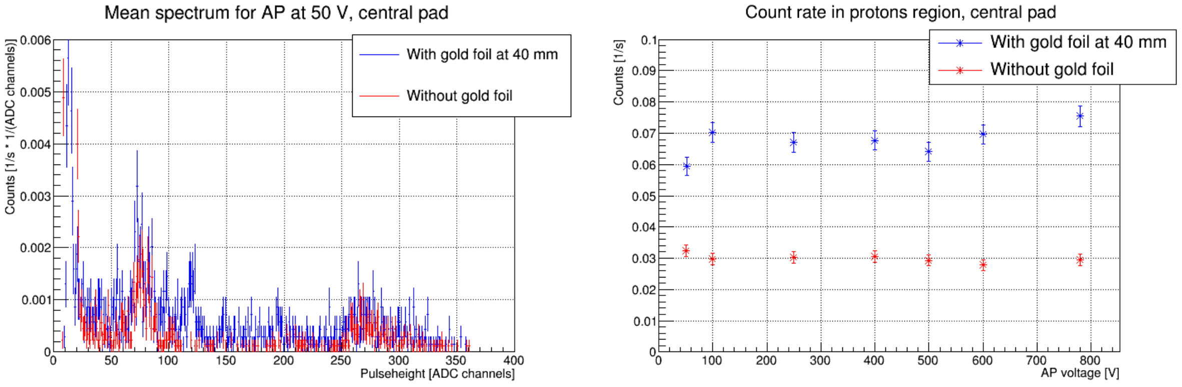

(a) Spectrum measured with AP at 50 V (zoom on lower peaks).

(b) AP dependence.

Figure 6.25: Comparison of data for the central pad with and without gold foil at 40 mm (centered on the external pad). Measurement with Det-HV at -15 kV during 21.2 hours without gold foil and during 15.6 hours with the gold foil.

The origin of the new peak is clearly related to the presence of electrons. This was confirmed by orienting the gold foil toward the Mirror (see Fig. 6.27): the electrons were emitted to the bottom part of the spectrometer. In this configuration, the new peak disappeared and the ion peak observed without source is fully visible. The count rate measured in the proton region, with the gold foil at 40 mm and toward the Mirror, was $(4.63 \pm 0.37) \cdot 10^{-2}\,\mathrm{s}^{-1}$. It was lower than the one with the gold foil toward the detector (see Tab. 6.2) and still higher than the one without gold foil. So, even if the electrons are not emitted toward the detector, they still influence the count rate in the proton region mainly by ionization processes of the rest gas molecules, or by

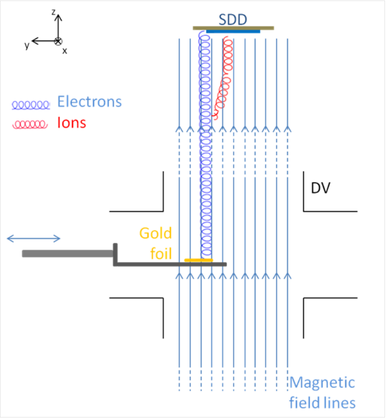

Figure 6.26: Sketch of the rest gas molecules ionization by the electrons from the gold foil. Before the SDD, the uExB electrodes generate a stronger drift (the electrons are too fast to be drifted, but the ions may be trapped).

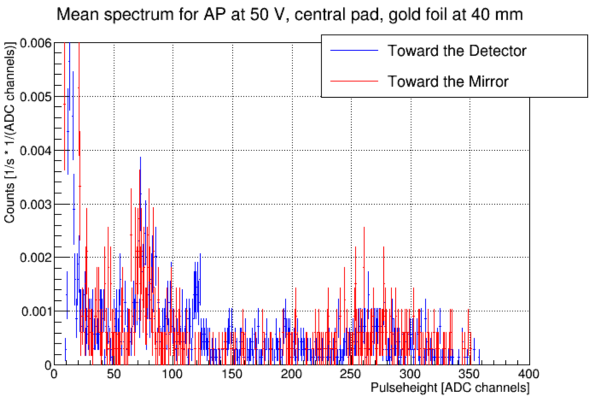

Figure 6.27: Spectrum measured at the central pad with AP at 50 V. The gold foil was placed at 40 mm and oriented toward the detector (blue) and toward the mirror (red). Both measurements with the same settings, Det-HV at -15 kV and in two consecutive days.

X-rays emission (hypotheses for the origin of the new peak). With the source oriented towards the detector, the new peak is detected at an energy of about 8 keV, this could correspond to X-rays from copper (see reference Tab. 6.1). These electrons have high energy and can traverse the detector chip, hit the holding structure and wires, and create X-rays there as well. These hypotheses have to be investigated. The dependence on the AP voltage of the new peak is negligible as shown in Fig. 6.28. We also performed a measurement with the gold foil at 40 mm toward the bottom of the spectrometer, but with the Mirror electrode set to 0 V. The difference observed is negligible: the count rate measured in the proton region was $(4.27 \pm 0.45) \cdot 10^{-2}\,\mathrm{s}^{-1}$. However, the gold foil and its support may stop the background from the Mirror.

As in section 6.2.4, we can calculate the influence on the coefficient a of the background in the proton region induced by the presence of ionizing particles. For the measurements considered in Fig. 6.24, with the standard configuration $\mathrm{lExB} = -0| - 200\,\mathrm{V}$ and $\mathrm{p} = 6.0 \cdot 10^{-10}\,\mathrm{mbar}$, the shift induced on $\frac{\Delta a}{a}$ is $+1.17^{+0.02}_{-0.02} \cdot 10^{-4}$. And with the same settings and $\mathrm{p} = 1.5 \cdot 10^{-9}\,\mathrm{mbar}$, the shift is $+1.71^{+0.02}_{-0.02} \cdot 10^{-4}$. This influence is at a low level. However, the gold foil only simulates the effect of electrons between the DV and the detector. The effect of the trap between the

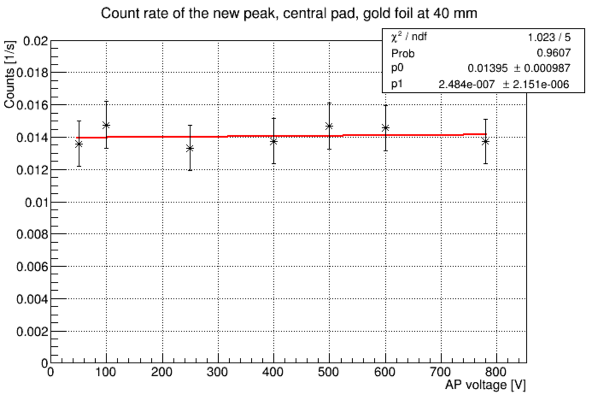

Figure 6.28: Dependence on the AP voltage of the count rate integrated around the new peak (ADC channels 110-130 in Fig. 6.25(a)) measured on the central pad with the gold foil at 40 mm. A linear fit is applied in red resulting in a slope of $0.25(2.15) \cdot 10^{-6}\,\mathrm{s}^{-1}\mathrm{V}^{-1}$.

AP and the Mirror is reduced due to removal of trapped particles by the source support. And, during a beam time, neutrons decays also into protons which can participate to the ionization processes.

6.4 The environment's influence

The preparation zone, where the spectrometer was installed in 2012, is close to a neutron guide[3] (see Fig. 6.29). This guide was finished during the offline tests of *a*SPECT. The shielding of this new guide was tested while making an offline measurement without gold foil and with standard electrodes settings. The test of the guide with the neutron beam affected one data file (see Fig. 6.30). The radiation leaks have led to the detection of more counts both in the proton

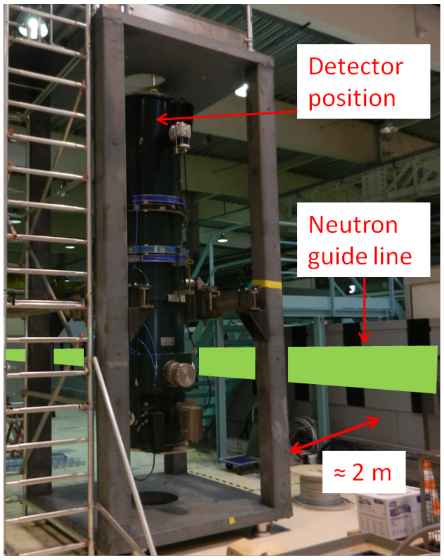

Figure 6.29: The spectrometer *a*SPECT installed in the preparation zone in 2012 next to a neutron guide.

---

[3] This neutron guide was built for a new instrument at ILL called IN16b.

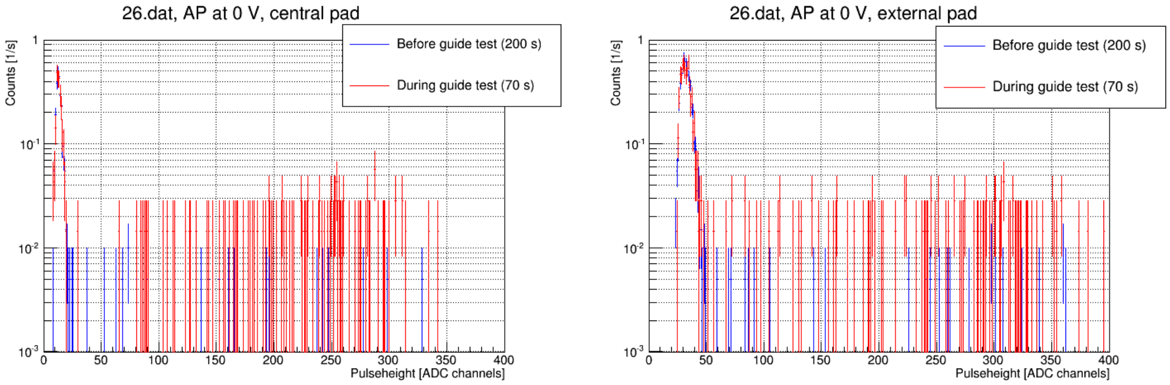

(a) Central pad (channel 20).

(b) External pad (channel 21).

Figure 6.30: One file measurement with AP at 0 V measured on 2012/11/15 while testing the new neutron guide close to *a*SPECT.

and the electron regions. For this file, the comparison between the first part without external perturbation and the last part during the test of the neutron guide gives an increase of the count rate in the proton region by a factor 2. For the count rate in the electron region, the increase is a factor 10.

This incident highlighted that the "internal" background (section 6.2) can be superposed by an external contribution related to the environment where the spectrometer is placed. In the preparation zone, it was close to one neutron guide with radiation leak problems. But the PF1b zone is surrounded by several neutron guides and experimental zones. As explained in section 6.2, the "internal" background was also measured in 2013 at PF1b before the reactor started. The conclusions obtained were the same as the offline measurements of 2012 with similar values for the count rates. At the end of the beam time of 2013, I performed one continuous measurement with the neutron shutter closed at PF1b (the general shutter of the guide H113 and the shutter inside the casemate) and all voltages set to 0 V. The reactor was still running for one day (see Fig. 6.31). By comparing with the same continuous measurement after the reactor stopped, we observed

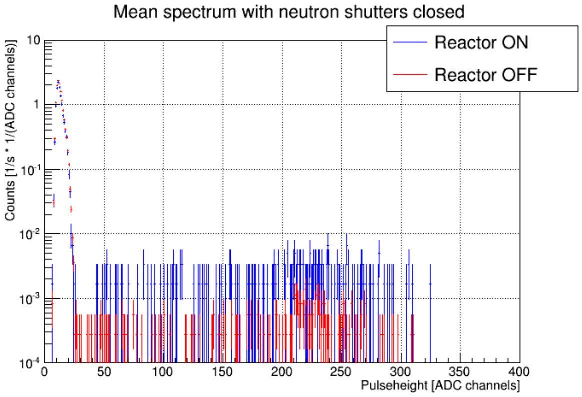

Figure 6.31: Measurements with neutron shutter closed at the end of the beam time of 2013. Comparison when the reactor was still running and after it stopped. Both measurements with all voltages set to 0 V.

a decrease of the count rate: in the proton region it was measured at $(3.56 \pm 0.31) \cdot 10^{-2}\,\mathrm{s}^{-1}$ when the reactor was still on, and measured at $(0.94 \pm 0.16) \cdot 10^{-2}\,\mathrm{s}^{-1}$ when the reactor was off.

During the continuous measurement with running reactor and aSPECT/PF1b shutters closed, some fluctuations were observed, as shown in Fig. 6.32. Some of these fluctuations seem to correspond to an action (open/close) of shutters in the experimental zone next to PF1b[4].

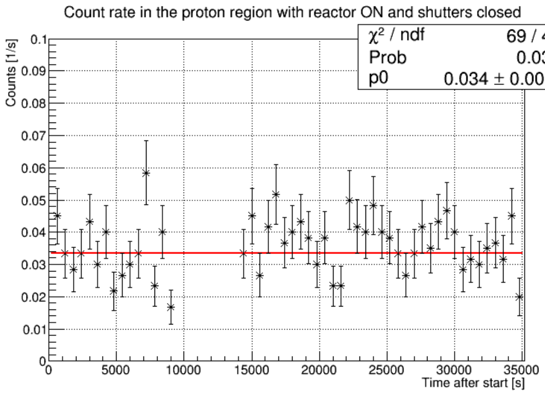

Figure 6.32: Count rate in the proton region during the continuous measurement with reactor on and shutter closed (all voltages set to 0 V). Each point correspond to a 600 s acquisition. The constant fit is just an indicative reference.

The count rates fluctuate around about $0.034\,\mathrm{s}^{-1}$ but the statistics is not sufficient to clearly identify an effect due to shutters. In the worst case, we obtained a difference in the count rate of $0.02\,\mathrm{s}^{-1}$ but not correlated to the AP voltage. In comparison, the "internal" background with lExB at -50|-1000 V in Fig. 6.13 was measured with a difference of about $0.01\,\mathrm{s}^{-1}$ in the count rate. This effect is comparable with the one presented here, and we can expect an effect on the coefficient a of about 10^{-4} or lower.

6.5 The experimental background

During the beam time in 2013, we investigated the background in experimental conditions. Continuous measurements are performed at a given electrodes setting. Typically, we applied several voltages between 50 and 780 V for the potential barrier at the AP. This last value, 780 V, is interesting as no protons from neutron decay can reach the detector with this potential barrier. This measurement is used to determine the rate of decay electrons in the detector. Thus, measurements with AP at 780 V allow to investigate the background during the beam time. It is important to note that in 2013, the preamplifier was modified (see section 3.6.1): its amplification was reduced by 23%. In the following descriptions, different conditions were applied for the measurements. They are resumed in Tab. 6.3. The reference of the configuration corresponding to the measurements are indicated in the title of figures.

6.5.1 Measurements in the beam-time conditions

Spectra measured with AP at 780 V and the neutron shutter open, show the presence of a peak in the proton region which is dominated by electrons (see Fig. 6.33). This was also observed during the beam time of 2011: the count rate in the proton region with AP at 780 V was measured at $(5.65 \pm 0.07)\,\mathrm{s}^{-1}$ in 2011, and at $(5.27 \pm 0.03)\,\mathrm{s}^{-1}$ in 2013, in the central pad and for the same settings. This peak could be induced by the presence of trapped particles above the

---

[4] More investigations could be done to know how the activities of the neighbor experimental zones affect our measurement.

Configurations	Settings					Shutter open time
	Det-HV	uExB	lExB	Mirror	e15	
Config. 1	-15 kV	-1.75|-2.25 kV	-1|-200 V	ON	sym.	200 s
Config. 2	-15 kV	-1.75|-2.25 kV	-200|-1 V	ON	sym.	200 s
Config. 3	-15 kV	-1.75|-2.25 kV	-200|-5 V	ON	sym.	(50, 100, 200) s
Config. 4	-15 kV	-1.75|-2.25 kV	-200|-5 V	ON	asym.	(50, 100, 200) s

Table 6.3: Configurations of the measurements considered in this analysis in 2013. As described in section 2.3.3, e15 is a dipole electrode. The settings for the electrode lExB were adjusted according to the tests described in section 6.1.4.

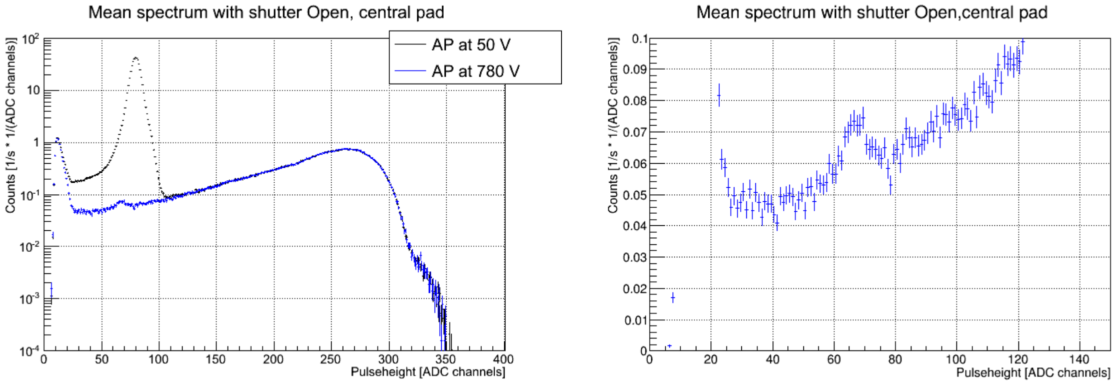

(a) Measurements with AP at 50 V and at 780 V. (b) Zoom on the protons region with AP at 780 V.

Figure 6.33: Mean spectrum measured on the central pad during the beam time of 2013 with the neutron shutter open. Measurement in Config. 1, for a total time of 18.6 hours: 4 hours with AP at 50 V, and 2.7 hours at 780 V.

potential barrier applied at the AP electrode. The peak is at lower pulseheight than the peak from decay protons but overlaps with this peak. According to the investigations in 2012 with the activated gold foil, this peak represents the contribution of ions from the rest gas molecules ionization by the neutron decay products.

By regarding the evolution in time of the count rate in the proton region (see Fig. 6.34), we observed that it was not constant for AP at 780 V. When the neutron shutter was opened, the count rate increased promptly: this is caused by the decay electrons that are not stopped by the AP. But then, while the neutron beam was opened, the count rate continued to increase slightly with an exponential behavior (see eq. (6.6)). After closing the neutron shutter, the count rate decreased promptly (decay electrons are absent) but it was not back to its initial value (level of the "internal" background). It decreased slightly and was back to the initial level when the AP ramped down to 0 V. These observations confirmed the contribution of charged particles which are created when the neutron shutter is opened. And these particles are trapped above the AP electrode: when the potential barrier is ramped to 0 V, the count rate decreased meaning that trapped particles are removed.

Thus, the background count rate is related to creation and removal processes. This evolution can be described by the following equation:

$$\frac{\mathrm{d}N}{\mathrm{d}t} \propto c_1\phi - c_2 N \tag{6.5}$$

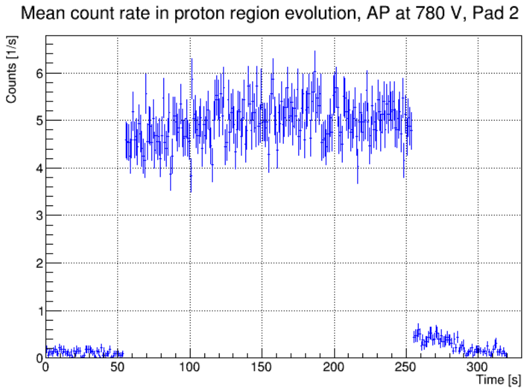

Figure 6.34: Evolution of the count rate in the protons region with AP at 780 V. The AP was ramped up to $U_A = 780\,\mathrm{V}$ at second 20. The shutter was opened at second 55 for 200 s. Then the AP was ramped down to 0 V after second 275. All measurements with AP at 780 V represent a global measurement time of 2.7 hours (Config. 1).

where N is the background count, ϕ is the neutron flux, and c_1 and c_2 are constants related to creation process (proportional to the flux) and to removal process (proportional to the content of the trap) respectively. The solution of this equation is an exponential build-up function with a constant offset:

$$f(t) = p_0 + p_1 \cdot \left(1 - \mathrm{e}^{-t/\tau}\right) \tag{6.6}$$

where the parameter p_0 represents the constant part of the background, p_1 is related to the saturation value of the background, and τ is the time constant. Thus, we find $c_1\phi = \frac{p_0+p_1}{\tau}$ and $c_2 = \frac{1}{\tau}$.

The increase and the decrease observed in measurement prove that particles are stored with the time constant of an exponential build-up function. This is dangerous as the trap depth may depend on the AP (see section 6.1). These characteristics are investigated in the following sections.

6.5.2 The time dependence

In Fig. 6.35, the function in eq. (6.6) is used to fit the count rate in the proton region while the neutron shutter was opened. With this data set, for AP at 780 V, the constant part of the background, p_0, is calculated at $(4.67 \pm 0.06)\,\mathrm{s}^{-1}$, the non-constant part, p_1, is at $(0.66 \pm 0.06)\,\mathrm{s}^{-1}$, and the time constant τ is $(51 \pm 10)\,\mathrm{s}$. For the lower AP voltages, the parameter p_1 tends to $0\,\mathrm{s}^{-1}$ (as shown in Fig. 6.36(a)) and the fit function can be assimilated to a constant fit whose parameter p_0 corresponds to the mean count rate with shutter open (i.e., integration on the proton region of the mean spectrum measured at U_A). It should be noted that at low AP voltages, the count rate is dominated by the protons from the decay and a potential time dependence is more difficult to quantify at the available statistics. The resulting time constants, shown in Fig. 6.36(b), can be fitted by a constant whose value is 56(7) s. The results are different from the one shown in Fig. 6.35 as they are extracted from different data sets.

The time dependence of the background is related to the traps filling and emptying time. The rest gas molecules are ionized when the neutron shutter is opened. The resulting charged particles are sensitive to the electric and magnetic fields and so to the potential traps. Then, these traps can be discharged [63] and the outgoing particles are accelerated and detected. This first analysis shows a potential dependence on the AP voltage due to the variation of the parameter

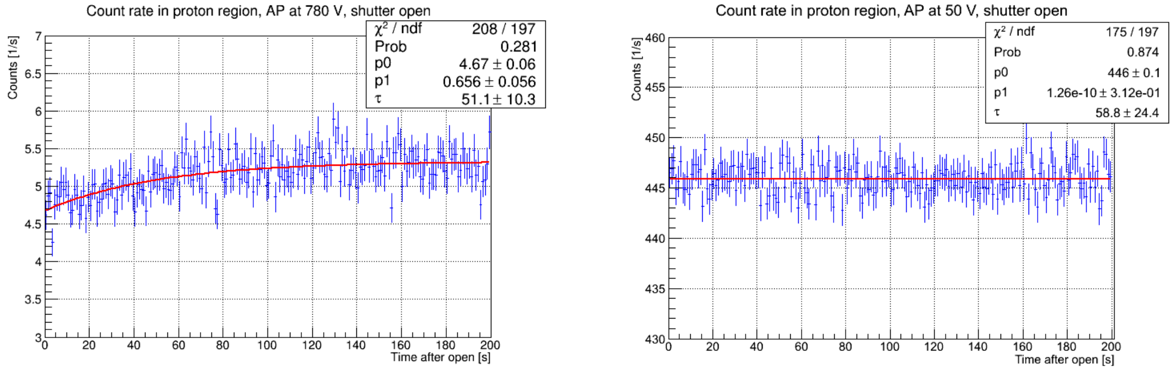

(a) With AP at 780 V. The measuring time was 10.5 hours.

(b) With AP at 50 V. The measuring time was 16 hours.

Figure 6.35: Evolution of the count rate in the proton region while the neutron shutter was opened. The fit function (6.6) is applied. Measurement in Config. 1, for a total time of 74.3 hours.

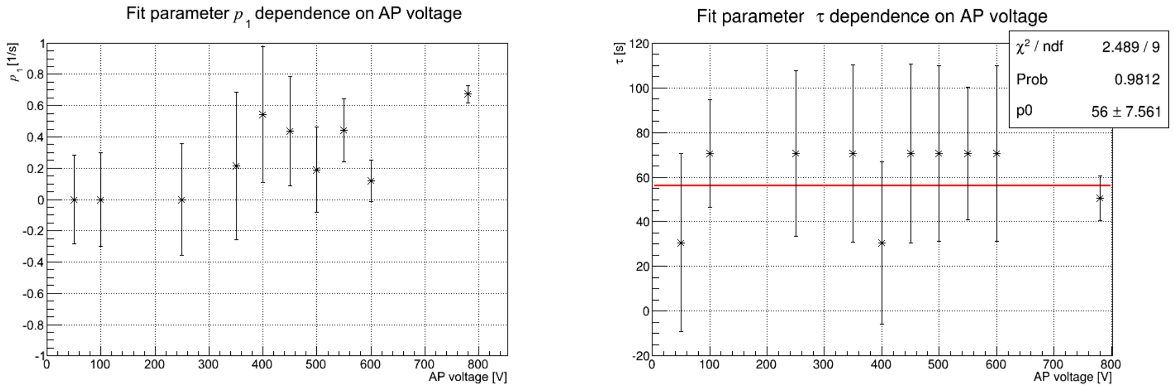

(a) Parameter p_1.

(b) Parameter τ. A constant fit (red) is applied.

Figure 6.36: Parameters from the fit function (6.6) applied for the different AP voltages.

p_1. This dependence is detailed in section 6.5.3. Furthermore, we tested different open times for the shutter: 50 s, 100 s and 200 s (config. 3 and 4 in Tab. 6.3). The new structure of the continuous measurement alternated blocks measured with these different open times (example in Fig. 6.37). This allows to test the dependence of the non-constant background (observed after closing the shutter) on the opening time. After the shutter is closed, the count rate is dominated by trapped particles and not by decay protons. This improves the sensitivity of the parameters for AP voltage below 780 V.

6.5.3 The AP dependence

As shown in Fig. 6.38(a), after closing the neutron shutter, the count rate in the proton region stayed higher than the initial level at the beginning of the measurement before opening the shutter. This effect is more pronounced with the AP at 780 V. In the last part of the measurement, when the AP is ramped to 0 V, the count rate is back to its initial value. This indicates trapped particles above the potential barrier at the AP electrode: with the shutter close, there is no decay products for the ionization process, the created ions during the period

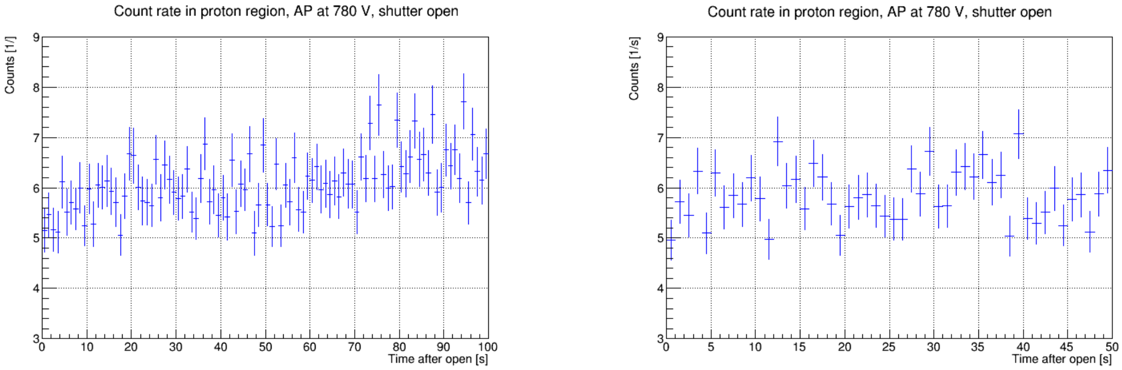

(a) Shutter open for 100 s. Mean spectrum for a measurement time of about 1 hour.

(b) Shutter open for 50 s. Mean spectrum for a measurement time of about 0.6 hour.

Figure 6.37: Evolution of the count rate in the proton region with AP at 780 V. Measurement in Config. 3.

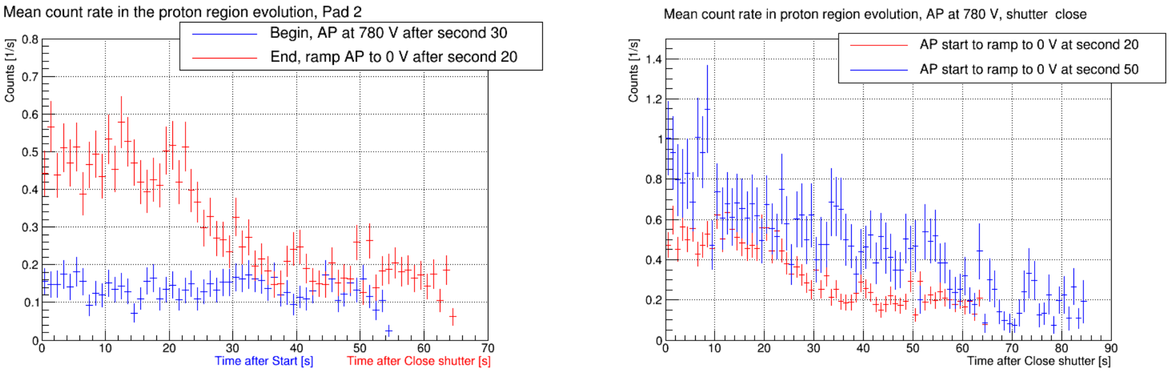

(a) Comparison before opening shutter ("Begin", blue) and after closing the shutter ("End", red).

(b) Comparison between two different time for "Close2" period (i.e. before ramping down the AP to 0 V): 20 s in red, 50 s in blue.

Figure 6.38: Evolution of the count rate in the proton region with closed shutter and AP at 780 V. Measurements in Config. 3 but considering only the 200 s open time.

with shutter open can be blocked by the potential at the AP and stored in the trap. In Fig. 6.39, we show the AP dependence of the count rate difference Close2 - Close1:

- Close1 represents the period of the measurement after ramping the AP to U_{A} and before opening the shutter,
- Close2 represents the period of the measurement after closing the shutter and before ramping the AP to 0 V.

Thus, the both parts are measured with the AP at U_{A}. However, with a longer time before ramping the AP to 0 V, in the Close2 period, the count rate decreases slightly (see Fig. 6.38(b)). So, the considered count rate for this period is integrated in the first 10-15 seconds after closing the shutter.

As indicated in the previous section, different open times for the shutter affect the background which stays after closing the shutter. From Fig. 6.40, we noted that the background in the proton

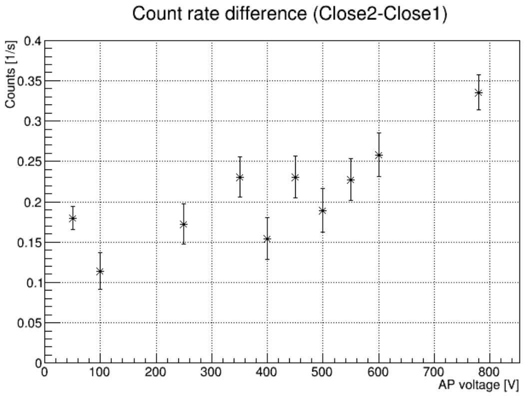

Figure 6.39: Count rate difference between the Close2 and the Close1 parts of the measurement in Config. 1, for a total time of 18.6 hours. This difference is calculated for the different AP voltages and for the proton region.

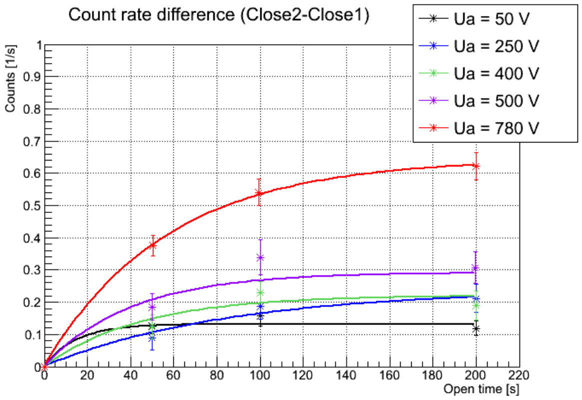

Figure 6.40: Count rate difference between the Close2 and the Close1 parts for different AP voltages and for different open times for the shutter. Measurement in Config. 3. The points are fitted by the function (6.6) with p_0 set to 0. These values are extracted from a different data set than those in Fig. 6.39.

region and after closing the shutter is related to the open time of the shutter and to the AP voltage: the effect of the longer open time is higher for AP at 780 V. The experimental points in Fig. 6.40 can be fitted with the exponential function (6.6) with the parameter $p_0 = 0$. The obtained parameters in Fig. 6.41 show an exponential increase toward higher AP voltage of the background count in the proton region after closing the shutter. The time constant parameters τ can be approximated by a constant whose value is consistent with the time constant obtained in the section 6.5.2 by fitting the evolution of the count rate with the shutter opened.

6.5.4 Background model

Based on the previous results, we can models the AP dependence of the background by fitting the count rate difference (Close2-Close1) graph. This difference is related to the parameter p_1 of the exponential function (6.6). As shown in Fig. 6.42(a), the dependence of the count rate difference is fitted by different functions: linear, quadratic and exponential are the functions considered for this investigation (see section 7.3 for further discussions).

The second term of the function (6.6), $p_1(1 - \mathrm{e}^{-t/\tau})$, describes the time dependence of the

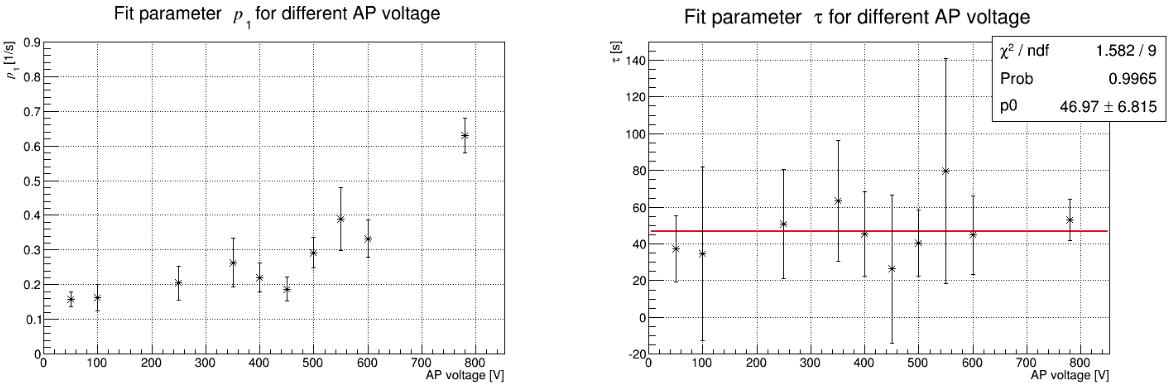

(a) Parameter p_1.

(b) Time constant parameter τ.

Figure 6.41: Parameters resulting from the fit of Fig. 6.40 with the function (6.6).

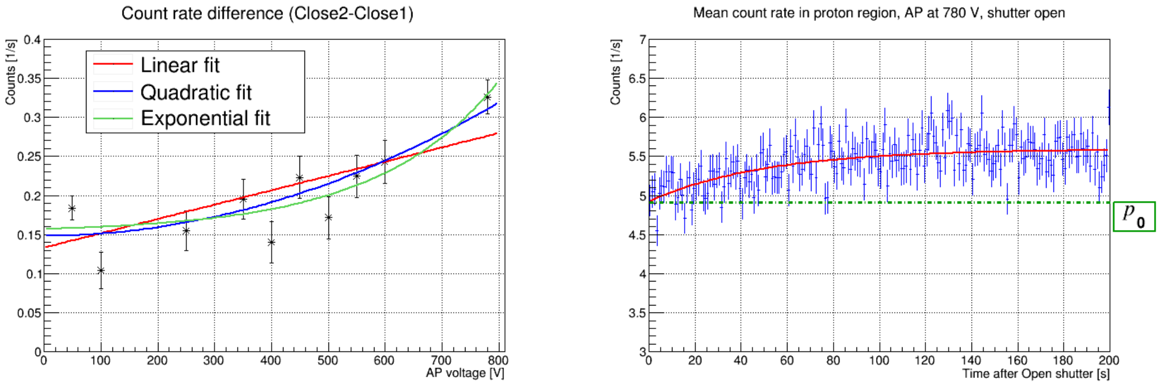

(a) Considered functions $f(U_A)$ to fit the count rate difference (Close2-Close1). Measurement in Config. 2.

(b) Evolution with AP at 780 V and shutter open.

Figure 6.42: Behavior of the background count rate.

non-constant part of the background. And its parameter p_1 can be replaced by $p_1(U_A)$ which is a function of the AP voltage based on the model $f(U_A)$ of the count rate (Close2-Close1). Thus, we can calculate the non-constant background for each AP voltage using the following relation:

$$\begin{aligned} BG(U_\mathrm{A}) &= \int_0^{t_\mathrm{op}} p_1(1-\mathrm{e}^{-t/\tau})\,\mathrm{d}t \\ &= p_1(U_\mathrm{A})\cdot\big(t_\mathrm{op}-\tau(1-\mathrm{e}^{-t_\mathrm{op}/\tau})\big) \end{aligned} \tag{6.7}$$

where t_op is the time during the neutron shutter is open, τ is the parameter from the exponential fit function. The term $p_1(U_\mathrm{A})$ is used to make the relation between the count rate measured at 780 V with shutter open and the one from the difference (Close2-Close1): $p_1(U_\mathrm{A}) = p_1 \cdot \frac{f(U_\mathrm{A})}{f(780\,\mathrm{V})}$. For the experiment point at 780 V, the non-constant background to subtract is the one measured in Fig. 6.42(b): the green line refers to the constant background, and the part above this line refers to the non-constant background. This corrects for possible losses of particles during the shutter movements.

6.5.5 Tests to empty the traps

We tested a new technical solution that had been implemented before the beam time of 2013 to reduce the background count rate from trapped particles close to the AP. As it was mentioned in section 2.3.3, the electrode e15, above the AP electrode (e14) was changed to a dipole electrode. The voltage applied to this electrode is coupled to the one applied at the AP with an additional resistor (see Tab. 2.1). With the dipole electrode, one side is set to the usual voltage, and the other side is set to a voltage in order to obtain an asymmetric configuration: a drift electric field is created above the AP electrode (see Fig. 6.43). The strength of the drift field is proportional to U_A. Thus, in the structure of one single measurement, this new drift electric field is present during all the time the AP is set to U_A: during the parts Open, Close1 and Close2. In a first time, simulations were done in order to check the effect of the new electrodes on the electrostatic potential. From Fig. 6.44, we calculated that the new shape of the AP (compared to the one used in 2011), and with the same e15, induces a reduction of the height of the electrostatic potential of about 0.35 mV. The new geometry of e15 (two half cylinders instead of a cylinder) shifts the potential of the new AP electrode by 0.05 mV and the position of the maximum by some tenths of a millimeter only. Some asymmetric configurations for e15 were also simulated by considering

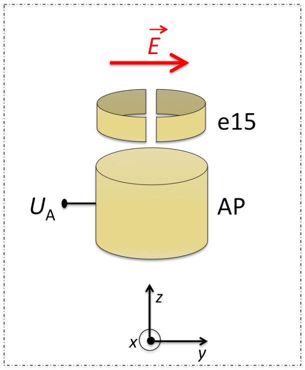

Figure 6.43: Electrode e15 above the AP in dipole geometry (AP electrode octagonal in 2013).

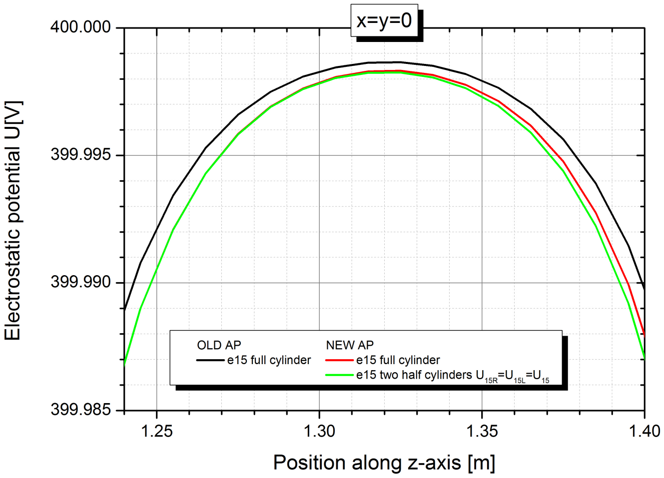

Figure 6.44: Simulation of the electrostatic potential in the AP electrode (e14) along the z-axis induced by a voltage of 400 V. Simulations done by Gertrud Konrad.

the right side of the electrode e15 set to the same voltage as the electrode e11 or e12 respectively. It was calculated that the height of the electrostatic potential is reduced by about 1.2 mV with e12, and by about 2.8 mV with e11. And the position of this potential is shifted towards the bottom by about 1.5 or 2.5 cm. The latter can be compensated with slightly different settings of the external Anti-Helmholtz coils.

The second step was to find the good configuration for the drift field. The voltage divider box for the electrodes system was modified to set the right electrode of e15 at the same voltage as the electrode e12 or e11 respectively (see Tab. 2.1): so at a lower potential than the left electrode e15. With these possible connections, the electric field strength is proportional to the AP and thus to the trap depth: a stronger field for deeper trap will result in stronger emptying. Furthermore, this is a simplest technical solution. In Fig. 6.45, the count rate in the proton region is affected by the presence of the electric field at e15. As shown in Tab. 6.4, the count rate is the lowest when setting the left side of the electrode e15 to the same potential as the electrode e11. The voltage of e11 is lower than the one of e12. The count rate evolution observed in section 6.5.2 was not visible and can be approximated by a constant fit. As shown in Fig. 6.46(a), the peak observed with shutter open and AP at 780 V is strongly reduced by the asymmetric configuration of the electrode e15. The effect of the count rate stabilization in time is more efficient with the higher electric field at e15: so by using the voltage of e11. In order to improve this effect, we acted on the lExB electrodes (see Fig. 6.46(b)). We observed that the background reduction was better with the inverted configuration for the lExB than we used before: so, the best configuration for the electrodes is to set the electric field created by the lExB in the same orientation as the one created by the e15.

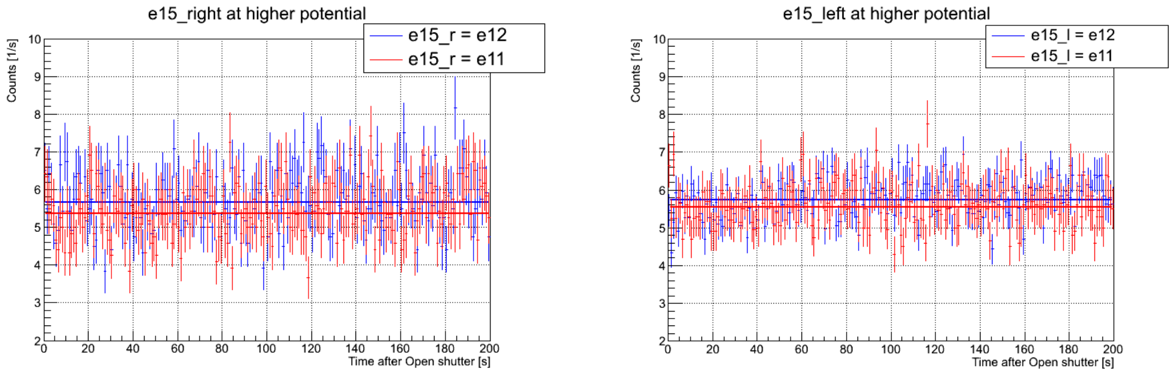

(a) The right electrode e15 is set at the potential of the electrode e11 or e12. Measurement time is about 1 hour for both measurements.

(b) The left electrode e15 is set at the potential of the electrode e11 or e12. Measurement time is about 1.6 hours with e12, and about 1 hour with e11.

Figure 6.45: Evolution of the count rate in the proton region with neutron beam Open and AP at 780 V using different configurations for the dipole e15. These measurements were performed with Config. 4 (only 200 s open time measurements). A constant fit is applied for the comparison, however it does not represent the count rate as there is a time dependence (explained after)

Connected to...	e15_right	e15_left
e12	(5.80 ± 0.05) s^{-1}	(5.83 ± 0.03) s^{-1}
e11	(5.54 ± 0.05) s^{-1}	(5.50 ± 0.03) s^{-1}

Table 6.4: Count rate in the proton region with AP at 780 V and e15 in asymmetric configuration.

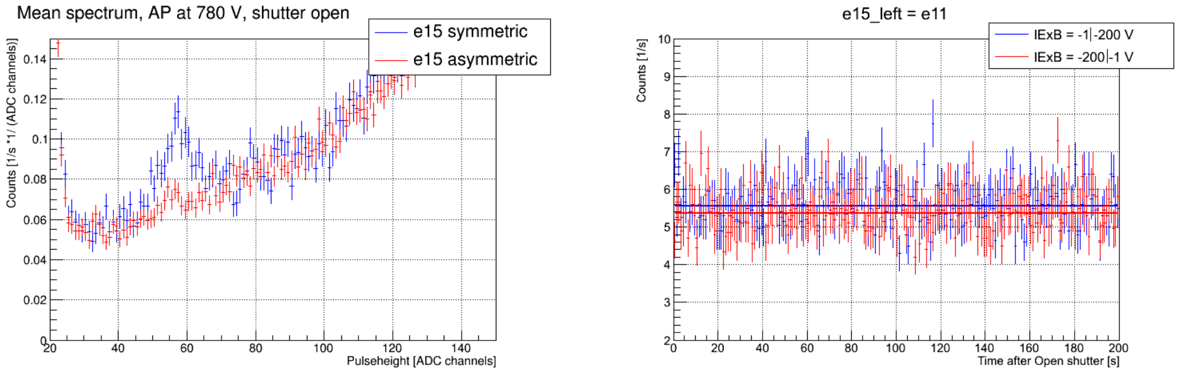

(a) Spectrum measured with the AP at 780 V and the neutron beam open. Comparison between e15 symmetric (blue) and asymmetric with e15_left connected to e11 (red).

(b) Evolution of the count rate in the proton region with the shutter Open and AP at 780. The e15_left is connected to the potential of e11. Two orientations of the lExB were compared.

Figure 6.46: Impact of an symmetric configuration for the electrode e15

The presence of the drift electric field at the electrode e15 has also a positive influence on the count rate after closing the neutron shutter. This residual background count rate, which was found dependent on the AP voltage, is now strongly reduced, as well as the mentioned dependence (see Fig. 6.47). However, the additional electric field is not homogenous and will therefore drift decay protons also perpendicular to the beam. This changes the edge effect whose impact has to be simulated.

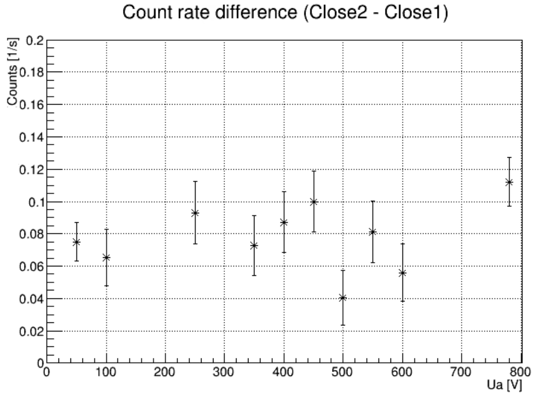

Figure 6.47: Count rate difference between the Close2 and the Close1 parts of the measurement with the electrode e15 in asymmetric configuration. This difference is calculated for the different AP voltages. This graph was obtained from a standard measurement with 200 s shutter open.

This configuration of the electrode e15 was also tested for different open times of the shutter. As shown in Fig. 6.48, the influence of the open time on the count rate was reduced by the asymmetric configuration of e15. There is still an AP dependence but reduced. The same method as in section 6.5.3, is applied (see Fig. 6.49). The resulting parameters p_1 for the different AP voltages are quite similar: the increase of the count rate induced by a longer open time of the shutter is strongly reduced than with symmetric configuration for e15, and the dependence on the AP voltage is negligible. The time constant τ is lower than the one obtained with e15 symmetric but the data set is insufficient for a precise determination of these times constants.

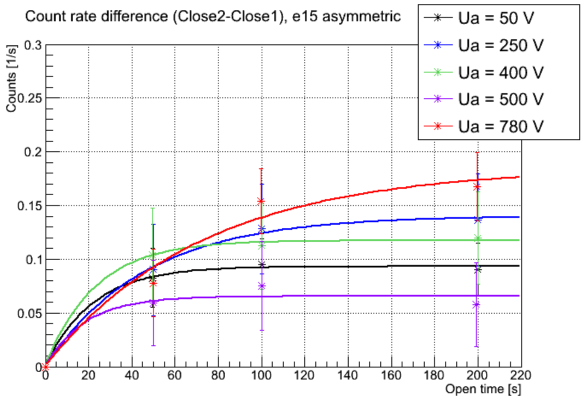

Figure 6.48: Count rate difference between the Close2 and the Close1 parts for different AP voltages, and with the electrode e15 set to asymmetric configuration. The points are fitted with the function (6.6) whose parameter p_0 is set at 0. Measurements with the Config. 4.

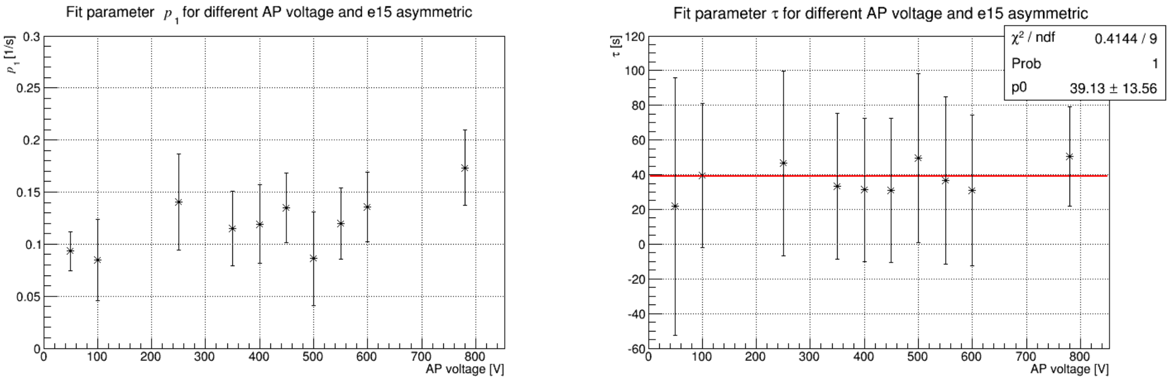

(a) Parameter p_1.

(b) Time constant parameter τ.

Figure 6.49: Parameters resulting from the fit of Fig. 6.48 with the function (6.6).

6.6 Status of the backgrounds in *a*SPECT

These investigations highlight a complex background composed of different parts. These background components are represented schematically in Fig. 6.50. The spectrometer-related background (also called “internal”) is present during the acquisition, is induced by the high-voltage and is AP-dependent. However, its influence on the coefficient a is low, in the order of 10^{-5}, in the case of a good vacuum, well below 10^{-9} mbar, and with favorable electrodes settings (especially $-0|-200$ V for the electrodes lExB) which reduce the AP dependence. The “internal” background can be superposed by an external contribution from the neighboring experimental zones. The external background is not related to the AP voltage but can influence the measurement of a if it changes in time. First estimations show that this influence on the coefficient a if low, in the order of 10^{-4}.

During the beam time, two further background components can be distinguished. One is due to presence of the electrons from the neutrons decay. This is a spontaneous, constant and AP-independent background which is present when the shutter is open. It is accounted for by the constant offset in the fit of a. The second part of the background is non-constant and AP-dependent. It is related to trapped particles. The particles responsible for this background are

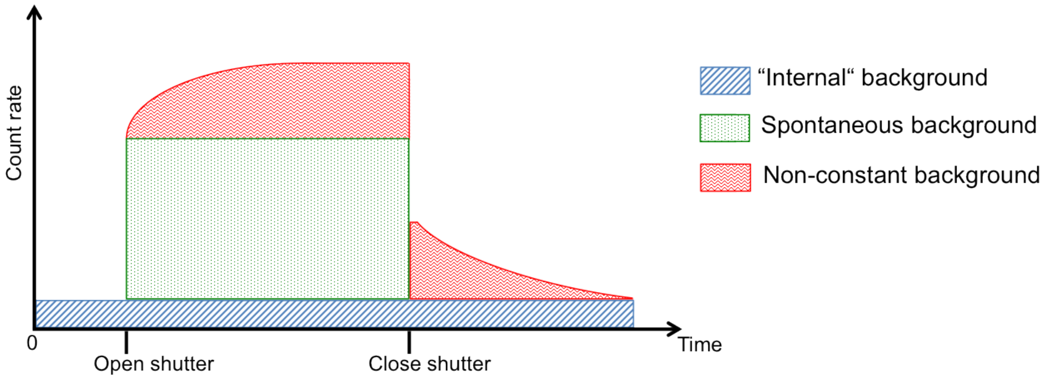

Figure 6.50: The background components in the experiment *a*SPECT (schematic). The "internal" background (blue), due to the X-rays and the ions, is present during all the acquisition. It can be mixed with an environmental contribution. The spontaneous background (green) is induced by the electrons from the neutrons decay and is constant when the shutter is open. The non-constant background (red) is due to trapped particles and increases when the shutter is open. After the shutter closed, the non-constant background count rate decreases.

trapped above the potential barrier: the depth of this trap depends on the voltage applied at the AP.

Different models are tested to describe the non-constant background. These models are used to apply the background correction for the coefficient a. The preliminary results are presented in the section 7.3.

Chapter 7

Measurement of the coefficient *a*

La mesure du coefficient de corrélation angulaire entre l'électron et l'antineutrino se fait via la mesure du spectre d'énergie des protons qu'il est possible de reconstruire grâce à la barrière de potentiel (AP) dont on peut changer la tension. L'extraction du coefficient a se fait via l'ajustement d'une fonction sur les points expérimentaux obtenus pour chaque valeur de l'AP. Cette fonction est construite à partir de la fonction de transmission et du spectre théorique des protons. Le taux de comptage pour AP à 0 V ainsi que le coefficient a font partie des paramètres libres de cette fonction. L'implication de la fonction de transmission nécessite une connaissance approfondie du champ magnétique (pour le rapport r_{B}) mais également du champ électrique (à savoir les configurations des électrodes). L'application d'une correction du bruit de fond suivant différents modèles induit une influence sur le coefficient a d'environ 3% à 7% suivant les conditions de mesure. De plus, les effets systématiques décrits dans le Chapitre 2 doivent également être étudiés. Cela vaut pour les effets de bords qui dépendent du profil du faisceau de neutron (étudié grâce à l'activation de feuilles de cuivre), de la configuration des électrodes uExB, de la position et de l'orientation du détecteur. Ces résultats sont préliminaires et nécessitent plus d'investigation et des simulations.

7.1 The blind analysis

In this chapter, I present results about the influence of different systematics on the coefficient a. The extraction of this coefficient, already described in section 4.3, is done via a blind analysis and the following values are noted a_{blind}. For the different considered measurements, the integrated proton spectrum is obtained and then fitted by the function (4.3) presented in section 4.3.2 which is included in the program DatFit developed by a collaborator who was not involved in the analysis. The fit result is sealed with a factor ε with $0.01 \leq \varepsilon \leq 0.1$ in the way as $a_{\mathrm{blind}} = (1 + \varepsilon) \cdot a$. This avoids a biased analysis but still allows for an easy interpretation of systematic effects. A similar procedure was also used in the previous data analysis of aSPECT and presented in the previous PhD theses [8, 9, 10, 11].

Another free parameter is added to this function and corresponds to an offset induced by the constant background due to the electrons. In this analysis, the offset is related to the non-subtraction of the background measured with the AP at 780 V. In section 7.3 about the background correction, the offset is still used and refers to the constant background part only as the considered models are used to subtract the non-constant background. Thus, the fit function used for this analysis has three free parameters: the coefficient a (with a_{blind} as output of DatFit), the count rate with AP at 0 V, and the offset related to a constant (AP independent) background.

The ratio r_{B} from the transmission function F_{tr} can be used as a free parameter of the fit function. However, it is measured independently: at the end or before a beam time, the electrodes system is moved out of the cryostat and it is possible to map the magnetic field inside the bore tube via a hall probe (see Appendix B). So, in this condition, we can fix this parameter: $r_{\mathrm{B}} = 0.203$ in the following analysis. Another parameter for the DatFit is the offset $\mathrm{d}U$ for the AP voltage. For the following analysis, this offset is fixed to 0: $\mathrm{d}U = 0$.

The results presented in this chapter are from the measurement on the central pad of the detector. This analysis is preliminary as more investigations and simulations are required to complete it.

7.2 Influence of the integration limits

In section 3.5.2, I presented the effect of the temperature on the proton peak position during one continuous measurement. This variation of the proton peak position can have an influence on the extraction of the proton count rate due to non-appropriated integration limits: if the proton peak is shifted towards lower energies, a fixed upper integration limit can include electrons with higher energy, and a lower integration limit can be inside the electronic noise part.

The coefficient a is dependent on the lower integration limit if one starts to cut into the proton peak from below. As shown in Fig. 7.1, if the lower integration limit is at higher ADC channel, one cuts more of the low-energy protons (they are located preferentially at the lower side of the peak). Therefore the value of a_{blind} gets more positive. For the same reason, the a value has a low dependence on the lower integration limit in the region between the electronic noise and the proton peak: more low-energy protons are cut as this region is due to backscattering of protons. But the effect is much weaker as shown in Fig. 7.2(a). The ideal cut would be at 0 proton energy (not 0 ADC channel) which cannot be reached. In Fig. 7.2(b), we note that the upper limit for the integration has a low influence on the extraction of the coefficient a.

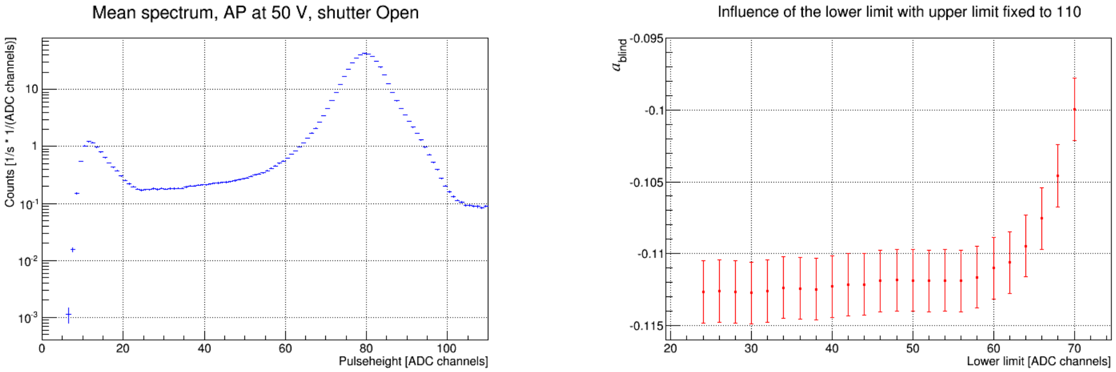

(a) Zoom on the mean spectrum measured with AP at 50 V and shutter open.

(b) Variation of the blinded coefficient a due to the lower integration limit.

Figure 7.1: Dependence on the lower integration limit with a fixed upper limit at 110 ADC channels. Measurement done with Det-HV at -15 kV, uExB = -1.75|-2.25 kV, lExB = -1|-200 V, Mirror ON, and the standard aperture for the neutron beam profile.

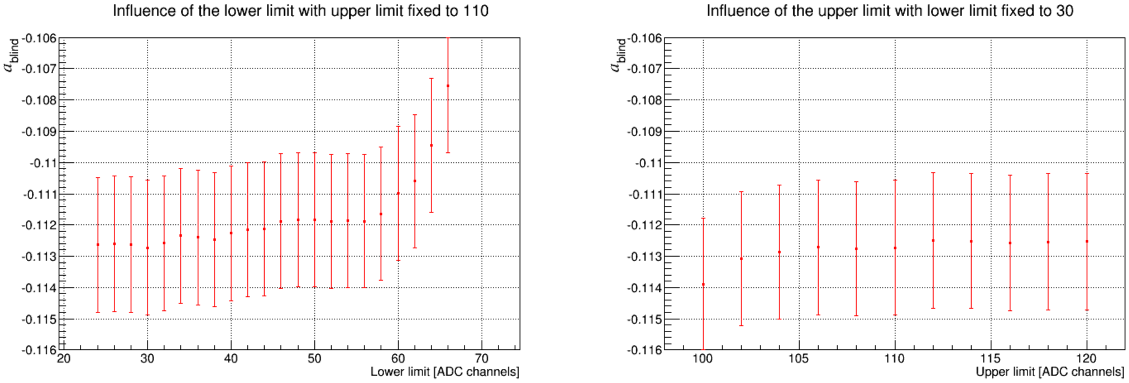

(a) Zoom from Fig. 7.1(b).

(b) Different upper limit with the lower one fixed at 30 ADC channel.

Figure 7.2: Influence of the integration limits for the proton count rate on the coefficient a_{blind}.

From the mean spectra obtained for each AP voltage for one continuous measurement (a standard one with shutter opened for 200 s), the influence on the a_{blind} value was tested. First, I used a "manual" method by taking [30-110] ADC channels as the integration range. The measured coefficient a_{blind} is considered as reference ("standard"). In a second time, I applied the method described in section 3.8.1, using the mean spectrum with AP at 50 V. For the same continuous measurement (the one of 2013/06/28), the new integration range was [25-109] ADC channels. The resulting shift in a_{blind} was $(a_{\text{blind, stand}} - a_{\text{blind, [25-109]}}) \approx -1.4 \cdot 10^{-4}$.

To compensate the effect of the variation of the proton peak position, the method to find the integration limits was used block per block: one continuous measurement is divided in several blocks which contain the measurements with the given AP voltages. Each block is separated from the next one by a measurement with AP at 0 V in order to reset the voltages of the lExB and Mirror electrodes. The integration limits are defined for each block from the mean of six files measured with AP at 50 V (each block contains six measurements at 50 V). The variation of the proton peak position is so taken into account and the integration regions are adapted. I obtained a small difference on the coefficient a_{blind}: relative variation from the last calculus using the correction method on the mean spectra over the global continuous measurement, $(a_{\text{blind, [25-109]}} - a_{\text{blind, block per block}}) \approx -0.3 \cdot 10^{-4}$.

However, this method induces a change of considered statistics in the integration region. As shown in Fig. 7.3, the integrated count rate for each AP voltage differs from the "manual" method with the limits [30-110] ADC channels: with the new method to find the integration limits, the count rate integrated in the proton region is higher. Thus, a change of 0.3 Hz for the background count rate would induce a shift on $\frac{\Delta a}{a}$ of about 0.41%.

7.3 Background correction

In Chapter 6, we defined a model for the non-constant background measured during a beam time, $BG[U_{\text{A}}]$ in eq. (6.7). Considering the analysis in section 6.5, we assume that the time constant τ is fixed for the different AP voltages. Thus, this parameter is extracted from the fit of the evolution of the count rate with AP at 780 V and shutter opened during 200 s. The second parameter from this fit, p_1, is combined with the function $f(U_{\text{A}})$ which describes the dependence of the count rate difference (Close2-Close1) on the AP voltage: this allows to calculate the factor $p_1(U_{\text{A}})$. In this way, the eq. (6.7) has only one variable: the open time t_{op}. Thus, the

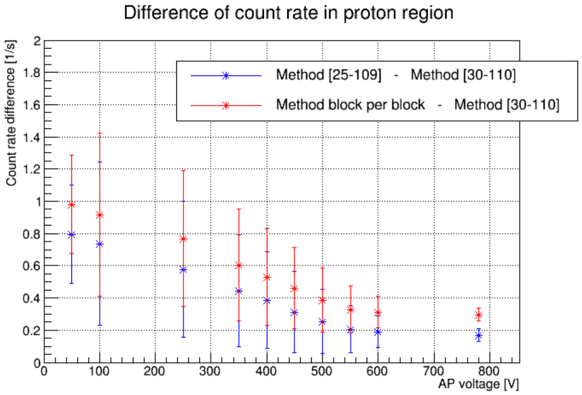

Figure 7.3: Difference of the count rate integrated in the proton region between the new integration method and the "standard" one with [30-100] ADC channels.

integrated proton spectrum is built by subtracting the non-constant background for each AP voltage considered:

$$Cps[U_\mathrm{A}] = Cps[U_\mathrm{A}]_\mathrm{integrated} - BG[U_\mathrm{A}] \tag{7.1}$$

where $Cps[U_\mathrm{A}]_\mathrm{integrated}$ is the count rate integrated on the proton region.

As described in section 6.5.4, I considered three fit functions to obtain $f(U_\mathrm{A})$: a linear fit ($b + c \cdot U_\mathrm{A}$, where b and c are the fit parameters), a quadratic fit ($b + c \cdot (U_\mathrm{A})^2$) and an exponential fit ($b + c \cdot \exp(U_\mathrm{A}/d)$). The aim is to determine the effect of these models on the extraction of the coefficient a. The DatFit is used to calculate the value a_blind. In Fig. 7.4, the relative variations of the coefficient a_blind were calculated by taking the value with constant background as reference ("1" in the figure). These data are from a measurement with 200 s as open time for the shutter, Det-HV at -15 kV and the e15 in symmetric settings. For a background correction based on the quadratic or exponential models, this induces a shift on the coefficient a_blind of about 3%. The difference between the quadratic and the exponential models represents a shift on a_blind of $-2.3 \cdot 10^{-4}$ and an increase of $\frac{\Delta a}{a}$ of about 1.8%.

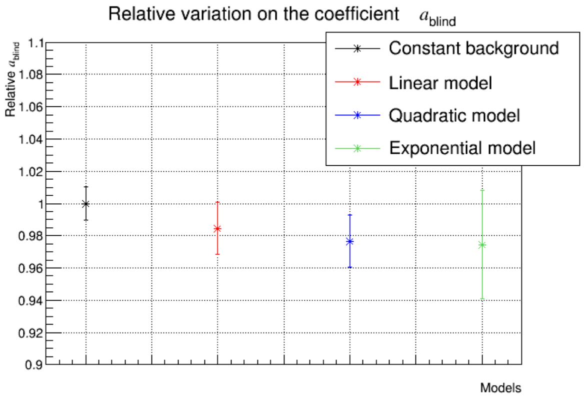

Figure 7.4: Relative influence on the coefficient a_blind corrected with different background models. Measurement with Config. 1.

The same tests were made on the measurement with the different open times for the neutron shutter (see Fig. 7.5). For the 200 s open time, the observations are similar but a shift is induced on the coefficient a of about 4.2% with the quadratic model and e15 symmetric. In the case of

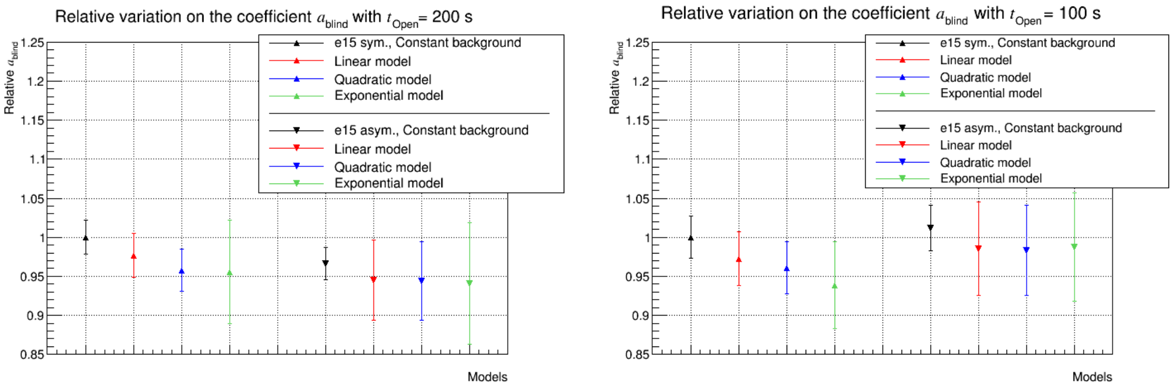

(a) Shutter open for 200 s. (b) Shutter open for 100 s.

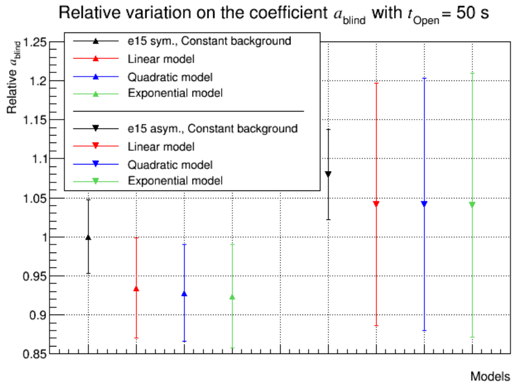

(c) Shutter open for 50 s.

Figure 7.5: Relative influence on the coefficient a for different background models correction and for different open times of the neutron shutter (Config. 3). And also for the measurement with the electrode e15 in asymmetric configuration (Config. 4).

100 s open time, the shift on a_{blind} is about 4% with the quadratic model and about 6% with the exponential one. With the open time at 50 s, the three models induce a shift of about 7%. The time constant τ is about 50 s, so for these three considered open times, the data are still influenced by the non-constant background. We noted also that there is a shift between the relative coefficient a_{blind} extracted from the different considered measurements at different open times without background correction (see Fig. 7.6). However, this also results into an increase of the statistical error: due to short t_{Open}, the correction methods of the count rate are more sensitive to the statistical fluctuations (as we saw it in Chapter 6).

Furthermore, we assumed during this analysis a fixed time constant. The lack of statistics did not allow a more detailed analysis about a possible dependence of the parameter τ on the AP voltage (see Fig. 6.41). This consideration will give an additional systematic uncertainty about the background.

With the electrode e15 in asymmetric configuration, we observed that the background was partially reduced by the generated electric drift field. In Fig. 7.5, without background model correction ("e15 asym., Constant background"), the shift induced on a_{blind} by the e15 in asymmetric settings is about 3% in the case where the neutron shutter is opened for 200 s, about 2% for 100 s and about 8% for an open time of 50 s. From the value without background correction, still with e15 in asymmetric settings, the correction models considered induce a shift of about

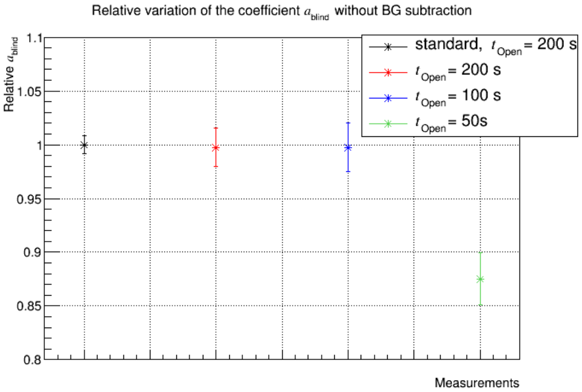

Figure 7.6: Relative variation between the a coefficient without background correction for the different considered measurements. In this "standard" refers to the first measurements dedicated to a which were run with the shutter opened for 200 s. The others measurements were performed by alternating the different open times for the shutter: 200 s, 100 s and 50 s.

2-4%. It also important to note that the asymmetric configuration for the electrode e15 changes the edge effect which has to be investigated by comparing the experimental measurements and simulations (see the scan of uExB in section 4.4.3).

7.4 Measurements with different systematics

In addition to the background, other systematic effects (see section 2.4) can be investigated by measuring with different configurations. The impact on the coefficient a is calculated from the data analysis and its comparison with the simulations. This is the case of the proton transmission which depends on the magnetic field ratio r_{B} and the trap conditions in aSPECT. The ratio r_{B} can be measured experimentally. The trapping effects are tested by measuring with a different magnetic field gradient in the DV (see section 7.4.1), with and without the Electrostatic Mirror (see section 4.4.5), and by investigating for the lExB configurations (see section 6.1.4).

Another example is the edge effect (see section 2.4.5). In this case the quantification of its impact on the coefficient a is related to several investigations. This effect is strongly dependent on the neutron beam profile. Thus, we tested a reduced profile (see section 7.4.2). Furthermore, the edge effect depends also on the position of the detector relative to the magnetic field and the electrode: we characterized the position and the orientation of the detector (see section 4.4.2), and we investigated for the ideal settings for the uExB electrodes (see section 4.4.3). These data combining with the simulations of the electric and the magnetic fields are used to estimate the correction due to the edge effect on the extraction of the coefficient a.

In the section 6.5.5, we found a solution to reduced the non-constant background during the measurement with the electrode e15 in asymmetric configuration. However, this additional drift electric field can induce a change in the systematic effects as for example the edge effect: this drift may change the proton trajectories before the adjustment induced by the uExB. That is why, we measured in 2013 with the two configurations for the e15. This will be used to estimate the change due to the asymmetric setting.

7.4.1 Test of the magnetic field gradient in the Decay Volume

During the beam time of 2013, we made a measurement with a reduced magnetic field gradient in the DV. In their standard configuration, the correction coils c3 and c5 are respectively set to 35 A and 15 A. For this test in 2013, they were set respectively to 30 A and 20 A. The proton count rate is integrated for the spectra shown in Fig. 7.7. For AP at 50 V, we calculate a difference of count rate in the proton region of about 1.02 Hz between the measurement with the standard gradient and the one with the reduced gradient. This confirms that less protons are reflected towards the detector. With AP at 780 V, this difference is about 0.62 Hz. As less protons and electrons are reflected, this induces a smaller ionization and so a decrease of background count rate.

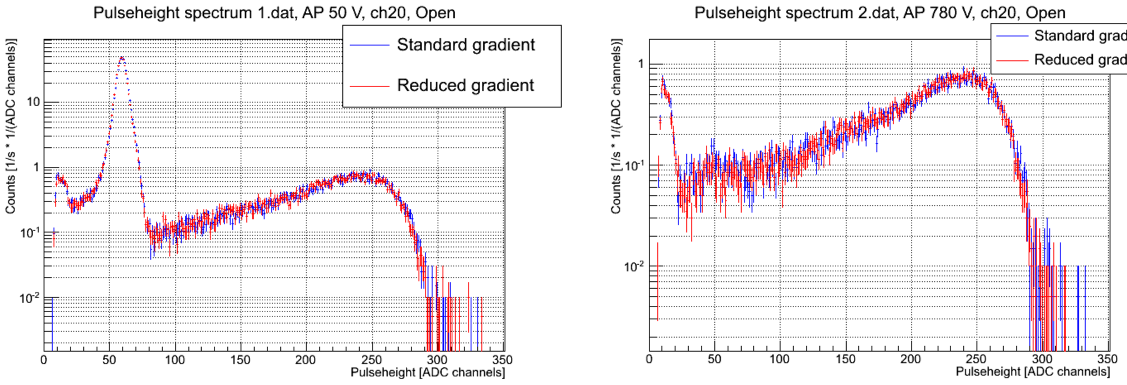

(a) AP at 50 V.

(b) AP at 780 V.

Figure 7.7: Comparison of spectrum measured with the standard and the reduced gradient in the DV. Measurement in Config. 2 and with the shutter opened for 200 s.

7.4.2 Tests with a reduced neutron beam profile

As described in Chapter 4, the neutron beam line is defined by a collimation system placed before the Decay Volume. And one of the apertures composing this system can be changed to a smaller one (see the neutron beam profiles in section 4.4.1). The purpose of using a reduced beam profile is to have two different edge effects so that we can check our simulation of these effects. The first consequence of a reduced neutron beam profile is a decrease in the count rate as shown in Fig. 7.8. The shift between the two spectra is explained by the temperature effect on the electronics as it is described in Chapter 3. The smaller aperture which was used for this test, was made in order to center the reduced neutron beam with the position of the detector (see section 4.4.2).

The background measured with the AP at 780 V is also influenced by this reduction as we see in section 6.5 that it is related to the neutron flux: the background is reduced. In Fig. 7.9(a), we note that the peak in the proton region observed with the standard beam profile, is not present with reduced profile. And in Fig. 7.9(b), the time dependence of the count rate in the proton region is reduced and can be approximated by a constant fit. The influence of a reduced neutron beam profile is more visible measuring with the electrode e15 in asymmetric configuration (see Fig. 7.10). This impacts on the extraction of the coefficient a_{blind} in this configuration (see Tab. 7.5).

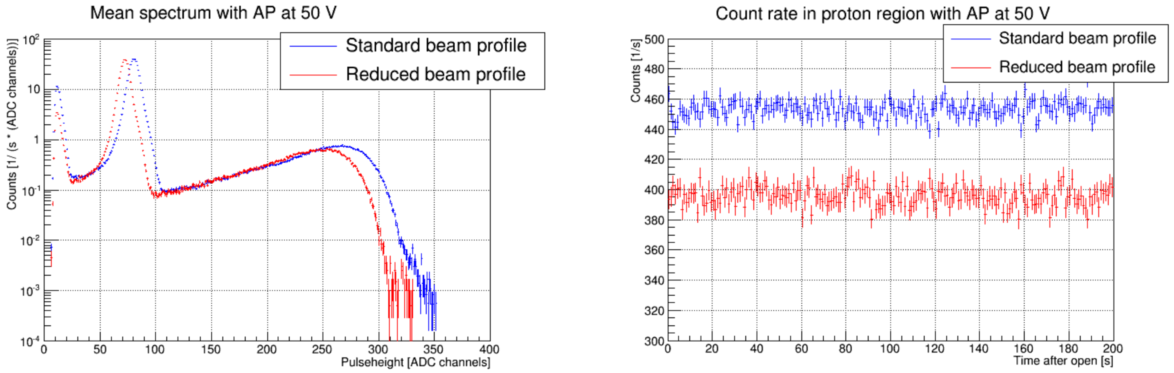

(a) Spectrum measured with the neutron shutter open.

(b) Evolution of the count rate in the proton region with the neutron shutter open.

Figure 7.8: Comparison between measurements with the standard neutron beam profile and the reduced one. Both measurements were made with AP at 50 V, and Config. 2. The measurement time with the standard beam profile was about 6.5 hours, and for the one with the reduced beam profile it was run for about 3.7 hours.

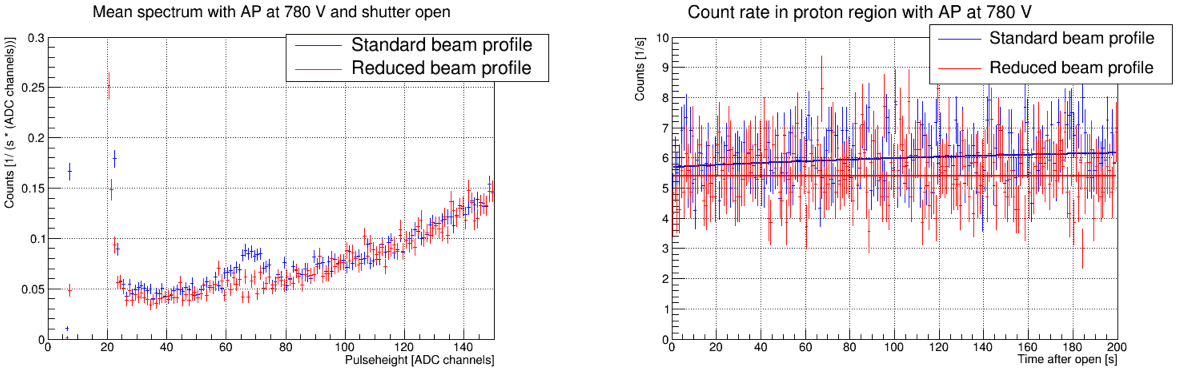

(a) Spectrum measured with the neutron shutter open. Zoom on the proton region.

(b) Evolution of the count rate in the proton region with the neutron shutter open.

Figure 7.9: Comparison between measurements with the standard neutron beam profile and the reduced one. Both measurements were made with AP at 780 V, and Config. 2. The measurement time with the standard beam profile was about 6.5 hours, and for the one with the reduced beam profile it was run for about 3.7 hours.

7.4.3 Coefficient a for the different systematics

From the measurements performed for the different systematic tests, we can extract the value a_{blind} for the coefficient. The proton spectra are built with the count rate corrections (proton peak position and dead time) but without background correction: the background is considered as an AP-independent offset in the fit function (4.3). For each considered configuration, the time of the measurement is referenced, the value a_{blind} is extracted and also the value of the offset. In the case of several measurements for a given configuration, a constant fit is applied to extract a mean value of the coefficient.

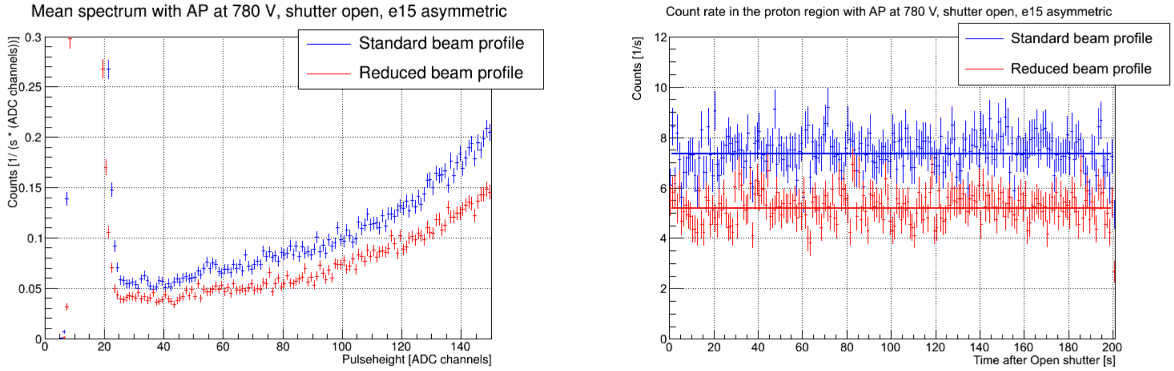

(a) Spectrum measured with the neutron shutter open. Zoom on the proton region.

(b) Evolution of the count rate in the proton region with the neutron shutter open.

Figure 7.10: Comparison between measurements with the standard neutron beam profile and the reduced one, with e15 asymmetric. Both measurements were made with AP at 780 V, and Config. 4 with just 200 s open time. The measurement time about 8.7 hours for both measurements.

Measurements with e15 symmetric, in standard configurations

These measurements were done with the Det-HV at -15 kV, the uExB at -1.75|-2.25 kV, the lExB at -1|-200 V, with the Mirror and with the electrode e15 in symmetric configuration. Typically, this configuration, called "standard", is optimized for the measurement of the coefficient a. The neutron shutter was opened during 200 s for each file. The extracted values of a_{blind} are presented in Tab. 7.1. The resulting average value of a_{blind} is obtained with a statistical uncertainty of about 1%.

Measurements	**Time [h]**	a_{blind}	**Offset [1/s]**	**Constant fit**	
				a_{blind}	χ^2**/ndf**
06/28, run 1	18.6	-0.1125(22)	5.283(27)	-0.1097(11)	4.2/3
06/29, run 2	16.7	-0.1059(24)	5.356(29)		
06/30, run 3	20.8	-0.1092(21)	5.122(25)		
07/02, run 4	18.8	-0.1105(23)	5.473(27)		

Table 7.1: Coefficients a_{blind} for standard measurements with e15 symmetric.

Measurements with e15 symmetric, with/without Mirror

These measurements have the same settings as the standard one. The difference is that the blocks of the continuous measurement structure alternate configurations with and without the electrostatic Mirror: one block with the Mirror switched on followed by a block with the Mirror switched off. The open time for the neutron shutter was 200 s. The results for a_{blind} in this configuration are presented in Tab. 7.2. The statistical accuracy of the averages is 3% only. As expected, the value with Mirror agrees with that from Tab. 7.1 (measurements with Mirror on only). Because of the magnetic gradient in the DV, the transmission function is not integrated to $\theta = 90°$ (see section 2.2.2) but to larger angles. This changes the transmission function and may explain the different result with Mirror off. A quantitative analysis needs to be done.

Measurements		**Time [h]**	$a_{\mathbf{blind}}$	**Offset [1/s]**	**Constant fit**	
					$a_{\mathbf{blind}}$	χ^2**/ndf**
07/05	Mirr	4.3	-0.106(4)	5.85(6)		
run 5 - 6	No Mirr	8.2	-0.104(5)	4.68(4)	$-0.1096(31)_{\mathrm{Mirr}}$	1.4/2
07/06	Mirr	2.2	-0.113(6)	5.97(8)		
run 7 - 8	No Mirr	6	-0.105(6)	5.23(4)	$-0.1038(30)_{\mathrm{No\ Mirr}}$	0.05/2
07/07	Mirr	2.2	-0.100(7)	6.33(8)		
run 9 - 10	No Mirr	5.8	-0.103(6)	4.58(4)		

Table 7.2: Coefficients a_{blind} for measurements with and without the Mirror, and with e15 symmetric.

Measurement with e15 symmetric, with a reduced $\overrightarrow{B}$ field gradient in the DV

This measurement (run 11) is presented in the section 7.4.1. It was done with the Det-HV at -15 kV, the uExB at -1.75|-2.25 kV, the lExB at -200|-1 V, with the Mirror and with the electrode e15 in symmetric configuration. The time of measurement was about 2.8 hours, and the open time for the neutron shutter was 200 s. This results in a coefficient $a_{\mathbf{blind}}$ of -0.100(7) and an offset from the fit function of 5.04(2). The proton integrated spectrum for this measurement was built with only three points: one for AP at 50 V, one for 500 V, and the last one for 780 V. The statistical uncertainty of the extracted value is 7%. With this large uncertainty, the result is consistent with the standard measurement in Tab. 7.1.

Measurements with e15 symmetric, in standard configuration but with different open time for the shutter

This kind of measurement is presented in the Chapter 6 about the background investigations. The runs were done with the Det-HV at -15 kV, the uExB at -1.75|-2.25 kV, the lExB at -200|-5 V, with the Mirror and with the electrode e15 in symmetric configuration. The blocks of the continuous measurement structure alternate open time of 50 s, 100 s and 200 s for the neutron shutter. The extracted coefficients a_{blind} are presented in Tab. 7.3. From these measurements, we find a statistical accuracy of about 3.9% for the average value in the case of the open time of

Measurements		**Time [h]**	$a_{\mathbf{blind}}$	**Offset [1/s]**	**Constant fit**	
	t_{Op}				$a_{\mathbf{blind}}$	χ^2**/ndf**
07/22	50 s	6.5	-0.108(7)	5.33(9)		
run 12, 13, 14	100 s	7	-0.109(5)	5.89(7)	$-0.108(4)_{50\mathrm{s}}$	0.5/3
	200 s	6.5	-0.109(4)	5.71(4)		
07/24	50 s	2.2	-0.102(12)	7.77(18)	$-0.1094(29)_{100\mathrm{s}}$	3.4/3
run 15, 16, 17	100 s	4.3	-0.101(6)	6.25(8)		
	200 s	2.3	-0.110(7)	5.76(8)	$-0.1082(23)_{200\mathrm{s}}$	6.2/3
07/25	50 s	2.2	-0.106(12)	5.24(15)		
run 18, 19, 20	100 s	4.3	-0.116(6)	6.46(8)		
	200 s	3.8	-0.099(5)	5.60(6)	$-0.1088(17)_{\mathrm{All}}$	10.3/11
07/25	50 s	6.5	-0.111(7)	6.32(9)		
run 21, 22, 23	100 s	4.3	-0.111(6)	6.62(8)		
	200 s	4.7	-0.115(5)	6.07(7)		

Table 7.3: Coefficients a_{blind} for measurements in standard configuration for different open times of the neutron shutter, and with e15 symmetric.

50 s, a statistical accuracy of about 2.7% for the open time of 100 s, and a statistical accuracy of about 1.8% for the open time of 200 s. The values for 100 s and 200 s agree with each other and with the standard measurements in Tab. 7.1. The values for 50 s is influenced by the statistical fluctuations and maybe also by the different background contribution (see Chapter 6). The average coefficient is consistent with the standard measurements.

Measurements with e15 asymmetric, in standard configuration but with different open time for the shutter

These measurements are also presented in the Chapter 6 in the same way as for the previous one. This time, the electrode e15 is set in asymmetric configuration: the e15_left electrode was connected to the electrode e11 (see details in the section 6.5.5). The results for the coefficients a_{blind} are presented in Tab. 7.4. In this configuration, the statistical accuracy for the open time of 50 s is about 4.9%, for the open time of 100 s it is about 2.7%, and for the open time of 200 s it is about 1.8%. For the value averaged over all the measurements, the result is close to the one with the e15 symmetric. A similar observation than in Tab. 7.3 is made for the measurement at 50 s: the value deviates due to the statistical fluctuation in these measurement conditions.

Measurements		**Time [h]**	$a_{\textbf{blind}}$	**Offset [1/s]**	**Constant fit**	
	t_{Op}				$a_{\textbf{blind}}$	χ^2**/ndf**
07/26	50 s	7.8	-0.105(7)	5.78(9)		
run 24, 25, 26	100 s	8.7	-0.109(4)	5.53(5)	$-0.103(5)_{\text{50s}}$	0.5/2
	200 s	8.7	-0.106(3)	5.95(4)		
07/27	50 s	2.2	-0.095(12)	6.84(17)	$-0.1106(30)_{\text{100s}}$	1.6/2
run 27, 28, 29	100 s	4.3	-0.107(6)	6.91(8)		
	200 s	2.2	-0.107(6)	5.88(8)	$-0.1077(22)_{\text{200s}}$	1.4/2
07/28	50 s	6.5	-0.103(7)	6.86(10)		
run 30, 31, 32	100 s	5.4	-0.117(6)	7.38(8)	$-0.1079(16)_{\text{All}}$	5.5/8
	200 s	6.5	-0.111(4)	5.48(4)		

Table 7.4: Coefficients a_{blind} for measurements in standard configuration for different open times of the neutron shutter, and with e15 asymmetric.

Measurements in standard configuration but with different open time for the shutter and with a reduced neutron beam profile

In Chapter 4, we described the neutron beam line and the collimation system. One of the aperture can be changed to a smaller one: this was presented in the section 7.4.2. This configuration was tested with the electrode e15 in the asymmetric configuration and in the symmetric one. The results from the fit are shown in Tab. 7.5. With the reduced neutron beam profile, the statistical uncertainty obtained on the average value is about 2.8% in the case of e15 asymmetric, and of about 3.4% with the e15 symmetric. The shift from the mean value in the "standard" configuration is about 2.7% with e15 asymmetric, and about 8.2% with e15 symmetric. These drifts may be explained by the edge effect for the full beam profile and the reduced beam profile. The asymmetric setting for e15 causes an additional drift of the protons which can change the edge effect. Therefore this may be visible in the symmetric case but compensated by the additional drift in the asymmetric case. For the full beam profile, the edge effect is smaller resulting in consistent a_{blind} values for the symmetric and the asymmetric e15 configurations. Simulations will be performed in order to quantify the edge effects for the different settings and to interpret the results of the systematic effects.

Measurements	t_{Op}	**Time [h]**	$a_{\mathbf{blind}}$	**Offset [1/s]**	**Constant fit**	
					$a_{\mathbf{blind}}$	χ^2**/ndf**
07/26	50 s	3.8	-0.112(10)	4.16(10)	-0.107(3)	0.5/2
run 33, 34, 35	100 s	4.3	-0.104(6)	3.71(6)		
e15 asymmetric	200 s	8.7	-0.108(3)	3.92(3)		
08/01	50 s	2.2	-0.123(13)	3.60(12)	-0.119(4)	0.2/2
run 36, 37, 38	100 s	2.2	-0.117(9)	3.88(9)		
e15 symmetric	200 s	3.7	-0.120(5)	4.11(5)		

Table 7.5: Coefficients a_{blind} for measurements in standard configuration for different open times of the neutron shutter, with a reduced neutron beam profile, and for both configurations for the electrode e15.

7.4.4 Preliminary results

The results of the raw analysis are presented and resumed in Fig. 7.11. We note some variations between the coefficients a_{blind} measured with different open times and for a given configuration. However, the values are consistent within the statistical errors of these measurements. The measurements with different systematic settings scatter between -4.5% and +8.2% relative to the value obtained with standard settings, whereas the statistical precision per configuration is about 1%. These differences are caused by different sizes of systematic effects between the settings. For example, some measurements were performed with a reduced beam profile which increases the edge effect. As indication for the size of the effect, the correction of the edge effect on the coefficient a was found to be -1.5% for the standard beam profile in 2008 [10]. The observed shift of a few percent for the reduced beam profile may therefore be due to the changed edge effect. Similar shifts may be expected for asymmetric e15 settings which also modify the

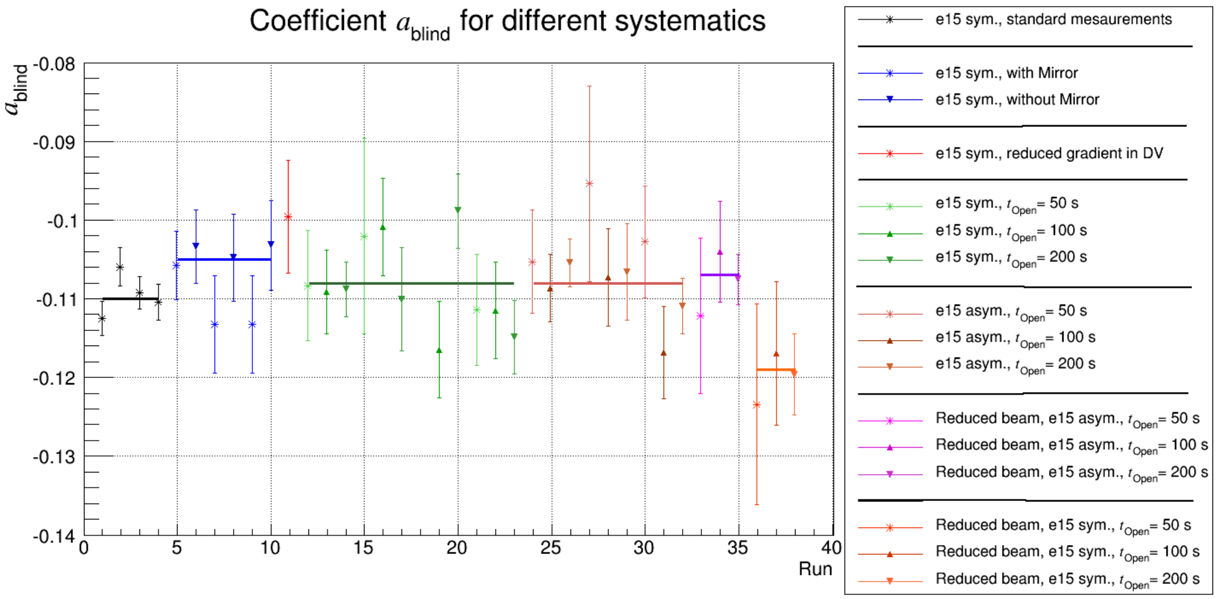

Figure 7.11: Coefficient a_{blind} extracted from the measurements with different systematics performed during the beam time in 2013. A constant fit is applied for the measurements of each configuration tested. These values are for the central pad of the detector and resulted from a raw analysis.

edge effect.

Furthermore, the background correction is not yet applied as more investigations are required in order to identify the best model for the background. With the models considered in this analysis, the background correction is up to 7% on the coefficient a, depending on the settings. Applying the background correction may reduce the difference between the results.

The corrections have to be calculated by simulations and after further studies of the background models. However, the observed small differences between the results with different settings are encouraging in the aim to obtain a final accuracy of 1% after applying the corrections.

Conclusion

Le spectromètre aSPECT a pour objectif d'obtenir le coefficient de corrélation angulaire a via une mesure précise du spectre d'énergie des protons émis dans la désintégration du neutron libre. Entre 2011 et 2013, plusieurs travaux ont été réalisés fin d'améliorer les performances du spectromètre tant sur le plan technique (surface des électrodes, qualité du vide...) que sur les méthodes d'analyse. Au cours de cette thèse, j'ai participé à la mise en place de nouveaux composants notamment pour le système de détection. Ceci a permis de supprimer des problèmes de saturation électronique rencontrés précédemment tout en conservant une excellente séparation des évènements protons par rapport au bruit électronique. Les protons étant émis à des énergies inférieures à 1 keV, ils sont sélectionnés par une barrière de potentiel, accélérés par un potentiel de -15 kV et ensuite comptés par le détecteur (Silicon Drift Detector). Le spectre des protons est dérivé des mesures à différentes tensions pour la barrière de potentiel.

L'observation de décharges en 2011, a conduit au point central de ma thèse concernant l'analyse du bruit de fond. En ajustant le barrière de potentiel en présence du faisceau de neutrons il est possible de bloquer tous les protons et de mesurer ainsi un bruit de fond principalement dominé par les électrons issus de la désintégration du neutron. Ce taux de comptage est de l'ordre de 5 Hz dans la région d'amplitude des protons (pour le plus bas potentiel de sélection, le taux de comptage est de l'ordre de 440 Hz). En 2012, des mesures hors faisceau de neutron ont révélé la présence d'un bruit de fond "interne". Il s'agit principalement de rayons-X, dus aux processus d'émission par effet de champ, et d'ions provenant de l'ionisation des molécules du gaz résiduel ou des adsorbats de surface. Ce gaz a été identifié via une analyse de spectrométrie de masse et est principalement composé d'hydrogène, d'eau et d'azote. Ce bruit de fond induit un taux de comptage dans la région des protons de l'ordre de 10^{-2} Hz et présente une sensibilité aux conditions de vide et à la configuration des électrodes. Selon les simulations, son influence sur $\frac{\Delta a}{a}$ est de l'ordre de 10^{-5} à 10^{-4} suivant les conditions de mesure. Toujours en étant hors faisceau, l'impact des électrons a été mesuré à l'aide d'une pastille d'or activée placée dans le spectromètre. En plus du bruit de fond généré par leur détection, les électrons ionisent le gaz résiduel. Ceci résulte en une composante additionnelle du bruit de fond "interne" qui impact sur $\frac{\Delta a}{a}$ à l'ordre de 10^{-4} .

L'analyse du bruit de fond a été complétée avec les données du temps de faisceau en 2013. Durant la période où le faisceau traverse le spectromètre et avec la barrière de potentiel bloquant tous les protons, on observe une dépendance dans le temps du taux de comptage. Cette dépendance peut être modélisée par une fonction dont le premier paramètre renvoie au bruit de fond constant dominé par les électrons et le second terme exponentiel concerne un bruit de fond non-constant, dû à des particules piégées, de l'ordre de 10^{-1} Hz. Cette dernière composante se révèle également dépendante sur la tension de la barrière de potentiel : après fermeture du faisceau, un taux de comptage supérieur à celui mesuré avant l'ouverture du faisceau est détecté plus élevé pour les hautes tensions appliquées sur la barrière de potentiel. Cette dépendance peut être décrite par une fonction (plusieurs fonctions ont été testées) qui, combinée avec le terme exponentiel de la dépendance dans le temps, permet de construire un modèle du bruit de fond non-constant pour les différentes tensions de la barrière de potentiel. Cette correction de bruit de fond sur $\frac{\Delta a}{a}$ est de l'ordre de 3% pour des mesures standards et jusqu'à environ 7% dans des conditions non-favorables.

Afin de réduire le bruit de fond pendant les mesures, un nouveau champ électrique de dérive est généré au-dessus de la barrière de potentiel. Au cours des mesures avec tous les protons bloqués, on note une diminution de la contribution dépendante dans le temps, dans la région des protons, d'environ 75% par rapport aux mesures standards précédentes. La dépendance dans le temps précédente est toujours présente mais avec des paramètres plus faibles comme par exemple une constante de temps plus courte que dans le cas standard. L'impact d'une correction de bruit de fond, avec e15 asymétrique, sur le coefficient a est d'environ 2% à 4% par rapport à la valeur obtenue dans les mêmes conditions et sans correction.

Il faut noter que la statistique des données présentées permet certaines approximations pour le modèle du bruit de fond. Cependant, des investigations détaillées avec plus de statistiques fourniront d'avantage d'information sur les incertitudes systématiques De plus, l'utilisation d'un potentiel électrique de dérive supplémentaire a probablement un impact sur les effets de bord qui doit être estimé. Pour cela des mesures complémentaires et des simulations seront effectuées.

Plusieurs configurations expérimentales, complémentaires à celles standards, ont été testées, comme la suppression du miroir électrostatique (angle solide de détection d'environ 2π) ou encore la réduction du profil de faisceau de neutrons. La précision statistique $(\frac{\Delta a}{a})_{\mathrm{stat.}}$ était d'environ 1% dans les conditions standards et de 3.4% dans le cas d'un faisceau de neutrons réduits. Une analyse brute sans aucune correction montrent des différences entre les valeurs du coefficient a pour différentes configurations d'environ $\pm 5\%$. Ces différences sont de l'ordre des corrections attendues pour les effets systématiques. Dans la suite de l'analyse, le modèle de bruit de fond doit être affiné et les corrections des effets systématiques doivent être calculées via des simulations. La conclusion principale de cette analyse préliminaire est que les résultats sont encourageants dans la détermination du coefficient a avec une précision de 1%.

Conclusion

The aim of the spectrometer *a*SPECT is to obtain a value of the angular correlation coefficient *a* from a precise measurement of the proton spectrum in free neutron decay. From 2011 to 2013, several improvements were realized to optimize the technical characteristics of the spectrometer (electrode surfaces, vacuum...) and the methods for the analysis. During this PhD thesis, I participated in the implementation of new components especially for the detection system. This allowed us to avoid an earlier electronic saturation problem while maintaining the excellent separation of the proton events from the electronic noise. As the protons are emitted with energies below 1 keV, they are energy-selected by a potential barrier, accelerated by a -15 kV potential and then counted by the detector (Silicon Drift Detector). The proton spectrum is derived from measurements with different voltages for the potential barrier.

The observation of discharges in 2011, led to the central point of my thesis about the background analysis. By adjusting the potential barrier in the presence of the neutron beam, it is possible to block all protons and to measure the background dominated by the electrons from neutron decay. This count rate is of the order of about 5 Hz in the proton region of the pulse-height (for a low voltage of the potential barrier, the count rate is about 440 Hz). In 2012, measurements without neutron beam have revealed an "internal" background. It consists mainly of X-rays, due to field emission processes, and ions from the ionization of rest gas molecules or surface adsorbates. This gas was identified using mass spectrometer measurements and it is mainly composed of hydrogen, water and nitrogen. This background induces a count rate of the order of 10^{-2} Hz in the proton region and is sensitive to the electrode settings and the vacuum conditions. From simulations, its influence on $\frac{\Delta a}{a}$ is of the order of 10^{-5} to 10^{-4} depending on the measurement conditions. Still without neutron beam, the influence of electrons was measured by placing an activated gold foil inside the spectrometer. In addition to their detection, the electrons ionize the rest gas. This results in an additional background to the "internal" one with an influence on $\frac{\Delta a}{a}$ of the order of 10^{-4}.

The background analysis was completed with data from the beam time of 2013. In the presence of the neutron beam and with all protons blocked by the potential barrier, we observed a time dependence of the count rate. This dependence can be modeled by an exponential build-up function with a constant offset. This last term represents the constant background dominated by the electrons. In saturation the build-up term contributes at the order of 10^{-1} Hz and corresponds to a non-constant background due to trapped particles. This contribution was also found to depend on the voltage of the potential barrier: after closing the beam, the count rate is higher than before opening the neutron beam and it is higher for a high voltage applied to the potential barrier. This dependence can be described by a function (different functions were tested) combined with the exponential build-up time dependence to model the non-constant background for all barrier potential voltages. This background correction on $\frac{\Delta a}{a}$ is at the order of 3% for standard measurements and up to about 7% in unfavorable configurations.

In order to reduce the background during measurement, an additional drift electric field was generated above the potential barrier. By measuring with all protons blocked, we observed a decrease of the time-dependent contribution in the proton region of about 75% from the value without the new drift field. The previous time dependence is still present but with improved parameters as for example a shorter time constant compared to the one in standard configuration. The influence of the background correction, with e15 asymmetric, on the coefficient a is about 2-4% from the value obtained in the same configuration without correction.

Several experimental configurations, complementary to the standard one, were tested, as for example without the electrostatic mirror (detection in a solid angle of about 2π) or with a reduced neutron beam profile. The statistical accuracy $(\frac{\Delta a}{a})_{\text{stat.}}$ was about 1% in the standard conditions and 3.4% in the case of a reduced beam profile. A raw analysis without any corrections showed differences between the coefficients a for the different configurations of about ±5%. These differences are of the order of the expected corrections for systematic effects. In the further analysis, the background model has to be refined and the corrections of systematic effects have to be calculated by simulations. The main conclusion of this preliminary analysis is that the results are encouraging in the aim to determine the coefficient a with an accuracy of 1%.

Appendix A

Vacuum procedures

In order to reach a good vacuum at the order of 10^{-9} mbar inside the main volume of *a*SPECT, we follow a procedure consisting of different steps. At the end of the installation of the spectrometer, the electrodes system, the uExB electrodes are inside. The top aperture is closed with the shutter, the bottom chamber is also installed. The windows are mounted at the entrance and the exit side of the Decay Volume. On the side ports, the external getter pump is mounted behind a shutter which is closed at the beginning, and on the other side, the cross-piece. On this cross-piece, a turbo pump is mounted connected to a primary pump. Between these two pumps, a second turbo pump is connected in cascade to improve and stabilize the vacuum. As the detector mechanics is not yet installed at the beginning, another turbo pump is connected to the top aperture (at the shutter above the uExB). This turbo pump is also connected to a cascading pump and finally to a primary one.

First, we started to pump with the primary and turbo pumps on the top and at the cross-piece. When the pressure decreased below 10^{-1} mbar, the cascading pumps are activated to improve the pumping efficiency. In Fig. C.1, we observed that the pressure decreased quickly in the first hours after switching on the pumps. At this step, we connected a leak tester after the cascading pump at the bottom. This leak tester used is from Pfeiffer vacuum [66] and allows detecting any change in pressure when we spray the different flanges and tubes connections with helium (see Fig. C.2). After fixing the potential found leaks, the pumping continues and to further improve the vacuum, outgasing was made on the tubes (see Fig. C.1). For this, the

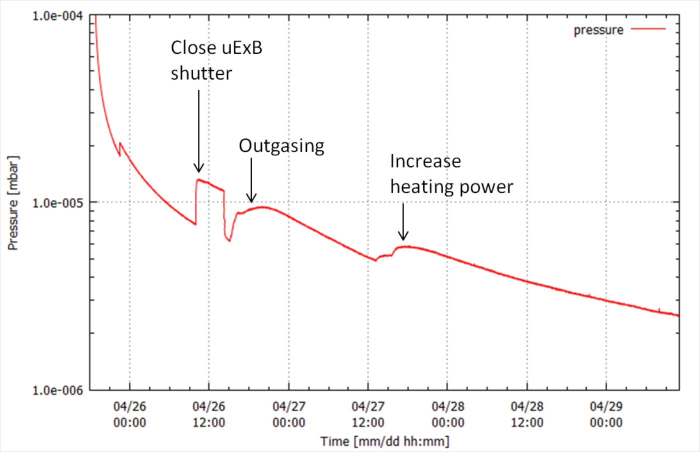

Figure A.1: First step to achieve good vacuum in *a*SPECT. The shutter at the uExB was closed in order to test the connection and to be sure that there is no leak at this place.

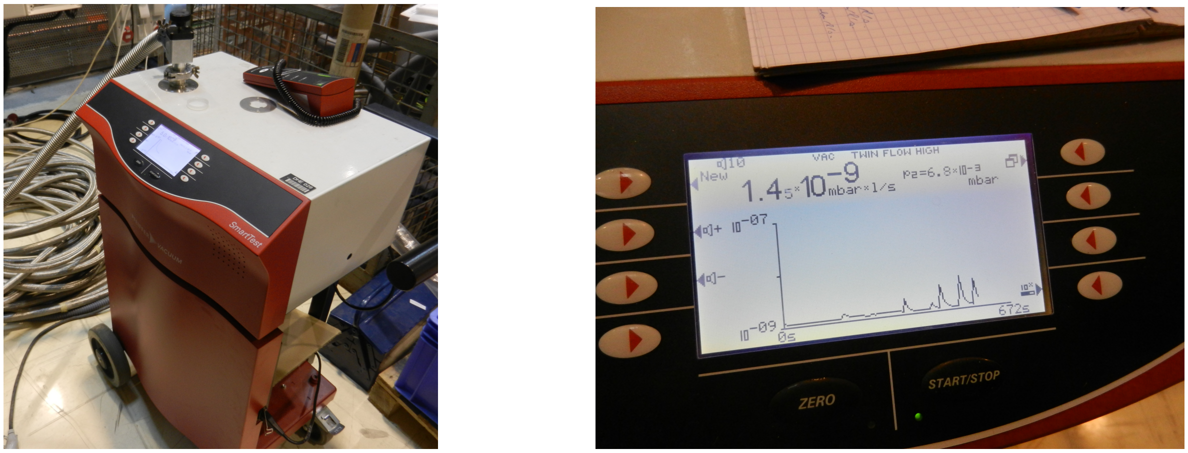

(a) Leak tester.

(b) Level of small leaks detected.

Figure A.2: Leak search in *a*SPECT.

cross-piece, the bottom chamber, the tube of turbo pumps... are surrounded with heating bands. Step by step, we increased the heating power and the pressure increased inside the main volume meaning that molecules were removed from the surfaces of tubes. These molecules were then evacuated by the pumping efficiency and the pressure started to decrease again.

In a second main time, the internal getter pumps connected to the electrodes system were activated (see Fig. C.3). This kind of pumps adsorbs gases by a chemical reaction. They use

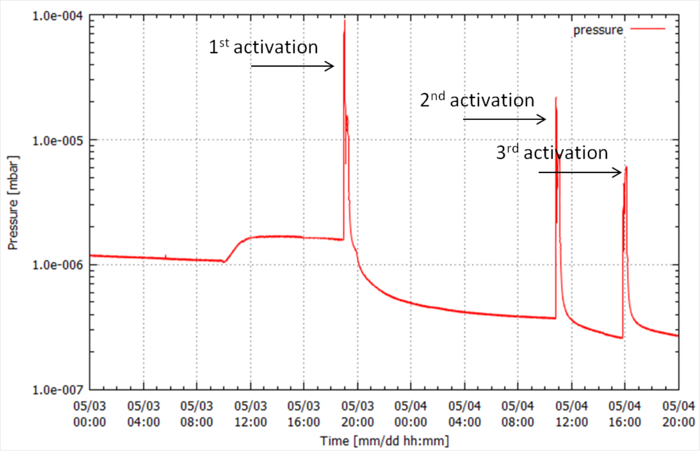

Figure A.3: Activation of the internal getter pumps.

very reactive alloys, generally made of zirconium or titanium, which are configured in a high efficiency getter cartridge structure. Active gas molecules colliding against the cartridge surface are dissociated and trapped in the form of stable chemical compounds. But first, the getter pump has to be activated by heating the cartridge at a certain temperature (∼400-500 °C) and for a given time (∼1 hour) [71]. This treatment allows surface oxides and carbides covering the surface to decompose and diffuse inside the getter material bulk structure, leaving a clean and reactive metal surface, available to gas sorption. This is the similar procedure for the external pump which was activated before to be connected to the main volume of *a*SPECT. The shutter behind the external getter pump then stayed closed.

In the last step, the vacuum is quietly stabilized after the activation of the internal getter pump, after opening the shutter for the external getter pump, and after stopping the outgassing processes. In Fig. C.4, the cryocoolers were switched on and the temperature started to decreased

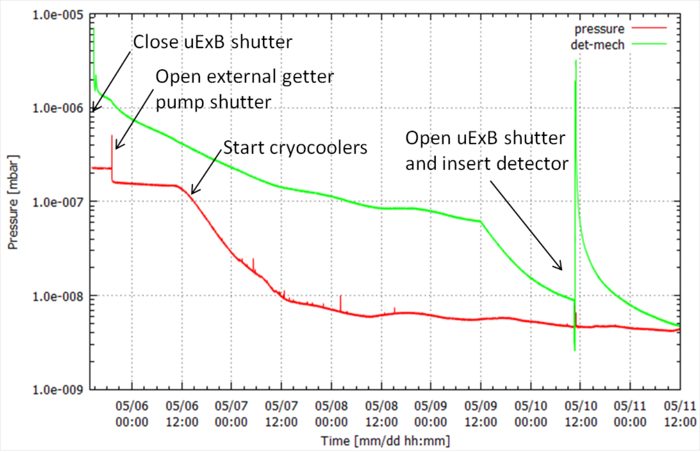
Close uExB shutter
Open external getter pump shutter
Start cryocoolers
Open uExB shutter and insert detector

Figure A.4: Cool down the cryostat and installation of the detector mechanics. The pressure in the main volume is still indicated in red and the pressure inside the detector mechanics (det-mech) is in green.

and well as the pressure. The turbo pump on the top was removed after closing the shutter at uExB. This was to install the detector mechanics with the detector placed inside. The mechanics was fixed on the top of the shutter and was then pumped by two turbo pumps connected to one cascading pump and a primary pump. The pressure in the main volume was stabilized after reaching the low temperature of the cryostat. In parallel, outgassing was applied to the detector mechanics where the pumping efficiency is quite higher due to the small volume to pump and the presence of two turbo pumps. After a couple of days, the shutter at uExB was opened without perturbation of the main volume (this problem was solved after the beam time of 2011). Then the detector was slowly introduced in the main volume. However this action induced a spike in the pressure of the detector mechanics due to some rest gas molecules still being inside. Finally, the pressure is stabilized in the order of 10^{-9} mbar in the main volume.

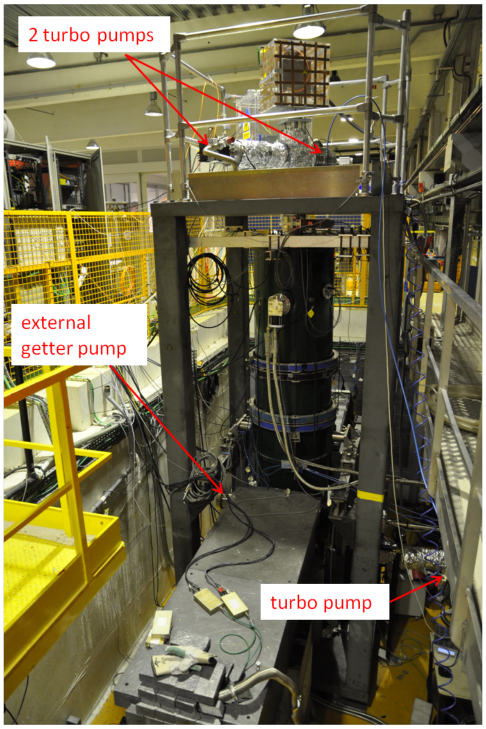

Figure A.5: Different external pumps connected to the spectrometer aSPECT installed at PF1b at ILL in 2013.

Appendix B

Magnetic field measurement

To complete a beam time with *a*SPECT, a magnetic field measurement is performed. The principle of the adiabatic transmission, explained in Chapter 2, is strongly related to the magnetic field intensity in the Decay Volume and the one in the Analyzing Plane. For this, we measured the magnetic field using a hall probe inserted along the z-axis inside the main volume. So, the spectrometer is empty: no electrodes, no detector mechanics... However, to switch on the magnet, the coils have to be cold but if the top and bottom apertures stay opened, the cooling efficiency would not be good enough. Therefore, a Dewar tube is inserted in the main bore tube: its external diameter is equal to the internal diameter of the main bore tube. The Dewar is fixed at the top and bottom of the cryostat. The principle of this kind of tube is that it has double walls with an evacuated space between them. This space is filled with water which is renewed via a circuit allowing to keep a thermal isolation between the cold bore tube and the space at the open air (see Fig. D.1).

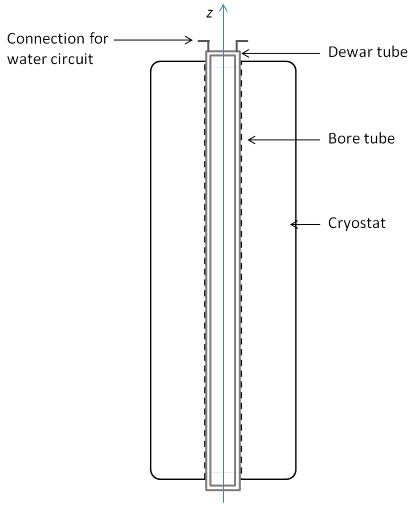

Figure B.1: Simplified sketch of the installation of the Dewar tube inside the main bore tube. The free space between the double walls of the dewar is filled with water to isolate thermally the cryostat from the open air space in the center. Then, the hall probe can be moved from the top aperture along the z-axis until the bottom aperture.

The hall probe used for the magnetic field measurement of *a*SPECT is provided by Group3 Technology Ltd.® [72]: a miniature standard sensitivity hall probe (MPT-141 with DTM-151 teslameter). This is a small hall probe that we fixed on a cylinder holder which is also fixed to a graduated rod. This hold is introduced inside a guiding tube of about 2 cm diameter placed along the z-axis in the center of the Dewar tube.

The distance of the hall probe is calculated considering the center of the Decay Volume as z = 0. First, the sensitive area of the hall probe was centered on the z-axis. The Fig. D.1 shows a complete scan of the magnetic field along the z-axis. A more detailed scan is necessary on the Decay Volume: a small slope of the magnetic field is present in this region and can be adjusted by the correction coil. The other aim of a precision measurement in the DV is to know the ratio between the magnetic field in the AP and the one in the DV: this ratio is a parameter of the transmission function and so an important part of the adiabatic motion of the protons inside the spectrometer.

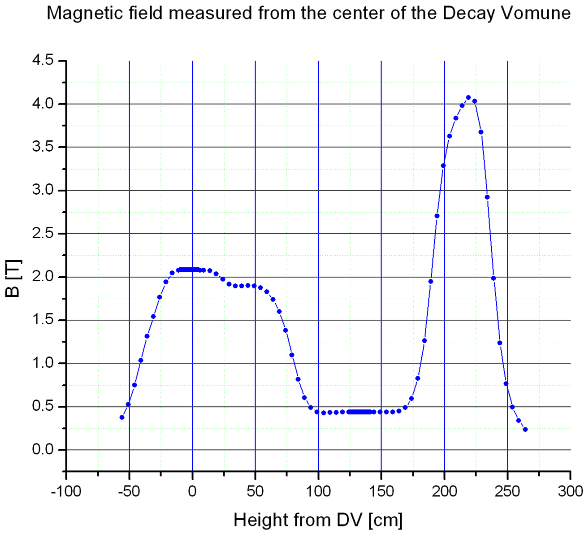

Figure B.2: Magnetic field along the z-axis.

Appendix C

Data files structure

This Appendix is based on the information from [8]. After the acquisition, data are recorded in a ".dat" file for each measurement. These files have a quite inconvenient structure to work with. The data are transferred to the structure of the ROOT data analysis framework with a program called "online_decode" developed by previous users. We adapted this program to the new shaper during the beam-time in 2011, "online_decode_new". For each ".dat" file we obtain a ".root" file containing a tree with information about the measurement [57]. During the decoding process, the events are read from the data file, analyzed and filed into the tree. The tree consists of 9 branches used for the analysis:

- "channel_id" refers to the channel of the sADC in which the event occurred. With the new shaper, six channels are used: 19, 20 and 21 are called the "protons" channels, 22, 23 and 24 are called the "beta" channels.
- "HistMax" is the highest ADC value for each event.
- "Baseline_value" is the average value of the first 15 ADC bins, calculated during the decode process. In combination with "HistMax", the pulse-height can be calculated for each event.
- "timestamp" represents of clock cycles of the sADC. In the raw data structure, 30 bit are reserved for this value. The clock frequency is of 20 MHz which leads to an overflow every 53.7 s. If the length of the measurement is longer, the "timestamp" starts at 0 again.
- "time_interval" is increased by one when the "timestamp" starts to 0 again. So the time t_{evt} at which an event occurred can be calculated as:

$$t_{\text{evt}} = \frac{t_{\text{stamp}}}{2 \cdot 10^7} + t_{\text{interval}} \frac{2^{30}}{2 \cdot 10^7} \tag{C.1}$$

- "time_diff_us" gives the time difference of the current to the previous event in microseconds. This is calculated from $t_{\text{evt}}$for two consecutive events.
- "nslices" is the length of the event as number of sADC bins.
- "adc_slices" is an array with the length specified in "nslices" which contains the single value of each ADC bin that was stored around the event.
- "evtype" refers to the type of the event. The type 1 is for the normal data events, the type 2 for the events written in the heartbeat mode of the sADC, and the type 3 for the events from the temperature sensor.

Appendix D

New Data Acquisition system

In 2013, we decided to test a new data acquisition system provided by the Instrument Control Service of the ILL. This team has developed their own instrument control software called NOMAD. It is written in C++ and Java and they can adapt it to an experiment. The problem with the actual DAQ system of aSPECT, is that it was developed by the group E18 at the Technical University Munich for the COMPASS experiment: this means no direct support available in case of incident. On the other hand, it is connected to a quite "old" computer with very specific hard- and software. This computer communicates with another one to control all the system of aSPECT: acquisition, electrodes settings, pressure and temperature reading...

Figure D.1: New DAQ.

The new acquisition system is built around a commercial Analog to Digital Converter (ADC): a V1724 card made by CAEN[1]. This V1724 is equipped with an 8 channels, 14 bit and 100 MHz sampling frequency flash ADC[2]. There are also several FPGAs dedicated to the energy calculation of an event directly implemented on this card. The main difference compared to the old DAQ is the high resolution (14 bits instead of 12 bits). Thus the full dynamic range of the preamplifier can be covered still providing sufficient resolution for the small proton signal. With this system, the shaper is no longer required: the digitization is made as soon as possible, just after the preamplifier. Once digitized the signal is directly treated by the algorithms programmed into the FPGAs of the board. The digital treatment has advantages as a great reproducibility and a great flexibility through FPGAs programmation.

This new DAQ is too big to be installed inside the plexiglas box on the top of the spectrometer. It was installed inside the second plexiglas with the power supply and the transformer. A new cable was made to connect the output signal from the preamplifier to the input of the new DAQ.

---

[1] Costruzioni Apparecchiature Elettroniche Nucleari. This company is specialized in "the design, the production and the supply of electronic instrumentation for radiation and low light sensors".

[2] A flash ADC compares the input voltage with a certain number of reference voltages. All those comparisons are made at the same time, in parallel, resulting in a very high sampling rate. However the better the resolution the more comparators you need: $2^n - 1$ for a n-bit conversion.

The isolation was improved as there is still the high voltage for the acceleration potential of -15 kV.

The energy calculation with the new DAQ is made via a trapezoidal filter applied on the input signal directly at the V1724 board. This digital filter transforms the typical exponential decay signal into a trapezoid, as shown in Fig. B.2. The baseline value is calculated by averaging a certain number of trapezoidal filter samples before the pulse. The rise and fall time are always the same. The flat top level allows to determine the energy by subtracting the baseline value from it. The longer the sampling time (trapezoid length), the better the energy resolution but also the pile-up probability. The energy is directly proportional to the height of the flat top of the trapezoid minus the baseline value and is given as a 15 bit integer. All those parameters (baseline length, rise time of the trapezoid, flat top length etc.) can be defined in NOMAD which serves as interface.

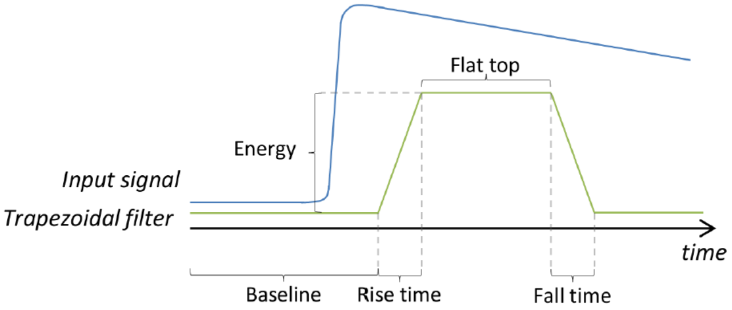

Figure D.2: Energy calculation.

In comparison with the actual DAQ system, the time resolution of the new one is 10 ns. In order to treat only the relevant data, a digital pulse triggering filter continuously analyses the input signals. To efficiently discrime noise and not to loose any event, this trigger algorithm is a digital version of an analog RC-(CR)^2 filter. The RC filter (also called integration filter) is a low-pass filter and thus suppresses high-frequency noise whereas the CR filter (also called derivative filter) is a high-pass one and suppresses low-frequency noise such as ground loops. It also applies a baseline restorer, resulting in a very stable baseline for the trigger.

After the filter treatment, the pulse is transformed into a bipolar signal (see Fig. B.3). When the signal amplitude goes above the threshold value the trigger is armed and it is only when the baseline ("zero") is crossed again that the trigger signal is sent: it is the “timestamp” of the triggered event. As a result the definition of the “timestamp” of an event is not dependent of the pulse amplitude.

Once a trigger is sent the event is saved and the corresponding window is defined by the total number of samples and the number of samples before the trigger, as shown in Fig. B.4. During this window no other events can be saved[3] and piled-up events that occur in the event window can be treated with an offline analysis.

The data structure. The acquisition output from NOMAD is a "list mode" binary file (extension .lst) with a defined structure (see Fig. B.5): it is a succession of 32 bit words, with the 4 first words of a file being "dummy words" and thus ignored. For a 4 μs event length, each event will be composed of 203 words. The first one is the number of ADC slices divided by 2. Since

---

[3] An online pile-up rejection system is available on the new DAQ but his behavior is not reliable: for unknown reasons the timestamp is lost when a pile-up occurs with this option activated. As a result it was not used.

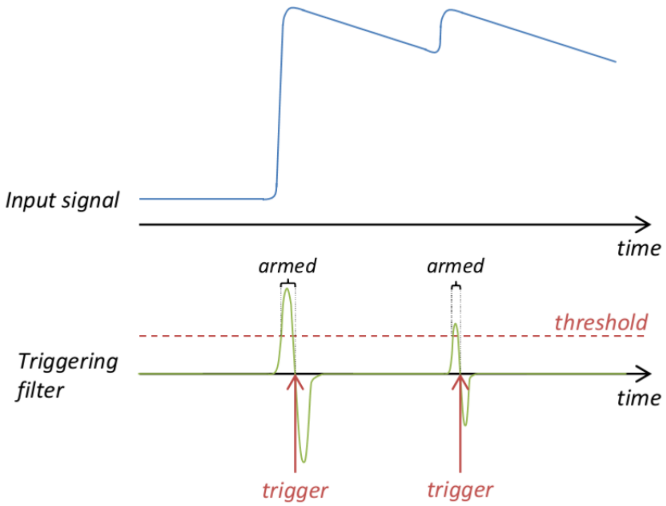

Figure D.3: Trigger example for two consecutive events. When the triggering filter signal exceeds the threshold, the trigger is armed and will only be sent when a zero-crossing occurs. However if the trigger is armed and no zero-crossing happens before a defined delay, no trigger will be sent.

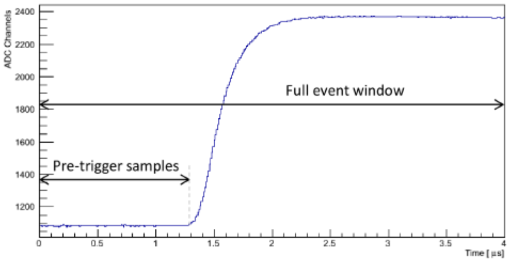

Figure D.4: Example of an event waveform with the new DAQ.

the time resolution is 10 ns all events contains 400 ADC slices, meaning that the first word will always be 200. The next 200 words are those ADC slices, with a 14-bit resolution. Finally the two last words contain the board number (in case of multiple ADC cards), the channel number of the event, the energy calculated from the trapezoid filter, the time interval (called TimeLoop counter in Fig. B.5) and the timestamp of the event. The “timestamp” has a 30 bit resolution. Therefore, after about 10.74 s (10 ns × 2^{30}) of acquisition this value is reset to 0 and the time interval is incremented by one (see Appendix C).

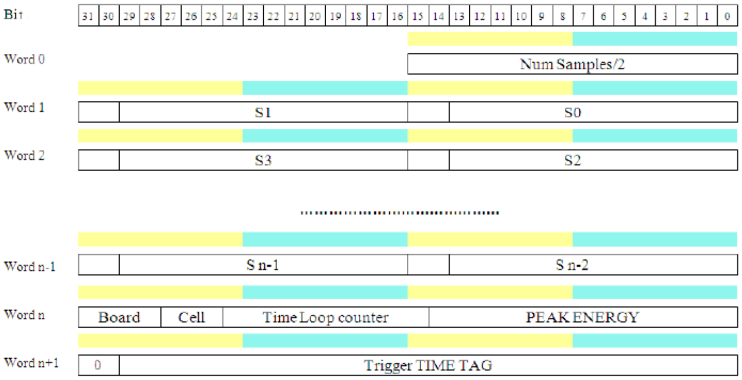

Figure D.5: List mode data structure of the NOMAD output binary file.

Appendix E

Perspectives for the proton asymmetry measurement

The spectrometer *a*SPECT was designed to measure with high precision the proton energy spectrum from neutron decay. This can be used for the measurement of the proton asymmetry parameter C. As shown in Fig. 1.3, the proton asymmetry is a coefficient defined between the proton momentum (noted $\uparrow$) and the spin of the neutron (noted $\Uparrow$). This parameter can be expressed in terms of the beta asymmetry coefficient A and the antineutrino asymmetry coefficient B, and also in terms of the ratio of the weak coupling constants [75]:

$$C = -x_C(A+B) \quad \Longleftrightarrow \quad C = x_C \frac{4\lambda}{1+3\lambda^2} \tag{E.1}$$

with $x_C = -0.27484$.

Experimentally, the proton asymmetry parameter C is related to the difference between the rate of protons emitted in the same direction as the neutron's spin, $N^{\Uparrow\uparrow}$, and the rate of protons emitted in the opposite direction, $N^{\Downarrow\uparrow}$ [7, 20, 73]. Thus, the parameter C measured experimentally can be expressed with the following equation:

$$C_{\text{exp}} = \frac{N^{\Uparrow\uparrow} - N^{\Downarrow\uparrow}}{N^{\Uparrow\uparrow} + N^{\Downarrow\uparrow}} \tag{E.2}$$

The proton rates are inferred from the proton spectra measured with a polarized neutron beam: in a first time with the spin *up* ($\Uparrow$) and in a second time with spin *down* ($\Downarrow$). From Fig. E.1, the protons count rates are integrated on each spectrum in order to calculate C. In comparison with the *a*SPECT experiment described in Chapter 2, a new condition has to be considered: the polarization of the neutron beam.

The last measurement of C was done with the experiment PERKEO II in 2008 at ILL and gave the last value of the proton asymmetry coefficient, $C = -0.2377(26)$ [73]. This result has a statistical precision of 0.4% and a systematic precision of 1%. For this experiment, the neutron beam at PF1b was polarized using two super mirrors polarizer in X-SM geometry [74].

One characteristic of the spectrometer *a*SPECT is that it measures protons in solid angle of 4π thanks to the electrostatic Mirror electrode placed below the Decay Volume (see Fig. 2.1). But, for the proton asymmetry, we want to measure protons in a single direction (same or opposite as neutron's spin). So, the Mirror electrode would have to be set to 0 V for this measurement. Using a polarized neutron beam, the principle would be to measure protons with

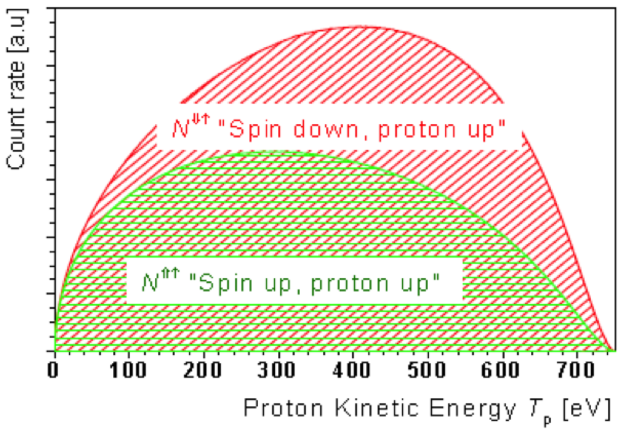

Figure E.1: Energy spectra of the protons emitted in the direction of the neutron's spin (green) and of the protons emitted in the opposite direction (red).

a neutron's spin *up* beam and then with a neutron's spin *down* beam. The protons would be detected in one hemisphere, and the equation (E.2) has to be completed:

$$C_{\text{exp}} = \frac{N^{\Uparrow\uparrow} - N^{\Downarrow\uparrow}}{N^{\Uparrow\uparrow} + N^{\Downarrow\uparrow}} = \frac{C}{2} \tag{E.3}$$

Considering the experimental measurement with *a*SPECT, we can estimate the statistical accuracy which could be reached for a proton asymmetry measurement with this experiment. During the beam time of 2013, we performed measurements without the Mirror electrode. After applying the corrections (see Chapter 7) and subtracting the background, the count rate measured in the protons region without Mirror is $(222.05 \pm 0.18)\,\text{s}^{-1}$ (this value was calculated with the AP at 50 V and for the central pad of the detector). This count rate was obtained with an unpolarized neutron beam: this value "contains" protons emitted both in the direction of the neutron's and in the opposite direction. Thus, we assume the following consideration: $N = N^{\Uparrow\uparrow} + N^{\Downarrow\uparrow} = 222.05\,\text{s}^{-1}$ per pad. This is the case with an unpolarized neutron beam.

To measure the parameter C with *a*SPECT, we would need to add a polarizer in the neutron beam line. For the PERKEO II experiment, the polarizer system used was two super-mirrors in a cross-geometry [74]. According to the investigations and measurements, this system induced an attenuation of the neutron beam intensity by about 12%. Thus, the total count rate N is considered to be attenuated by a factor 10. In order to compensate for this loss of events, we propose to increase the surface of detection by using a 3×3 pads detector. This new SDD would have nine pads but the four on the corners would be too close to the detector cup. They would be affected. So, we would consider five pads and we could expect that $N = 111.03\,\text{s}^{-1}$ for the five pads. The estimation of the statistical accuracy of the parameter C is calculated using the statistical error of the count rate as $\sqrt{N}$.

$$\left(\frac{\Delta C}{C}\right)_{\text{stat}} = \sqrt{N}\left(\frac{1}{N^{\Uparrow\uparrow} + N^{\Downarrow\uparrow}} + \frac{1}{N^{\Uparrow\uparrow} - N^{\Downarrow\uparrow}}\right) \tag{E.4}$$

Using the equation (E.3), the statistical accuracy of the proton asymmetry can be rewritten:

$$\left(\frac{\Delta C}{C}\right)_{\text{stat}} = \frac{1}{\sqrt{N}}\left(1 + \frac{2}{C}\right) \tag{E.5}$$

We take the actual world value $C = -0.2377$. In the case where we consider ten days of measurement with spin up and spin down, we could expect an statistical precision on the proton asymmetry of $\left(\frac{\Delta C}{C}\right)_{\text{stat}} = 0.08\%$.

Another system could be used to polarize the neutron beam. It was investigated at the neutron beam line of PF1b at ILL by Christine Klauser: opaque cells of polarized ^{3}He filter [76]. The last results show that the polarization of the beam can be obtained at the level of 10^{-4}. The attenuation of the neutron beam intensity induced by this system is about 6-7%. This could help to increase the precision of the measurement.

As mentioned above, some modifications would be proposed for the detector. To compensate the loss of count rate due to the polarizer system, we will use three detectors placed side by side. However, as shown in Fig. E.2, the pads in the corner would be affected by additional edge effects from the detector cup electrode around. That is why, we will consider five pads for the count rates measurements. The four other pads could give information about, for example, the edge effect.

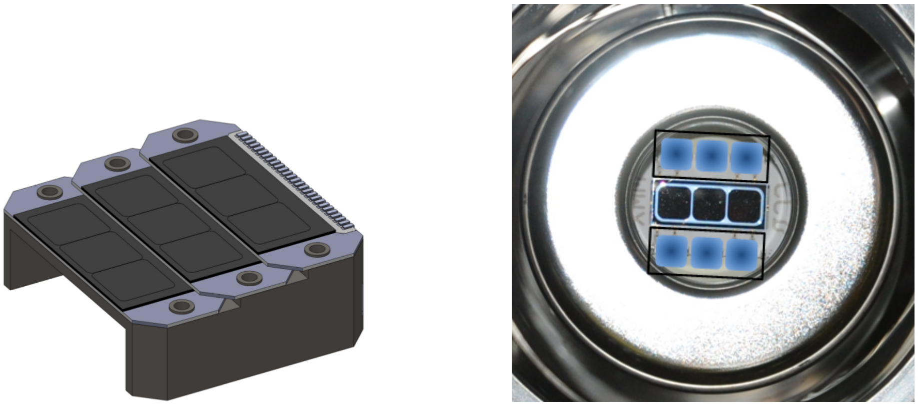
(a) Sketch of a new holder for the three SDD.

(b) Photo and draw of detector installed on its holder and the detector cup electrode around.

Figure E.2: Prevision for the 3 × 3 pads detector.

For the measurement of C, another systematic effect would have to be investigated: the magnetic mirror effect. If the magnetic field is not constant in the Decay Volume, some protons could be reflected and it would lead to a loss of count rate. To know this, measurements with the Mirror electrode active would be done still using a polarized neutron beam. The magnetic mirror effect will be characterized by the ratio R.

$$R = \frac{N^{\Uparrow\uparrow} + N^{\Downarrow\uparrow}}{N_{\text{Mirror}}} \tag{E.6}$$

One last point to work on for the measurement of C is about the magnetic field. Actually, in its configuration, there are two zero field regions at the entrance and at the exit of the Decay Volume. These would cause a problem to keep the polarization of the neutron beam.

Bibliography

[1] Adrian Signer, “The Standard Model”, Institute for Particle Physics Phenomenology, University of Durham, 2002. 5

[2] Pierre van Baal, “A course in field theory”, Institute Lorentz for Theoretical Physics, University of Leiden, 1998. 5

[3] Cabibbo N., “Unitary Symmetry and Leptonic Decays”, Phys. Rev. Lett. 10(12), 531-533, 1963. 7

[4] Kobayashi M. and Maskawa T., “CP violation in the renormalizable theory of weak interaction”, Prog. Theo. Phys. 49, 652, 1973. 7

[5] Higgs P. W., “Broken Symmetries and the Masses of Gauge Bosons”, Phys. Rev. Lett. 13, 508–509, 1964. 7

[6] Englert F., Brout R., “Broken Symmetry and the Mass of Gauge Vector Mesons”, Phys. Rev. Lett. 13, 321–323, 1964. 7

[7] Severijns N., Beck M., Naviliat-Cuncic O., “Test of the standard electroweak model in beta decay”, Reviews of Modern Physics, 78, 991, 2006. 8, 10, 14, 159

[8] Martin Simson, PhD thesis, “Measurement of the electron antineutrino angular correlation coefficient a with the neutron decay spectrometer aSPECT”, Technische Universitat Munchen, Lehrstuhl fur Experimentalphysik E18, submitted in August 2010. viii, 8, 24, 26, 28, 40, 41, 43, 46, 49, 50, 51, 55, 60, 103, 129, 153

[9] Mickael Börg, PhD thesis, “The electron antineutrino angular correlation coefficient a in free neutron decay: testing the Standard Model with the aSPECT-spectrometer”, Johannes Gutenberg-Universität in Mainz, Fachbereich 08 Physik, Mathematik und Informatik, submitted in December 2010. 8, 24, 25, 27, 28, 29, 30, 34, 35, 39, 68, 69, 70, 91, 95, 129

[10] Gertrud Konrad, PhD thesis, “Measurement of the proton recoil spectrum in neutron beta decay with the spectrometer aSPECT: study of systematic effects”, Johannes Gutenberg-Universität in Mainz, Fachbereich Physik, Mathematik und Informatik, submitted in August 2011. 8, 24, 28, 31, 36, 95, 129, 140

[11] Fidel Ayala Guardia, PhD thesis, “Characterization of electromagnetic fields in the aSPECT spectrometer and reduction of systematic effects”, Johannes Gutenberg-Universität in Mainz, Fachbereich Physik, Mathematik und Informatik, submitted in October 2011. 8, 24, 28, 36, 129

[12] Chadwick J., “The existence of a neutron”, Proc. R. Soc. Lond. A 136, 692-708, 1932. 8

[13] Beringer J. *et al.*, Phys. Rev. D86, 010001, 2012. 8, 13, 18

[14] Jackson J. D. *et al.,* “Possible Tests of Time Reversal Invariance in Beta Decay”, Phys. Rev., 106(3):517-521, 1957. 8

[15] Abele H., “The neutron. Its properties and basic interactions”, Prog. Part. Nucl. Phys., 60(1):1-81, 2008. 8

[16] Byrne J., “An Overview Of Neutron Decay”, Physics & Astronomy Subject Group School of Chemistry, Physics & Environmental Science University of Sussex, Brighton BN1 9QJ, U.K. 8, 14

[17] Fermi E., 1934, "Fermi’s Theory of Beta Decay (English translation by Fred L. Wilson, 1968)", American Journal of Physics, 36, 12. 8

[18] Wu C. S. *et al.*, “Experimental test of parity conservation in beta decay”, Phys. Rev., 105(4):1413-1415, 1957. 10

[19] Gamow G. and Teller E., “Selection rules for the β-disintegration”, Phys. Rev., 49(12):895-899, 1936. 9

[20] Gluck F. *et al.*, “Measurable parameters of neutron decay”, Nuc. Phys. A, 593(2):125-150, 1995. 9, 12, 159

[21] Dawber P. G. *et al.*, “Determination of the electron-antineutrrino correlation coefficient a in neutron β-decay by measurement of the integrated proton spectrum”, Nucl. Instr. and Meth. A, 440(3):543-547, 2000. 16

[22] Wietfeldt F.E. *et al.*, “aCORN: An experiment to measure the electron-antineutrino correlation in neutron decay”, Nucl. Instr. and Meth. A, 611(2-3):207-210, 2009. 19

[23] Grigorev V.K. *et al.*, “Experimental test of parity conservation in beta decay”, Sov. J. Nucl. Phys., 6:239, 1968. 18

[24] Stratowa C. *et al.*, ’Ratio $\left|\frac{g_\mathrm{A}}{g_\mathrm{V}}\right|$ derived from the proton spectrum in free-neutron decay”, Phys. Rev. D, 18(11):3970-3979, 1978. 13, 18

[25] Byrne J. *et al.*, “Determination of the electron-antineutrino angular correlation coefficient a_0 and the parameter $|\lambda| = |G_A/G_V|$ in free neutron β-decay from measurements of the integrated energy spectrum of recoil protons stored in an ion trap”, J. Phys. G, 28:1325-1349, 2002. 13, 18, 19

[26] Bopp P. *et al.*, “Beta-decay asymmetry of the neutron and $g_\mathrm{A}/g_\mathrm{V}$”, Physical Review Letters, vol. 56, num. 9, 3 March 1986. 13

[27] Yerozolimsky B. *et al.*, “Corrigendum: Corrected value of the beta-emission asymmetry in the decay of polarized neutrons measured in 1990”, Physics Letters B 412, 240-241, 30 October 1997. 13

[28] Liaud P. *et al.*, “The measurement of the beta asymmetry in the decay of polarized neutrons”, Nuclear Physics A 612, 53-81, 1997. 13

[29] Abele H. *et al.*, “Is the unitarity of the quark-mixing CKM matrix violated in neutron β-decay?”, Physical Review Letters vol. 88, num. 21, 27 May 2002. 13

[30] Liu J. *et al.*, “Determination of the axial-vector weak coupling constant with ultracold neutrons”, Physical Review Letters, PRL 105, 181803, 2010. 13

[31] Mund D. *et al.*, “Determination of the weak axial vector coupling $\lambda = g_A/g_V$ from a measurement of the β-asymmetry parameter A in neutron beta decay”, arXiv:1204.0013v1, 30 March 2012. 13

[32] Mendenhall M. P. *et al.*, “Precision measurement of the neutron beta-decay asymmetry”, arXiv:1210.7048v3, 19 February 2013. 13

[33] Czarnecki A., Marciano W.J., and Sirlin A.,”Precision Measurements and CKM Unitarity”, Phys. Rev. D70, 093006 (2004) [hep-ph/0406324] 13

[34] Towner I. S. and Hardy J. C., “The evaluation of Vud and its impact on the unitarity of the Cabibbo–Kobayashi–Maskawa quark-mixing matrix”, Rep. Prog. Phys. 73 046301, 2010. 13

[35] Hardy J. C. and Towner I. S., “CKM unitarity normalization tests, present and future”, Ann. Phys. (Berlin) 525, No. 7, 443–451 (2013) / DOI 10.1002/andp.201300004 13, 14

[36] Hardy J. C. and Towner I. S., “The measurement and interpretation of superallowed $0^+ \rightarrow 0^+$ nuclear β-decay”, arXiv:1312.3587v1 [nucl-ex], 12 Dec 2013. 13

[37] Severijns N. and Naviliat-Cuncic O., “Structure and symmetries of the weak interaction in nuclear beta decay”, Phys. Scr. T152 (2013) 014018. 14, 20

[38] Beck M. *et al.*, “First detection and energy measurement of recoil ions following beta decay in a Penning trap with the WITCH experiment”, Eur. Phys. J. A 47 (2011) 45 (arXiv:1008.0207v1 [nucl-ex]). 14, 20, 21

[39] Ban G. et al., “Precision measurements in nuclear β-decay with LPCTrap”, Annalen der Physik 525 (2013) 567, DOI: 10.1002/andp.201300043. 14, 20, 21

[40] Zimmer O., “V_{ud} from neutron beta decay”, Proceedings of CKM 2012, the 7th International Workshop on the CKM Unitarity Triangle, University of Cincinnati, USA, 28 September - 2 October 2012. 14

[41] Konrad G., Heil W., Baeßler S., Počanić D., Glück F., “Impact of neutron decay experiments on non-standard model physics”, World Scientific, November 2, 2012, arXiv:1007.3027v2. 14

[42] Gaponov Yu. V., “Possible Contribution of an Intermediate-Leptoquark-Boson Mechanism to Free-Neutron Beta Decay”, Physics of Atomic Nuclei, Vol. 63, No. 7, 2000. 14

[43] Dubbers D. and Schmidt M. G., “The neutron and its role in cosmology and particle physics”, arXiv 18 May 2011. 14

[44] Yerozolimsky B., “New approaches to investigations of the angular correlations in neutron decay”, arXiv:nucl-ex/0401014, 1996. 19

[45] Balashov S. and Mostovoy Y., Preprint IAE-5718/2, Russian Research Center KurchatovInstitute, Moscow, 1994. 19

[46] Počanić D. *et al.*, “Nab: Measurement principles, apparatus and uncertainties”, Nucl. Instr. and Meth. A 611, 211, 2009. 19

[47] Konrad G. *et al.*, “Neutron Decay with PERC: a Progress Report”, Journal of Physics: Conference Series 340 (2012) 012048. 19, 20

[48] Gluck F. *et al.*, “The neutron decay retardation spectrometer *a*SPECT: electromagnetic design and systematics effects”, Europhys. J. A., 23(1):135-146, 2005. 19, 24, 26, 35, 37, 94

[49] Zimmer O., Byrne J., van der Grinten M.G.D., Heil W., Glück F., “aSPECT - a new spectrometer for the measurement of the angular correlation coefficient a in neutron beat decay”, Nucl. Ins. Meth. A 440, 548, 2000. 28, 35

[50] Alexander Wunderle, PhD thesis (ongoing) on the experiment aSPECT. 28

[51] M. Simson *et al.*, “Detection of low-energy protons using a silicon drift detector”, Nucl. Instr. and Meth. A, 581(3):772-775, 2007. 45

[52] M. Simson *et al.*, “Measuring the proton spectrum in neutron decay—Latest results with aSPECT“, Nucl. Instr. and Meth. in Phys. Res. A, 611, 203–206, 2009. 45

[53] E. Gatti and P. Rehak, “Semiconductor drift chamber - an application of a novel charge transport scheme”, Nucl. Instr. and Meth. A, 225(3):608-614, 1984. 45

[54] William R. Leo, “Techniques for nuclear and particle physics experiments”, Second revised edition, Spinger-Verlag, 1992. 45, 64, 97

[55] Glenn F. Knoll, “Radiation detection and measurement”, Fourth edition, Wiley, 2010. 45

[56] PNSensor GmbH (http://www.pnsensor.de) 46

[57] http://root.cern.ch 49, 153

[58] http://www.ltspiceiv.com 53

[59] Lawrence Berkeley National Laboratory X-Ray Data Booklet, http://xdb.lbl.gov xiii, 57, 60, 102

[60] http://www.nucleide.org/ 57, 60

[61] http://www.ill.eu 65, 66

[62] H. Abele *et al.*, “Characterization of a ballistic supermirror neutron guide”, Nucl. Instr. and Meth. A, 562(1):407 - 417, 2006. 66

[63] F. Glück, “The Penning discharge”, internal KATRIN document, 7 March 2007. 82, 118

[64] Romain Virot, Master thesis, “Characterization of the new data acquisition system and the detector alignment of the aSPECT experiment”, Grenoble INP - Phelma Ecole Nationale Superieure de Physique, Electronique et Matériaux, 2013. 62, 74, 75, 78, 79

[65] F.E. James, “Statistical methods in experimental physics”, 2nd edition, World Scientific Publishing Co. Pte. Ltd., 2006. 97, 110

[66] http://www.pfeiffer-vacuum.com/ 86, 147

[67] Pfeiffer, “Partial pressure measurement in vacuum technology”, Prisma Plus documentation. 89, 90, 93

[68] R. H. Fowler and Dr. L. Nordheim, “Electron Emission in Intense Electric Fields”, Proceedings of the Royal Society of London, vol. 119, no 781, p. 173–181, 1st may 1928. 102

[69] E. Browne and J. K. Tuli. Nuclear data sheets for a = 65. Nucl. Data Sheets, 111:1093, 2010. 74

[70] B. Singh. Nuclear data sheets for a = 64. Nucl. Data Sheets, 108:197, 2007. 74

[71] http://www.saesgetters.com 148

[72] Group3 Technology LtD. www.group3technology.com 151

[73] Schumann M. *et al.*, "Measurement of the Proton Asymmetry Parameter C in Neutron Beta Decay",Phys. Rev. Lett. 100:151801, 2008. 13, 159

[74] Kreuz M. *et al.*, "The crossed geometry of two super mirror polarisers—a new method for neutron beam polarisation and polarisation analysis", Nucl. Instr. Meth. A 547, 583, 2005. 159, 160

[75] Glück F., "The proton asymmetry in neutron decay ", Phys. Lett. B 376, 25, 1996. 159

[76] Christine Klauser, PhD thesis, "High precision neutron polarization for PERC", Technische Universität Wien Atominstitut, submitted in 2013. 161

Résumé

La désintégration β du neutron est définie par divers coefficients de corrélation mesurables qui sont utilisés pour déterminer des paramètres du Modèle Standard et rechercher de la nouvelle physique. L'objectif du spectromètre aSPECT est de mesurer le coefficient a de corrélation angulaire entre l'électron et l'antineutrino dans la décroissance du neutron avec une précision sans précédent de 1%. Ce coefficient est extrait à partir d'une mesure de haute précision du spectre d'énergie des protons.

Un point central de cette thèse est l'analyse du bruit de fond, motivée par les observations de décharges durant le temps de faisceau de 2011, et par une précédente indication d'une dépendance sur le potentiel de sélection des protons. Au cours de cette thèse, plusieurs mesures ont été réalisées hors ligne, en absence de particules ionisantes issues de la désintégration du neutron. Un bruit de fond "interne" (rayons-X et ions) a été identifié. Son influence sur $\Delta a/a$ est de l'ordre de 10^{-5} à 10^{-4} suivant le niveau du vide ($\sim 10^{-9}$ mbar) et la configuration du spectromètre.

L'analyse des données du temps de faisceau en 2013 a permis de construire un modèle de correction des différents bruits de fond présents dans l'expérience de désintégration du neutron, en considérant sa dépendance dans le temps. La correction est d'environ 3% sur le coefficient pour une configuration et un vide standard, mais elle peut atteindre 7% dans une configuration défavorable. Pour réduire ce bruit de fond, un champ électrique de dérive a été appliqué près du maximum du potentiel de sélection. Des mesures supplémentaires réalisées durant ce temps de faisceau incluaient des tests systématiques comme les effets de bord (profil du faisceau) et différentes configurations des électrodes. Afin d'obtenir le résultat final, l'analyse doit être complétée en incluant les différentes corrections et en la comparant avec des simulations des effets systématiques.

Abstract

Neutron β-decay is parametrized by several measurable correlation coefficients which are used to determine parameters of the Standard Model and to search for new physics. The aim of the retardation spectrometer aSPECT is to measure the electron-antineutrino angular correlation coefficient a in neutron decay with an unprecedented accuracy of well below 1%. The coefficient is extracted from a high precision measurement of the proton energy spectrum.

A central point of this PhD thesis is the analysis of the background, motivated by the observations of discharges during the beam time of 2011, and an earlier indication for a dependence on the retardation potential. During this thesis, several measurements were conducted off-line, without ionizing particles from neutron decay. An "internal" background (X-rays and ions) was identified. It has an influence of 10^{-5}-10^{-4} on $\Delta a/a$ depending on the vacuum level ($\sim 10^{-9}$ mbar) and the spectrometer settings.

Within the analysis of the data from the beam time in 2013, a model was built to correct for backgrounds present in the neutron decay experiment, taking into account its time dependence. The correction is about 3% on the coefficient for standard settings and vacuum but it can reach 7% for unfavorable settings. To reduce the background, a drift electric field was applied close to the maximum of the retardation potential. Additional measurements performed during this beam time included tests of systematics, in particular the edge effect (beam profile) and different electrode settings. In order to obtain the final result, the analysis has to be extended by including the different corrections and by comparing with simulations of the systematic effects.